Understanding Reactive Organometallic Complexes through Mass Spectrometry



Institute for Molecules and Materials

Jaya Mehara

RADBOUD UNIVERSITY PRESS

Radboud Dissertation Series

Understanding Reactive Organometallic Complexes through Mass Spectrometry

Jaya Mehara

Author: Jaya Mohansingh Mehara

Title: Understanding Reactive Organometallic Complexes through Mass Spectrometry

Radboud Dissertations Series

ISSN: 2950-2772 (Online); 2950-2780 (Print)

Published by RADBOUD UNIVERSITY PRESS Postbus 9100, 6500 HA Nijmegen, The Netherlands www.radbouduniversitypress.nl

Design: Proefschrift AIO | Annelies Lips Cover: Proefschrift AIO | Guntra Laivacuma

Printing: DPN Rikken/Pumbo

ISBN: 9789465150161

DOI: 10.54195/9789465150161

Free download at: www.boekenbestellen.nl/radboud-university-press/dissertations

© 2024 Jaya Mohansingh Mehara

RADBOUD UNIVERSITY PRESS

This is an Open Access book published under the terms of Creative Commons Attribution-Noncommercial-NoDerivatives International license (CC BY-NC-ND 4.0). This license allows reusers to copy and distribute the material in any medium or format in unadapted form only, for noncommercial purposes only, and only so long as attribution is given to the creator, see http://creativecommons.org/licenses/by-nc-nd/4.0/.

Understanding Reactive Organometallic Complexes through Mass Spectrometry

Proefschrift ter verkrijging van de graad van doctor
aan de Radboud Universiteit Nijmegen
op gezag van de rector magnificus prof. dr. J.M. Sanders,
volgens besluit van het college voor promoties
in het openbaar te verdedigen op

donderdag 12 december 2024 om 12.30 uur precies

door

Jaya Mohansingh Mehara

Promotor:

Prof. dr. J. Roithová

Manuscriptcommissie:

Prof. dr. A.P.M. Kentgens

Prof. dr. P. Chen (ETH Zürich, Zwitserland)

Prof. dr. S. Harutyunyan (Rijksuniversiteit Groningen)

Understanding Reactive Organometallic Complexes through Mass Spectrometry

Dissertation to obtain the degree of doctor

from Radboud University Nijmegen

on the authority of the Rector Magnificus prof. dr. J.M. Sanders,

according to the decision of the Doctorate Board

to be defended in public on

Thursday, December 12, 2024 at 12.30 pm

by

Jaya Mohansingh Mehara

Supervisor:

Prof. dr. J. Roithová

Manuscript Committee:

Prof. dr. A.P.M. Kentgens

Prof. dr. P. Chen (ETH Zürich, Switzerland)

Prof. dr. S. Harutyunyan (University of Groningen)

Contents

Chapter 1	Introduction	9
Chapter 2	Methods	43
Chapter 3	Competing Mechanisms in Palladium-Catalyzed Alkoxycarbonylation of Styrene	55
Chapter 4	Mechanistic Studies of the Palladium-Catalyzed S,O-Ligand Promoted C–H Olefination of Aromatic Compounds.	115
Chapter 5	Cationic Gold(II) Complexes: Experimental and Theoretical Study	145
Chapter 6	Binding interactions in copper, silver, and gold π -complexes	203
Chapter 7	Copper(II)-TEMPO interaction	239
Appendices	Summary Samenvatting Concluding remarks Research Data Management List of Publications Curriculum Vitae Acknowledgements List of abbreviations	288 290 292 293 295 296 297 300
		0



Chapter 1

Introduction

The work in this Introduction chapter is published as Perspective in Chemical Science: Mehara, J.; Roithová, J. Identifying Reactive Intermediates by Mass Spectrometry. Chem. Sci. **2020**, 11 (44), 11960–11972.

Development of new reactions requires finding and understanding novel reaction pathways. In complex reactions such as C-H activations, these pathways often involve highly reactive intermediates, which are the key to our understanding but are challenging to study. Mass spectrometry has a unique sensitivity for detecting low abundant charged species; therefore, it is increasingly used for the detection of such elusive intermediates, particularly in the realm of metal-catalyzed- and organometallic reactions. This introduction chapter aims to provide an overview of recent developments in the field of mass spectrometric research of reaction mechanisms with a particular focus on going beyond traditional mass-detection. Sections describe the advantages of collision-induced dissociation, ion mobility, and ion spectroscopy to elucidate the structures of the detected intermediates. Additionally, it delves into the relationship between the condensed phase chemistry and mass spectrometric species detection in solution.

Introduction

Progress in chemistry is driven by findings of new chemical transformations that allow us to construct new molecules and materials. The further advances are based on our understanding of chemical reactions and ability to use this knowledge to control the reactivity. Hence, the development of new reactions always goes hand in hand with mechanistic studies that rationalize these reactions and give us a handle to build upon them further.

Many spectroscopic methods are used to monitor chemical reactions. The in situ methods such as optical spectroscopies (IR or UV-Vis spectroscopy) or NMR spectroscopy can determine rates of transformation of reactants to the products and in connection with modern physical organic chemistry methods provide deep insight into reaction mechanisms.¹⁻³ Detection of key reaction intermediates is another important part in elucidation of reaction mechanisms. It can be easy for some reactions, but it could be rather challenging for other ones.4 Especially in recent organometallic, photocatalytic, electrocatalytic, or other catalytic reactions that are based on the generation of highly reactive species in solution, detection of intermediates can be challenging.

Reactive intermediates, often short-lived and present in low concentrations, necessitate specialized detection methods. In situ detection of these species often relies on their unique properties that help suppress the signals of dominant species in solution. An example could be EPR (electron paramagnetic resonance) spectroscopy for radical intermediates or NMR spectroscopy based on metal elements present just in a metal-based catalyst and its complexes. Another strategy relies on ex situ approaches. The popular ex situ approach is crystallization of a metal-complex intermediate out of the reaction mixture. X-ray crystallography offers many details about these intermediates and therefore provides valuable data. However, it also has pitfalls. Firstly, the effort to crystalize the intended reactive intermediates is often accompanied by modifications of the complexes in order to make them more stable, which can introduce a bias to the study. Secondly, crystallization may yield off-cycle intermediates rather than reactive intermediates.

Mass spectrometry analysis serves as another ex situ approach, offering extreme sensitivity for the detection of minor species. The reaction mixtures can be directly analyzed using an electrospray ionization interface.⁵ The simple implementation and broad availability of mass spectrometers resulted in the growing popularity of mass spectrometry analysis in the investigation of reaction mechanisms. Particularly, catalytic organometallic reactions are often addressed by mass spectrometry, because metal-containing intermediates are usually easily ionized (or present as ions in solution per se) and thus selectively detected.^{6,7} Despite its advantages, mass spectrometry analysis lacks direct structural information, and blind assignment of ions generated by electrospray ionization may lead to misinterpretation of reaction mechanisms. This chapter discusses the various methods developed to address these challenges, providing a comprehensive understanding of mass spectrometry analysis of reaction intermediates.8

Detection of reactive intermediates by ESI-MS

Mass spectrometry detects ions. Hence, reactions involving charged intermediates are easily monitored by electrospray ionization mass spectrometry.^{5,9-11} Typically, such intermediates are operative in reactions catalyzed by cationic complexes of gold, silver, copper, rhodium, or ruthenium with non-coordinating counterions such as SbF₆, BF₄, PF₆, etc. Other examples are organocatalytic reactions proceeding via iminium ions and basic intermediates. The latter can be easily detected as protonated or as sodiated ions. 12,13

The C-C coupling reactions belong to the most important chemical transformations. These reactions are typically catalyzed by palladium complexes, which are often neutral in solution. They can be detected as protonated ions or as anions, 14,15 but it is by far not a general rule. Therefore, these intermediates are often studied using the charge-tagging approach. Either substrate or a ligand of the catalyst is decorated by a permanently charged group placed in a position that does not affect the reaction itself.¹⁶⁻²⁰ Thereby, the intermediates can be detected as ions, yet the "neutral reaction intermediate core" is unaffected.

An example of using the charge-tagging method could be a study of palladiumcatalyzed C-H functionalization. Palladium-catalyzed C-H activation using a directing group leads to palladium(II) intermediates such as complex 1 in Figure 1.²¹ The activated carbon atom can be coupled with various reactants.²²⁻²⁴ Czyz et al. explored a mechanism of the coupling with iodine promoted by photoexcitation of the palladium(II) complex (Figure 1).²⁵ Using the charge tagging method they could monitor the starting complex (m/z 535, blue triangle), formation of the product (m/z) 516, green circle) and also formation of ions with m/z 748 (red box) corresponding either to palladium(IV) intermediates or to palladium(II) complex with the product.

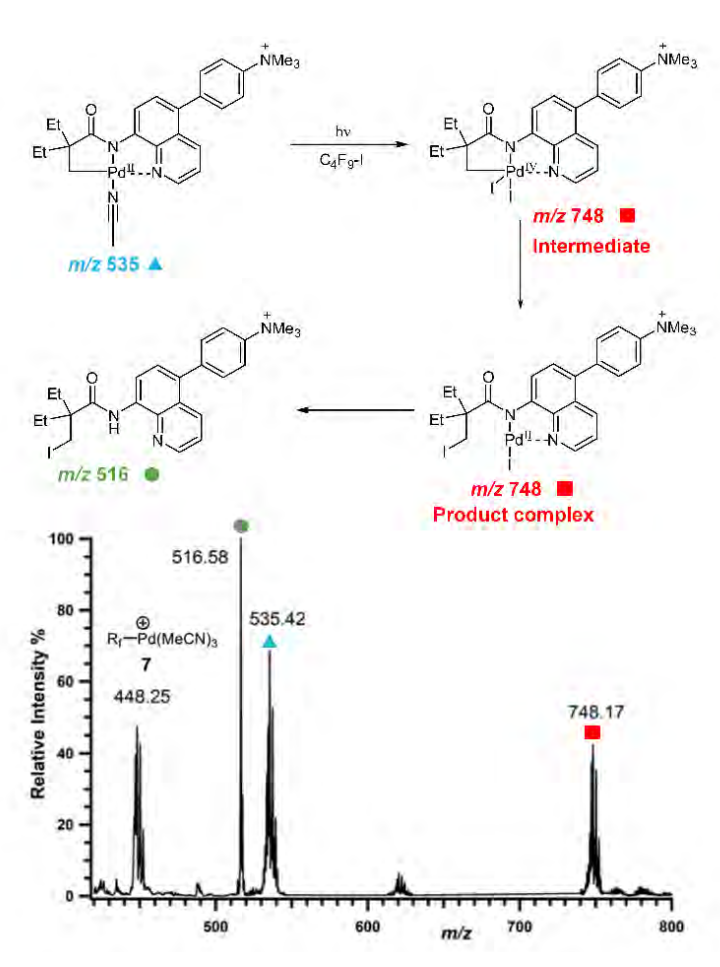


Figure 1. ESI-MS detection of intermediates in a palladium-catalyzed photochemical reaction. Adapted with changes from Ref. [25] under CC BY 3.0 license.²⁶

Without going into the details of this reaction, we want to focus on the common problem in the investigation of organometallic reactions. According to the textbook knowledge, the expected reaction intermediates and the product complexes are often connected by a reductive elimination step and thus have a different structure, but the same mass. It can be tempting to assign the detected complexes to the intermediates and thus provide the desired indices for the expected reaction mechanism. Nevertheless, it could be misleading, if the ions actually correspond to the product complexes that were formed by a different pathway. The mere observation of "the correct mass" is insufficient, instead every effort must be made to relate the mass spectra to the reaction intermediates and to the reaction mechanism.

Structure of reactive intermediates by ESI-MS²

Assigning possible structures to the detected ions has been classically done based on their fragmentation pattern. In the detection of intermediates for organometallic reactions (such as shown in Figure 1), this simple approach is complicated by the fact that the intermediates and the product complexes can follow the same or similar fragmentation pathways (Figure 2). This is especially true if the energy barrier between the intermediate and the product complex is small and the energy demands for the fragmentations are large. For example, if the energy demand for the intermediate fragmentation is much larger than the energy of the transition state for the rearrangement to the product complex (blue vs. black pathway in Figure 2). In that case, we will observe the same or similar fragmentation pattern for the intermediate and the product complex.

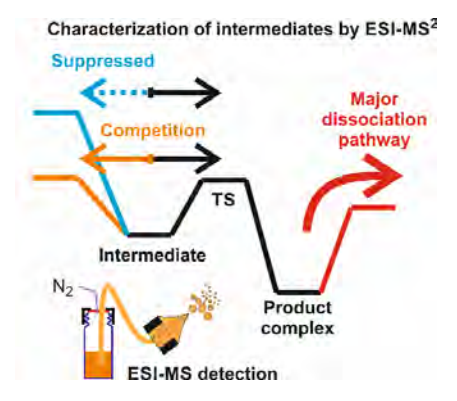


Figure 2. An example of a potential energy surface for gas-phase dissociation of reactive intermediates and product complexes connected by a simple reaction step such as reductive elimination (see e.g. Figure 1).

Characterization of the intermediates by ESI-MS² is possible if the fragmentation energy and the energy of the transition structure for the rearrangement to the product complex are similar (orange pathway in Figure 2). Experimentally, this approach requires a control experiment with the complex generated from the catalyst and the independently prepared product. This is nicely shown in the work of Parera et al.²⁷ The authors studied cyclotrimerization reaction, which is extremely demanding in terms of possible detection of isobaric complexes (Figure 3, the grey panel). The authors detected rhodacyclic intermediate (in red, Figure 3) and they were able to differentiate it from the product complex (in green). The reason for this successful ESI-MS² characterization is that the homolytic cleavage of the tosyl group in the intermediate can kinetically compete with the reductive elimination leading to the product (Figure 3). The product complex is dominantly losing the neutral product and does not eliminate the tosyl radical as the authors showed in a separate experiment.²⁷

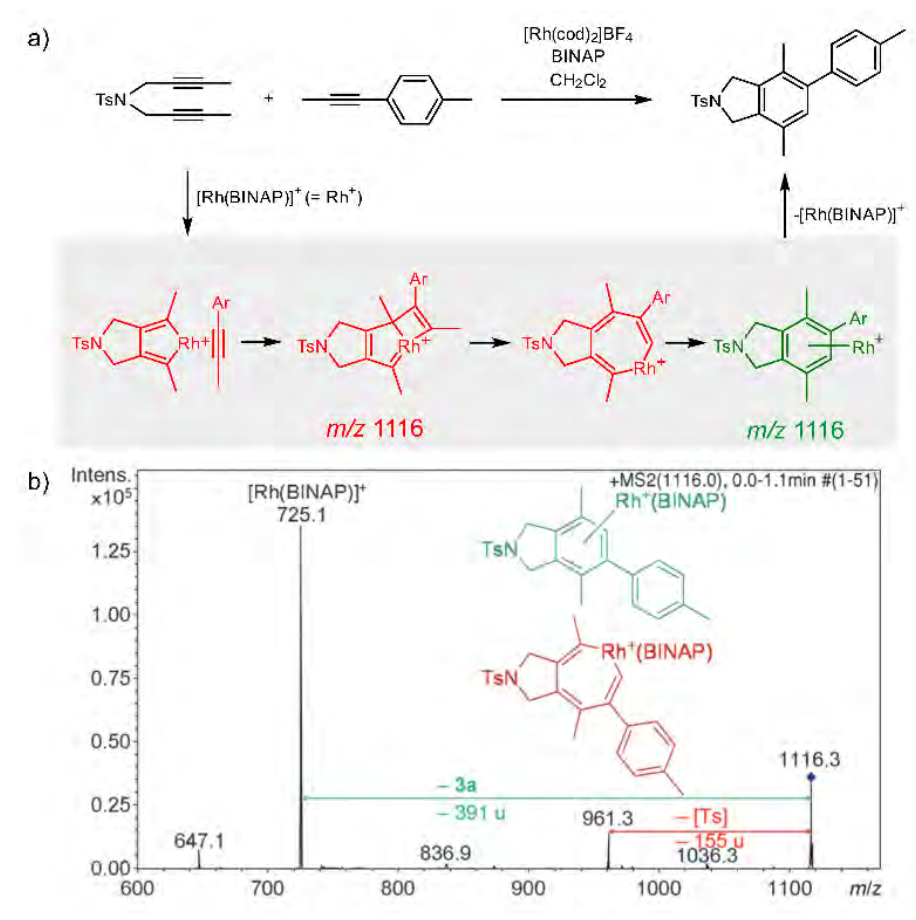


Figure 3. Catalytic cycle proposed for the [2+2+2] cycloaddition of diynes and monoynes under Rh/ bisphosphine catalysis (the BINAP ligand has been omitted for clarity) with CID mass spectrum of the ion at m/z = 1116.3 from the reaction mixture. Adapted with permission from Ref. [27] Copyright 2012 WILEY-VCH Verlag GmbH & Co. KGaA, Weinheim.

The work of Auth et al. shows how to use ESI-MS² for the investigation of the transformation from the reactive complex to the product.²⁸ The authors studied transmetallation reaction within phenylborate complexes. They mixed Li(BPh₄) salt with AgOTf and studied the possible transfer of the phenyl group from boron to either lithium or silver. The ESI-MS detected $[(BPh_a)^TM^+(BPh_a)^T]$ anionic complexes

(see Figure 4 for the structure). These complexes either fragment to the [(BPh,)-M+] ion pair and the (BPh_a)⁻ anion, or they undergo transmetallation to yield [(BPh_a) M(Ph)] and neutral BPh₃. The latter is observed only for silver complexes, proving that transmetallation is possible with silver but not lithium.

The approach of transferring complexes of this type to the gas phase and triggering the desired transformation by collisional heating offers a good control over the overall process. Hence, it creates defined conditions for systematic investigation of various metals as well as of the organic groups in transmetallation reactions. The authors demonstrated this in the study of metal clusters of various sizes and evaluated the trends (the energy demand for the transmetallation decreases in larger clusters).

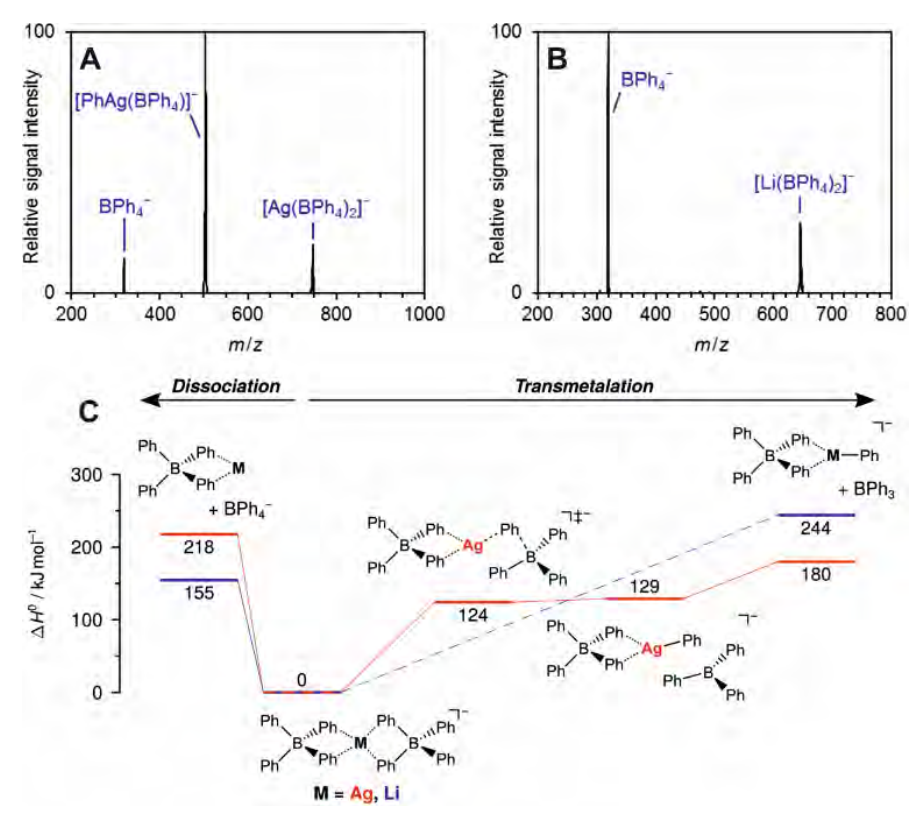


Figure 4. Collision-induced dissociation spectra of mass-selected [M(BPh,),] anions. A) M=Ag, B) M=Li. C) Potential energy surface for dissociation of [M(BPh_a),]⁻. Reprinted (adapted) with permission from Ref. [28]. Copyright 2020, American Chemical Society.

Collision-induced dissociation (CID) of mass-selected ions can also be used to quantitatively evaluate bond dissociation energies.²⁹⁻³¹ Kinetic modeling of the energy-dependent fragmentation yield in a CID experiment provides threshold energy for the given dissociation (e.g., Figure 5b). The threshold energy is the minimum energy required for the given dissociation and thus corresponds to bond-dissociation energy. There are various experimental approaches to obtain the relevant data and various ways to perform kinetic modeling. 30,31 This section is limited to the discussion of an example from Peter Chen's group. They presented an elegant study to describe a complex that can be considered as a model for a transmetallation transition structure (see Figure 5a). Using a thermodynamic cycle shown in Figure 5a they could estimate stabilization of this complex by copper-palladium interaction (9 kcal mol⁻¹).³² The approach of using tandem mass spectrometry to investigate reaction intermediates can be extended even further. For example, Waters et al. used the ESI-MSⁿ method to investigate the whole catalytic cycle of methanol oxidation by [Mo₂O₂(OH)]⁻ (and other metal oxides) in the gas phase.³³ This research extends toward the classical gas-phase chemistry approach for studying reactions and will not be further discussed here.34-36 Instead, the following section focuses on the methods providing more structural information about the reactive intermediates directly detected from the solution.

Beyond mass-analysis: Ion mobility separation

Ion mobility separation is an increasingly popular addition to the mass spectrometry analysis.^{37–40} It separates isobaric ions based on their ion mobilities which essentially reflect their shapes. Clearly, this is an ideal approach to solve the dilemma of detecting reactive intermediate vs. the product complex discussed in the previous section. The intermediates and the product complexes have the same mass but should have different molecular volumes and, thus, different ion mobility cross sections. Hence, we should be able to separate them and thus eliminate the problem of mass overlap. The ion mobility cross-section can be obtained from theoretical calculations, and thus, the experimental value can be compared with the predicted cross-sections and assigned to a particular isomer/conformer.

An excellent example of separating a multitude of possible isomeric intermediates comes from the Hashmi and Kappes groups.⁴¹ They have investigated the goldcatalyzed cycloisomerization reaction of a 1,5-bis-terminal diyne followed by a coupling reaction with benzene (Figure 6a).41 The reaction is catalyzed by two gold cations, and at every point, several possible isomers can be formed. All the

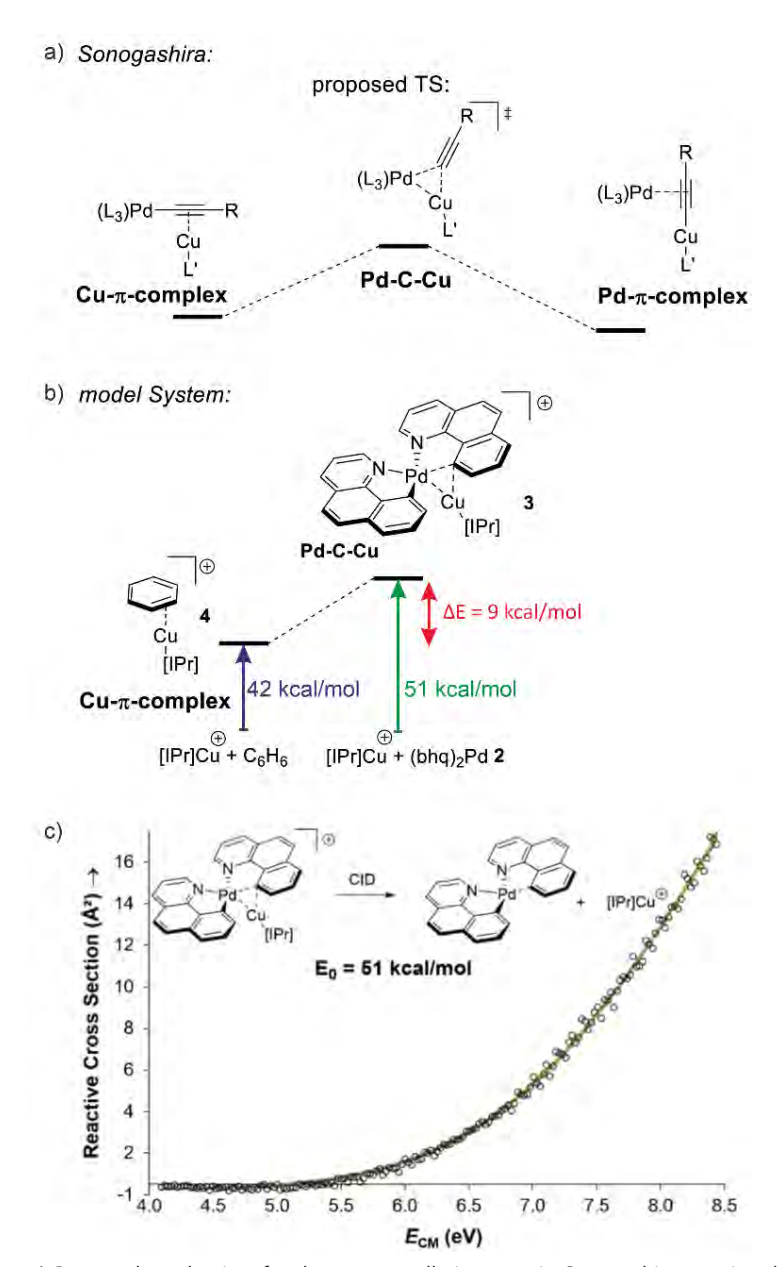


Figure 5. a) Proposed mechanism for the transmetallation step in Sonogashira reaction. b) Model to evaluate metal-metal interaction in a complex mimicking transmetallation transition structure. The binding energies of the ligated copper cation to benzene and the palladium complex can be determined from the energy-resolved collision-induced dissociation experiment. The binding energy was determined by kinetic modeling using the L-CID program.²⁹ c) Zero-pressure-extrapolated cross sections (circles) with L-CID-fitted curves (lines). Inset: Reaction scheme for CID of the palladium complex with the corresponding activation energy (E_n) . Reprinted (adapted) with permission from Ref. [32]. Copyright 2017, American Chemical Society.

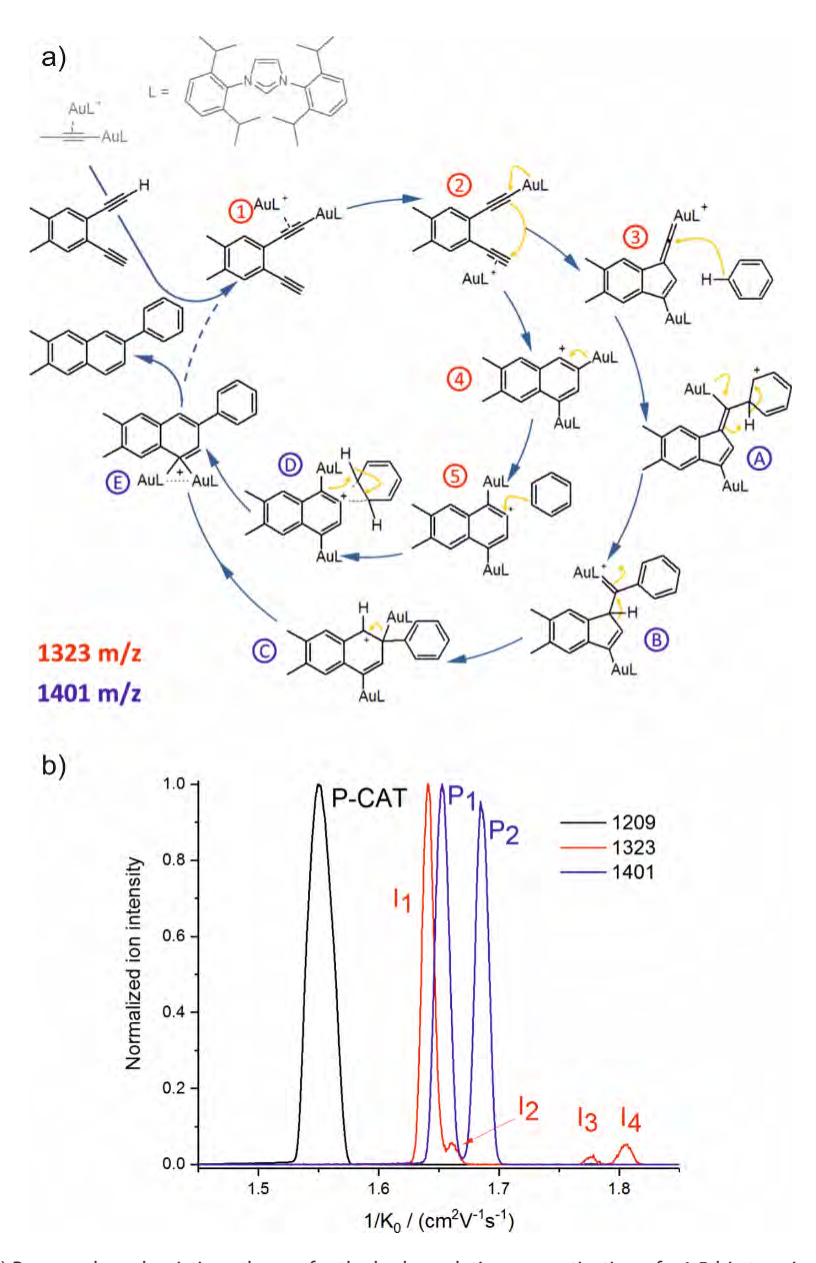


Figure 6. a) Proposed mechanistic pathways for the hydroarylating aromatization of a 1,5-bis-terminal diyne R1 as catalyzed by the synergistic interplay of two gold centers [(L)Au]⁺. b) Mobilograms: the $[(L)_2Au_2(C_3H_3)]^+$ precatalyst (m/z 1209, black, P-CAT); the $[(L)_2Au_2(R1-H)]^+$ intermediate (m/z 1323, black, P-CAT). red, I1–I4)), and the $[(L)_2Au_2(R1-H)(C_6H_6]^+$ intermediate after the reaction with benzene (m/z 1401, blue; P1 and P2). Reprinted (adapted) with permission from Ref. [41]. Copyright 2018, American Chemical Society.

complexes along the catalytic cycle can be easily detected by ESI-MS, because they are cationic. However, it would be impossible to study this reaction just by means of ESI-MSⁿ, because all the complexes' fragmentation patterns will be similar.

Figure 6b shows signals of individual mass-selected ions separated according to the ion mobilities of the contributing isomers. The reaction is catalyzed by cationic gold, and the authors used $[(L)Au(C_2H_2)]$ (L = IPr, see the structure in Figure 6a) as the precatalyst. It can be detected by ESI-MS as dimeric [(L)₂Au₂(C₂H₂)]⁺ cations. As expected, these ions are present as only one isomer, thus represented by a single peak in the mobilogram (Figure 6b).

The first family of reaction intermediates is formed by activation of the diyne by two cationic gold complexes ([(L)₂Au₂(R1-H)]⁺, see complexes labeled by a red label in Figure 6a). The authors detected four of these intermediates (red line in Figure 6b). The experiments can provide collision cross-sections of these ions, which can be compared with theoretical calculations for various possible isomers. Such analysis allowed the authors to assign the detected ions to intermediates 1 – 4 in Figure 6a. The next step is a coupling between [(L),Au,(R1-H)]+ and benzene. Again, a multitude of intermediates can be, in principle, detected (complexes labeled in blue in Figure 6a). However, only two complexes corresponding to these intermediates were trapped by ESI-MS (purple line in Figure 6b). A comparison of experimental and theoretical cross-sections suggested that the authors probably trapped intermediates B and C (see Figure 6a). Hence, the authors detected intermediates along both reaction pathways, as shown in Figure 6a. Here, both pathways lead to the same product, hence the branching between the pathways does not affect the outcome of the reaction. However, in other cases, the branching of reaction pathways can affect reaction selectivity. This ESI-IMS-MS approach offers an easy tool to check how reaction conditions affect the branching between the reaction pathways, which might facilitate reaction optimization.

Another example of how ion mobility separation can add another dimension to the mass-spectrometric investigation of reaction intermediates comes from the group of Guo.⁴² They studied intermediates formed in an organocatalytic reaction developed for C-N couplings.¹ This type of reaction is well suited for mass spectrometry investigation because the intermediates are either charged iminium ions (e.g., I, in Figure 7) or easily protonated amines or enamines (e.g., 5 in Figure 7).⁴³ The organocatalytic reactions are often used for stereoselective reactions.⁴⁴ Here, product 4 is formed as R or S stereoisomer at the α -carbon atom of the aldehyde. The stereochemistry is predetermined by the configuration of the key enamine

intermediate 5.1 The key finding of this study is that the ratio of enamine intermediates Z-5 and E-5 can be easily determined by the ESI-IMS-MS approach, which the authors verified by NMR spectroscopy. ESI-IMS-MS detection could be an alternative to NMR or chromatography detection of these intermediates. More importantly, it can be the tool of choice for shorter-lived intermediates that cannot be easily detected by NMR or chromatography.

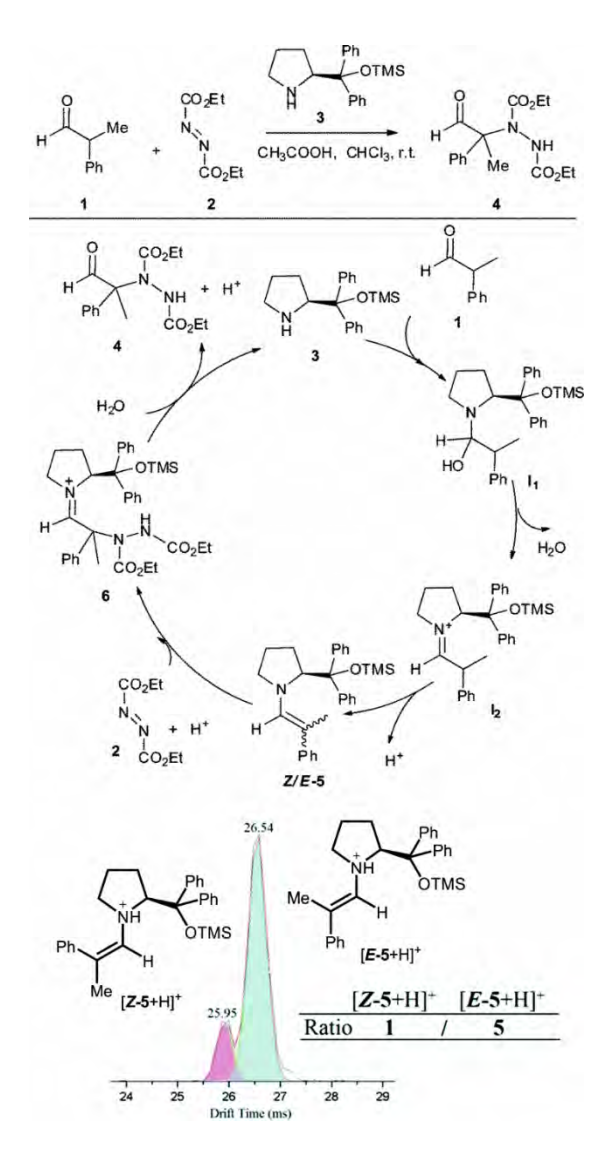


Figure 7. Organocatalytic reaction for C-N bond coupling. The key reactive enamine intermediate 5 was detected by ESI-MS, and its Z- and E-isomers were separated by ion mobility. Adapted from Ref. [42] with permission from The Royal Society of Chemistry.

The final example showing a great promise of ion mobility separation for the investigation of reaction intermediates and reaction mechanisms is from the group of Schröder. 45 They have used ESI-IMS-MS to study epimerization of a bis-Tröger bases (Figure 8). Tröger bases are trapped as enantiomers due to the steric strain that hinders epimerization by inversion at the nitrogen atoms. Yet, these bases can epimerize by bond-breaking processes, which could either correspond to the formation of iminium ions upon protonation or to the retro Diels Alder reaction (Figure 8a).

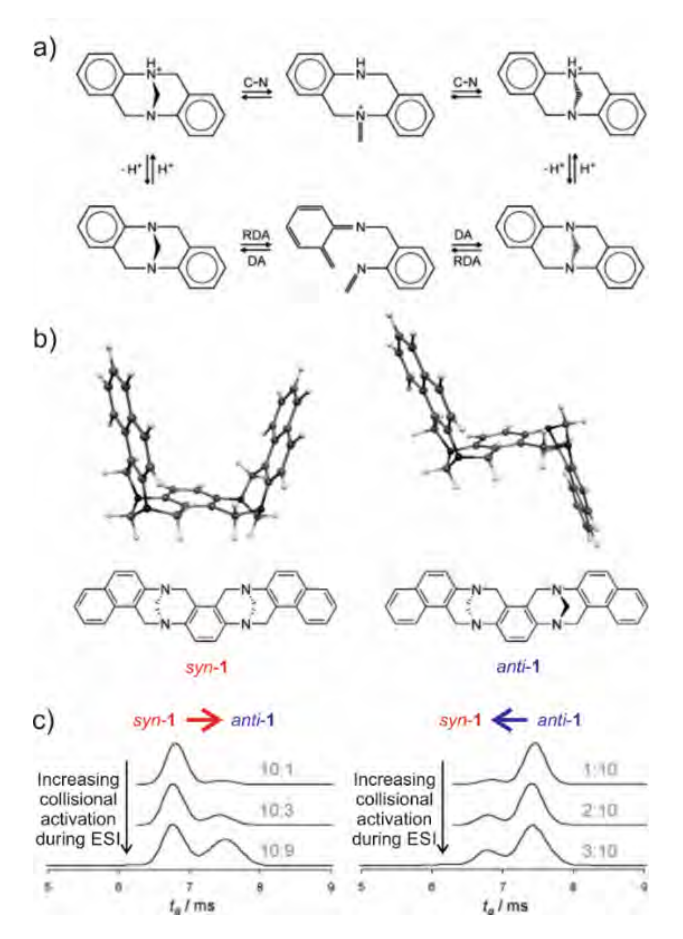


Figure 8. a) Proposed pseudo-epimerization mechanisms of Tröger bases via iminium ions (top) and via retro-Diels-Alder sequence (bottom). b) Bis-Tröger bases syn-1 and anti-1 and their structures predicted by DFT theory. c) Ion-mobility traces of mass-selected syn-1H+ (left) and anti-1H+ (right) as a function of the increasing cone voltage. The grey numbers are the ratios of integrated areas of the peaks corresponding to syn-1 and anti-1, respectively. Adapted with permission from Ref. [45] Copyright 2011 WILEY-VCH Verlag GmbH & Co. KGaA, Weinheim.

The bis-Tröger base 1 can have either syn or anti configuration (Figure 8b). The diastereoisomers syn-1 and anti-1 are stable and can be separated by chromatography. Electrospray ionization of these bases yields protonated ions syn-1H⁺ and anti-1H⁺. The anti-isomer has a more extended molecular shape, which correlates with a larger collisional cross section and thus a longer arrival time in the ion mobility experiment (Figure 8c). The researchers used a variation of electrospray ionization conditions to study the pseudo-epimerization process. With increasing collisional activation during ESI, they observed increasing epimerization of the starting isomer to the other. The syn \rightarrow anti isomerization required less energy than the reverse process, suggesting that the anti-isomer is thermodynamically more stable.

The researchers also studied sodiated ions syn-1Na⁺ and anti-1Na⁺ in analogous experiments. However, these ions showed no isomerization, although the retro-Diels-Alder pathway should be accessible. Hence, this study showed that pseudoepimerization could efficiently proceed upon protonation via the iminium ion formation, whereas the retro-Diels-Alder pathway is mechanistically disfavored.

Beyond mass analysis: Ion spectroscopy

Ion spectroscopy is another technique that adds more dimensions to mass spectrometric separation. 46-48 Ion spectroscopy provides IR, Vis, and UV spectra of mass-selected ions, adding information about their molecular and electronic structure. Small densities of mass-selected ions in a mass spectrometer do not usually permit direct measurements of absorbance/transmittance as in classical optical spectroscopies. Instead, the absorption of photons is detected indirectly by monitoring ion fragmentation caused by photon absorption. That is why ion spectroscopy is often referred to as photodissociation spectroscopy. 49-51

IR and UV/Vis spectra of mass-selected ions are usually assigned based on theoretical calculations. The fact that the spectra belong to isolated ions in a "vacuum" simplifies the theoretical calculations, and results are often in excellent agreement. Access to this spectroscopic information solves the problem of mass overlap for detected intermediates with product complexes. In addition, it provides important structural information and thus gives deeper information about the nature of the intermediates.

The first example of using IR photodissociation spectroscopy for the characterization of reaction intermediates is from gold chemistry.⁵² Gold activated alkynes can be oxidized by an oxygen-transfer reagents such as pyridine N-oxide (Figure 9a). It has been postulated that the oxidation leads to elusive gold(I) α -oxocarbenes that react further. If the reaction proceeds in acetonitrile, the reaction continues to oxazole products (see Figure 9a). Electrospray ionization of the reaction mixture provides ions with m/z 782 and m/z 744 (among others). These ions can correspond to reaction intermediates (upper structures in the colored boxes in Figure 9a). The ions with m/z 782 can also represent an isomer of the primary intermediate (lower structure in the green box in Figure 9a). This isomer can be protodeaurated to yield α -pyridinium ketone – a by-product in the reaction. The ions with m/z 744 can also correspond to the complexes between the oxazole product and the gold catalyst (the lower structure in the red box in Figure 9a).

The IR photodissociation spectra of the detected ions show that none corresponds to the primary intermediates (Figures 9b,c). The spectrum of the gold complex of α -pyridinium ketone clearly displays C=O stretching vibration of the ketone function (Figure 9b). In contrast, the spectrum of the gold complex of oxazole features C=N and C=C stretching bands of the oxazole ring. This simple example shows that IR photodissociation spectroscopy can provide a direct link to the structure of the detected ions and thus assist in the correct evaluation of the results (see also discussion in the next section).

Another example comes from the field of reaction development and concerns silver-catalyzed C-O and C-N coupling reactions.⁵⁴ The group of Ribas envisaged a catalytic cycle based on silver(I) complexes. They designed a reaction starting with a silver(I) complex, which undergoes oxidative addition with an aryl iodide to form a silver(III) intermediate. This intermediate should exchange iodide with an N- or O-based nucleophile. The reaction sequence is completed by reductive elimination to form the new C-N or C-O bond, respectively (Figure 10a). They demonstrated that the idea worked for a range of N- and O-nucleophiles for a substrate shown in Figure 10. They used mass spectrometry and ion spectroscopy to prove that the reaction proceeds via the envisaged silver(III) intermediates.

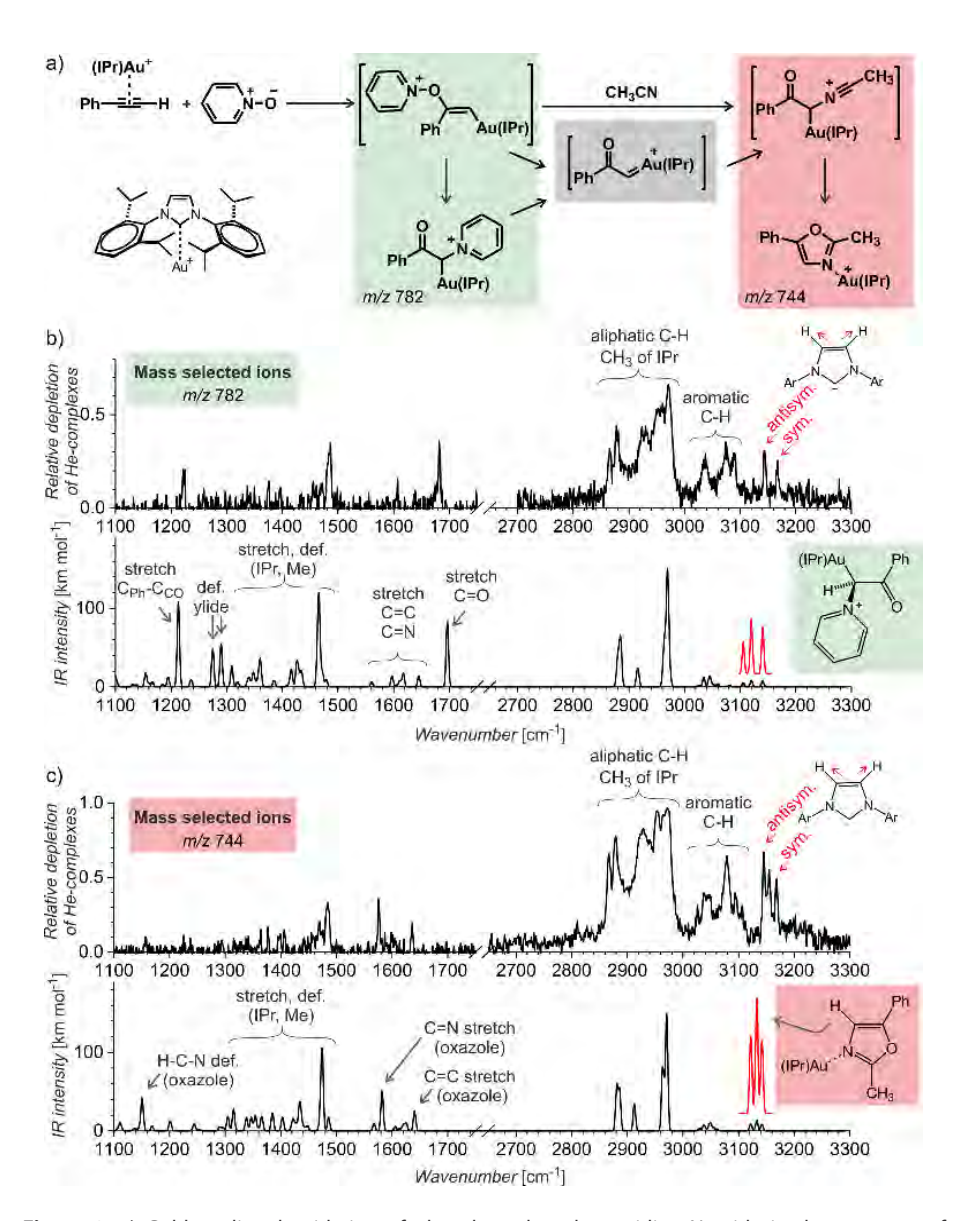


Figure 9. a) Gold-mediated oxidation of phenylacetylene by pyridine N-oxide in the presence of acetonitrile. b,c) IR photodissociation spectra of ions with (b) m/z 782 and (c) m/z 744 measured by the helium-tagging method⁵³ and their comparison with DFT predicted IR spectra of the product complexes.⁵² Adapted with permission from Ref. [52] Copyright 2016 WILEY-VCH Verlag GmbH & Co. KGaA, Weinheim.

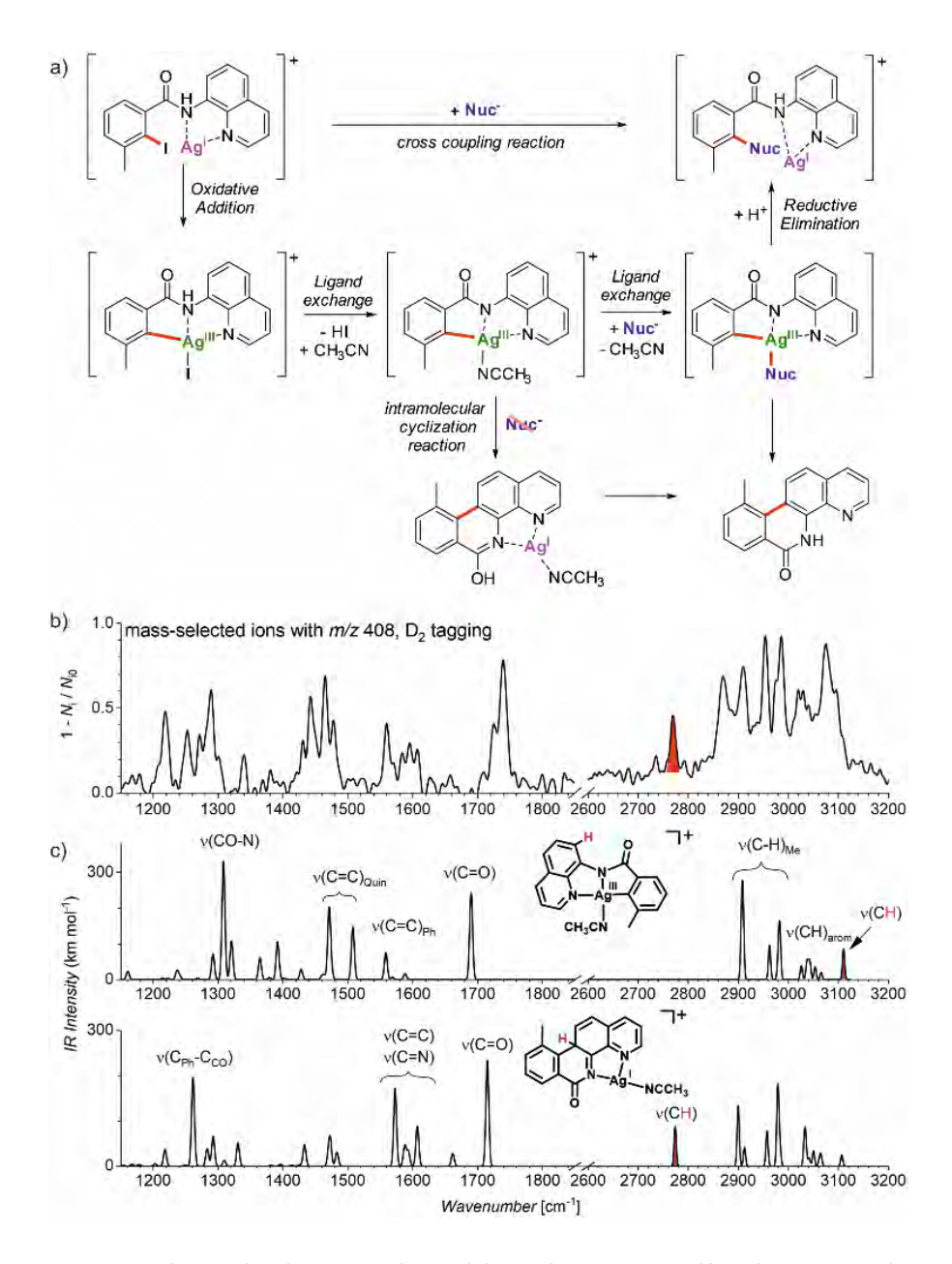


Figure 10. a) Silver catalyzed C-Nuc coupling and the mechanism proposed based on ESI-MS and ion spectroscopy study. b) IR photodissociation spectrum of ions with m/z 408 isolated from the reaction mixture measured by the D_2 -tagging method.^{55,56} c) DFT predicted spectra for possible isomers of the detected intermediates with m/z 408. Reprinted (adapted) with permission from Ref. [54]. Copyright 2018, American Chemical Society.

ESI-MS of the reaction mixture showed ions with m/z 408 that formally corresponded to the expected silver(III) intermediates bearing an acetonitrile molecule instead of iodine (see the central complex in Figure 10a). However, the infrared photodissociation spectrum of these ions did not correspond to the expected silver(III) complex (Figure 10b). Instead, the spectrum contained bands that could have been explained only by intramolecular cyclization of the aromatic substrate to form the tetracyclic product ions (Figure 10c, see e.g., the bands highlighted in red).

The detection of the tetracyclic product complexes of silver(I) was surprising. However, their formation can only be rationalized if the transient silver(III) intermediates were formed in the first place. A simple mechanistic sequence with a rollover of the quinoline group then explains the formation of the cyclized product. This initially purely mass spectrometric observation was later confirmed also synthetically. The authors performed the very same reaction without the addition of the nucleophile. Indeed, they isolated the tetracyclic product as the major product of the reaction. Hence, this example shows that a detailed mass spectrometry study can not only elucidate the reaction mechanism but also lead to the discovery of new reaction pathways that would be neglected otherwise.

The last example shows how mass spectrometry and photodissociation spectroscopy can intersect the key intermediates and help assign the correct mechanistic pathways. The investigated reaction used palladium catalysis and organocatalysis to enable a rather complex transformation to form spiro compounds (Figure 11).¹⁴ One of the substrates was α,β-unsaturated aldehyde known to react with (chiral) pyrrolidine-based organocatalysts. The so-formed iminium intermediates readily react with nucleophiles. The second reactant (1) must be activated by palladium to become reactive as the nucleophile. However, the question was how this activation happens.

Substrate 1 contains a pyrazole ring, which is easily protonated. Hence, the mass spectrometry analysis relied on charging by substrate protonation rather than designing charge-tagged reactants. Accordingly, the electrospray ionization of the substrate (1) and the palladium catalyst led to the detection of 1H+ and the protonated complex between 1 and palladium (Figure 11).

The infrared photodissociation spectrum of the mass-selected palladium complex revealed that the activation of 1 proceeds via the opening of the seven-membered ring. The intermediate corresponds to a palladium-stabilized zwitter-ion. The

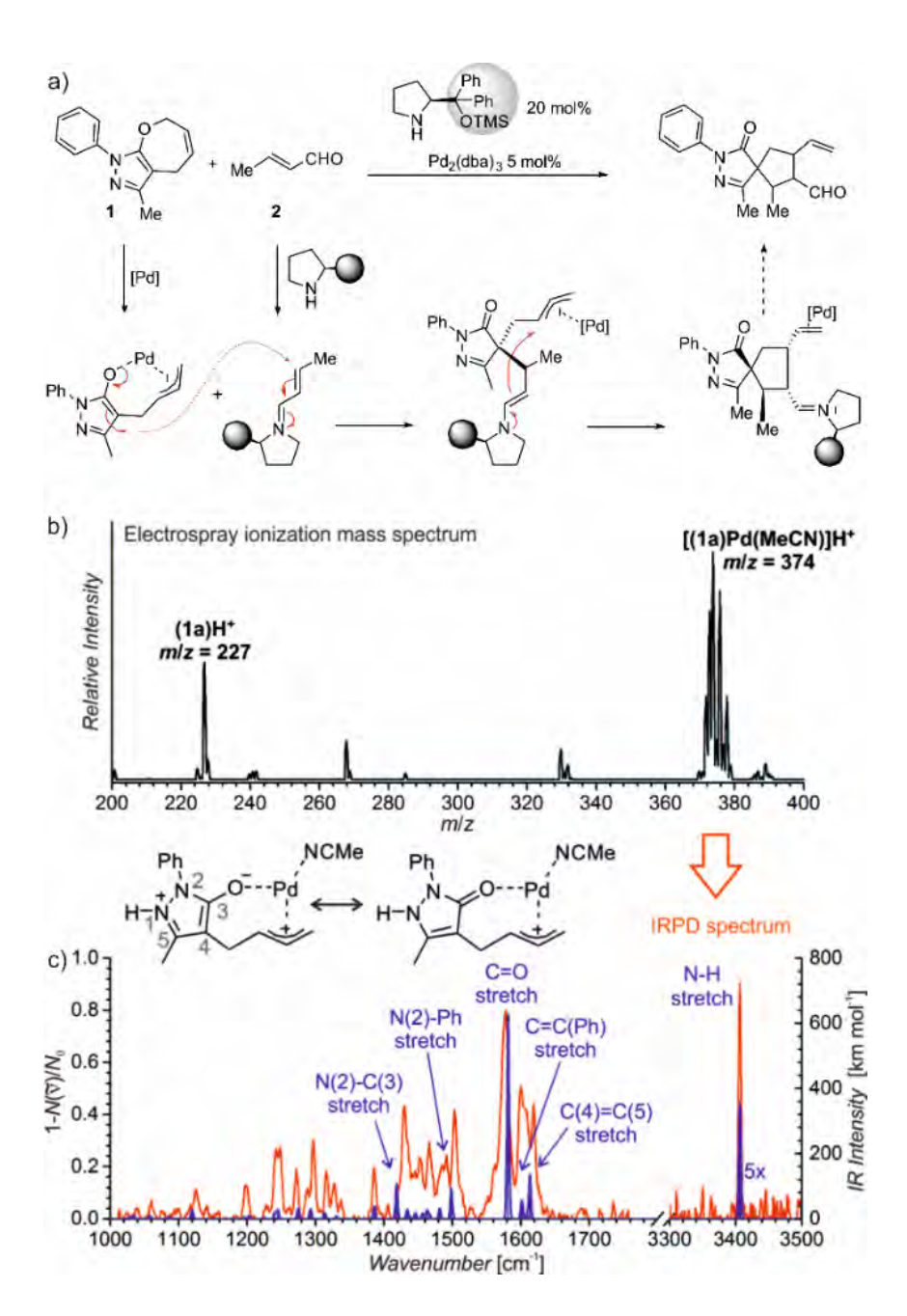


Figure 11. (a) Synergistic catalysis for enantioselective synthesis of spiropyrazolones and the proposed mechanism. (b) ESI-MS spectrum of 9 mM solution of 1 in CH₃CN/CH₂Cl₂ (4:1 v/v) with 2.5 mol% Pd₂(dba)₃. (c) Helium tagging infrared photodissociation spectrum of [(1)Pd(CH₃CN)]H⁺ (*m/z* 374; red line) and theoretically predicted spectrum (purple line) of the depicted complex. Adapted with changes from Ref. [14] under CC BY 3.0 license.²⁶

negative charge is localized at the oxygen atom and at the pyrazole ring, where the intermediate gets protonated. The structure of the protonated intermediate could be assigned based on excellent agreement between the theoretical prediction of the IR spectrum of the given complex and the experimental IRPD spectrum. Knowing the structure of the intermediate, the mechanism could be rationalized. The negatively charged part of the palladium intermediate couples with the activated α,β-unsaturated aldehyde, while palladium(0) stabilizes the allylcation fragment. The following step corresponds to the nucleophilic attack at the allyl cation.

These examples showed how ion spectroscopy can nail down the structures of the mass-spectrometry-detected intermediates. The first two examples showed that the detected ions corresponded to product complexes, which is often the case in mass spectrometric investigations of reaction mechanisms. However, these examples show that even if the ions are stable product ions, their detection can help resolve the reaction mechanism or attest indirectly to the nature of the intermediate.

Linking mass spectra with solution chemistry

A frequent criticism of the mass spectrometry investigation of reaction intermediates and reaction mechanisms evolves from the fact that the studied processes commonly proceed in solution. In contrast, the detection is based on the isolated species in the gas phase. This is undoubtedly a problem that must be well addressed in each mass spectrometric study addressing solution chemistry. The problems that occur are:

- 1. The electrospray ionization process is associated with large concentration changes. Hence, ESI-MS can detect the formation of larger clusters, which are artifacts of the ESI process and do not originate from solutions. Increasing the concentration can also substantially accelerate some reactions. 13,44,57 Hence, processes that are important at high concentrations can be selectively detected, although they do not play a role at standard conditions in solution. The concentration of the solution during the spray process accelerates all condensation reactions, and it has even been tested as an alternative approach for bulk synthesis.58-60
- Electrospray ionization generates ions in the 3 -5 kV field. This can lead to the 2. formation of ions that are not present in the solution. For example, palladiumcatalyzed reactions often proceed in neutral palladium complexes. However,

electrospray ionization can detect the ionized species either because of the anionic ligand loss or protonation. 14 The detection of the ionized complexes can still report about the reaction mechanism or the intermediates, but one has to be aware of the possible effect of ionization. It is also important to keep in mind that the electric field and the concentration changes can lead to the formation of species that do not have anything in common with the solution chemistry.

- The ion response in electrospray ionization is not linear.⁶¹ Therefore, the signal 3. intensities cannot be generally correlated with concentrations. However, the relative changes of the signal intensities can often be related qualitatively to the relative changes in concentrations of the given ions in solution. This is frequently applied in reaction monitoring using ESI-MS (see below).
- 4. Ion suppression is another problem affecting the ESI-MS detection of various species from solution. This is especially problematic if the concentration of the studied solution is above the usual analytical range (< 10⁻⁵ M), which is often the case in investigations of reaction mixtures.⁶² The ion suppression might be especially problematic if the ionization efficiencies of reactants, intermediates, and products differ. For example, the formation of an easily ionizable product can lead to an increasing suppression of signals of other ions during the reaction monitoring. Hence, the time evolution of some ESI-MS signals may appear to correspond to the reaction intermediate, but in reality, it might be a by-product accumulated in the solution.

Considering all these possible complications, we can use ESI-MS for reaction monitoring. Many such studies originate from the McIndoe group. 63,64 The following section describes an example of their study of the Suzuki-Miyaura reaction. Without going into details of the reaction mechanism, we focus on real-time monitoring of the reaction progress with ESI-MS.⁶³

The palladium-catalyzed cross-coupling reactions operate in the catalytic cycles between palladium(0) complexes and palladium(II) complexes bearing two anionic ligands. Hence, the key intermediates are neutral. The McIndoe group showed that the intermediates can be detected using a change-tagging strategy.⁶⁵ The permanently charged group can be attached to a phosphine ligand coordinated to palladium (e.g., one of the phenyl groups in the Ph₃P ligand can be sulfonated)⁶⁶ or to a reactant.⁶³ The advantage of charge tagging is that the ion transfer process during electrospray is quasi-identical for all the charged tagged ions, and thus, it allows their simultaneous monitoring and even evaluation of the signal intensity changes during the monitoring.

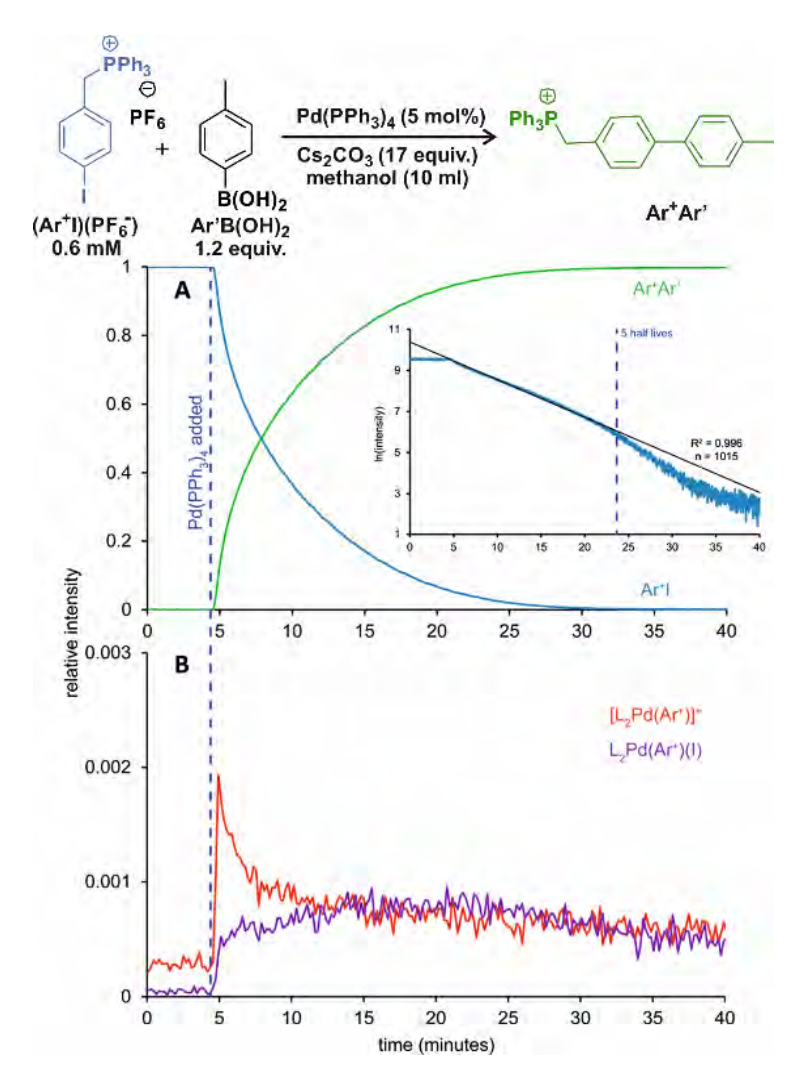


Figure 12. Suzuki- Miyaura coupling between a charged tagged aryl iodide (Ar⁺l) and para-tolyl boronic acid catalyzed by Pd(PPh,),. A) The ion-signal evolution of Ar+I and product Ar+Ar'. B) Palladium intermediates. Inset: natural log of the intensity of Ar⁺I over time showing well-behaved pseudo-firstorder kinetics out to 5 half-lives. Reprinted (adapted) with permission from Ref. [63]. Copyright 2018, American Chemical Society.

One of the examples of their work is the investigation of transmetallation mechanisms in Suzuki-Miyaura coupling (Figure 12).63 They have shown that using charge-tagging of the reactant can allow quantitative monitoring of reaction kinetics. Under the standard coupling conditions, they showed that ESI-MS data can reproduce the first-order kinetics of this reaction (see the inset in Figure 12A). They also monitored the palladium-containing intermediates (Figure 12B).

In principle, it is possible to obtain quantitative information on the concentration of given species from mass spectrometry experiments. The quantification requires the use of isotopically labeled standards with known concentrations. For example, spiking of a reaction mixture with an isotopically labeled product of the given reaction could be used to monitor the reaction progress by ESI-MS quantitatively. This approach could be an alternative to other means of reaction progress monitoring (e.g., IR or NMR spectroscopy). However, the strength of mass spectrometry is in detecting minor reactive intermediates that other spectroscopies cannot address. For these reactive intermediates, no isotopically labeled "standards" could be prepared.

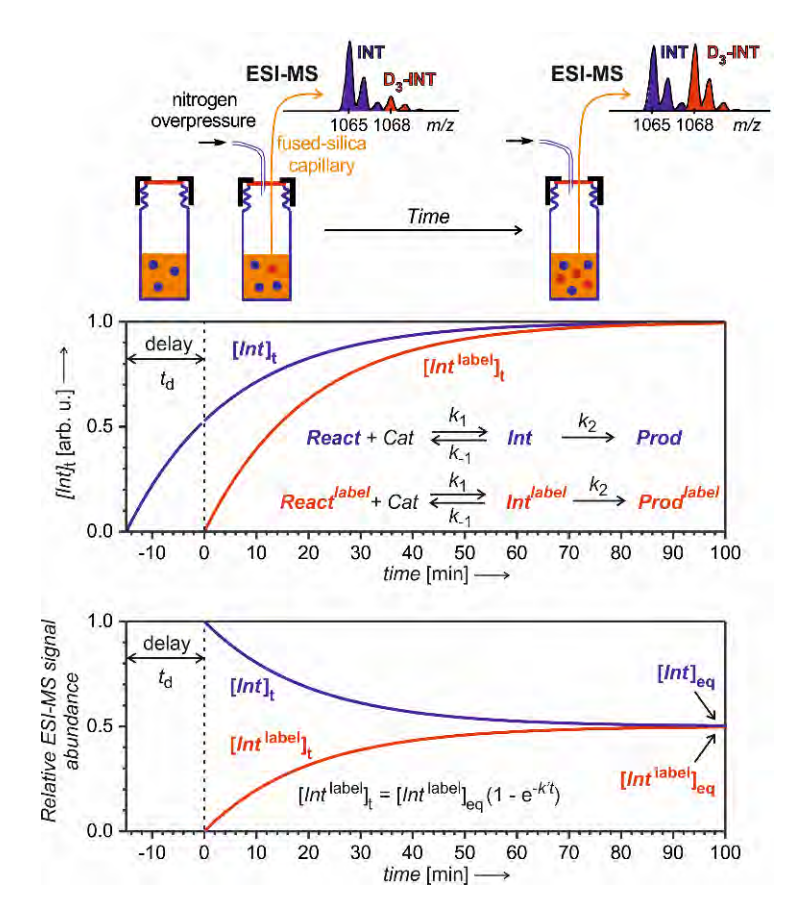


Figure 13. Delayed reactant labeling method for the investigation of reaction intermediates formed in a steady state approximation. Delay $t_{\rm d}$ is when the reaction runs only in the presence of unlabeled reactants; then, an isotopically labeled reactant is added to the reaction mixture, resulting in an out-of-equilibrium situation. Monitoring of the mutual evolution of the ESI-MS signals of the intermediates (bottom panel) allows determination of half-lives in steady-state approximation (see the equation: $k' = k_{.1} + k_{.2}$; this particular simulation is for an intermediate with $k' = 0.05 \, {\rm min}^{-1}$, hence with $t_{1/2} = 14 \, {\rm min}$).

To enable the quantification of reactive intermediates and to overcome the problem of non-existing isotopically labeled standards, Jašíková et al. from the Roithová group have designed the "Delayed reactant labeling" method (Figure 13).⁶⁷ This method works with a reaction mixture containing isotopically labeled and unlabeled reactants added at different times. The time delay introduces relative concentration differences that can be kinetically evaluated.

The example in Figure 13 shows a reaction that proceeds via intermediates in steady-state approximation. The reaction starts with isotopically unlabeled reactants, leading to the formation of unlabeled intermediates and products. After a time delay, the addition of the isotopically labeled reactant allows the formation of isotopically labeled intermediates and products. Right after the mixing, the reaction mixture is out of equilibrium. The mutual evolution of the intermediates' signals reflects the equilibrium's establishment (Figure 13, bottom). Similarly, the mutual evolution of products can be qualitatively evaluated, albeit in a bit more complex way (see Ref. 67 for details). Note that the isotopic labeling should be remote so that no kinetic isotope effect affects the reaction (or it has to be taken into account).

This method can investigate intermediates with half-lives on the order of minutes. If the intermediates have a very short lifetime, then the equilibrium is established before the reaction solution arrives at the electrospray ionization source. Hence, the signal intensities of the intermediates will only reflect the relative concentrations of the isotopically labeled and unlabeled reactants. The same applies to all "artifact" species that do not originate from the solution but are formed during the electrospray ionization. For such species, no mutual signal intensity changes evolve.

Figure 14 shows an example of the use of Delayed reactant labeling for determination of half-lives of diaurated intermediates in gold-catalysed addition of methanol to alkynes. Intermediates in this reaction can be described by the steady-state approximation, and their half-time is ideal for mass spectrometric investigation. The changes in the half-life of the intermediates induced by changing reaction conditions directly correlate with changes in the overall reaction rate determined by NMR.⁶⁷⁻⁶⁹ Hence, it was possible to evaluate the effect of adding an acid, changing concentrations of reactants, effects of counter ions, and the effect of added silver salts directly on the kinetics associated with intermediates. 67-69

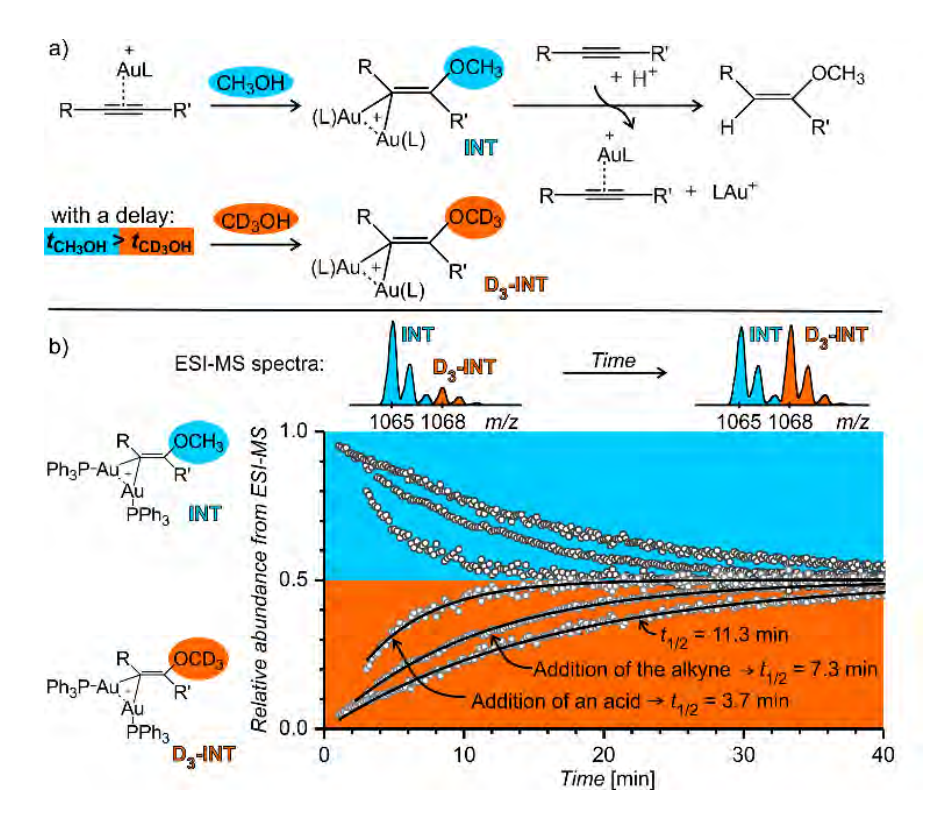


Figure 14. Determination of half-lives of diaurated intermediates in gold catalyzed methanol addition to alkynes. a) Simplified reaction mechanism involving diaurated intermediates. Delayed labeling was done by diluting the reaction mixture in CH₃OH by CD₃OH to a double volume after 5 minutes. See the exact condition in Ref. 67. b) Mutual evolution of ESI-MS signals (open points) of isotopically unlabeled (INT) and labeled (D₃-INT) intermediates. The data show acceleration of the reaction (decrease of the half-live of the intermediates) by changing reaction conditions (increasing alkyne concentration and addition of *para*-toluene sulphonic acid). The half-lives were determined by fitting with the function shown in Figure 13 (solid lines). Reprinted (adapted) with permission from Ref. [67]. Copyright 2015, American Chemical Society.

Next to the quantitative kinetics evaluation, Delayed reactant labeling can also serve to qualitatively evaluate different reaction pathways. The gold-mediated oxidation of alkynes shown in Figure 9 is a good example.⁵² As shown above, the IR photodissociation experiments revealed that the ESI-MS methods detect ions in the green and red boxes in Figure 9. The question to be resolved is, whether the pyridine group in the gold-α-oxocarbenoid intermediates could be replaced by acetonitrile (in an SN2 reaction) and thus the intermediates could yield the desired oxazole product (Figure 15a).

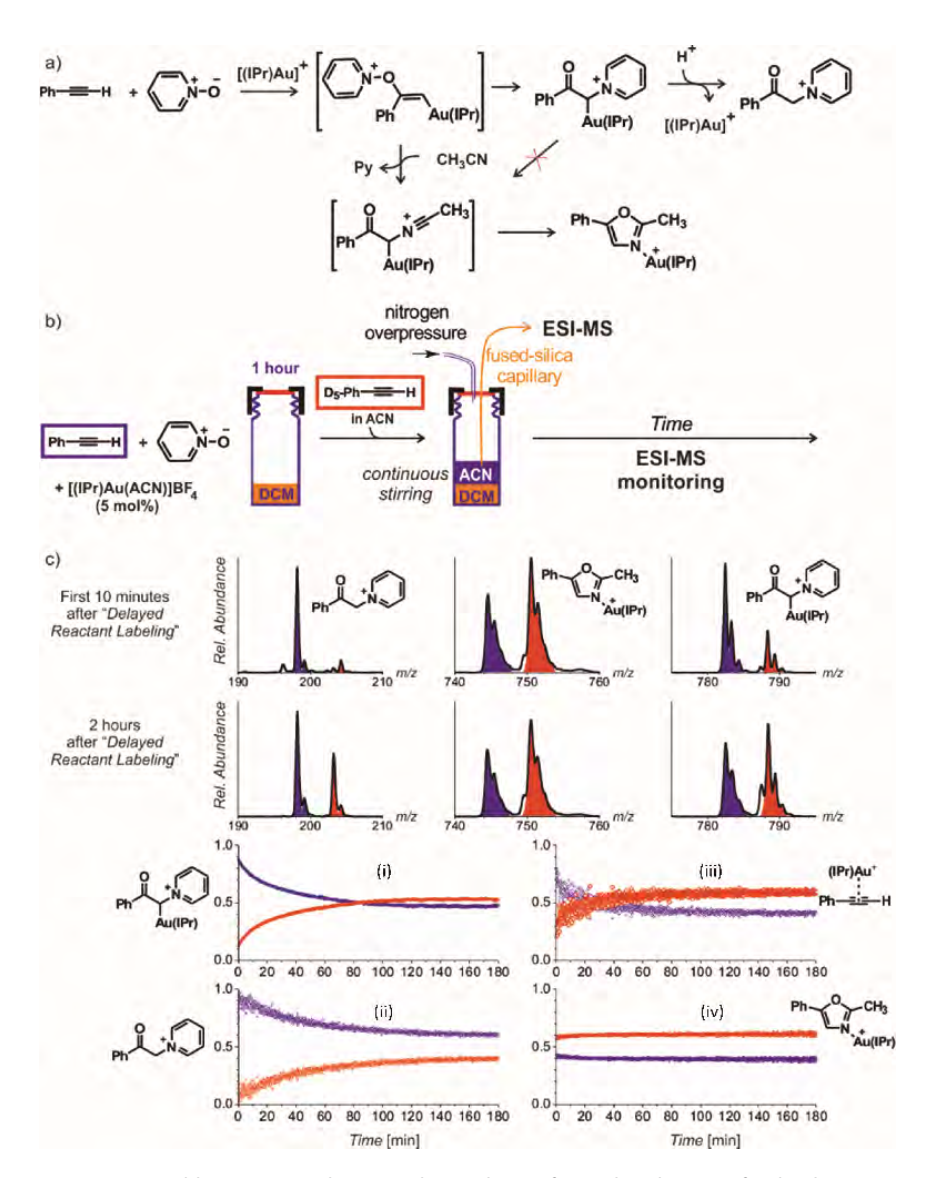


Figure 15. a) Possible reaction pathways in the synthesis of oxazoline. b) Setup for the determination of possible pathways. c) Results of delayed reactant labeling with the addition of acetonitrile only after the time delay. The opposite relative intensities of isotopically labeled and unlabeled oxazole product complex (iv) show that the reaction pathway is independent of that toward the formation of pyridinium gold-α-oxocarbenoid (i).⁵² Adapted with permission from Ref. [52] Copyright 2016 WILEY-VCH Verlag GmbH & Co. KGaA, Weinheim.

As the reaction starts with only unlabeled reactants in dichloromethane, the reaction could only proceed via the pyridinium gold-α-oxocarbenoid intermediates towards the formation of α-pyridinium ketone product. After a time delay, isotopically labeled alkyne and acetonitrile were added to the reaction mixture (Figure 15b). The mutual evolution of the signals (Figure 15c) of the pyridinium gold-α-oxocarbenoid intermediates (i) attest the initial larger concentration of the unlabeled intermediate in solution (the blue curve) and it shows that this intermediate in a relatively slow reaction degrades to form α-pyridinium ketone products (ii) (Compare the blue curves (i) and (ii) that correspond to the degradation of the unlabeled pyridinium gold-α-oxocarbenoid intermediate to the unlabeled α-pyridinium ketone product respectively). The reaction with the labeled alkyne is reflected in the red curves (compare the evolution of curves in Figure 15c).

Inspection of the mutual intensities of the gold-oxazole product complexes (iv) immediately shows that the signal intensities of the unlabeled and labeled product complexes are reversed. Thus, these complexes are not formed by the reaction of pyridinium gold- α -oxocarbenoid intermediates (i). If the pyridinium gold-α-oxocarbenoid intermediate led to the gold-oxazole product, we would expect to observe more of the unlabeled product (in blue) in the initial reaction time instead of the labeled product (in red), which is not the case in Figure 15c (iv). Instead, the intensities of gold-oxazole product complexes roughly mirror the mutual intensities of the gold-alkyne complexes (iii), reflecting concentrations of the alkynes in solution.

This last section shows that ESI-MS monitoring can be used to evaluate reaction kinetics in solution, albeit it requires some tricks. Either way, we should strive to make the ionization process for the detected species uniform, which can be achieved by charge-tagging. Or, we have to use relative determination of concentrations by spiking the reaction mixture with isotopically labeled standards. In the particular case of the reactive species, these standards could only be formed in situ, and we are thus left to work with relative signals as in the presented Delayed reactant labeling method.

Conclusions

Electrospray ionization provides a link between solution-phase chemistry and mass spectrometry detection. This chapter shows how this link can be utilized to monitor reactions in solution directly. Mass spectrometry has unique sensitivity; therefore, it could help detect key reaction intermediates or other low-abundant species from the solution. The trade-off is that the detection is not quantitative and that the solution-gas phase transfer might create artifacts. This introductory chapter has explained these difficulties and provided guidelines for overcoming them.

Mass spectrometric detection provides information about the elemental composition of the detected ions. However, the mere mass of the detected ions cannot be taken as proof of detecting a particular species from the solution. Collision-induced dissociation, ion mobility, and ion spectroscopy emerge as indispensable techniques to obtain information about the structures of detected ions. Sections show that the knowledge of the structure of the detected ions is key in the evaluation of the relevance of the detected species for the solution chemistry and for the investigated reaction mechanism.

This chapter demonstrates the valuable contributions of ESI-MS in investigating key reaction steps and tracking reaction pathways through the examples presented. However, we believe that ESI-MS could go even further and be used to discover new reactions. ESI-MS sensitivity could be employed in testing ideas for new chemical conversions.

References

- (1) Burés, J.; Armstrong, A.; Blackmond, D. G. Kinetic Correlation between Aldehyde/Enamine Stereoisomers in Reactions between Aldehydes with a -Stereocenters and Chiral Pyrrolidine-Based Catalysts. Chem. Sci. 2012, 3 (4), 1273-1277.
- (2) Zehnacker, A. Optical Spectroscopy Coupled with Mass Spectrometry Methods. Phys. Chem. Chem. Phys. 2015, 17 (39), 25672-25675.
- (3) Seegerer, A.; Nitschke, P.; Gschwind, R. M. Combined In Situ Illumination-NMR-UV/Vis Spectroscopy: A New Mechanistic Tool in Photochemistry. Angew. Chemie 2018, 130 (25), 7615-7619.
- (4) Gärtner, T.; Henze, W.; Gschwind, R. M. NMR-Detection of Cu(III) Intermediates in Substitution Reactions of Alkyl Halides with Gilman Cuprates. J. Am. Chem. Soc. 2007, 129 (37), 11362-11363.
- (5) Schröder, D. Applications of Electrospray Ionization Mass Spectrometry in Mechanistic Studies and Catalysis Research. Acc. Chem. Res. 2012, 45 (9), 1521–1532.
- (6) Traeger, J. C. Electrospray Mass Spectrometry of Organometallic Compounds. Int. J. Mass Spectrom. 2000, 200 (1-3), 387-401.
- (7) Sabino, A. A.; Machado, A. H. L.; Correia, C. R. D.; Eberlin, M. N. Probing the Mechanism of the Heck Reaction with Arene Diazonium Salts by Electrospray Mass and Tandem Mass Spectrometry. Angew. Chemie - Int. Ed. 2004, 43 (19), 2514-2518.
- (8) Roithová, J. Characterization of Reaction Intermediates by Ion Spectroscopy. Chem. Soc. Rev. 2012, 41 (2), 547-559.
- (9) Iacobucci, C.; Reale, S.; De Angelis, F. Elusive Reaction Intermediates in Solution Explored by ESI-MS: Reverse Periscope for Mechanistic Investigations. Angew. Chemie - Int. Ed. 2016, 55 (9), 2980-
- (10) Santos, L. S. Online Mechanistic Investigations of Catalyzed Reactions by Electrospray Ionization Mass Spectrometry: A Tool to Intercept Transient Species in Solution. European J. Org. Chem. 2008, No. 2, 235-253.
- (11) Santos, L. S. Reactive Intermediates: MS Investigations in Solution; 2010.
- (12) Santos, V. G.; Godoi, M. N.; Regiani, T.; Gama, F. H. S.; Coelho, M. B.; De Souza, R. O. M. A.; Eberlin, M. N.; Garden, S. J. The Multicomponent Hantzsch Reaction: Comprehensive Mass Spectrometry Monitoring Using Charge-Tagged Reagents. Chem. - A Eur. J. 2014, 20 (40), 12808-12816.
- (13) Basuri, P.; Gonzalez, L. E.; Morato, N. M.; Pradeep, T.; Cooks, R. G. Accelerated Microdroplet Synthesis of Benzimidazoles by Nucleophilic Addition to Protonated Carboxylic Acids. Chem. Sci. 2020.
- (14) Meazza, M.; Kamlar, M.; Jašíková, L.; Formánek, B.; Mazzanti, A.; Roithová, J.; Veselý, J.; Rios, R. Synergistic Formal Ring Contraction for the Enantioselective Synthesis of Spiropyrazolones. Chem. Sci. 2018, 9 (30), 6368-6373.
- (15) Marsh, B. M.; Iyer, K.; Cooks, R. G. Reaction Acceleration in Electrospray Droplets: Size, Distance, and Surfactant Effects. J. Am. Soc. Mass Spectrom. 2019, 30 (10), 2022–2030.
- (16) Hinderling, C.; Adlhart, C.; Chen, P. Olefin Metathesis of a Ruthenium Carbene Complex by Electrospray Ionization in the Gas Phase. Angew. Chemie - Int. Ed. 1998, 37 (19), 2685–2689.
- (17) Wu, W. Y.; Chen, S. N.; Tsai, F. Y. Recyclable and Highly Active Cationic 2,2'-Bipyridyl Palladium(II) Catalyst for Suzuki Cross-Coupling Reaction in Water. Tetrahedron Lett. 2006, 47 (52), 9267–9270.

- (18) Schade, M. A.; Fleckenstein, J. E.; Knochel, P.; Koszinowski, K. Charged Tags as Probes for Analyzing Organometallic Intermediates and Monitoring Cross-Coupling Reactions by Electrospray-Ionization Mass Spectrometry. J. Org. Chem. 2010, 75 (20), 6848-6857.
- (19) Oliveira, F. F. D.; Dos Santos, M. R.; Lalli, P. M.; Schmidt, E. M.; Bakuzis, P.; Lapis, A. A. M.; Monteiro, A. L.; Eberlin, M. N.; Neto, B. A. D. Charge-Tagged Acetate Ligands as Mass Spectrometry Probes for Metal Complexes Investigations: Applications in Suzuki and Heck Phosphine-Free Reactions. J. Org. Chem. 2011, 76 (24), 10140-10147.
- (20) Zhu, H.; Janusson, E.; Luo, J.; Piers, J.; Islam, F.; McGarvey, G. B.; Oliver, A. G.; Granot, O.; Scott McIndoe, J. Phenol-Selective Mass Spectrometric Analysis of Jet Fuel. Analyst 2017, 142 (17), 3278-3284.
- (21) Santrač, D.; Cella, S.; Wang, W.; Ackermann, L. Palladium-Catalyzed C-H Arylation of Amides by Triazole Assistance. European J. Org. Chem. 2016, 2016 (32), 5429-5436.
- (22) Xiao, B.; Fu, Y.; Xu, J.; Gong, T. J.; Dai, J. J.; Yi, J.; Liu, L. Pd(II)-Catalyzed C-H Activation/Aryl-Aryl Coupling of Phenol Esters. J. Am. Chem. Soc. 2010, 132 (2), 468-469.
- (23) Yang, F.; Song, F.; Li, W.; Lan, J.; You, J. Palladium-Catalyzed C-H Activation of Anilides at Room Temperature: Ortho-Arylation and Acetoxylation. RSC Adv. 2013, 3 (25), 9649–9652.
- (24) Zhang, Z.; Tanaka, K.; Yu, J. Q. Remote Site-Selective C-H Activation Directed by a Catalytic Bifunctional Template. Nature 2017, 543 (7646), 538-542.
- (25) Czyz, M. L.; Weragoda, G. K.; Horngren, T. H.; Connell, T. U.; Gomez, D.; O'Hair, R. A. J.; Polyzos, A. Photoexcited Pd(Ii) Auxiliaries Enable Light-Induced Control in C(Sp3)-H Bond Functionalisation. Chem. Sci. 2020, 11 (9), 2455-2463.
- (26) Creative Commons. Creative Commons Attribution 3.0 Unported CC BY 3.0. Creative Commons. https://creativecommons.org/licenses/by/3.0/ (accessed 2020-08-27).
- (27) Parera, M.; Dachs, A.; Solà, M.; Pla-Quintana, A.; Roglans, A. Direct Detection of Key Intermediates in Rhodium(I)-Catalyzed [2+2+2] Cycloadditions of Alkynes by ESI-MS. Chem. - A Eur. J. 2012, 18 (41), 13097-13107.
- (28) Auth, T.; Koszinowski, K.; O'Hair, R. A. J. Dissecting Transmetalation Reactions at the Molecular Level: Phenyl Transfer in Metal Borate Complexes. Organometallics 2020, 39 (1), 25-33.
- (29) Narancic, S.; Bach, A.; Chen, P. Simple Fitting of Energy-Resolved Reactive Cross Sections in Threshold Collision-Induced Dissociation (T-CID) Experiments. J. Phys. Chem. A 2007, 111 (30), 7006-7013.
- (30) Zins, E.-L.; Pepe, C.; Schröder, D. Energy-Dependent Dissociation of Benzylpyridinium Ions in an Ion-Trap Mass Spectrometer. J. Mass Spectrom. 2010, 45 (11), 1253–1260.
- (31) Armentrout, P. B. The Power of Accurate Energetics (or Thermochemistry: What Is It Good For?). J. Am. Soc. Mass Spectrom. 2013, 24 (2), 173-185.
- (32) Oeschger, R. J.; Chen, P. Structure and Gas-Phase Thermochemistry of a Pd/Cu Complex: Studies on a Model for Transmetalation Transition States. J. Am. Chem. Soc. 2017, 139 (3), 1069–1072.
- (33) Waters, T.; O'Hair, R. A. J.; Wedd, A. G. Catalytic Gas Phase Oxidation of Methanol to Formaldehyde. J. Am. Chem. Soc. 2003, 125 (11), 3384-3396.
- (34) Böhme, D. K.; Schwarz, H. Gas-Phase Catalysis by Atomic and Cluster Metal Ions: The Ultimate Single-Site Catalysts. Angew. Chemie - Int. Ed. 2005, 44 (16), 2336–2354.
- (35) Božović, A.; Feil, S.; Koyanagi, G. K.; Viggiano, A. A.; Zhang, X.; Schlangen, M.; Schwarz, H.; Bohme, D. K. Conversion of Methane to Methanol: Nickel, Palladium, and Platinum (d 9) Cations as

- Catalysts for the Oxidation of Methane by Ozone at Room Temperature. Chem. A Eur. J. 2010, 16 (38), 11605-11610.
- (36) Schwarz, H. Chemistry with Methane: Concepts Rather than Recipes. Angew. Chemie Int. Ed. **2011**, 50 (43), 10096-10115.
- (37) Simon, A. L.; Chirot, F.; Choi, C. M.; Clavier, C.; Barbaire, M.; Maurelli, J.; Dagany, X.; MacAleese, L.; Dugourd, P. Tandem Ion Mobility Spectrometry Coupled to Laser Excitation. Rev. Sci. Instrum. 2015, 86 (9), 094101.
- (38) Choi, C. M.; Simon, A. L.; Chirot, F.; Kulesza, A.; Knight, G.; Daly, S.; MacAleese, L.; Antoine, R.; Dugourd, P. Charge, Color, and Conformation: Spectroscopy on Isomer-Selected Peptide Ions. J. Phys. Chem. B 2016, 120 (4), 709-714.
- (39) Choi, C. M.; Macaleese, L.; Dugourd, P.; Choi, M. C.; Chirot, F. Photo-Induced Linkage Isomerization in the Gas Phase Probed by Tandem Ion Mobility and Laser Spectroscopy. Phys. Chem. Chem. Phys. **2018**, 20 (17), 12223-12228.
- (40) Paul, M.; Detmar, E.; Schlangen, M.; Breugst, M.; Neudörfl, J. M.; Schwarz, H.; Berkessel, A.; Schäfer, M. Intermediates of N-Heterocyclic Carbene (NHC) Dimerization Probed in the Gas Phase by Ion Mobility Mass Spectrometry: C-H···:C Hydrogen Bonding Versus Covalent Dimer Formation. Chem. - A Eur. J. 2019, 25 (10), 2511-2518.
- (41) Greisch, J. F.; Weis, P.; Brendle, K.; Kappes, M. M.; Haler, J. R. N.; Far, J.; De Pauw, E.; Albers, C.; Bay, S.; Wurm, T.; Rudolph, M.; Schulmeister, J.; Hashmi, A. S. K. Detection of Intermediates in Dual Gold Catalysis Using High-Resolution Ion Mobility Mass Spectrometry. Organometallics 2018, 37 (9), 1493-1500.
- (42) Zhang, J. T.; Wang, H. Y.; Zhang, X.; Zhang, F.; Guo, Y. L. Study of Short-Lived and Early Reaction Intermediates in Organocatalytic Asymmetric Amination Reactions by Ion-Mobility Mass Spectrometry. Catal. Sci. Technol. 2016, 6 (17), 6637–6643.
- (43) Regiani, T.; Santos, V. G.; Godoi, M. N.; Vaz, B. G.; Eberlin, M. N.; Coelho, F. On the Mechanism of the Aza-Morita-Baylis-Hillman Reaction: ESI-MS Interception of a Unique New Intermediate. Chem. Commun. 2011, 47 (23), 6593-6595.
- (44) Sahota, N.; Abusalim, D. I.; Wang, M. L.; Brown, C. J.; Zhang, Z.; El-Baba, T. J.; Cook, S. P.; Clemmer, D. E. A Microdroplet-Accelerated Biginelli Reaction: Mechanisms and Separation of Isomers Using IMS-MS. Chem. Sci. 2019, 10 (18), 4822-4827.
- (45) Révész, Á.; Schröder, D.; Rokob, T. A.; Havlík, M.; Dolenský, B. In-Flight Epimerization of a Bis-Tröger Base. Angew. Chemie - Int. Ed. 2011, 50 (10), 2401-2404.
- (46) Wolk, A. B.; Leavitt, C. M.; Garand, E.; Johnson, M. A. Cryogenic Ion Chemistry and Spectroscopy. Acc. Chem. Res. 2014, 47 (1), 202-210.
- (47) Corinti, D.; Crestoni, M. E.; Chiavarino, B.; Fornarini, S.; Scuderi, D.; Salpin, J.-Y. Insights into Cisplatin Binding to Uracil and Thiouracils from IRMPD Spectroscopy and Tandem Mass Spectrometry. J. Am. Soc. Mass Spectrom. 2020, 31 (4), 946-960.
- (48) Maitre, P.; Scuderi, D.; Corinti, D.; Chiavarino, B.; Crestoni, M. E.; Fornarini, S. Applications of Infrared Multiple Photon Dissociation (IRMPD) to the Detection of Posttranslational Modifications. Chem. Rev. 2020, 120 (7), 3261-3295.
- (49) Gerlich, D. Infrared Spectroscopy of Cold Trapped Molecular Ions Using He-Tagging. J. Chinese Chem. Soc. 2018, 65 (6), 637-653.
- (50) Jašíková, L.; Roithová, J. Infrared Multiphoton Dissociation Spectroscopy with Free-Electron Lasers: On the Road from Small Molecules to Biomolecules. Chem. - A Eur. J. 2018, 24 (14), 3374–3390.

- (51) Martens, J.; van Outersterp, R. E.; Vreeken, R. J.; Cuyckens, F.; Coene, K. L. M.; Engelke, U. F.; Kluijtmans, L. A. J.; Wevers, R. A.; Buydens, L. M. C.; Redlich, B.; Berden, G.; Oomens, J. Infrared Ion Spectroscopy: New Opportunities for Small-Molecule Identification in Mass Spectrometry - A Tutorial Perspective. Anal. Chim. Acta 2020, 1093, 1-15.
- (52) Schulz, J.; Jašík, J.; Gray, A.; Roithová, J. Formation of Oxazoles from Elusive Gold(I) α-Oxocarbenes: A Mechanistic Study. Chem. - A Eur. J. 2016, 22 (28), 9827–9834.
- (53) Roithová, J.; Gray, A.; Andris, E.; Jašík, J.; Gerlich, D. Helium Tagging Infrared Photodissociation Spectroscopy of Reactive Ions. Acc. Chem. Res. 2016, 49 (2), 223–230.
- (54) Capdevila, L.; Andris, E.; Briš, A.; Tarrés, M.; Roldán-Gómez, S.; Roithová, J.; Ribas, X. Silver(I)-Catalyzed C-X, C-C, C-N, and C-O Cross-Couplings Using Aminoquinoline Directing Group via Elusive Aryl-Ag(III) Species. ACS Catal. 2018, 8 (11), 10430–10436.
- (55) Menges, F. S.; Perez, E. H.; Edington, S. C.; Duong, C. H.; Yang, N.; Johnson, M. A. Integration of High-Resolution Mass Spectrometry with Cryogenic Ion Vibrational Spectroscopy. J. Am. Soc. Mass Spectrom. 2019, 30 (9), 1551-1557.
- (56) Esser, T. K.; Knorke, H.; Siro-Brigiano, F.; Galimberti, D. R.; Asmis, K. R.; Gaigeot, M. P.; Lisy, J. M. Influence of Argon and D2 Tagging on the Hydrogen Bond Network in Cs+(H2O)3; Kinetic Trapping below 40 K. Phys. Chem. Chem. Phys. 2018, 20 (45), 28476–28486.
- (57) Zhong, X.; Chen, H.; Zare, R. N. Ultrafast Enzymatic Digestion of Proteins by Microdroplet Mass Spectrometry. Nat. Commun. 2020, 11 (1), 1-9.
- (58) Ingram, A. J.; Boeser, C. L.; Zare, R. N. Going beyond Electrospray: Mass Spectrometric Studies of Chemical Reactions in and on Liquids. Chem. Sci. 2016, 7 (1), 39–55.
- (59) Yan, X.; Bain, R. M.; Cooks, R. G. Organic Reactions in Microdroplets: Reaction Acceleration Revealed by Mass Spectrometry. Angew. Chemie - Int. Ed. 2016, 55 (42), 12960–12972.
- (60) Liu, C.; Li, J.; Chen, H.; Zare, R. N. Scale-up of Microdroplet Reactions by Heated Ultrasonic Nebulization. Chem. Sci. 2019, 10 (40), 9367-9373.
- (61) Omari, I.; Randhawa, P.; Randhawa, J.; Yu, J.; McIndoe, J. S. Structure, Anion, and Solvent Effects on Cation Response in ESI-MS. J. Am. Soc. Mass Spectrom. 2019, 30 (9), 1750–1757.
- (62) Tang, K.; Page, J. S.; Smith, R. D. Charge Competition and the Linear Dynamic Range of Detection in Electrospray Ionization Mass Spectrometry. J. Am. Soc. Mass Spectrom. 2004, 15 (10), 1416–1423.
- (63) Yunker, L. P. E.; Ahmadi, Z.; Logan, J. R.; Wu, W.; Li, T.; Martindale, A.; Oliver, A. G.; McIndoe, J. S. Real-Time Mass Spectrometric Investigations into the Mechanism of the Suzuki-Miyaura Reaction. Organometallics 2018, 37 (22), 4297-4308.
- (64) Thomas, G. T.; Janusson, E.; Zijlstra, H. S.; McIndoe, J. S. Step-by-Step Real Time Monitoring of a Catalytic Amination Reaction. Chem. Commun. 2019, 55 (78), 11727-11730.
- (65) Vikse, K. L.; Ahmadi, Z.; Manning, C. C.; Harrington, D. A.; McIndoe, J. S. Powerful Insight into Catalytic Mechanisms through Simultaneous Monitoring of Reactants, Products, and Intermediates. Angew. Chemie - Int. Ed. 2011, 50 (36), 8304-8306.
- (66) Vikse, K. L.; Henderson, M. A.; Oliver, A. G.; McIndoe, J. S. Direct Observation of Key Intermediates by Negative-Ion Electrospray Ionisation Mass Spectrometry in Palladium-Catalysed Cross-Coupling. Chem. Commun. 2010, 46 (39), 7412-7414.
- (67) Jašíková, L.; Anania, M.; Hybelbauerová, S.; Roithová, J. Reaction Intermediates Kinetics in Solution Investigated by Electrospray Ionization Mass Spectrometry: Diaurated Complexes. J. Am. Chem. Soc. 2015, 137 (42), 13647–13657.
- (68) Anania, M.; Jašíková, L.; Zelenka, J.; Shcherbachenko, E.; Jašík, J.; Roithová, J. Monoaurated: Vs. Diaurated Intermediates: Causality or Independence? Chem. Sci. 2020, 11 (4), 980-988.
- (69) Jašíková, L.; Rodrigues, M.; Lapešová, J.; Lízal, T.; Šindelář, V.; Roithová, J. Bambusurils as a Mechanistic Tool for Probing Anion Effects. Faraday Discuss. 2019, 220, 58–70.



Chapter 2

Methods

Electrospray Ionization Mass Spectrometry (ESI-MS)

In the research presented in this thesis, an electrospray ionization (ESI) source was used as the source for mass spectrometers, except in cases specifically mentioned otherwise. The selection of ESI as the ionization method is based on its classification as a "soft" ionization technique. This characteristic makes ESI particularly well-suited for the analysis of reaction mixtures. 1-6 One of the significant benefits of employing ESI is its ability to ionize complex molecules with minimal fragmentation. This is crucial for our objectives, as it allows for the potential detection of reaction intermediates intact, offering a distinct advantage over the more fragmentary nature of ionization observed in Electron Ionization (El) sources. By minimizing molecular fragmentation, ESI facilitates a more accurate characterization of the chemical species present in the reaction mixture, enabling a detailed investigation of the mechanistic pathways under investigation.

Sample Injection Methods: Offline vs. Online MS Studies

The method of introducing samples into the mass spectrometers was tailored to align with the nature of the study - distinguishing between offline and online analysis. The choice of method was influenced by the sample's characteristics and the experimental prerequisites.

Offline Sample Injection: Samples of a reaction mixture are taken at predetermined intervals, which are then filtered, diluted, and injected into the mass spectrometer from a syringe using a syringe pump. This offline approach offers precise control over the sample's flow rate into the mass spectrometer.

Online Sample Injection: For experiments involving reaction mixtures or samples that require sequential addition of reagents or gases (such as nitrogen, carbon monoxide, hydrogen, or oxygen), the pressurized sample infusion electrospray ionization mass spectrometry (PSI-ESI-MS) technique is preferred.^{7,8} This method typically involves pressurizing a sealed vial containing the sample with inert gas. A silica capillary, with one end submerged in the sample, facilitates the sample's entry into the mass spectrometer under the overpressure of nitrogen. This approach is suited for dynamic studies where the reaction conditions or the sample's composition changes over time.

The injection method was selected to suit the specific requirements of the sample and the experimental setup. This strategic choice ensured that the analysis was conducted optimally and accurately, providing reliable insights into the mechanisms under investigation.

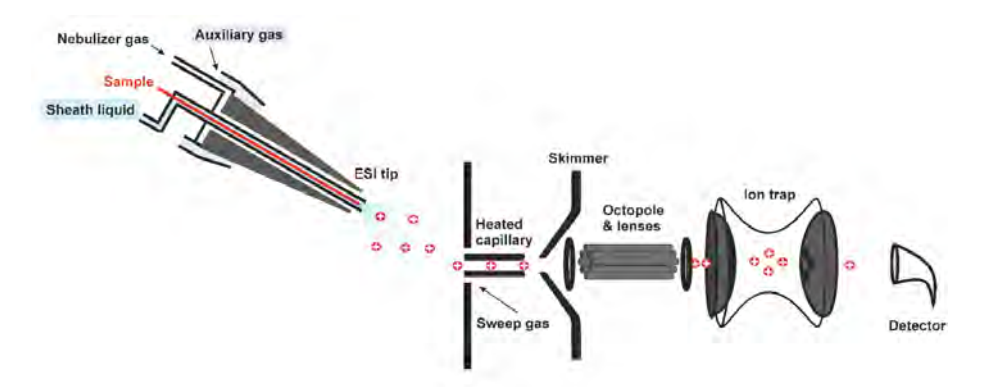


Figure 1: Electrospray ionization (ESI) source depicting the sheath liquid and auxiliary gas inlet and interface to mass spectrometry.

Additionally, in Chapter 6 (study of binding energies for the [(L)M(alkyne)]+ complex), for certain cases where challenges were encountered with generating metal complexes bound to alkynes/alkene in the solution phase, we adopted another strategy. To facilitate the formation of these complexes, we indirectly introduced the alkyne (or alkene) using the sheath liquid or auxiliary gas inlet (Figure 1). This helped to overcome obstacles that hinder direct binding, potentially caused by factors like stronger solvent(/2nd 'L') binding to the metal center, and the desired generation of [(L)M(alkyne)]⁺ complex is achieved in the gas phase.

Delayed reactant labeling

Our group developed the "delayed reactant labeling" method (Figure 2), which is used to investigate the kinetics of reaction intermediates in solution via electrospray ionization mass spectrometry (ESI-MS).¹⁰ It involves the analysis of mixtures containing isotopically labeled and unlabeled reactants over varied reaction times, enabling the determination of rate constants for the degradation of reaction intermediates. By introducing a labeled reactant to the reaction mixture containing an unlabeled reactant after a time delay, this method allows for quantitative evaluation as long as the intermediates are in a steady state. Delayed reactant labeling not only helps in overcoming the challenges of correlating ions detected in the gas phase by ESI-MS directly with the species present in the reaction solution but also facilitates the differentiation between product complexes and intermediates.^{11–13} This technique proves especially valuable for studying intermediates that are present in low concentrations or exhibit high reactivity, providing deeper insights into their behavior and significance in the overall reaction mechanism.

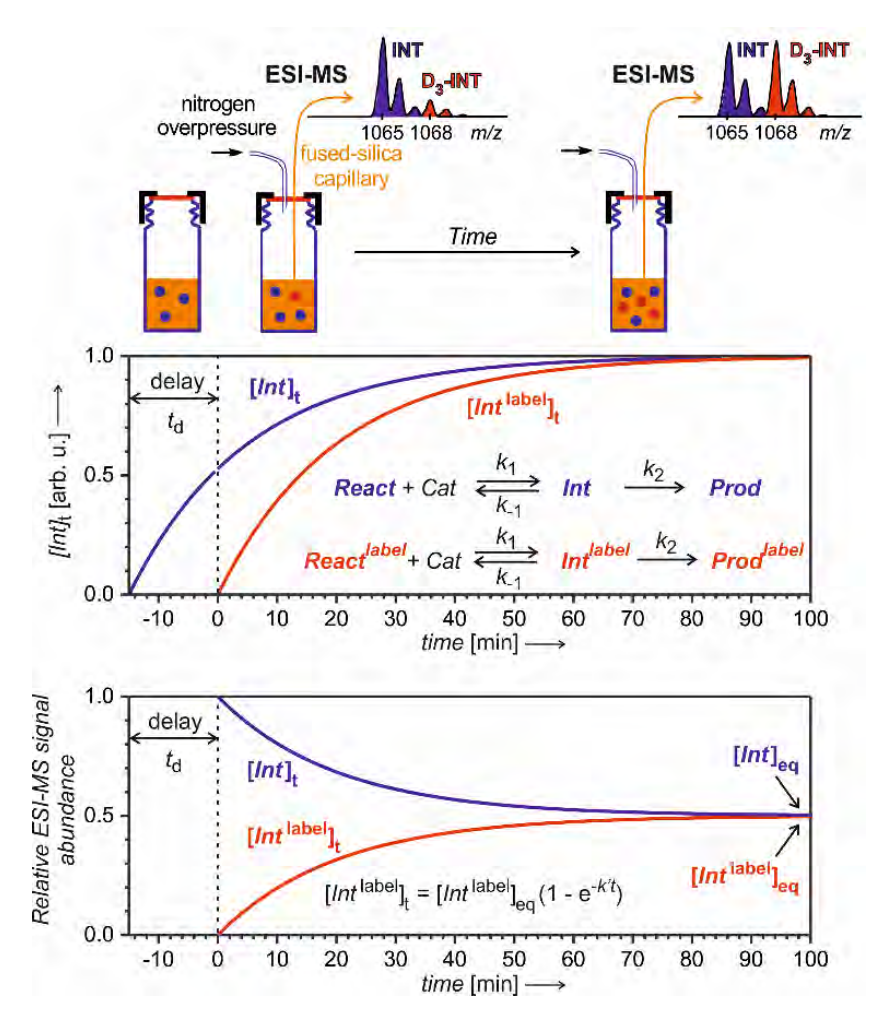


Figure 2. Delayed reactant labeling method for the investigation of reaction intermediates formed in a steady state approximation. Delay $t_{\rm d}$ is when the reaction runs only in the presence of unlabeled reactants; then, an isotopically labeled reactant is added to the reaction mixture, resulting in an out-of-equilibrium situation. Monitoring of the mutual evolution of the ESI-MS signals of the intermediates (bottom panel) allows the determination of half-lives in steady-state approximation (see the equation: $k' = k_{-1} + k_{2}$; this particular simulation is for an intermediate with $k' = 0.05 \, {\rm min}^{-1}$, hence with $t_{1/2} = 14 \, {\rm min}$). Reproduced from Ref. 6 with permission from the Royal Society of Chemistry.

In Chapter 3, we utilized the delayed reactant labeling method to study the relative kinetics of different catalytic cycles in the palladium-catalyzed alkoxycarbonylation reaction of styrene, offering a more accurate reflection of reaction dynamics and mechanisms 14

Energy-resolved collision-induced dissociation (Energy-resolved CID)

Energy-resolved collision-induced dissociation (CID) is a method in mass spectrometry that determines the bond dissociation energy or fragment's appearance energies. It involves selecting a precursor ion and colliding it with a neutral gas within an ion trap or other mass spectrometric instrument to cause fragmentation (Figure 3b). This fragmentation data allows for the experimental calculation of binding energy (Figure 3c). Precise calibration of the energy scale is crucial and is done using thermometer ions with known fragmentation patterns as benchmarks. 15,16

In this thesis, the energy-resolved collision-induced dissociation (CID) experiments were conducted using an LCQ Deca mass spectrometer (ion trap) with an ESI source. The collision energies for the positive ions (Chapters 5-7) were calibrated using benzylpyridinium and benzhydrylpyridinium thermometer ions using Schröder's method.^{15,16} Similarly, carboxylate ions^{17,18} of known bond dissociation energies were used for calibration for the negatively charged ions (Chapter 3).¹⁴

Infrared and Visible Ion Spectroscopy

The infrared and visible photodissociation spectra of the ions were measured using the ISORI (Ion Spectroscopy of Reaction Intermediates) instrument equipped with an electrospray ionization (ESI) source.¹⁹ Figure 4 depicts the schematics of the homebuilt ISORI instrument built by modification of TSQ 7000 instrument.

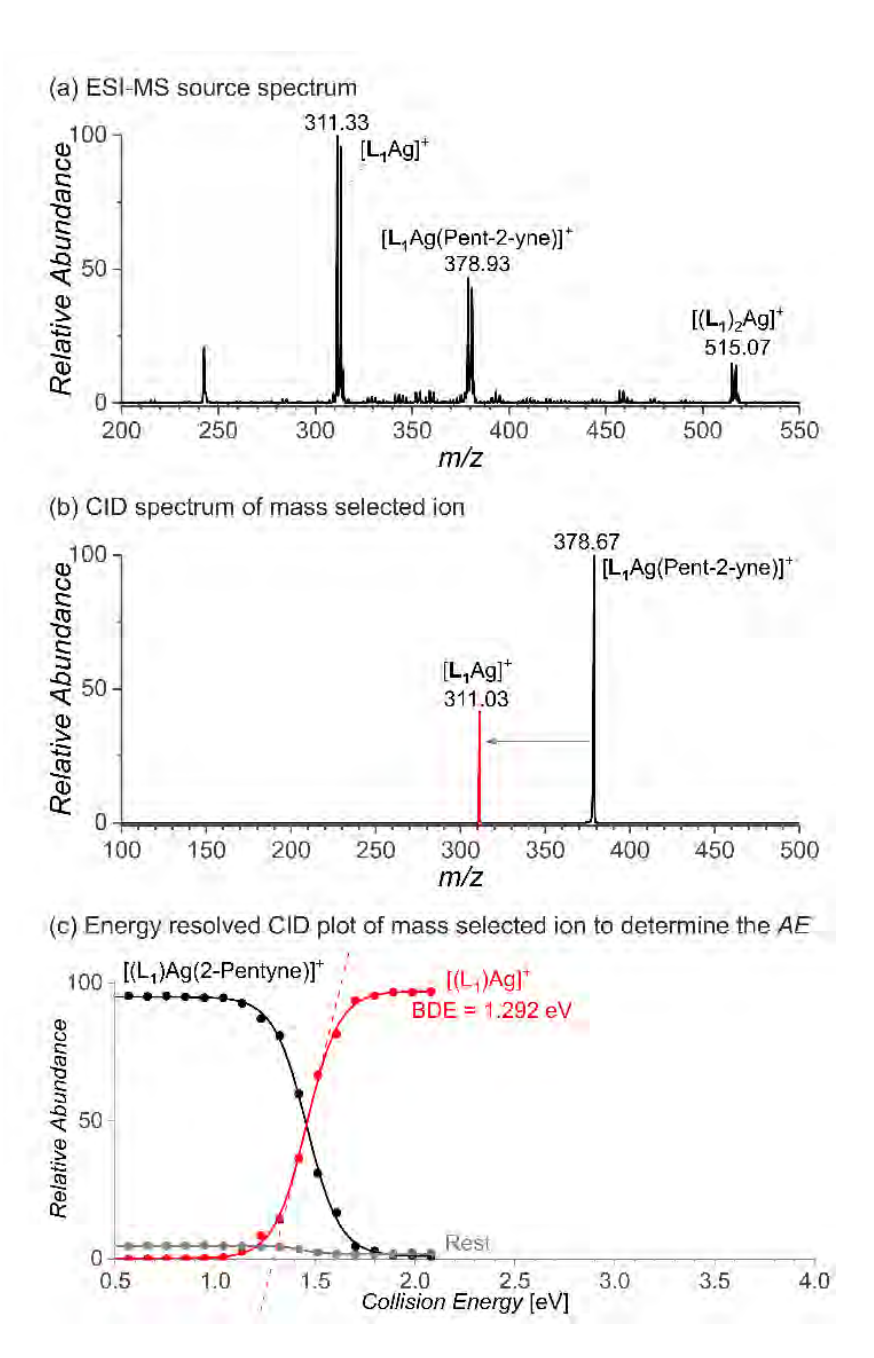


Figure 3. An example of experimental appearance energy calculation9: (a) ESI-MS spectrum of dichloromethane solution of AgPF $_{6'}$ L $_1$ and pent-2-yne, (b) CID spectrum of mass-selected ion m/z 379 [L $_1$ Ag(2-pentyne)] $^+$ and (c) Energy-resolved CID spectrum of m/z 379 [L $_1$ Ag(2-pentyne)] $^+$ and the extrapolation of the fragmentation onset to determine the appearance energy.

Infrared photodissociation spectroscopy (IRPD) is carried out using helium tagging. The ions of interest generated by ESI were mass-selected by the quadrupole mass filter and transferred via a bender and octopole guide to a cold ion trap operated at 3-5 K.²⁰ Collisions with helium atoms cool the ions, and the thermalized ions attach to a helium atom. These helium-tagged ions were then used for spectroscopic experiments. The ions were in alternative cycles irradiated. After irradiation, the ions were extracted, mass analyzed by a quadrupole, and detected by a Daly-type detector. The spectra are constructed as $1-N(_{ij})/N_{0i}$, where $N(_{ij})$ is the number of helium complexes after the irradiation, and N_0 is the number of helium complexes in alternative cycles without the irradiation. The photon source was OPO/OPA LaserVision pumped by Nd: YAG laser Surelite EX from Continuum (tuning range 600-4700 cm⁻¹, FWHM ~ 1.5 cm⁻¹, 10 ns pulse length) for the infrared spectra and SuperK Extreme laser (420-650 nm) for the visible photodissociation (visPD) spectra. Due to the low absorption efficiency, the electronic spectra were measured with simple photodissociation, not helium tagging. For IRPD, helium tagging was primarily used; in cases where attaching helium to the complexes is challenging, a mixture of neon or argon (1-5% concentration) with helium is used as an alternative.

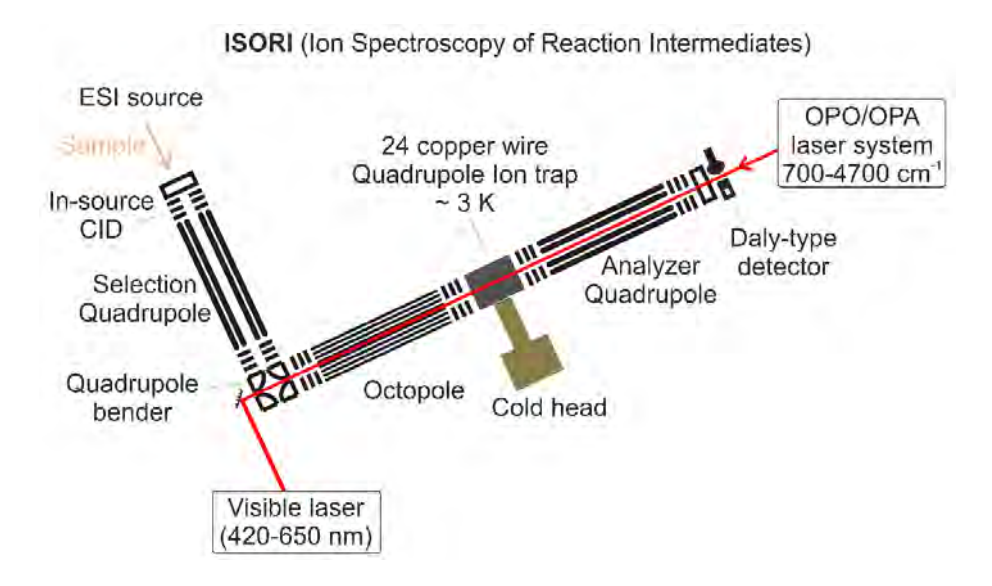


Figure 4. Helium tagging Infrared spectroscopy (He-IRPD) and visible photodissociation spectroscopy (visPD) on the ISORI instrument. Adapted with permission from Ref 19. Copyright 2016 American Chemical Society.

Theoretical calculations

Density functional theory (DFT)

Gaussian 16²¹ was used to calculate the theoretical infrared and visible spectra of specified complexes in this thesis. The functional and basis sets used are mentioned in the appendices of the chapters. In all cases, optimized structures were checked to ensure that the frequency calculation contained no imaginary frequency; this also provided us with the theoretical IR spectra of the complexes. For the theoretical visible spectra of the complexes, time-dependent DFT (TD-DFT) was performed.²²

Collision cross-section (CCS)

We performed ion mobility separation experiments on Bruker timsTOF. The mass and mobilities were calibrated using a standard calibration solution.²³ The experimental CCS was determined using the DataAnalysis and Bruker Compass mobility calculator. To compare these experimentally obtained CCS data, we calculated the theoretical CCS using the Collidoscope program.²⁴ For these calculations (Chapter 3), we used the optimized geometries of the complexes. Collidoscope calculations using the 'trajectory method' based CCS calculator with N_2 as the collision gas were performed.

References

- (1) Schröder, D. Applications of Electrospray Ionization Mass Spectrometry in Mechanistic Studies and Catalysis Research. Acc. Chem. Res. 2012, 45 (9), 1521-1532.
- lacobucci, C.; Reale, S.; De Angelis, F. Elusive Reaction Intermediates in Solution Explored by ESI-MS: (2) Reverse Periscope for Mechanistic Investigations. Angew. Chemie - Int. Ed. 2016, 55 (9), 2980–2993.
- (3) Santos, L. S. Online Mechanistic Investigations of Catalyzed Reactions by Electrospray Ionization Mass Spectrometry: A Tool to Intercept Transient Species in Solution. European J. Ora. Chem. 2008, No. 2, 235-253.
- (4) Chen, P. Electrospray Ionization Tandem Mass Spectrometry in High-Throughput Screening of Homogeneous Catalysts. Angew. Chemie Int. Ed. 2003, 42 (25), 2832-2847.
- Yunker, L. P. E.; Stoddard, R. L.; McIndoe, J. S. Practical Approaches to the ESI-MS Analysis of Catalytic Reactions. J. Mass Spectrom. 2014, 49 (1), 1-8.
- Mehara, J.; Roithová, J. Identifying Reactive Intermediates by Mass Spectrometry. Chem. Sci. 2020, 11 (44), 11960-11972.
- (7) Thomas, G. T.; Donnecke, S.; Chagunda, I. C.; McIndoe, J. S. Pressurized Sample Infusion. Chemistry-Methods 2022, 2 (1).
- Bütikofer, A.: Chen, P. Cyclopentadienone Iron Complex-Catalyzed Hydrogenation of Ketones: An Operando Spectrometric Study Using Pressurized Sample Infusion-Electrospray Ionization-Mass Spectrometry. Organometallics 2022, 41 (16), 2349–2364.
- Mehara, J.; Watson, B. T.; Noonikara-Poyil, A.; Zacharias, A. O.; Roithová, J.; Rasika Dias, H. V. Binding Interactions in Copper, Silver and Gold Π-Complexes. Chem. – A Eur. J. 2022, 28 (13).
- (10) Jašíková, L.; Anania, M.; Hybelbauerová, S.; Roithová, J. Reaction Intermediates Kinetics in Solution Investigated by Electrospray Ionization Mass Spectrometry: Diaurated Complexes. J. Am. Chem. Soc. 2015, 137 (42), 13647-13657.
- (11) Schulz, J.; Jašík, J.; Gray, A.; Roithová, J. Formation of Oxazoles from Elusive Gold(I) α-Oxocarbenes: A Mechanistic Study. Chem. - A Eur. J. 2016, 22 (28), 9827–9834.
- (12) Duez, Q.; Tinnemans, P.; Elemans, J. A. A. W.; Roithová, J. Kinetics of Ligand Exchange in Solution: A Quantitative Mass Spectrometry Approach. Chem. Sci. 2023, 14 (36), 9759–9769.
- (13) Duez, Q.; Marek, L.; Váňa, J.; Hanusek, J.; Roithová, J. Autocatalysis in Eschenmoser Coupling Reactions. Chem. - A Eur. J. 2024, 30 (9).
- (14) Mehara, J.; Anania, M.; Kočovský, P.; Roithová, J. Competing Mechanisms in Palladium-Catalyzed Alkoxycarbonylation of Styrene. ACS Catal. 2024, 14, 5710–5719.
- (15) Zins, E.-L.; Pepe, C.; Schröder, D. Energy-Dependent Dissociation of Benzylpyridinium lons in an Ion-Trap Mass Spectrometer. J. Mass Spectrom. 2010, 45 (11), 1253–1260.
- (16) Rahrt, R.; Auth, T.; Demireva, M.; Armentrout, P. B.; Koszinowski, K. Benzhydrylpyridinium Ions: A New Class of Thermometer Ions for the Characterization of Electrospray-Ionization Mass Spectrometers. Anal. Chem. 2019, 91 (18), 11703-11711.
- (17) Hanzlová, E.; Váňa, J.; Shaffer, C. J.; Roithová, J.; Martinů, T. Evidence for the Cyclic CN 2 Carbene in the Gas Phase. Org. Lett. 2014, 16 (20), 5482-5485.
- (18) Surendran, A. K.; Tripodi, G. L.; Pluhařová, E.; Pereverzev, A. Y.; Bruekers, J. P. J.; Elemans, J. A. A. W.; Meijer, E. J.; Roithová, J. Host-guest Tuning of the CO 2 Reduction Activity of an Iron Porphyrin Cage. Nat. Sci. **2023**, 3 (1).

- (19) Roithová, J.; Gray, A.; Andris, E.; Jašík, J.; Gerlich, D. Helium Tagging Infrared Photodissociation Spectroscopy of Reactive Ions. Acc. Chem. Res. 2016, 49 (2), 223-230.
- (20) Jašík, J.; Žabka, J.; Roithová, J.; Gerlich, D. Infrared Spectroscopy of Trapped Molecular Dications below 4 K. Int. J. Mass Spectrom. 2013, 354-355, 204-210.
- (21) Frisch, M. J.: Trucks, G. W.: Schlegel, H. B.: Scuseria, G. E.: Robb, M. a.: Cheeseman, J. R.: Scalmani, G.; Barone, V.; Petersson, G. a.; Nakatsuji, H.; Li, X.; Caricato, M.; Marenich, a. V.; Bloino, J.; Janesko, B. G.; Gomperts, R.; Mennucci, B.; Hratchian, H. P.; Ortiz, J. V.; Izmaylov, a. F.; Sonnenberg, J. L.; Williams; Ding, F.; Lipparini, F.; Egidi, F.; Goings, J.; Peng, B.; Petrone, A.; Henderson, T.; Ranasinghe, D.; Zakrzewski, V. G.; Gao, J.; Rega, N.; Zheng, G.; Liang, W.; Hada, M.; Ehara, M.; Toyota, K.; Fukuda, R.; Hasegawa, J.; Ishida, M.; Nakajima, T.; Honda, Y.; Kitao, O.; Nakai, H.; Vreven, T.; Throssell, K.; Montgomery Jr., J. a.; Peralta, J. E.; Ogliaro, F.; Bearpark, M. J.; Heyd, J. J.; Brothers, E. N.; Kudin, K. N.; Staroverov, V. N.; Keith, T. a.; Kobayashi, R.; Normand, J.; Raghavachari, K.; Rendell, a. P.; Burant, J. C.; Iyengar, S. S.; Tomasi, J.; Cossi, M.; Millam, J. M.; Klene, M.; Adamo, C.; Cammi, R.; Ochterski, J. W.; Martin, R. L.; Morokuma, K.; Farkas, O.; Foresman, J. B.; Fox, D. J. G16_C01. 2016, p Gaussian 16, Revision C.01, Gaussian, Inc., Wallin. https://gaussian.com/citation/.
- (22) Adamo, C.; Jacquemin, D. The Calculations of Excited-State Properties with Time-Dependent Density Functional Theory. Chem. Soc. Rev. 2013, 42 (3), 845–856.
- (23) Chen, X.; Duez, Q.; Tripodi, G. L.; Gilissen, P. J.; Piperoudis, D.; Tinnemans, P.; Elemans, J. A. A. W.; Roithová, J.; Nolte, R. J. M. Mechanistic Studies on the Epoxidation of Alkenes by Macrocyclic Manganese Porphyrin Catalysts. European J. Org. Chem. 2022, 2022 (35).
- (24) Ewing, S. A.; Donor, M. T.; Wilson, J. W.; Prell, J. S. Collidoscope: An Improved Tool for Computing Collisional Cross-Sections with the Trajectory Method. J. Am. Soc. Mass Spectrom. 2017, 28 (4), 587-596.



Chapter 3

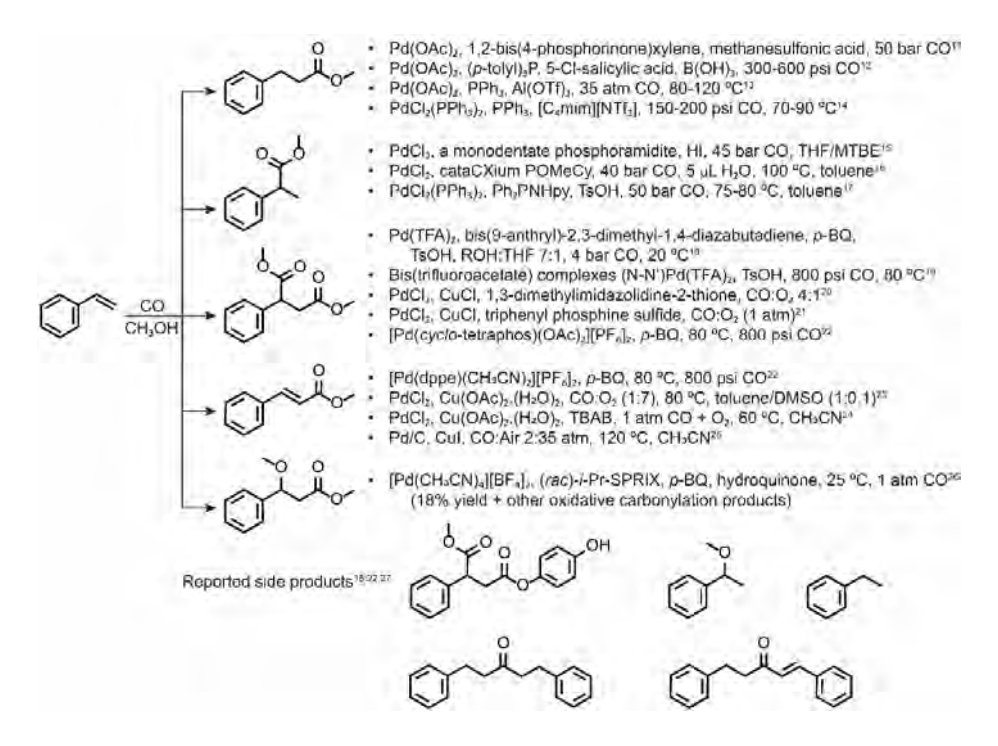
Competing Mechanisms in Palladium-Catalyzed Alkoxycarbonylation of Styrene

The work in this chapter is published: <u>Mehara, J.</u>; Anania, M.; Kočovský, P.; Roithová, J. Competing Mechanisms in Palladium-Catalyzed Alkoxycarbonylation of Styrene. *ACS Catal.* **2024**, *14*, 5710–5719.

Palladium-catalyzed carbonylation is a versatile method for the synthesis of various aldehydes, esters, lactones, or lactams. Alkoxycarbonylation of alkenes with carbon monoxide and alcohol produces either saturated or unsaturated esters as a result of two distinct catalytic cycles. The existing literature presents an inconsistent account of the procedures favoring oxidative carbonylation products. In this study, we have monitored the intermediates featuring in both catalytic cycles of the methoxycarbonylation of styrene PhCH=CH₂ as a model substrate, including all short-lived intermediates, using mass spectrometry. Comparing the reaction kinetics of the intermediates in both cycles in the same reaction mixture shows that the reaction proceeding via alkoxy intermediates [Pd^{II}]-OR, which gives rise to the unsaturated product PhCH=CHCO₂Me, is faster. However, with advancing reaction time, the gradually changing reaction conditions begin to favor the catalytic cycle dominated by palladium hydride [Pd"]-H and alkyl intermediates, affording the saturated products PhCH₂CO₂Me and PhCH(CO₂Me)CH₃ preferentially. The role of the oxidant proved to be crucial: using p-benzoguinone results in a gradual decrease of the pH during the reaction, swaying the system from oxidative conditions towards the palladium hydride cycle. By contrast, copper(II) acetate as oxidant guards the pH within the 5 - 7 range and facilitates the formation of the alkoxy palladium complex [Pd"]-OR, which favors the oxidative reaction producing PhCH=CHCO₃Me with high selectivity. Hence, it is the oxidant, rather than the catalyst, that controls the reaction outcome by a mechanistic switch. Unraveling these principles broadens the scope for developing alkoxycarbonylation reactions and their application in organic synthesis.

Introduction

Carbonylation reactions convert alkenes/alkynes into aldehydes, acids, esters, or lactones in a one-pot catalytic reaction.¹⁻³ The catalysts are usually based on transition metals, such as Rh, Ru, Ir, Pd, Co, and Fe.1,4 Palladium-catalyzed carbonylation reactions, in particular, have garnered significant attention owing to their potentially broad applicability.^{5,6} However, unless an intervention of a neighboring group is involved, 7-10 these reactions typically exhibit low selectivity; thus, carbonylation of α -olefins can give various products with only a limited level of control (Scheme 1), which reduces the synthetic applicability of this methodology. Nevertheless, empirical tuning of the reaction conditions by selection of the ligand (phosphines, imines, NHCs, and thioureas, etc.), oxidant, additives (acids, salts), temperature, and CO pressure, has allowed, to some extent, to steer the reaction toward the desired product (Scheme 1).11-27



Scheme 1. Different conditions steer the methoxycarbonylation of styrene to different products. For more details on the ligands employed, please refer to the original literature.

Previous mechanistic studies suggested that the alkoxycarbonylation can occur via two competing pathways (Figure 1). The first pathway ("Hydride cycle") involves palladium(II) hydride complexes [PdII]-H (1) as the key intermediates. The palladium hydride complexes react with alkenes by 1,2-insertion to form palladium alkyl complexes 2a/2b. In the next step, a 1,1-insertion of CO leads to the formation of acyl-palladium complexes 3a/3b. The final step is alcoholysis, leading to the saturated ester product 4a/4b and regeneration of palladium(II) hydride intermediate 1.28-30 This "hydride" mechanism is favored under acidic conditions31 and does not require an additional oxidant.

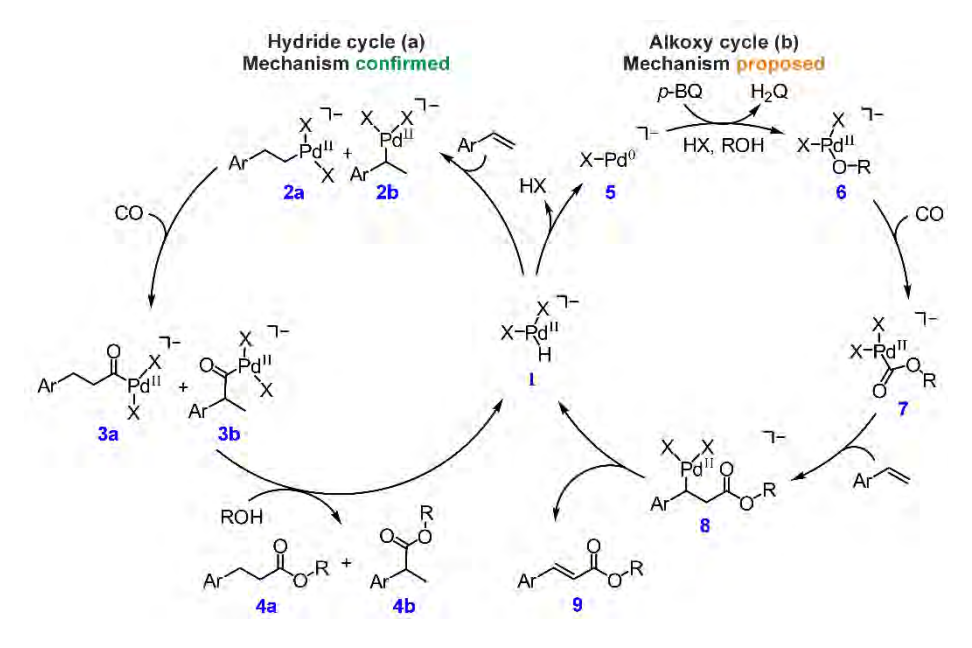


Figure 1. Palladium-catalyzed carbonylation: (a) Palladium-hydride mechanism and (b) palladiumalkoxy mechanism. The formulas assume negatively charged ligands 'X'. If one or both 'X' are neutral ligands, then the overall charge of the complexes changes accordingly.

All intermediates in the hydride cycle were studied by NMR spectroscopy.³²⁻³⁸ The structures of palladium hydride complexes and acyl-palladium complexes were characterized by X-ray spectroscopy. 33,38,39 Further mechanistic studies involved DFT, deuterium labeling, HPLC-MS, and GC-MS techniques. 33,34,39-41

The alternative mechanism ("Alkoxy cycle") can be conjectured to feature alkoxypalladium complexes 6 as the key intermediates, which are likely to insert CO, generating alkoxycarbonyl palladium intermediates 7. Subsequent steps would involve 1,2-insertion of an alkene (8), followed by β -H elimination, ultimately yielding the unsaturated ester product 9 and palladium-hydride complex 1 in analogy with the classical Heck reaction (Figure 1). Palladium hydride 1 can release a proton (H⁺) or eliminate acid (HX) by reductive elimination, leading to the formation of palladium(0) complex 5. The alkoxy cycle would then continue with the reoxidation of palladium(0) concomitant with the reformation of the alkoxypalladium complex 6. For phosphine-based ligands, alkoxycarbonyl palladium complexes were prepared and studied previously by NMR spectroscopy. 42,43

Controlling the selectivity of the alkoxycarbonylation reaction would require controlling the competition between these two cycles at the branching point of the formation of palladium hydride 1. The alkoxy cycle can be easily suppressed by adding an acid, disfavoring the reductive elimination step. The reaction then proceeds selectively towards the saturated products 4a/4b, 16,36-38,41 The conditions favoring unsaturated products are more challenging to achieve. 23,24

Several protocols for selective alkoxycarbonylation to afford unsaturated products were published, which, however, do not offer common ground for a mechanistic rationale of the observed selectivity.^{22–25,42,43} One of us has previously highlighted the significant role of acetonitrile in the oxidative alkoxycarbonylation of terminal alkenes toward α,β-unsaturated esters, suggesting the key role of acetonitrile as a ligand to the palladium intermediates, provided Cu(OAc), •H₂O is employed as the oxidant.²⁴ Nevertheless, the actual role of this ligand, i.e., how it swings the reaction toward the unsaturated ester, was unclear. Furthermore, when CuCl₂ was used instead of Cu(OAc)₂, the reaction did not proceed even in acetonitrile.²⁴ Wang et al., who used copper(II) acetate, also reported a palladium-catalyzed oxidative alkoxycarbonylation of alkenes.²³ Unlike the previous study, which emphasized the importance of acetonitrile as a ligand, Wang et al. employed a toluene/dimethyl sulfoxide (DMSO) mixture as a solvent with no additional ligands. They proposed that acetate ions play a key role in alcohol activation and Pd(II) regeneration. In this respect, it is pertinent to note that various reactions based on palladium catalysts and DMSO (or its congeners) as a ligand have been reported, where oxygen acts as the sole oxidant for Pd(II) regeneration.⁴⁴⁻⁵¹ Maffei et al. utilized a heterogenous palladium source (Pd/C) and copper iodide to achieve effective oxidative alkoxycarbonylation of olefins to produce unsaturated esters.²⁵ They suggested that this process required homogenous palladium (leaching from the support) and a low concentration of carbon monoxide. In the very first example of oxidative carbonylation, Cometti and Chiusoli demonstrated the conversion of styrene into methyl cinnamate and also noted that the low CO pressure favored the desired product.⁵² On the other hand, higher CO pressure, in combination with certain ligands, led to the formation of the dicarbonylated products.^{25,52} Bianchini et al. successfully controlled the selectivity of the methoxycarbonylation of styrene by steering it either toward methyl cinnamate or to dimethyl phenyl succinate by employing palladium precursors with various phosphine ligands.²²

In light of the numerous conditions published to date, this chapter describes our efforts to decipher the competition between two mechanisms. By using mass spectrometry to monitor reactive intermediates, we have investigated the effects of various reaction conditions on both the kinetics of the reaction and the proportional occurrence of individual pathways.

Results and Discussion

We focused on the interplay of intermediates in the two catalytic cycles in the methoxycarbonylation of styrene (Figure 1) under oxidative conditions by electrospray ionization mass spectrometry (ESI-MS). This technique is particularly suited for detecting low-abundance intermediates present in reaction mixtures.^{53–55} We mainly focused on PdCl₂ as the catalyst in an acetonitrile/methanol solvent mixture using p-benzoquinone or Cu(OAc),•H,O as oxidants. In addition, we have also tested toluene/DMSO solvent and PdCl₂(PPh₂)₂ and PdCl₂(dppf) catalysts. The intermediates were detected as negative ions in the absence of phosphine ligands $(X = CI^{-})$ in Figure 1) or as positive ions when supported by phosphines (both X are neutral phosphine ligands in Figure 1, changing the charge of the complexes to +1; see Figures S1-S4 and S37-S45).

The palladium-hydride cycle

First, we monitored the reaction mixture of PdCl₂, p-benzoquinone, styrene, and CO in CH₂CN/CH₂OH by offline sampling (for details, see SI). Aliquots of the reaction mixture were filtered, diluted, and analyzed using ESI-MS (Figures 2b and S1-S3). Initially, we observed [PdCl₃] and [PdCl₃(CO)] as dominant species. Other palladium complexes included the hydrido-palladium complex [PdCl₃(H)]⁻ (m/z 177) and complexes formally corresponding to [PdCl₃(H,styrene)]⁻ (m/z 281, blue) and $[PdCl_2(H,styrene,CO)]^{-1}$ (m/z 309, red) (Figure 2b). These palladium complexes were stable at room temperature and could be detected over a long reaction time (20-120 minutes).

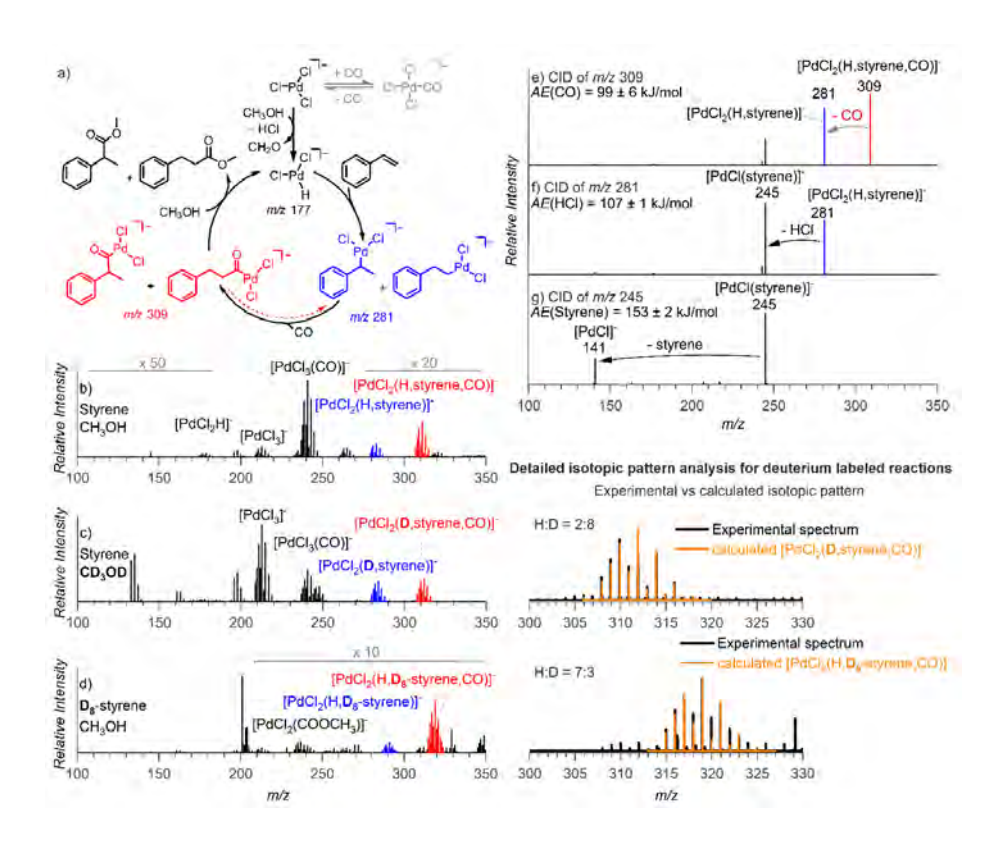


Figure 2. Palladium-hydride cycle: (a) Reaction mechanism with the detected intermediates. (b-d) Electrospray-ionization mass spectra of the reaction mixture; (b) PdCl₂ (100 μM), p-benzoquinone (1 mM), styrene (5 mM) in CH₂CN and CH₂OH (1:1) under the CO atmosphere at 40 °C; (c) styrene with CD₂OD; and (d) D₀-styrene with CH₂OH, the detailed spectra on the right show the isotopic patterns of the acyl-palladium complexes; the calculated H:D ratio refers to the hydrogen atom build-in as hydride - the ratio varied between 1:9 to 3:7 depending on the reaction time. (e-g) Collision-induced dissociation spectra of mass-selected ions indicated in the graphs. Bond dissociation energies (BDEs) were determined from energy-resolved experiments (see Figures S21-S23).

We have further investigated the detected complexes by collision-induced dissociation (CID) experiments (Figure 2e-q). The detected [PdCl₃(H,styrene)]⁻ intermediate, arising from [PdCl₂(H,styrene,CO)]⁻ (Figure 2e), loses HCl (Figure 2f), indicating that it corresponds to the σ-bound alkyl palladium [PdCl₂(CH₂-CH₂-Ph)]⁻ or $[PdCl_{3}(CH(CH_{3})-Ph)]^{-}$ rather than to a complex with π -coordinated styrene, which would be expected to lose preferentially styrene. The observed HCl loss must be preceded by the reversed 1,2-insertion of styrene (blue in Figure 2). Hence, the [PdCl(styrene)] fragment should contain π -coordinated styrene. Accordingly, [PdCl(styrene)] eliminates neutral styrene in the follow-up collision-induced dissociation experiment (Figure 2g).

The detected [PdCl_(H,styrene,CO)] complex eliminates CO (red in Figures 2b, 2e) in the collision-induced dissociation. The CO elimination can be interpreted either as the reversed 1,1-insertion reaction from [PdCl₃(CO-C₃H,Ph)]⁻ or dissociation of CO from [PdCl₂(C₂H₄Ph)(CO)]⁻. To assess which complex was detected, we compared the experimental appearance energies of the given fragmentations (AEs) with the theoretically calculated bond-dissociation energies (BDEs). The calculated BDE of CO in the [PdCl₂(CH(CH₃)-Ph)(CO)]⁻ and [PdCl₂(CH₂-CH₂-Ph)(CO)]⁻ complexes, featuring tetra-coordinated palladium with one ligand being CO, is 71 kJ mol⁻¹ and 77 kJ mol⁻¹, respectively (Table S1). On the other hand, the BDE of CO in the acylpalladium intermediates [PdCl₂(CO-CH(CH₂)-Ph)]⁻ and [PdCl₂(CO-CH₂-CH₂-Ph)]⁻ are 95 kJ mol⁻¹ and 96 kJ mol⁻¹, respectively. Since the latter figures are consistent with the experimental value of 99 ± 6 kJ mol⁻¹ obtained by the energy-resolved collisioninduced dissociation experiment, 56,57 the detected complex [PdCl₃(H,styrene,CO)]⁻ can be assigned the acyl-palladium structure, i.e., [PdCl₂(CO-C₂H₄-Ph)]⁻.

The [PdCl₂(CO-C₂H₄-Ph)]⁻ assignment was corroborated by isotopic labeling: In analogy with the previous experiment, the reaction of D₈-styrene and D₄-methanol generated the perdeuterated complex [PdCl₂(CO-C₂D₄-Ph^{D5})]⁻ (m/z 318, Figure S10). Collisioninduced dissociation of this intermediate led to the consecutive elimination of CO and DCI, as expected. The reaction of D_s-styrene and unlabeled methanol led to [PdCl₃(CO-C₃D₃H-Ph^{D5})]⁻ (m/z 317, Figure 2d), which sequentially extruded CO and DCI or HCI in the collision experiments (Figure S11).

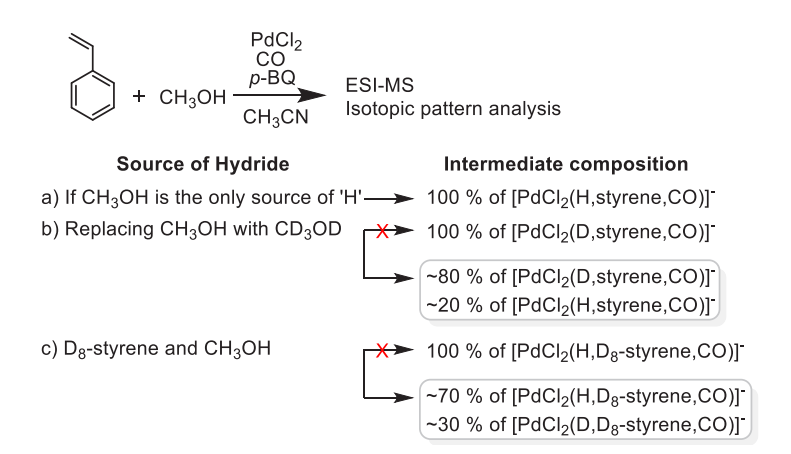
Using ion-mobility separation (IMS), we have endeavored to identify the isomers of the detected ions. Under catalytic conditions (p-benzoquinone as an oxidant), we observed only single IMS peaks for the detected palladium complexes (Figure S27). Interestingly, with stoichiometric PdCl₂ concentration, the acyl-palladium intermediates showed two isomers, indicating a reduced selectivity (Figures S28, S29, and Table S3). The appearing minor isomer has a smaller size (collision cross section) than the dominant isomer that prevails at the catalytic conditions. According to the theoretical calculations, the branched [PdCl₃(CO-CH(CH₃)-Ph)]⁻ isomer is smaller (Table S3). Hence, the major detected acyl-palladium complexes correspond to the linear isomer [PdCl₂(CO-CH₂-CH₂-Ph)]⁻.

For the alkylpalladium complexes, we observed both isomers only if we used D₈-styrene and a stoichiometric amount of PdCl₂ (Figure S29). The minor isomer is larger than the dominant one (Figure S29). The calculations again suggest that the branched isomer is smaller than the linear one (Table S2). Accordingly, the

dominant alkyl palladium complex detected from the solution is the branched isomer [PdCl₂(CH(CH₂)-Ph)]⁻.

The final confirmation of the structure for the observed complexes was obtained using infrared multiphoton dissociation (IRMPD) spectroscopy. The IRMPD spectrum of mass-selected [PdCl₃(H,styrene)]⁻ (m/z 281, Figure S30) agrees better with the theoretical IR spectrum of the branched alkylpalladium complex. The IRMPD spectrum of [PdCl₂(H,styrene,CO)]⁻ (m/z 309, Figure S31) agrees best with the linear [PdCl₂(CO-CH₂-CH₂-Ph)]⁻ complex.

The findings about the detected isomeric palladium complexes can serve as a nice demonstration of the Curtin-Hammett principle.⁵⁸ The branched α-phenylalkyl palladium complexes are more stable than their linear counterparts β -phenylalkyl palladium complexes (Table S2). Therefore, they prevail in the solution. However, the linear alkyl palladium complexes react faster in the insertion step, which results in the predominant formation of the linear products (Table S3).



Scheme 2. Summary of the labeling experiment and the resulting isotopic composition of the hydride intermediate [PdCl₂(H,styrene,CO)] observed experimentally (Figures 2c and 2d).

Finally, we addressed the origin of the hydride ligand in 1 (Figure 1). A priori, the palladium hydride intermediates 1 can either be formed by the reaction of the starting palladium complex with methanol or originate from β-hydrogen elimination of the styrene-containing intermediate 8 in the alkoxy-cycle (Figure 1). To shed light on this issue, we further analyzed the labeling experiments. In the reaction of unlabeled styrene with CD₂OD (Figure 2c, Scheme 2b), the ESI-MS spectra showed an almost exclusive formation of [PdCl₂(D,styrene,CO)]⁻

(m/z 310), which suggests that the hydride originates from methanol. However, the ion intensities in the isotopic pattern do not match exactly, indicating the presence of about 20% of [PdCl₂(H,styrene,CO)]⁻ (m/z 309) with H originating from β-hydrogen elimination from the styrene-containing intermediates. In the reaction of labeled D_s-styrene with unlabeled CH₃OH (Figure 2d), we detected [PdCl₂(H,D_sstyrene,CO)]⁻ (m/z 317). Closer inspection of the isotopic pattern revealed about 30% contribution of [PdCl₂(D,D₂-styrene,CO)]⁻ (m/z 318) with D arising by β-deuterium elimination from the D_o-styrene-containing intermediate. These results demonstrate the interconnection of both cycles via the hydride intermediate.

The alkoxy-palladium cycle

The operation of this cycle was inferred from the generally observed reactivity of palladium complexes. However, to date, the intermediates have not been detected directly. Since we assumed them to be short-lived, we opted for the pressurized sample infusion-electrospray ionization-mass spectrometry (PSI-ESI-MS) monitoring.^{59,60} Our experiments showed that, indeed, the intermediates can be detected at room temperature using a CO balloon at reaction times below 30 min. At longer times, the palladium hydride intermediates prevailed (Figure S34). The onset of the palladiumhydride intermediates is linked with the occurrence of palladium black in the reaction vessel, suggesting an insufficient regeneration of the palladium(II) complex, which then results in the formation of larger palladium(0) clusters.

At short reaction times, we have detected the Pd-methoxycarbonyl precursor complexes $[PdCl_3(COOCH_3)]^-$ (m/z 235) and $[PdCl_3(COOCH_3,CO)]^-$ (m/z 263) (Figure 3a and 3b); this assignment was confirmed by the experiments carried out in CD₂OD (Figures 3 and S1-S4). The initially formed [PdCl₂(COOCH₂)]⁻ complex undergoes fragmentation by elimination of α -acetolactone (Figure S5) to give the [Pd"Cl₂(H)] fragment. Similarly, [PdCl₂(COOCD₂)] (m/z 238) eliminates deuterated α -acetolactone and yields $[Pd^{\parallel}Cl_{\alpha}(D)]^{-}$. Interestingly, the kinetic isotope effect in the deuterated intermediate decreases the abundance of the rearrangement required for this fragmentation and opens the competing fragmentation path via the loss of CO (Figure S6). The Pd-methoxycarbonyl intermediates were also observed to arise in toluene and other nonpolar solvents or in the presence of phosphine ligands (Figures S39 and S40).

After adding styrene to the reaction mixture containing the alkoxy precursor complexes, the formation of styrene-containing intermediates $[PdCl_{3}(styrene,COOCH_{3})]^{-}$ (m/z 339) was observed (Figure 3b). Notably, the latter intermediate adds another CO molecule to the 4th coordination site, yielding

[PdCl₂(styrene,COOCH₂,CO)]⁻ (m/z 367) (Figure 3b). In collision-induced dissociation, the [PdCl₂(styrene,COOCH₂)]⁻ complex lost HCl (Figure 3d), which corresponds to β-hydrogen elimination. The fragmentation appeared at a low collision energy $(85 \pm 3 \text{ kJ mol}^{-1})$, indicating a low energy barrier for this process.

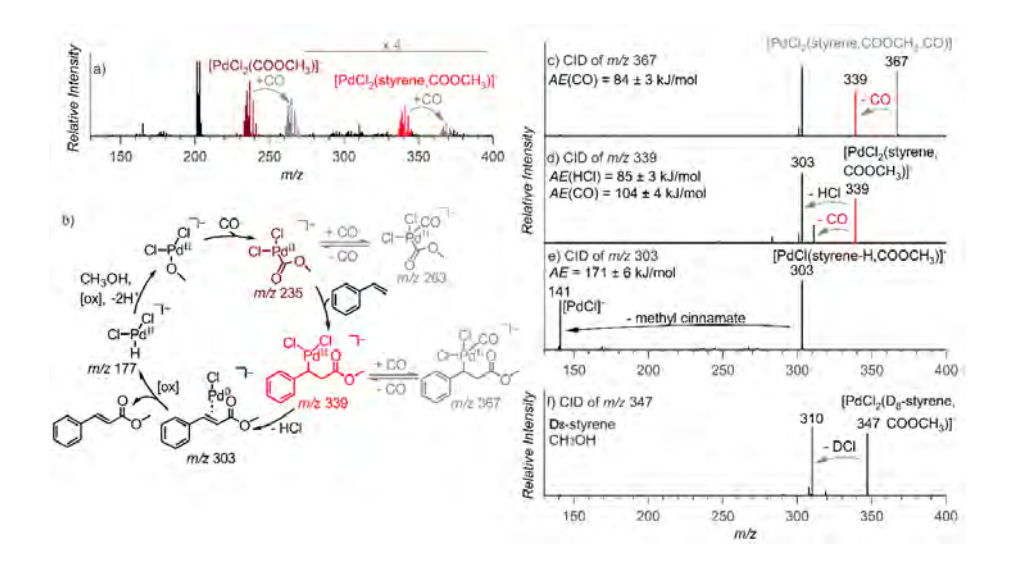


Figure 3. Palladium-alkoxy cycle: (a) PSI-ESI-MS spectrum of the reaction mixture of PdCl₂ (100 μM), p-benzoquinone (1 mM), and styrene (5 mM) in acetonitrile and CH₂OH (1:1) ratio under the CO atmosphere (using a balloon) monitored online for < 20 min; (b) Reaction mechanism with the detected intermediates; (c-f) Collision-induced dissociation spectra of the indicated mass-selected ions. Bond dissociation energies (BDEs) were determined from the energy-resolved collision-induced dissociation experiments (see Figures S24 - S26).

Interplay of the catalytic cycles

The decisive splitting between the hydride and alkoxy catalytic cycles occurs at the point of the palladium hydride formation (Figure 1). Either the hydride inserts the alkene $(1 \rightarrow 2a/2b)$ or is transformed into the alkoxypalladium complex $(1 \rightarrow 6)$. Hence, the kinetics of these steps affect the selectivity of the reactions. We employed delayed reactant labeling to shed light on the kinetics of these catalytic cycles.^{61,62} This method allows us to study the half-lives of the detected intermediates in solution by monitoring the equilibration of their isotopologs. Here, we added D_r-styrene to the running reaction of unlabeled reactants. In time, we observed the building up of the deuterated intermediates next to their unlabeled congeners already present. The kinetics of their equilibration reflect their lifetime in the solution.

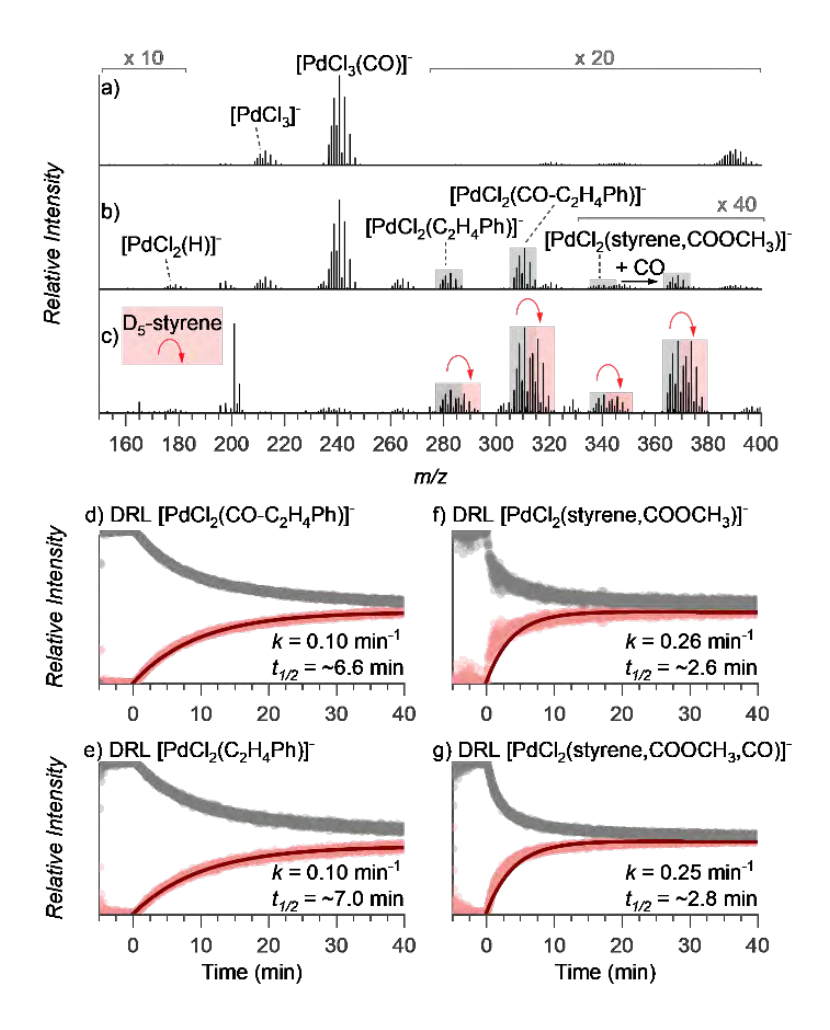


Figure 4. Snapshots of ESI-MS spectra during delayed reactant labeling experiments. The compositions were as follows: (a) $PdCl_2$ and oxidant (p-benzoquinone) in acetonitrile pre-stirred under CO atmosphere at 40 °C for 10-20 min; (b) styrene in methanol was added; (c) After a delay of 5 minutes, D_s -styrene in methanol was added and the reaction was further monitored by ESI-MS (red curly arrows indicate the corresponding intermediate with D_s -styrene); (d-g) Relative evolution of the signal intensities of the unlabeled (light grey) and labeled (light red) intermediates for the indicated complex. The fits (dark red) correspond to the $I_t = I_{eq}(1 - e^{-kt})$ function, where I_t and I_{eq} are relative signal intensities of the labeled ion and unlabeled ion at time t and the steady-state equilibrium, respectively, and k is the rate constant, $t_{1/2} = \ln 2/k$.

Figure 4 shows the experiment under the settings where the intermediates in both catalytic cycles are present in the reaction mixture. First, we set up the carbonylation reaction with unlabeled reactants. We detected the palladium hydride intermediates $[PdCl_2(C_2H_4Ph)]^-$ and $[PdCl_2(CO-C_2H_4Ph)]^-$ (Figure 4a and 4b),

as well as the palladium alkoxy intermediates [PdCl₂(styrene,COOCH₂)]⁻ and [PdCl₂(styrene,COOCH₂,CO)]⁻. After 5 min, we added D₅-styrene and saw the onset of the signals of the deuterated analogs of all detected intermediates (Figure 4c). The relative evolution of the non-deuterated and deuterated signals can be quantitatively evaluated because the ESI-MS detection efficiency is equal for different isotopologs (see Figures 4d-g).⁶³ Accordingly, we fitted the isotopolog equilibration kinetics with an exponential fit (data points: light grey and red; fit: dark red lines in Figures 4d-q). The derived half-life times of the intermediates in the solution revealed that the hydride-cycle intermediates have a much longer half-life (~6.6 min) than the alkoxy-cycle intermediates (~2.6 min).⁶⁰ The half-lives of the hydride-cycle intermediates [PdCl₂(C₂H₄Ph)]⁻ and [PdCl₃(CO-C₂H₄Ph)]⁻ are comparable, demonstrating that the CO insertion is fast and does not represent a bottleneck of the reaction (compare Figures 4d and 4e). Hence, the final methanolysis is most likely the rate-determining step in the hydride cycle.

The observed short lifetime of the intermediate [PdCl₃(styrene,COOCH₃)]⁻ in the alkoxy cycle suggests rapid β-hydrogen elimination, which agrees well with the low activation energy determined for the HCI elimination from the gaseous complex (Figure 3d). Equilibration of the off-cycle intermediates [PdCl₃(styrene,COOCH₃,CO)]⁻ is slightly slower, suggesting that both these palladium complexes are in equilibrium and CO addition does not significantly affect the reaction (at the given pressure). We also tested the kinetics of equilibration of Pd alkoxy precursor complexes [PdCl₃(COOCH₂)]⁻ (m/z 235) with labeled CD₃OH (Figure S32). As expected, these intermediates equilibrated almost immediately. Hence, the results clearly show that under the conditions that favor the formation of alkoxy intermediates, the catalytic cycle towards unsaturated products is faster and should, therefore, prevail. However, as the reaction progresses, the conditions in the reaction mixture begin to disfavor the formation of the alkoxy intermediates (vide infra), and, as a result, the hydride catalytic cycle starts to dominate.

To support the conclusion derived from the monitoring of the reactive intermediates, we have also monitored the progress and selectivity of the methoxycarbonylation of styrene by gas chromatography (Figure S35a). Using a stoichiometric amount of p-benzoquinone and 25 mol% PdCl₃ catalyst, we could detect about 1:1:1 ratio of two saturated- and one unsaturated esters after 30 min of the reaction time. At longer reaction times, the saturated products started to prevail, and the unsaturated product was fully converted into the product of double methoxycarbonylation. We also tested the reaction under the same conditions but with Cu(OAc)₂ oxidant. The reaction

was fully selective for the formation of the unsaturated ester product with a partial conversion to the product of double methoxycarbonylation (Figures S35b and S36).

Steering the catalytic cycles

Understanding the differences between the two catalytic cycles opens the way to identifying a possible steering wheel. As previously found, the pH of the reaction mixture is an important factor: In the presence of an acid, the hydride cycle becomes dominant, leading to an improved selectivity in carbonylation procedures by promoting the formation of the saturated products **4a/4b**. However, even without an added acid, we observed significant variations in the pH in experiments with various oxidants. Reaction mixtures with stoichiometric PdCl₂ and *p*-benzoquinone became acidic (pH < 3) after 30 minutes, while those with copper acetate monohydrate as oxidant retained the pH in the approximate range of 5 - 7. As demonstrated before, lower pH favors the hydride catalytic cycle. 16,17,29,37 Hence, the choice of the oxidant is critical for the outcome of the carbonylation reactions.

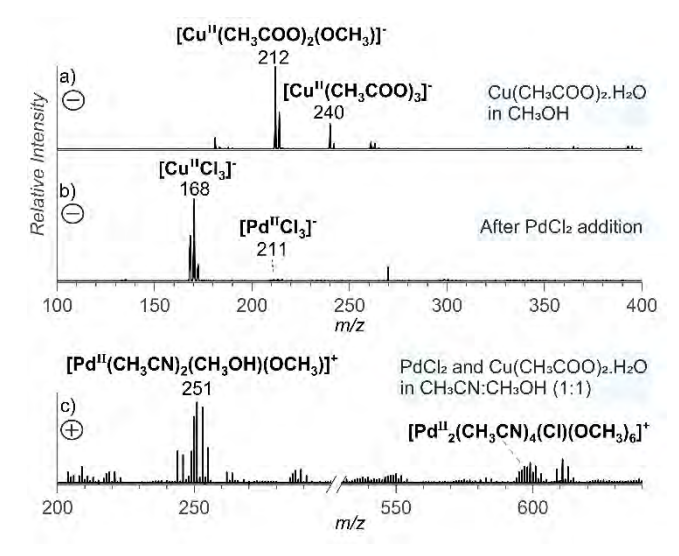


Figure 5. (a) ESI-MS spectrum (negative mode) of copper acetate monohydrate dissolved in methanol; (b) addition of PdCl₂ to the solution of copper acetate monohydrate in methanol; and (c) ESI-MS (positive mode) spectrum of copper acetate monohydrate and PdCl₃ in a mixture of CH₃CN: CH₃OH.

The transformation of palladium(II) hydride 1 into the palladium(II)-alkoxy intermediate 6 is the key factor in steering the reactivity towards the unsaturated product 9. To investigate the role of copper beyond being an oxidant in the catalytic cycle, we investigated the speciation of copper and palladium complexes in solution. Analysis of a solution of copper acetate in methanol revealed the

presence of [Cu(OAc)₂(OCH₂)]⁻ m/z 212 (Figure 5a), indicating the formation of methoxy complexes. Upon adding PdCl₂ to the solution, the copper complexes are transformed into [CuCl₃]⁻ ions (Figure 5b), suggesting the copper participation in facilitating the transfer of the methoxo and acetato ligands to the palladium center.^{24,64} The formation of mono- and di-Pd complexes with methoxy ligands is detected in the positive ionization mode (Figure 5c, Figure S46).

a)
$$\overset{\text{Cl}}{\overset{}{\overset{}{\vdash}}} \text{Pd} \overset{\text{Cl}}{\overset{}{\overset{}{\vdash}}} \text{Cu(OAc)}_2 + \text{Cu(OAc)}(\text{OMe}) \longrightarrow \overset{\text{AcO.}}{\overset{}{\vdash}} \overset{\text{OAc}}{\overset{}{\overset{}{\vdash}}} + \text{Cu}_2\text{Cl}_2 \downarrow + \text{AcOH}$$

b)
$$Cu_2X_2 + O_2 + 2H^+ \longrightarrow Cu_2(OH)_2X_2 \xrightarrow{MeOH} Cu_2(OMe)_2X_2$$

Scheme 3. Reaction pathway for transforming [Pd]-H into [Pd]-OMe in the presence of copper acetate as oxidant, based on the ions observed in Figure 5.'X' stands for any counter ion present in the solution.

During the methoxycarbonylation reaction, we detected many mixed palladiumcopper complexes, all corresponding to a palladium(II) interaction with copper(I). These complexes are thus likely intermediates in the reoxidation of palladium(0) by copper(II) in the solution. The speciation of the complexes changes with the progressing reaction time (Figure 6a). At the onset of the reaction, the complexes mostly contained Cl⁻ counterions. With increasing the reaction time, Cl⁻ was progressively exchanged by AcO^{-} (Figure 6b, green \rightarrow red \rightarrow blue). Finally, we detected dimeric copper(I) complexes bridged by MeO⁻ (Figure 6c, orange). This observation is consistent with removing Cl⁻ by Cu¹ from the solution (Scheme 3a). In addition, the reoxidation of copper(I) requires protons, which leads transiently to the formation of copper(II) hydroxide (Scheme 3b). This reaction helps to guard the pH during the reaction and supports the effective formation of the methanolato ligands required for the methoxycarbonylation reaction. Overall, this finding explains the significance of the copper-based oxidants in the alkoxy pathway, leading to the dominant formation of unsaturated esters (9) as the major products.

Our experiments were performed with the PdCl₂ catalyst precursor. The results imply that using Pd(OAc), instead should be advantageous as it would avoid the initial Cl⁻ to AcO⁻ exchange. The effect of Cl⁻ on pH using the copper oxidant is diminished due to the Cu_2Cl_2 precipitation. However, when using p-BQ or other oxidants, a palladium salt with counterions from weaker conjugated acids (e.g., AcO⁻) should be more inclined to drive the reaction toward the alkoxy cycle, which agrees with our earlier findings.²⁴

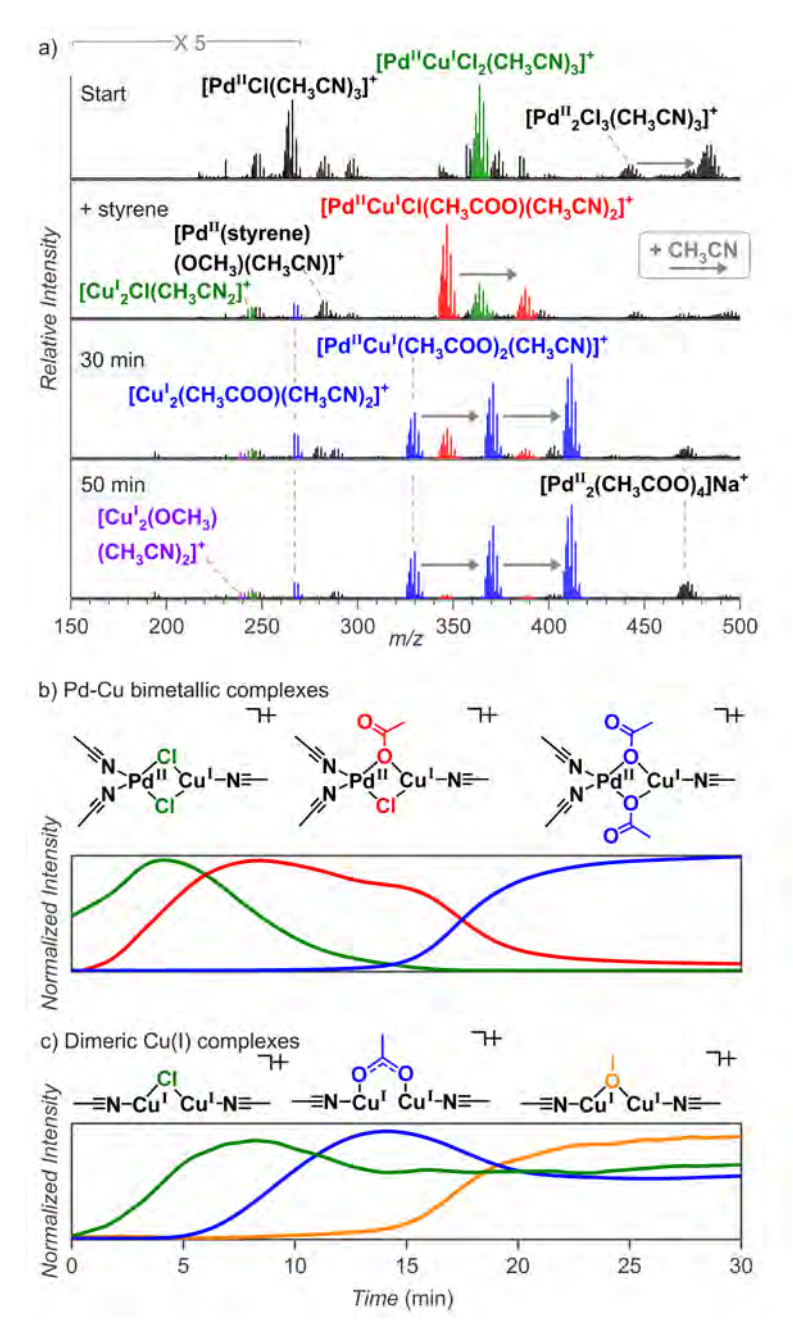


Figure 6. (a) Snapshots of ESI-MS (positive mode) spectra of PdCl₂ and copper acetate monohydrate in CH₃CN: CH₃OH under the CO and O₂ atmosphere at room temperature: at the start, after styrene addition, 30 min, and 50 min; the grey arrows indicate the complex with additional CH,CN. (b) Plot of normalized traces of specified bimetallic complexes vs. time; and (c) plot of normalized traces of specified dimeric Cu(I) complexes vs. time. For more information, see Figure S48.

The mechanism of reoxidation of palladium(0) complexes with quinones was studied previously, and the η^2 -Pd(II)-(p-BQ) and η^2 -Pd(0)-(p-BQ) were intercepted by NMR spectroscopy. 65-68 The reduction of p-benzoquinone to hydroquinone is associated with 2e⁻ oxidation of palladium(0) and consumption of 2 protons. Hence, efficient oxidation of palladium(0) with p-benzoquinone should not lead to a dramatic pH drop. Nevertheless, hydroquinone is a weak acid (pKa ~ 10); hence, even if the oxidation were efficient, hydroquinone could contribute to the pH drop. Overall, the pH drop and the low selectivity suggest that p-benzoguinone is not a good oxidant for oxidative palladium-catalyzed methoxycarbonylation reactions with PdCl₃. However, under optimized conditions, using phosphine ligands to stabilize palladium complexes, quinone oxidants can be sufficient.²² Note, that in other reactions, not involving palladium-hydride intermediates, p-benzoquinone can serve as an excellent oxidant. For example, in 1,4-difunctionalization of 1,3-dienes and in allylic oxidation of olefins, both in the presence of acetic acid. 69-72 However, these examples are mechanistically unrelated to the reaction studied here.

Conclusions

Two competing catalytic cycles in the palladium-catalyzed methoxycarbonylation reaction of styrene were investigated by using electrospray ionization mass spectrometry (Figure 1): catalytic cycle via alkylpalladium intermediates 2a/2b, yielding the saturated products 4a/4b, and catalytic cycle via alkoxypalladium intermediates 6, affording the unsaturated products 9. All key intermediates were detected, including the short-lived low-abundant alkoxycarbonyl species 8, which had never been detected before.

Isotopic labeling (with deuterium) allowed us to study the kinetics of the reactions of the intermediates in both catalytic cycles simultaneously in the same reaction mixture. A direct comparison shows the following: The reaction that proceeds via alkoxy intermediates, giving rise to the unsaturated product PhCH=CHCO₂CH₃, is faster than the competing reaction occurring via the alkylpalladium intermediate from which the saturated isomeric products PhCH₂CO₂CH₃ and PhCH(CO₂CH₃) CH₃ are obtained. However, the conditions during the reaction evolve, manifested by a gradual suppression of the alkoxypalladium cycle and the ultimate domination of the palladium hydride and alkylpalladium intermediates resulting in the formation of saturated products.

The oxidant has the key steering role in the reaction: p-benzoquinone causes a gradual decrease of pH, favoring the formation of palladium hydride intermediates, which leads to low reaction selectivity. By contrast, copper(II) acetate guards the pH in the 5 – 7 range. In addition, the copper ions form methoxy complexes by anion exchange with methanol, which facilitates the formation of palladium methoxy complexes. Hence, a mixture of copper(II) acetate and a palladium(II) salt is ideal for steering the alkoxycarbonylation reaction towards the unsaturated products, as demonstrated in the successful protocols – albeit until today without understanding the key role of the copper(II) acetate additive.

Overall, our findings provide the mechanistic understanding of the Pd-catalyzed alkoxycarbonylation of olefins but are likely to have significant implications in catalytic redox processes - far beyond the realm of palladium.

References

- 1. Peng, J. B.; Geng, H. Q.; Wu, X. F. The Chemistry of CO: Carbonylation. Chem 2019, 5 (3), 526–552.
- 2. Ma, K.; Martin, B. S.; Yin, X.; Dai, M. Natural Product Syntheses via Carbonylative Cyclizations. Nat. Prod. Rep. **2019**, 36 (1), 174–219.
- Haynes, A. Carbonylation Reactions. In Comprehensive Inorganic Chemistry II; Elsevier, 2013; Vol. 3. 6, pp 1-24.
- Wu, X. F.; Fang, X.; Wu, L.; Jackstell, R.; Neumann, H.; Beller, M. Transition-Metal-Catalyzed Carbonylation Reactions of Olefins and Alkynes: A Personal Account. Acc. Chem. Res. 2014, 47 (4), 1041-1053.
- Bai, Y.; Davis, D. C.; Dai, M. Natural Product Synthesis via Palladium-Catalyzed Carbonylation. J. Org. Chem. 2017, 82 (5), 2319-2328.
- 6. Sims, H. S.; Dai, M. Palladium-Catalyzed Carbonylations: Application in Complex Natural Product Total Synthesis and Recent Developments. J. Org. Chem. 2023, 88 (8), 4925–4941.
- Kočovský, P.; Bäckvall, J. E. The Syn/Anti-Dichotomy in the Palladium-Catalyzed Addition of 7. Nucleophiles to Alkenes. Chem. - A Eur. J. 2015, 21 (1), 36-56.
- Semmelhack, M. F.; Bodurow, C. Intramolecular Alkoxypalladation/Carbonylation of Alkenes. J. Am. Chem. Soc. 1984, 106 (5), 1496-1498.
- Kočovský, P.; Pour, M. Stereo- and Regiocontrol of Electrophilic Additions to Cyclohexene Systems by Neighboring Groups. Competition of Electronic and Stereoelectronic Effects and Comparison of the Reactivity of Selected Electrophiles. J. Org. Chem. 1990, 55 (21), 5580-5589.
- 10. Malkov, A. V.; Barłóg, M.; Miller-Potucká, L.; Kabeshov, M. A.; Farrugia, L. J.; Kočovský, P. Stereoselective Palladium-Catalyzed Functionalization of Homoallylic Alcohols: A Convenient Synthesis of Di- and Trisubstituted Isoxazolidines and β-Amino-δ-Hydroxy Esters. Chem. - A Eur. J. 2012, 18 (22), 6873-6884.
- 11. Nobbs, J. D.; Low, C. H.; Stubbs, L. P.; Wang, C.; Drent, E.; van Meurs, M. Isomerizing Methoxycarbonylation of Alkenes to Esters Using a Bis(Phosphorinone)Xylene Palladium Catalyst. Organometallics 2017, 36 (2), 391-398.
- 12. Vieira, T. O.; Green, M. J.; Alper, H. Highly Regioselective Anti-Markovnikov Palladium-Borate-Catalyzed Methoxycarbonylation Reactions: Unprecedented Results for Aryl Olefins. Org. Lett. **2006**, 8 (26), 6143-6145.
- 13. Williams, D. B. G.; Shaw, M. L.; Green, M. J.; Holzapfel, C. W. Aluminum Triflate as a Highly Active and Efficient Nonprotic Cocatalyst in the Palladium-Catalyzed Methoxycarbonylation Reaction. Angew. Chemie Int. Ed. **2008**, 47 (3), 560–563.
- 14. Klingshirn, M. A.; Rogers, R. D.; Shaughnessy, K. H. Palladium-Catalyzed Hydroesterification of Styrene Derivatives in the Presence of Ionic Liquids. J. Organomet. Chem. 2005, 690 (15), 3620-3626. https://doi.org/10.1016/j.jorganchem.2005.05.031.
- 15. Yao, Y.; Zou, X.; Wang, Y.; Yang, H.; Ren, Z.; Guan, Z. Palladium-Catalyzed Asymmetric Markovnikov Hydroxycarbonylation and Hydroalkoxycarbonylation of Vinyl Arenes: Synthesis of 2-Arylpropanoic Acids. Angew. Chemie Int. Ed. 2021, 60 (43), 23117–23122.
- 16. Li, H.; Dong, K.; Jiao, H.; Neumann, H.; Jackstell, R.; Beller, M. The Scope and Mechanism of Palladium-Catalysed Markovnikov Alkoxycarbonylation of Alkenes. Nat. Chem. 2016, 8 (12), 1159-1166.

- 17. Aguirre, P. A.; Lagos, C. A.; Moya, S. A.; Zúñiga, C.; Vera-Oyarce, C.; Sola, E.; Peris, G.; Bayón, J. C. Methoxycarbonylation of Olefins Catalyzed by Palladium Complexes Bearing P,N-Donor Ligands. Dalt. Trans. 2007, No. 46, 5419.
- 18. Fini, F.; Beltrani, M.; Mancuso, R.; Gabriele, B.; Carfagna, C. Selective Aryl α-Diimine/Palladium-Catalyzed Bis-Alkoxy- Carbonylation of Olefins for the Synthesis of Substituted Succinic Diesters. Adv. Synth. Catal. 2015, 357 (1), 177-184.
- 19. Bianchini, C.; Hon, M. L.; Mantovani, G.; Meli, A.; Oberhauser, W. Bis-Alkoxycarbonylation of Styrene by Pyridinimine Palladium Catalysts. New J. Chem. 2002, 26 (4), 387–397.
- 20. Dai, M.; Wang, C.; Dong, G.; Xiang, J.; Luo, T.; Liang, B.; Chen, J.; Yang, Z. Development of Thiourea-Based Ligands for the Palladium-Catalyzed Bis(Methoxycarbonylation) of Terminal Olefins. European J. Org. Chem. 2003, 2003 (22), 4346-4348.
- 21. Hayashi, M.; Takezaki, H.; Hashimoto, Y.; Takaoki, K.; Saigo, K. Phosphine Sulfides: Novel Effective Ligands for the Palladium-Catalyzed Bisalkoxycarbonylation of Olefins. Tetrahedron Lett. 1998, 39 (41), 7529-7532.
- 22. Bianchini, C.; Mantovani, G.; Meli, A.; Oberhauser, W.; Brüggeller, P.; Stampfl, T. Novel Diphosphine-Modified Palladium Catalysts for Oxidative Carbonylation of Styrene to Methyl Cinnamate. J. Chem. Soc. Dalt. Trans. 2001, 2 (5), 707-722.
- 23. Wang, L.; Wang, Y.; Liu, C.; Lei, A. CO/C-H as an Acylating Reagent: A Palladium-Catalyzed Aerobic Oxidative Carbonylative Esterification of Alcohols. Angew. Chemie Int. Ed. 2014, 53 (22), 5657-5661.
- 24. Malkov, A. V.; Derrien, N.; Barłóg, M.; Kočovský, P. Palladium-Catalyzed Alkoxycarbonylation of Terminal Alkenes To Produce α,β-Unsaturated Esters: The Key Role of Acetonitrile as a Ligand. Chem. - A Eur. J. 2014, 20 (16), 4542-4547.
- 25. Maffei, M.; Giacoia, G.; Mancuso, R.; Gabriele, B.; Motti, E.; Costa, M.; Della Ca', N. A Highly Efficient Pd/Cul-Catalyzed Oxidative Alkoxycarbonylation of α-Olefins to Unsaturated Esters. J. Mol. Catal. A Chem. **2017**, 426, 435–443.
- 26. Bajracharya, G.; Koranne, P.; Tsujihara, T.; Takizawa, S.; Onitsuka, K.; Sasai, H. Dicationic Palladium(II)-Spiro Bis(Isoxazoline) Complex for Highly Enantioselective Isotactic Copolymerization of CO with Styrene Derivatives. Synlett 2009, 2009 (02), 310-314.
- 27. Muñoz, B. K.; Godard, C.; Marinetti, A.; Ruiz, A.; Benet-Buchholz, J.; Claver, C. Pd-Catalysed Methoxycarbonylation of Vinylarenes Using Chiral Monodentate Phosphetanes and Phospholane as Ligands. Effect of Substrate Substituents on Enantioselectivity. Dalt. Trans. 2007, No. 47, 5524.
- 28. Kalck, P.; Urrutigoïty, M.; Dechy-Cabaret, O. Hydroxy- and Alkoxycarbonylations of Alkenes and Alkynes. Top. Organomet. Chem. 2006, 18, 97-123.
- 29. Brennführer, A.; Neumann, H.; Beller, M. Palladium-Catalyzed Carbonylation Reactions of Alkenes and Alkynes. ChemCatChem 2009, 1 (1), 28-41.
- 30. Liu, J.; Heaton, B. T.; Iggo, J. A.; Whyman, R. Methanolysis of Acyl-Pd(ii) Complexes Relevant to CO/ Ethene Coupling Reactions. Chem. Commun. 2004, No. 11, 1326–1327.
- 31. Tooze, R. P.; Whiston, K.; Malyan, A. P.; Taylor, M. J.; W.wilson, N. Evidence for the Hydride Mechanism in the Methoxycarbonylation of Ethene Catalysed by Palladium-Triphenylphosphine Complexes. J. Chem. Soc. Dalt. Trans. 2000, No. 19, 3441–3444.
- 32. Bianchini, C.; Meli, A.; Oberhauser, W.; Parisel, S.; Gusev, O. V.; Kal'sin, A. M.; Vologdin, N. V.; Dolgushin, F. M. Methoxycarbonylation of Styrene to Methyl Arylpropanoates Catalyzed by Palladium(II) Precursors with 1,1'-Bis(Diphenylphosphino)Metallocenes. J. Mol. Catal. A Chem. **2004**, *224* (1–2), 35–49.

- 33. Muñoz, B. K.; Santos Garcia, E.; Godard, C.; Zangrando, E.; Bo, C.; Ruiz, A.; Claver, C. HP-NMR Study of the Pd-Catalyzed Methoxycarbonylation of Styrene Using Monodentate and Bidentate Phosphane-Modified Systems. Eur. J. Inorg. Chem. 2008, 2008 (29), 4625–4637.
- 34. Eastham, G. R.; Tooze, R. P.; Kilner, M.; Foster, D. F.; Cole-Hamilton, D. J. Deuterium Labelling Evidence for a Hydride Mechanism in the Formation of Methyl Propanoate from Carbon Monoxide, Ethene and Methanol Catalysed by a Palladium Complex. J. Chem. Soc. Dalt. Trans. 2002, No. 8, 1613-1617.
- 35. Eastham, G. R.; Tooze, R. P.; Heaton, B. T.; Iggo, J. A.; Whyman, R.; Zacchini, S. Synthesis and Spectroscopic Characterisation of All the Intermediates in the Pd-Catalysed Methoxycarbonylation of Ethene. Chem. Commun. 2000, No. 7, 609–610.
- 36. del Río, I.; Claver, C.; van Leeuwen, P. W. N. M. On the Mechanism of the Hydroxycarbonylation of Styrene with Palladium Systems. Eur. J. Inorg. Chem. 2001, 2001 (11), 2719.
- 37. Seayad, A.; Jayasree, S.; Damodaran, K.; Toniolo, L.; Chaudhari, R. V. On the Mechanism of Hydroesterification of Styrene Using an in Situ-Formed Cationic Palladium Complex, J. Organomet. Chem. 2000, 601 (1), 100-107.
- 38. Naigre, R.; Chenal, T.; Ciprés, I.; Kalck, P.; Daran, J. C.; Vaissermann, J. Carbon Monoxide as a Building Block in Organic Synthesis. Part V. Involvement of Palladium-Hydride Species in Carbonylation Reactions of Monoterpenes. X-Ray Crystal Structure of [Ph3PCH2CHCHPh]4[PdCl6][SnCl6]. J. Organomet. Chem. 1994, 480 (1-2), 91-102.
- 39. Clegg, W.; Eastham, G. R.; Elsegood, M. R. J.; Heaton, B. T.; Iggo, J. A.; Tooze, R. P.; Whyman, R.; Zacchini, S. Characterization and Dynamics of [Pd(L-L)H(Solv)] + , [Pd(L-L)(CH 2 CH 3)] + , and [Pd(L-L)(C(O)Et)(THF)] + (L-L = 1,2-(CH 2 PBu t 2) 2 C 6 H 4): Key Intermediates in the Catalytic Methoxycarbonylation of Ethene to Methylpropanoate. Organometallics 2002, 21 (9), 1832–1840.
- 40. Ahmad, S.; Bühl, M. Computational Modelling of Pd-Catalysed Alkoxycarbonylation of Alkenes and Alkynes. Phys. Chem. Chem. Phys. 2021, 23 (30), 15869-15880.
- 41. Gallarati, S.; Dingwall, P.; Fuentes, J. A.; Bühl, M.; Clarke, M. L. Understanding Catalyst Structure-Selectivity Relationships in Pd-Catalyzed Enantioselective Methoxycarbonylation of Styrene. Organometallics 2020, 39 (24), 4544-4556.
- 42. Amadio, E.; Cavinato, G.; Dolmella, A.; Toniolo, L. Catalytic Properties of [Pd(COOMe)NX2-n(PPh 3)2] (n = 0, 1, 2; X = CI, NO2, ONO 2, OAc and OTs) in the Oxidative Carbonylation of MeOH. *Inorq.* Chem. 2010, 49 (8), 3721-3729.
- 43. Liu, J.; Heaton, B. T.; Iggo, J. A.; Whyman, R.; Bickley, J. F.; Steiner, A. The Mechanism of the Hydroalkoxycarbonylation of Ethene and Alkene-CO Copolymerization Catalyzed by PdII-Diphosphine Cations. Chem. - A Eur. J. 2006, 12 (16), 4417–4430.
- 44. Bancroft, D. P.; Cotton, F. A.; Verbruggen, M. Trans-(Dimethyl Sulfoxide-O)(Dimethyl Sulfoxide-S) Bis(Trifluoroacetato)Palladium(II); Alternative Ligation Modes of an Ambidentate Ligand. Acta Crystallogr. Sect. C Cryst. Struct. Commun. 1989, 45 (9), 1289–1292.
- 45. Diao, T.; White, P.; Guzei, I.; Stahl, S. S. Characterization of DMSO Coordination to Palladium(II) in Solution and Insights into the Aerobic Oxidation Catalyst, Pd(DMSO) 2 (TFA) 2. Inorg. Chem. 2012, *51* (21), 11898–11909.
- 46. Brasche, G.; García-Fortanet, J.; Buchwald, S. L. Twofold C-H Functionalization: Palladium-Catalyzed Ortho Arylation of Anilides. Org. Lett. 2008, 10 (11), 2207–2210.
- 47. McDonald, R. I.; Stahl, S. S. Modular Synthesis of 1,2-Diamine Derivatives by Palladium-Catalyzed Aerobic Oxidative Cyclization of Allylic Sulfamides. Angew. Chemie Int. Ed. 2010, 49 (32), 5529-5532.
- 48. Diao, T.; Stahl, S. S. Synthesis of Cyclic Enones via Direct Palladium-Catalyzed Aerobic Dehydrogenation of Ketones. J. Am. Chem. Soc. 2011, 133 (37), 14566–14569.

- 49. Lu, Z.; Stahl, S. S. Intramolecular Pd(II)-Catalyzed Aerobic Oxidative Amination of Alkenes: Synthesis of Six-Membered N -Heterocycles. Org. Lett. 2012, 14 (5), 1234–1237.
- 50. Weinstein, A. B.; Schuman, D. P.; Tan, Z. X.; Stahl, S. S. Synthesis of Vicinal Aminoalcohols by Stereoselective Aza-Wacker Cyclizations: Access to (–)-Acosamine by Redox Relay. Angew. Chemie Int. Ed. 2013, 52 (45), 11867-11870.
- 51. Malkov, A. V.; Lee, D. S.; Barłóg, M.; Elsegood, M. R. J.; Kočovský, P. Palladium-Catalyzed Stereoselective Intramolecular Oxidative Amidation of Alkenes in the Synthesis of 1,3- and 1,4-Amino Alcohols and 1,3-Diamines. Chem. - A Eur. J. 2014, 20 (17), 4901-4905.
- 52. Cometti, G.; Chiusoli, G. P. Palladium-Catalysed Synthesis of the Cinnamic Methyl Ester from Styrene, Carbon Monoxide and Methanol. J. Organomet. Chem. 1979, 181 (2), C14-C16.
- 53. Santos, L. S. Online Mechanistic Investigations of Catalyzed Reactions by Electrospray Ionization Mass Spectrometry: A Tool to Intercept Transient Species in Solution. European J. Org. Chem. 2008, No. 2, 235-253.
- 54. Mehara, J.; Roithová, J. Identifying Reactive Intermediates by Mass Spectrometry. Chem. Sci. **2020**, *11* (44), 11960–11972.
- 55. Vikse, K. L.; Henderson, M. A.; Oliver, A. G.; McIndoe, J. S. Direct Observation of Key Intermediates by Negative-Ion Electrospray Ionisation Mass Spectrometry in Palladium-Catalysed Cross-Coupling. Chem. Commun. 2010, 46 (39), 7412-7414.
- 56. Hanzlova, E.; Váňa, J.; Shaffer, C. J.; Roithová, J.; Martinu, T. Evidence for the Cyclic CN 2 Carbene in the Gas Phase. Org. Lett. 2014, 16 (20), 5482-5485.
- 57. Surendran, A. K.; Tripodi, G. L.; Pluhařová, E.; Pereverzev, A. Y.; Bruekers, J. P. J.; Elemans, J. A. A. W.; Meijer, E. J.; Roithová, J. Host-guest Tuning of the CO 2 Reduction Activity of an Iron Porphyrin Cage. Nat. Sci. **2023**, 3 (1).
- 58. Crabtree, R. H. The Organometallic Chemistry of the Transition Metals; John Wiley and Sons: Hoboken, NJ, 2014.
- 59. Thomas, G. T.; Donnecke, S.; Chagunda, I. C.; McIndoe, J. S. Pressurized Sample Infusion. Chemistry–Methods 2022, 2 (1).
- 60. Bütikofer, A.; Chen, P. Cyclopentadienone Iron Complex-Catalyzed Hydrogenation of Ketones: An Operando Spectrometric Study Using Pressurized Sample Infusion-Electrospray Ionization-Mass Spectrometry. Organometallics 2022, 41 (16), 2349-2364.
- 61. Jašíková, L.; Anania, M.; Hybelbauerová, S.; Roithová, J. Reaction Intermediates Kinetics in Solution Investigated by Electrospray Ionization Mass Spectrometry: Diaurated Complexes. J. Am. Chem. Soc. 2015, 137 (42), 13647-13657.
- 62. Duez, Q.; Tinnemans, P.; Elemans, J. A. A. W.; Roithová, J. Kinetics of Ligand Exchange in Solution: A Quantitative Mass Spectrometry Approach. Chem. Sci. 2023, 14 (36), 9759–9769.
- 63. Meija, J.; Mester, Z. Paradigms in Isotope Dilution Mass Spectrometry for Elemental Speciation Analysis. Anal. Chim. Acta 2008, 607 (2), 115-125.
- 64. A related exchange between PdCl, and R-HgOAc has been suggested to account for a smooth isolation of R-HgCl in those cases where the traditional quenching of the product of olefin alkoxymercuration with NaCl failed, reverting the product back to the starting olefin: Kočovský, P. Intramolecular Alkoxymercuration of Olefins and Stabilization of the Resulting Organomercurials. Organometallics 1993, 12 (5), 1969-1971.
- 65. Bäckvall, J.-E.; Gogoll, A.: Evidence for (π-allyl)palladium(II)(quinone) complexes in the palladiumcatalyzed 1,4-diacetoxylation of conjugated dienes. Tetrahedron Lett. 1988, 29, 2243-2246.
- 66. Grennberg, H.; Gogoll, A.; Bäckvall, J.-E.: Acid-Induced Transformations of Palladium(0)-Benzoquinone complexes to Palladium(II) and Organometallics 1993, 12, 1790-1793.

- 67. Bäckvall, J.-E.: Recent Developments in palladium-catalyzed oxidation. Pure Appl. Chem. 1996, 68, 535-538.
- Amatore, C.; Cammoun, C.; Jutand, A. Pd(OAc). /p-Benzoquinone-Catalyzed Anaerobic Electrooxidative Homocoupling of Arylboronic Acids, Arylboronates and Aryltrifluoroboronates in DMF and/or Water. Eur. J. Org. Chem. 2008, 27, 4567-4570.
- 69. McMurry, J. E.; Kočovský, P.: A method for the palladium-catalyzed oxidation of olefins. *Tetrahedron* Lett. 1984, 25, 4187.
- 70. Hanson, S.; Heumann, A.; Rein, T.; Åkermark, B.: Preparation of allylic acetates from simple alkenes by palladium(II)-catalyzed acetoxylation. J. Org. Chem. 1990, 55, 975.
- 71. Chen, M. S.; White, M. C.: A sulfoxide-promoted, catalytic method for the regioselective synthesis of allylic acetates from monosubstituted olefins via C-H oxidation.
- 72. Chen, M. S.; Prabagaran, N.; Labenz, N. A.; White, M. C.: Serial ligand catalysis: A highly selective allylic C-H oxidation. J. Am. Chem. So. 2005, 127, 6970.
- 73. Motloch, P.; Jašík, J.; Roithová, J. Gold(I) and Silver(I) π-Complexes with Unsaturated Hydrocarbons. Organometallics 2021, 40 (10), 1492-1502.
- 74. Becke, A. D. Density-functional Thermochemistry. III. The Role of Exact Exchange. J. Chem. Phys. 1993, 98 (7), 5648-5652.
- 75. Grimme, S.; Antony, J.; Ehrlich, S.; Krieg, H. A Consistent and Accurate Ab Initio Parametrization of Density Functional Dispersion Correction (DFT-D) for the 94 Elements H-Pu. J. Chem. Phys. 2010, 132 (15), 154104.
- 76. Frisch, M. J.; Trucks, G. W.; Schlegel, H. B.; Scuseria, G. E.; Robb, M. a.; Cheeseman, J. R.; Scalmani, G.; Barone, V.; Petersson, G. a.; Nakatsuji, H.; Li, X.; Caricato, M.; Marenich, a. V.; Bloino, J.; Janesko, B. G.; Gomperts, R.; Mennucci, B.; Hratchian, H. P.; Ortiz, J. V.; Izmaylov, a. F.; Sonnenberg, J. L.; Williams; Ding, F.; Lipparini, F.; Egidi, F.; Goings, J.; Peng, B.; Petrone, A.; Henderson, T.; Ranasinghe, D.; Zakrzewski, V. G.; Gao, J.; Rega, N.; Zheng, G.; Liang, W.; Hada, M.; Ehara, M.; Toyota, K.; Fukuda, R.; Hasegawa, J.; Ishida, M.; Nakajima, T.; Honda, Y.; Kitao, O.; Nakai, H.; Vreven, T.; Throssell, K.; Montgomery Jr., J. a.; Peralta, J. E.; Ogliaro, F.; Bearpark, M. J.; Heyd, J. J.; Brothers, E. N.; Kudin, K. N.; Staroverov, V. N.; Keith, T. a.; Kobayashi, R.; Normand, J.; Raghavachari, K.; Rendell, a. P.; Burant, J. C.; Iyengar, S. S.; Tomasi, J.; Cossi, M.; Millam, J. M.; Klene, M.; Adamo, C.; Cammi, R.; Ochterski, J. W.; Martin, R. L.; Morokuma, K.; Farkas, O.; Foresman, J. B.; Fox, D. J. G16_C01. 2016, p Gaussian 16, Revision C.01, Gaussian, Inc., Wallin. https://gaussian.com/citation/.
- 77. Clark, T.; Chandrasekhar, J.; Spitznagel, G. W.; Schleyer, P. V. R. Efficient Diffuse Function-Augmented Basis Sets for Anion Calculations. III. The 3-21+G Basis Set for First-Row Elements, Li-F. J. Comput. Chem. **1983**, 4 (3), 294–301.
- 78. Krishnan, R.; Binkley, J. S.; Seeger, R.; Pople, J. A. Self-consistent Molecular Orbital Methods. XX. A Basis Set for Correlated Wave Functions. J. Chem. Phys. 1980, 72 (1), 650-654.
- 79. Pritchard, B. P.; Altarawy, D.; Didier, B.; Gibson, T. D.; Windus, T. L. New Basis Set Exchange: An Open, Upto-Date Resource for the Molecular Sciences Community. J. Chem. Inf. Model. 2019, 59 (11), 4814–4820.
- 80. Schuchardt, K. L.; Didier, B. T.; Elsethagen, T.; Sun, L.; Gurumoorthi, V.; Chase, J.; Li, J.; Windus, T. L. Basis Set Exchange: A Community Database for Computational Sciences. J. Chem. Inf. Model. 2007, 47 (3), 1045-1052.
- 81. Ewing, S. A.; Donor, M. T.; Wilson, J. W.; Prell, J. S. Collidoscope: An Improved Tool for Computing Collisional Cross-Sections with the Trajectory Method. J. Am. Soc. Mass Spectrom. 2017, 28 (4), 587–596.
- 82. Chen, X.; Duez, Q.; Tripodi, G. L.; Gilissen, P. J.; Piperoudis, D.; Tinnemans, P.; Elemans, J. A. A. W.; Roithová, J.; Nolte, R. J. M. Mechanistic Studies on the Epoxidation of Alkenes by Macrocyclic Manganese Porphyrin Catalysts. European J. Org. Chem. 2022, 2022 (35).

Appendices

Experimental details:

Mass spectrometric experiments were performed on Thermo Scientific LTQ XL, Finnigan LCQ Deca XP mass spectrometer, or Bruker TIMSTOF, all equipped with electrospray ionization (ESI) sources.73 General conditions for LTQ and LCQ were as follows: sheath gas 5-40 arbitrary unit, auxiliary gas 0-10 arbitrary unit, capillary temperature 180-220, spray voltage 3-5 kV, capillary voltage -20 to 30 V, and tube lens - 40 to 50 V. The energy-resolved collision-induced dissociation (CID) experiments were performed on LCQ Deca mass spectrometer with an ESI source. The negative mode collision energies in the LCQ ion trap were calibrated based on the measurements of dissociation energies of carboxylate anions (trifluoroacetate, dichloroacetate, trichloroacetate, and benzoate).56,57 The mass-selected ions were collided with the He buffer gas with an activation time of 30 ms and activation q = 0.25. The complexes were repeated 2-4 times to determine the standard deviation of determined appearance energies (AEs).

General procedure for the offline sampling of reaction mixture: To a solution of PdCl₂ (100 μM) in a mixture of acetonitrile (1 ml) and methanol (1 ml), p-benzoquinone (1 mM) was added. The clear solution was pre-stirred under the carbon monoxide (CO) atmosphere (using a balloon) for 2-5 minutes, and styrene (1-5 mM) was added. The reaction mixture was then stirred at 40 for 20-80 minutes. Aliquots of the reaction mixture were then filtered (using a syringe filter) and analyzed on ESI-MS. The substrate and/or solvent were substituted for labeling experiments as indicated.

General procedure for the online sampling of the reaction mixture, i.e., pressurized sample infusion-electrospray ionization-mass spectrometry (PSI-ESI-MS)^{59,60} monitoring: To a solution of PdCl₂(100 µM) in a mixture of acetonitrile (1 ml) and methanol (1 ml), p-benzoquinone (1 mM) was added. The clear solution was pre-stirred under the carbon monoxide (CO) atmosphere (using a balloon) for 2-5 minutes. This stirred reaction mixture was directly sprayed into the ESI-MS inlet via silica capillary and N₂ or CO overpressure. When required, using a heating metal block, the desired temperature was achieved. Substrate styrene (1-5 mM) was injected during the acquiring MS data to monitor the evolution of the reaction intermediates. The substrate and/or solvent were modified for the labeling experiments as indicated.

GC-TOF measurements: We performed 1:10 dilution of the reaction mixture at specified intervals with dichloromethane (DCM), followed by extraction with water, The resulting organic layer was dried over sodium sulfate, filtered by syringe filter and injected into the GC-TOF. The Agilent 7890A GC-TOF used was fitted with an electron ionization (EI) source and HP-5MS column (30m x 0.25mm x 0.25mm). Method employed (15 min run time) started with the oven temperature at 100 (1 min hold), 20 increment until 320 (3 min hold). The detector was set at 2050 V. and a split ratio of 10.0:1 was applied.

pH measurements: As the reaction solvent(/s) i.e. acetonitrile and methanol are miscible with water, we prepared 1:1 dilution of the reaction mixture at selected interval with Milli-Q water, followed by mixing and syringe filtration to remove black precipitate. The resulting solution was tested with universal pH paper for qualitative pH estimation.

Source spectra

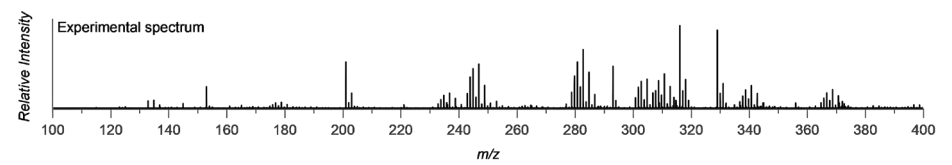
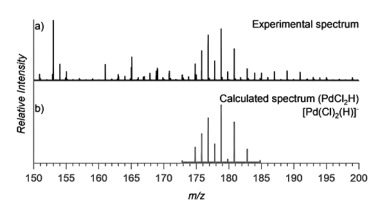


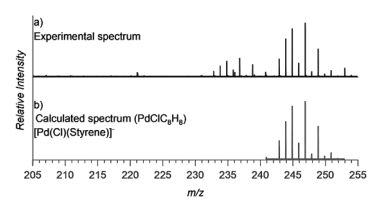
Figure S1. ESI-TOF spectra of the reaction mixture of $PdCl_2(100 \mu M)$, *p*-benzoquinone (1 mM), styrene (5 mM) in acetonitrile and CH_3OH (1:1) ratio under CO atmosphere at 40 after 30 minutes, the black particles were filtered using syringe filter.

Below are the zoomed experimental spectrum sections (top) plotted against the calculated spectrum (bottom) for isotopic pattern analysis of the palladium complexes.

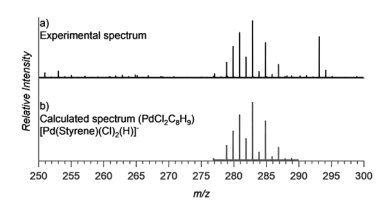
[PdCl₂(H)] m/z 177



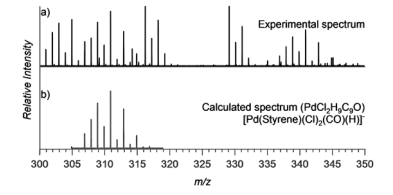
[PdCl(styrene)] m/z 245



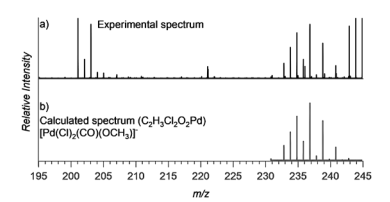
[PdCl₂(H,styrene)] m/z 281



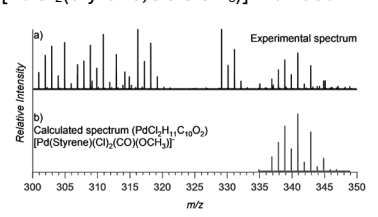
[PdCl₂(H,styrene,CO)] m/z 309



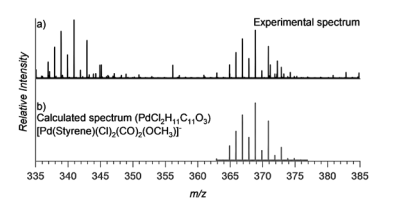
$[PdCl_2(COOCH_3)]^- m/z 235$



[PdCl₂(styrene,COOCH₃)]- m/z 339



[PdCl₂(styrene,COOCH₃,CO)]⁻ m/z 367



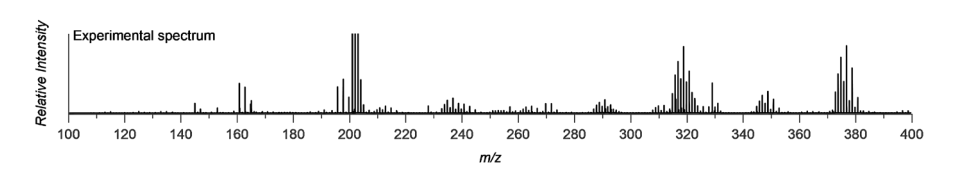
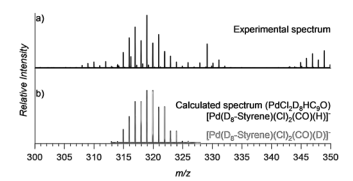


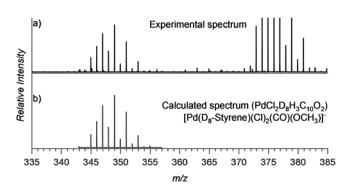
Figure S2. ESI-TOF spectra of the reaction mixture of PdCl₃(100 μM), p-benzoquinone (1 mM), D_a-styrene (5 mM) in acetonitrile and CH₃OH (1:1) ratio under CO atmosphere at 40 after 30 minutes, the black particles were filtered using syringe filter.

Below are the zoomed experimental spectrum sections (top) plotted against the calculated spectrum (bottom) for isotopic pattern analysis of the palladium complexes.

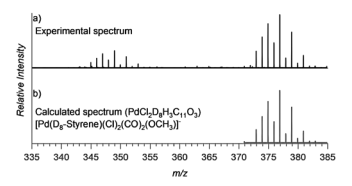
[PdCl₂(H,D₈-styrene,CO)]-m/z 317



[PdCl₂(D₈-styrene,COOCH₃)] m/z 347



[PdCl₂(D₈-styrene,COOCH₃,CO)]⁻ m/z 375



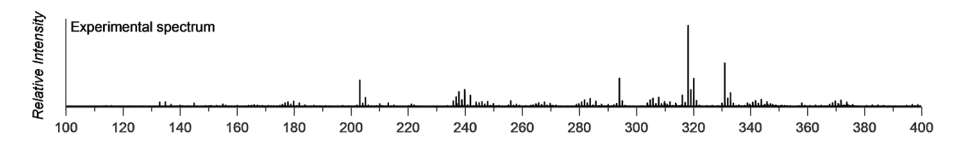
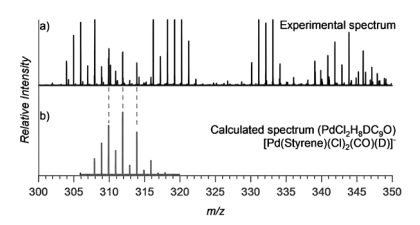


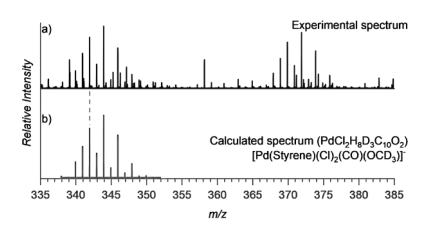
Figure S3. ESI-TOF spectra of the reaction mixture of PdCl₂(100 μ M), p-benzoquinone (1 mM), styrene (5 mM) in acetonitrile and CD₃OD (1:1) ratio under CO atmosphere at 40 after 30-45 minutes, the black particles were filtered using syringe filter.

Below are the zoomed experimental spectrum sections (top) plotted against the calculated spectrum (bottom) for isotopic pattern analysis of the palladium complexes.

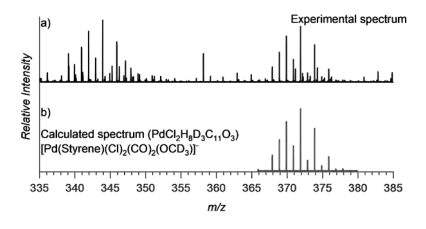
[PdCl₂(D,styrene,CO)] m/z 310



[PdCl₂(styrene,COOCD₃)]⁻ m/z 342



[PdCl₂(styrene,COOCD₃,CO)]- m/z 370



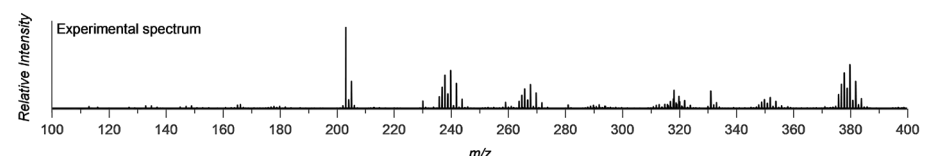
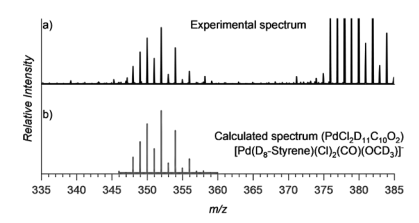


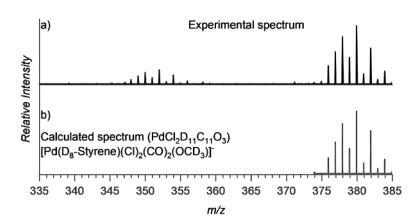
Figure S4. ESI-TOF spectra of the reaction mixture of PdCl₂(100 μ M), p-benzoquinone (1 mM), D₈styrene (5 mM) in acetonitrile and CD₃OD (1:1) ratio under CO atmosphere at 40 after 80 minutes, the black particles were filtered using syringe filter.

Below are the zoomed experimental spectrum sections (top) plotted against the calculated spectrum (bottom) for isotopic pattern analysis of the palladium complexes.

[PdCl₂(D₈-styrene,COOCD₃)] m/z 350



[PdCl₂(D₈-styrene,COOCD₃,CO)]⁻ m/z 378



The collision induced dissociation (CID) spectra of the ions with specified m/z

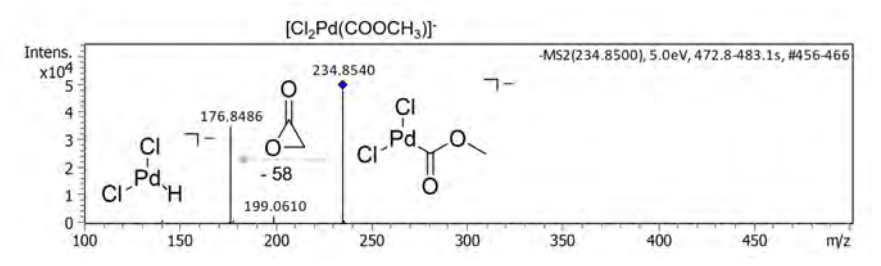


Figure S5. CID spectrum of the [PdCl₂(COOCH₂)]² with m/z 235 at collision energy 5 eV

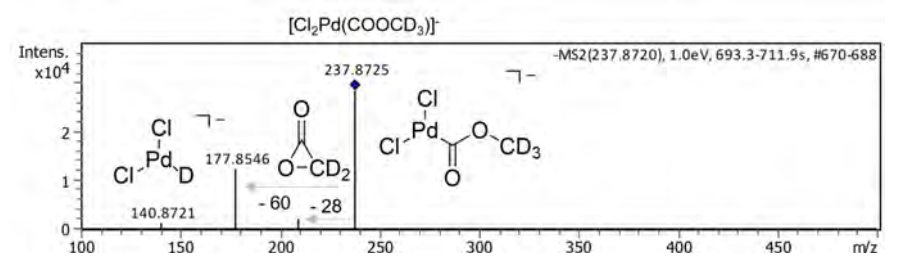


Figure S6. CID spectrum of the [PdCl₂(COOCD₂)]⁻ with m/z 238 at collision energy 1 eV

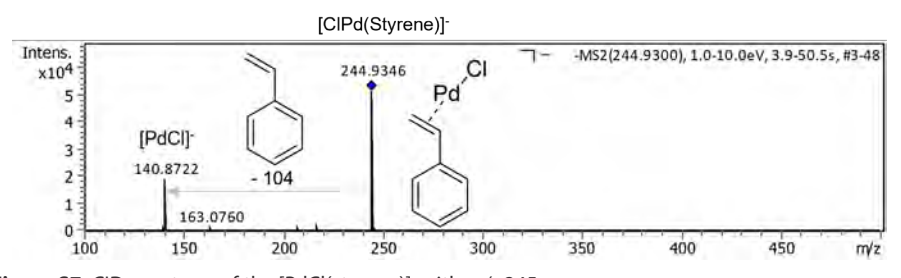


Figure S7. CID spectrum of the [PdCl(styrene)] with m/z 245

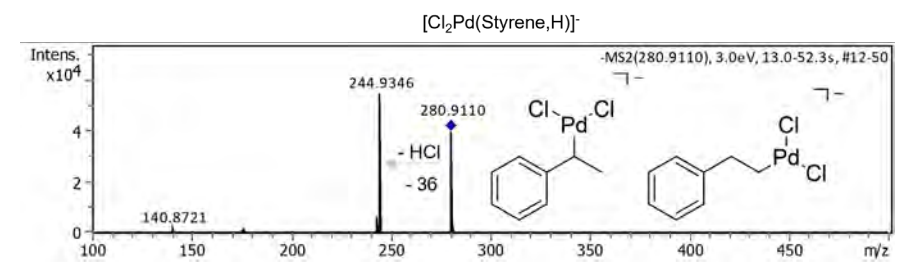


Figure S8. CID spectrum of the [PdCl₂(H,styrene)]² with m/z 281

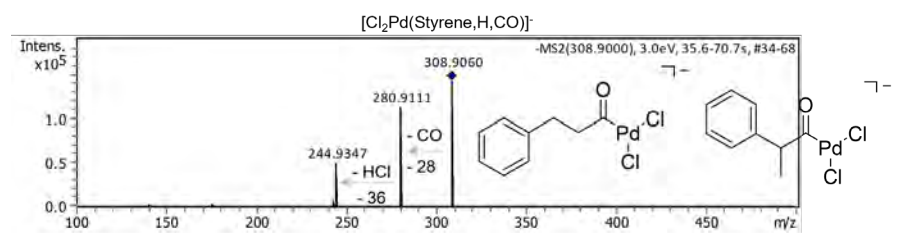


Figure S9. CID spectrum of the [PdCl₂(H,styrene,CO)]⁻ with m/z 309

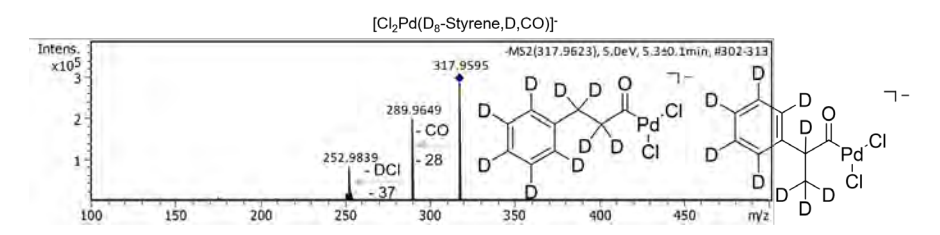


Figure \$10. CID spectrum of the [PdCl₂(D,D₈-styrene,CO)]⁻ with m/z 318

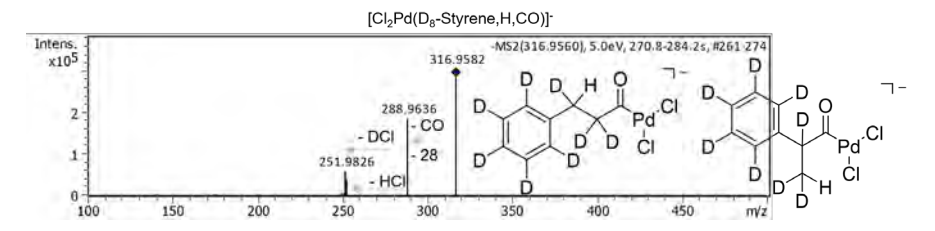


Figure S11. CID spectrum of the $[PdCl_2(H,D_g-styrene,CO)]^-$ with m/z 317

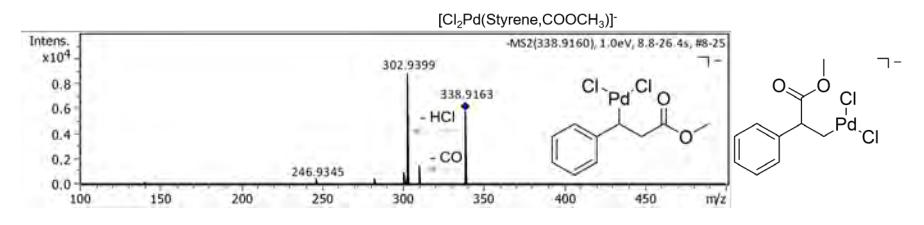


Figure S12. CID spectrum of the [PdCl₂(styrene,COOCH₃)]⁻ with m/z 339

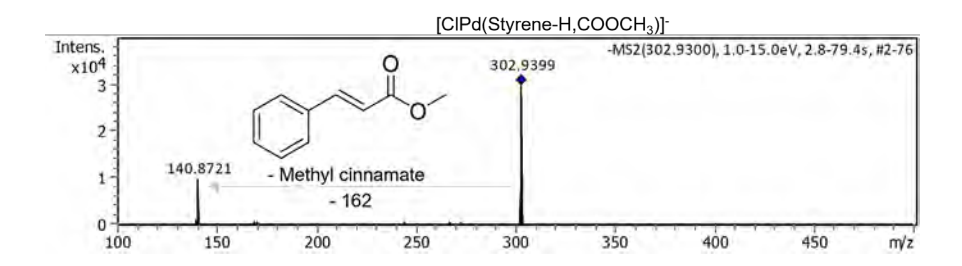


Figure S13. CID spectrum of the [PdCl((styrene-H)COOCH₂)]⁻ with m/z 303

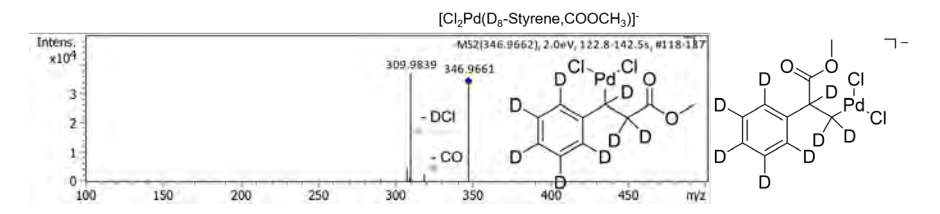


Figure S14. CID spectrum of the [PdCl₂(D₈-styrene,COOCH₃)]⁻ with m/z 347

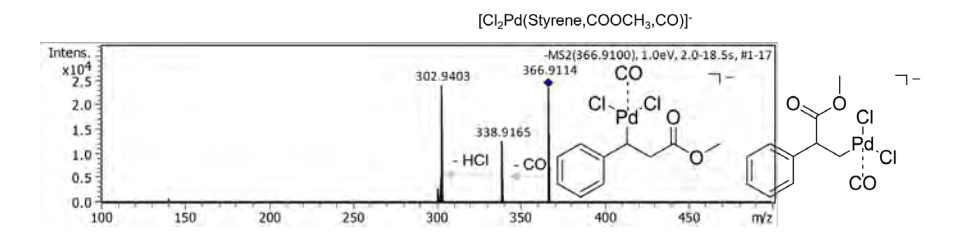


Figure S15. CID spectrum of the [PdCl₂(styrene,COOCH₃,CO)]⁻ with m/z 367

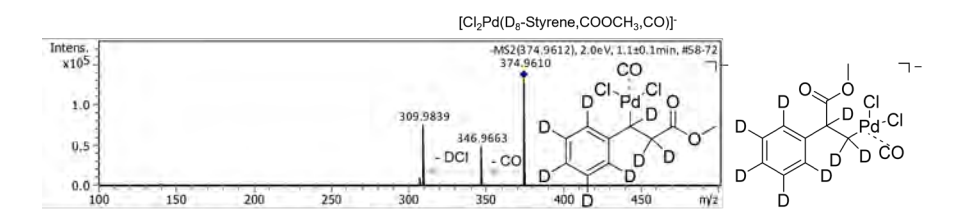


Figure \$16. CID spectrum of the PdCl₂(D₈-styrene,COOCH₃,CO)]⁻ with m/z 375

Energy Resolved Collision Induced Dissociation (CID) experiments

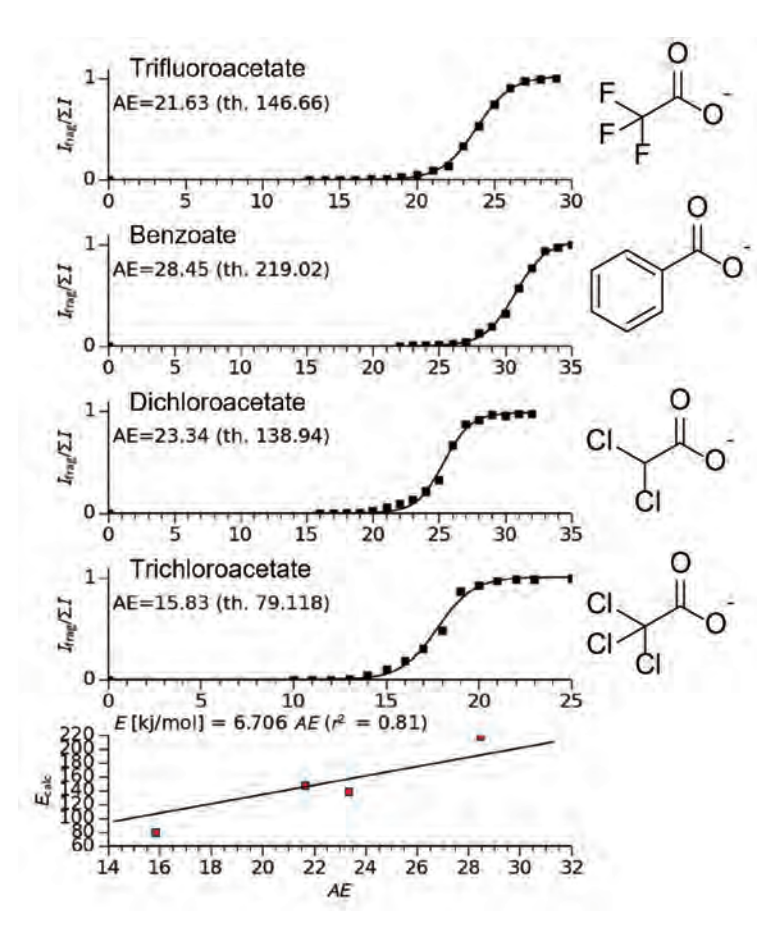


Figure S17. Calibration of the ion trap of the LCQ-Deca electrospray ionization mass spectrometer in the negative mode using specified carboxylate ions of known bond dissociation energies.^{56,57} The appearance energies (AEs) were obtained by sigmoidal fitting of the fragment intensity vs. applied collision energy.

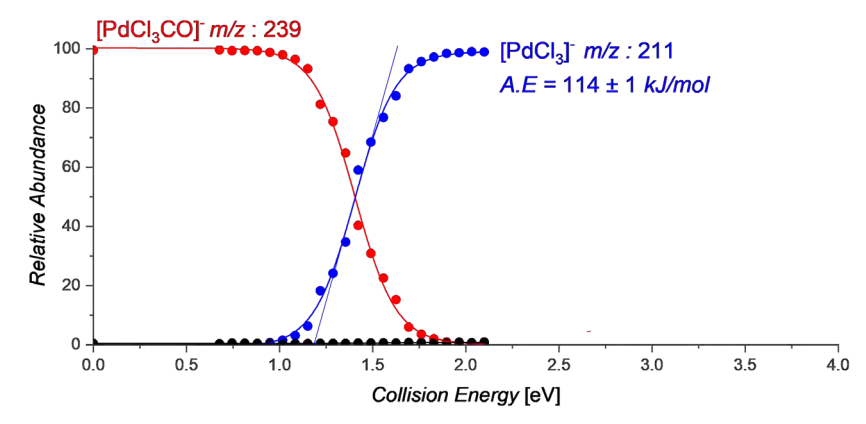


Figure 518. Energy resolved CID and extrapolation of fragmentation onset to determine the appearance energy (AE) of CO in the intermediate [PdCl₃(CO)]⁻ with m/z 239.

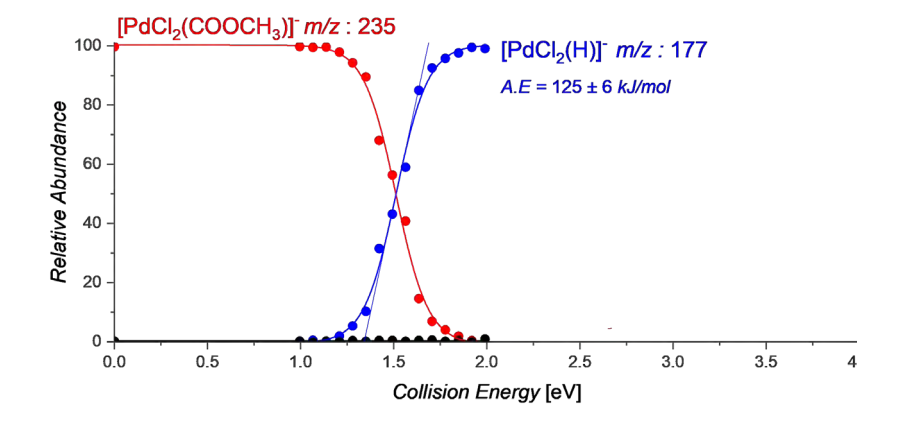


Figure S19. Energy resolved CID and extrapolation of fragmentation onset to determine the appearance energy (*AE*) of acetolactone in the intermediate [PdCI,(COOCH₃)]⁻ with *m/z* 235.

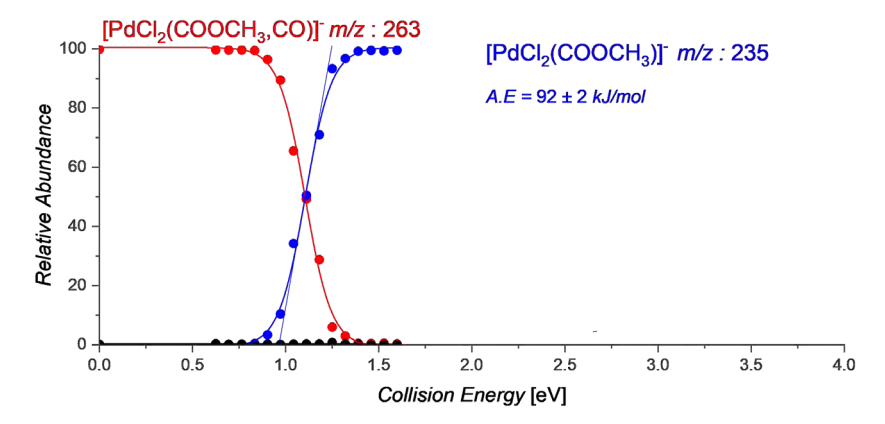


Figure S20. Energy resolved CID and extrapolation of fragmentation onset to determine the appearance energy (AE) of CO in the intermediate [PdCl₃(COOCH₃,CO)]⁻ with m/z 263.

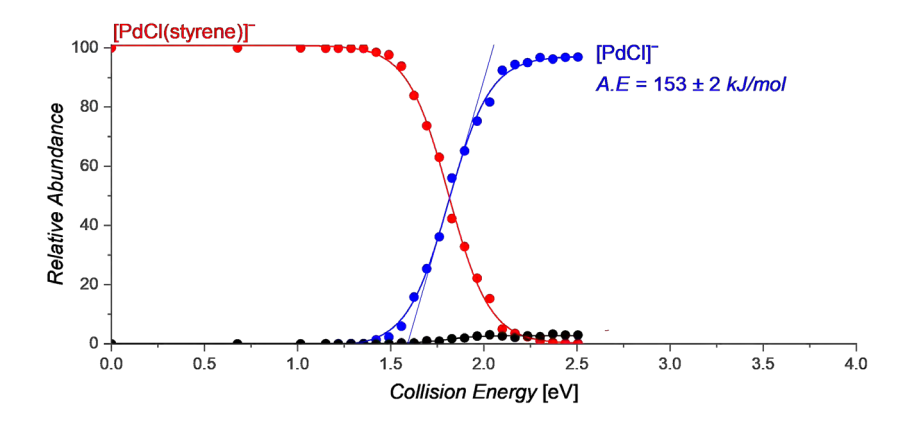


Figure S21. Energy resolved CID and extrapolation of fragmentation onset to determine the appearance energy (AE) of styrene in the intermediate [PdCl(styrene)] $^{-}$ with m/z 245.

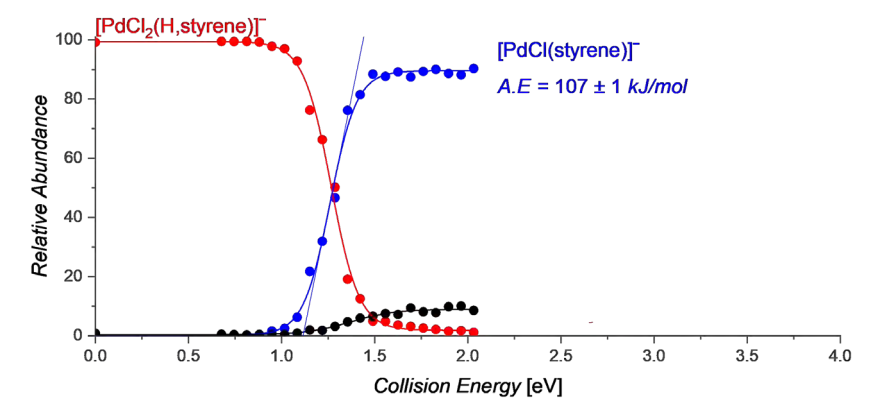


Figure S22. Energy resolved CID and extrapolation of fragmentation onset to determine the appearance energy (AE) of HCl in the intermediate $[PdCl_3(H, styrene)]^-$ with m/z 281.

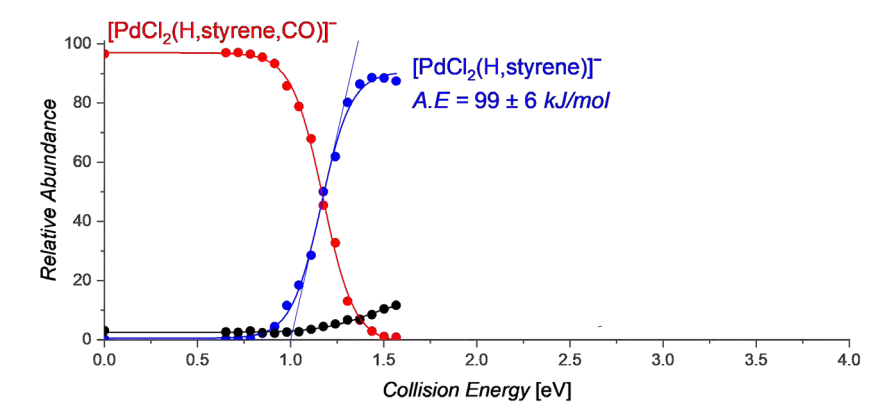


Figure S23. Energy resolved CID and extrapolation of fragmentation onset to determine the appearance energy (AE) of CO in the intermediate $[PdCl_3(H, styrene, CO)]^{-1}$ with m/z 309.

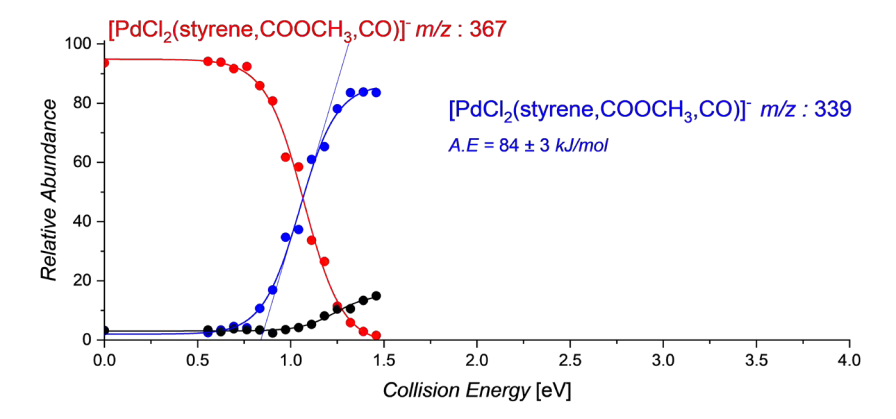


Figure 524. Energy resolved CID and extrapolation of fragmentation onset to determine the appearance energy (*AE*) of CO in the intermediate [PdCl_s(styrene,COOCH_s)] with *m/z* 367.

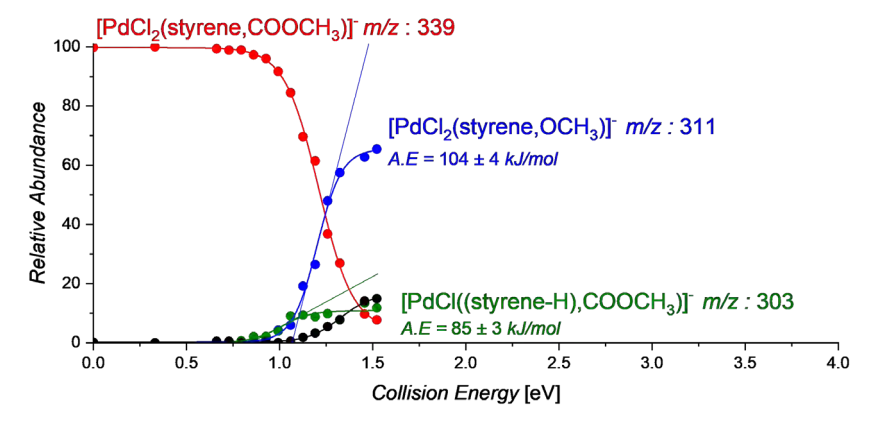


Figure S25. Energy resolved CID and extrapolation of fragmentation onset to determine the appearance energies (*AEs*) of CO and HCl in the intermediate [PdCl₃(styrene,COOCH₃)] with *m/z* 339.

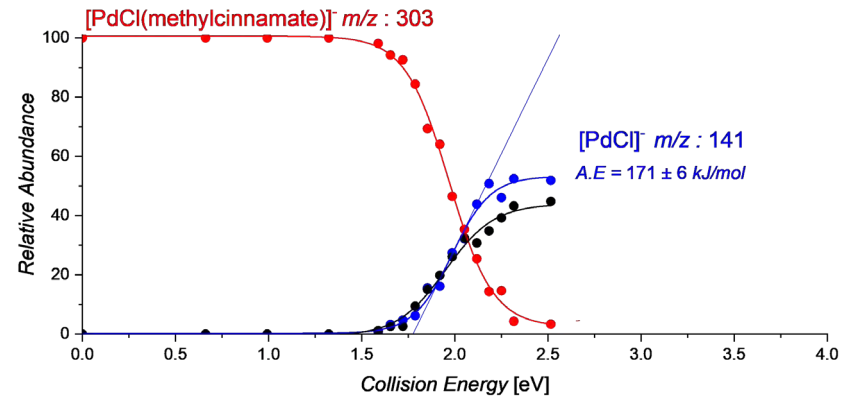


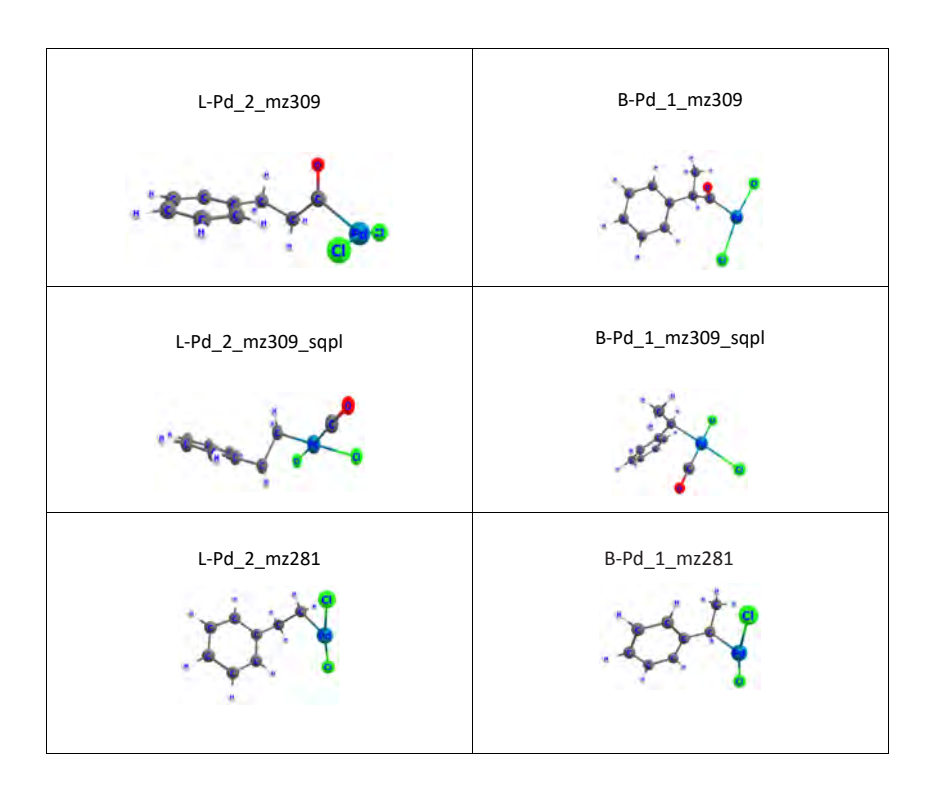
Figure S26. Energy resolved CID and extrapolation of fragmentation onset to determine the appearance energy (AE) of methyl cinnamate in the intermediate [PdCl((styrene-H)COOCH₂)]⁻ with m/z 303.

Bond dissociation energy (BDE) calculation for CO loss from the [PdCl₂(H,styrene,CO)] m/z 309

The DFT calculations were performed using the B3LYP74 functional with the D3 dispersion correction⁷⁵ as implemented in Gaussian 16.⁷⁶ All the calculations were carried out with the 6-311+G** basis set77,78 and SDD79,80 on palladium. The geometries were fully optimized by verifying that there were no imaginary frequencies.

Table S1. BDEs calculation in kJ mol-1 by DFT

[PdCl ₂ (H,styrene,CO)] ⁻		[PdCl ₂ (H,styrene)] ⁻		СО	BDE s
m/ z 309		m/ z 281			kJ mol ⁻¹
L-Pd_2_mz309	-1472.159686	L-Pd_2_mz281	-1358.77921	-113.344011	95.7388575
B-Pd_1_mz309	-1472.159518	B-Pd_1_mz281	-1358.786661		75.735173
L-Pd_2_mz309	-1472.159686	B-Pd_1_mz281	-1358.786661		76.176257
B-Pd_1_mz309	-1472.159518	L-Pd_2_mz281	-1358.77921		95.2977735
L-Pd_2_mz309_sqpl	-1472.15256	L-Pd_2_mz281	-1358.77921		77.0295445
B-Pd_1_mz309_sqpl	-1472.157674	B-Pd_1_mz281	-1358.786661		70.893751



Ion mobility separation

Oxidant: p-benzoquinone (p-BQ)

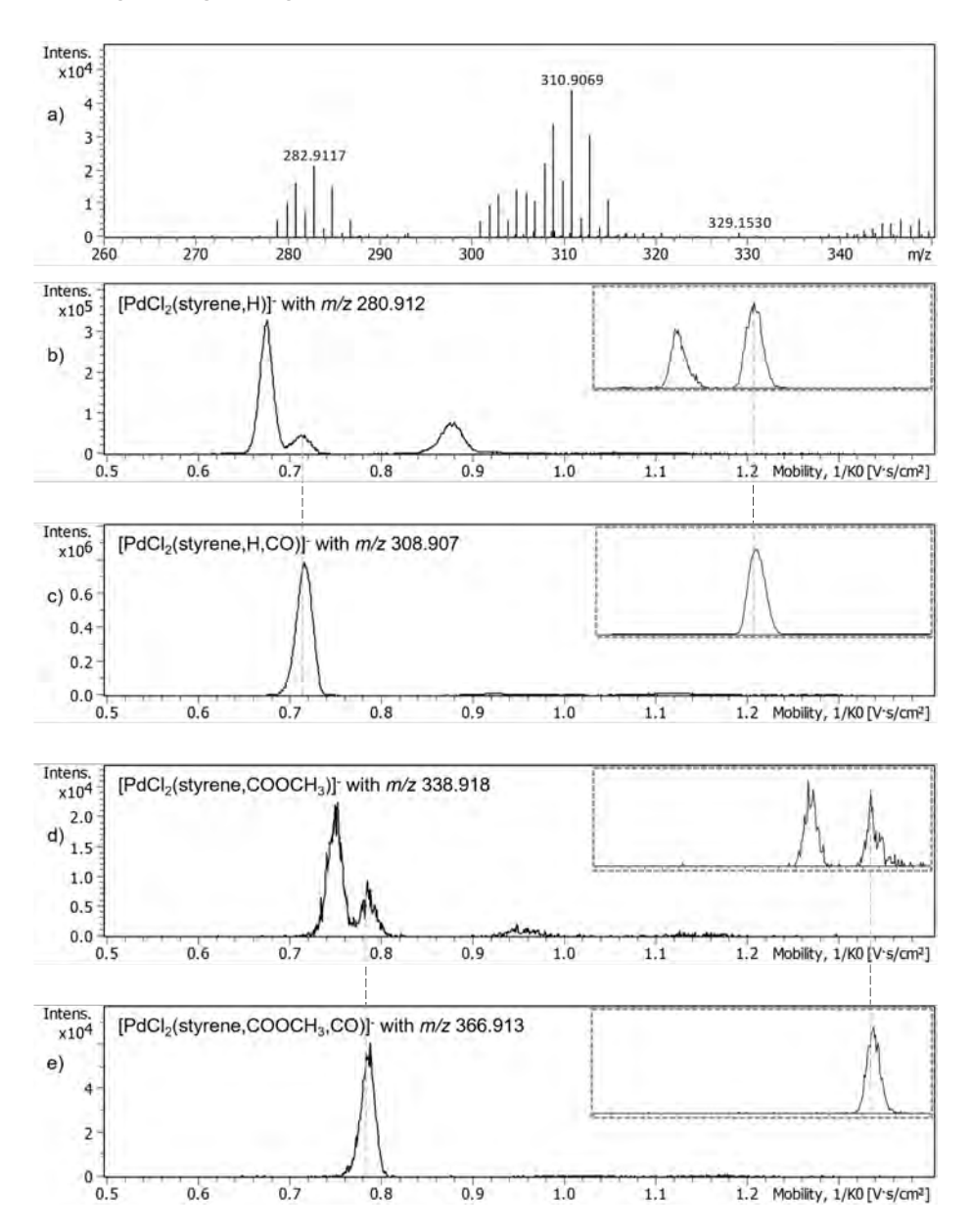


Figure S27. a) ESI-TOF spectra of the reaction mixture of PdCl₂ (200 µM) in a mixture of acetonitrile (1 ml) and methanol (0.5 ml), p-benzoquinone (1 mM), and styrene (5 mM) under the CO atmosphere at 40 for 30 min, black precipitation filtered by syringe filter; b) c) d) and e) Mobilogram of specified m/z with inset showing ultra resolution mobilogram from 0.65 to 0.85 range. Dashed line indicate isomer appearing due to fragmentation.

[PdCl₂(H,styrene)]⁻ (m/z 281, Figure S27 b): the peak with the $1/K_0 \sim 0.704$ is most likely due to the fragmentation of the ions with m/z 309 with the same $1/K_0$; hence, the detected ions with m/z 281 are most likely only one isomer. We note that ultra resolution of mobility conditions are more harsh and cause fragmentation of isomers. Peak at ~ 0.88 is due to higher clusters.

[PdCl₂(H,styrene,CO)]⁻ (m/z 309, Figure S27 c): one isomer only.

[PdCl₂(styrene,COOCH₃)]⁻ (m/z 339, Figure S27 d): the peak with the $1/K_0 \sim 0.786$ is most likely due to the fragmentation of the ions with m/z 367 with the same $1/K_0$, hence, the detected ions with m/z 339 are most likely only one isomer.

[PdCl₂(styrene,COOCH₂)(CO)]⁻ (m/z 367, Figure S27 e): one isomer.

No oxidant, stoichiometric PdCl₂ with styrene

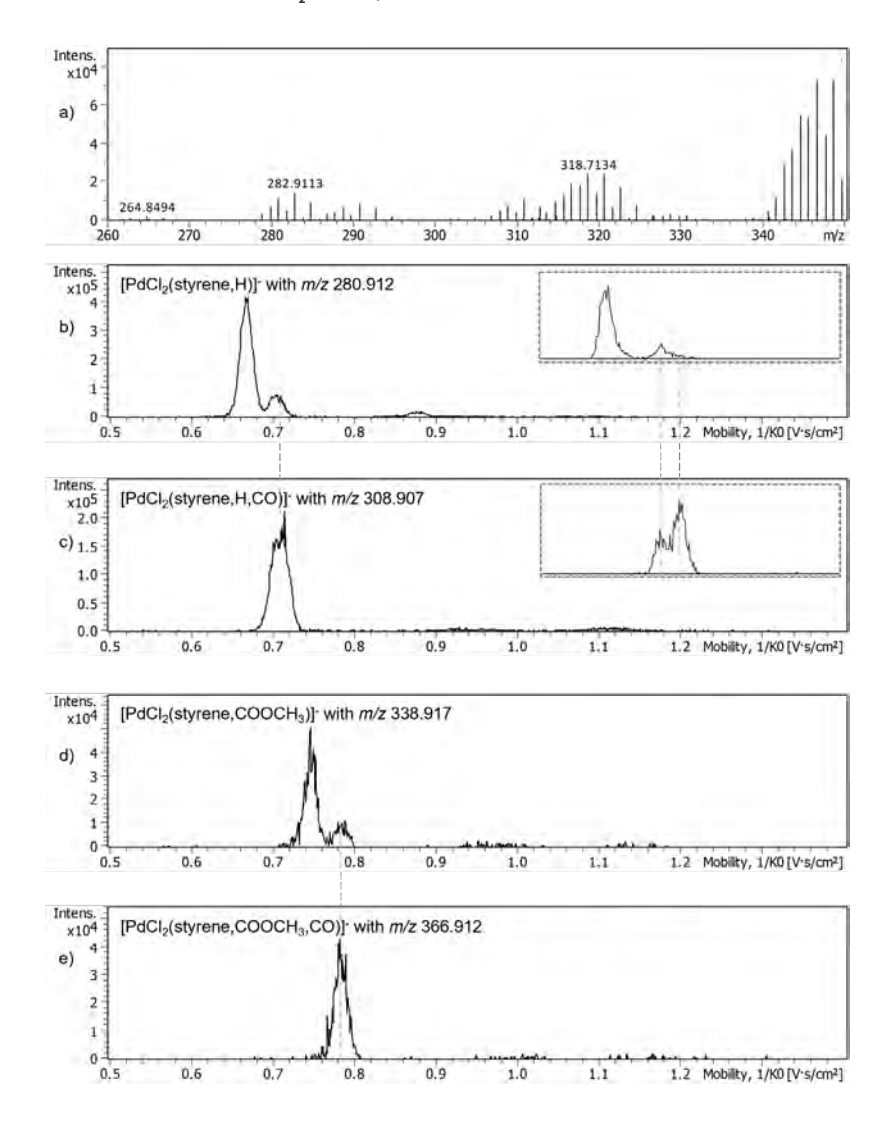


Figure S28. a) ESI-TOF spectra of the reaction mixture of excess of $PdCl_2$ and styrene in CH_3CN :MeOH under the CO atmosphere at 40 for 30 min, black precipitation filtered by syringe filter; b) c) d) and e) Mobilogram of specified m/z with inset showing ultra resolution mobilogram from 0.65 to 0.85 range. Dashed line indicates isomer appearing due to fragmentation.

[PdCl₂(H,styrene,CO)]⁻ (m/z 309, Figure S28 c): Ultra resolution inset graph confirms detection of 2 isomers. When compared to Figure S27 c, new isomer with smaller reduced mobility is detected.

No oxidant, stoichiometric PdCl, with Do-styrene

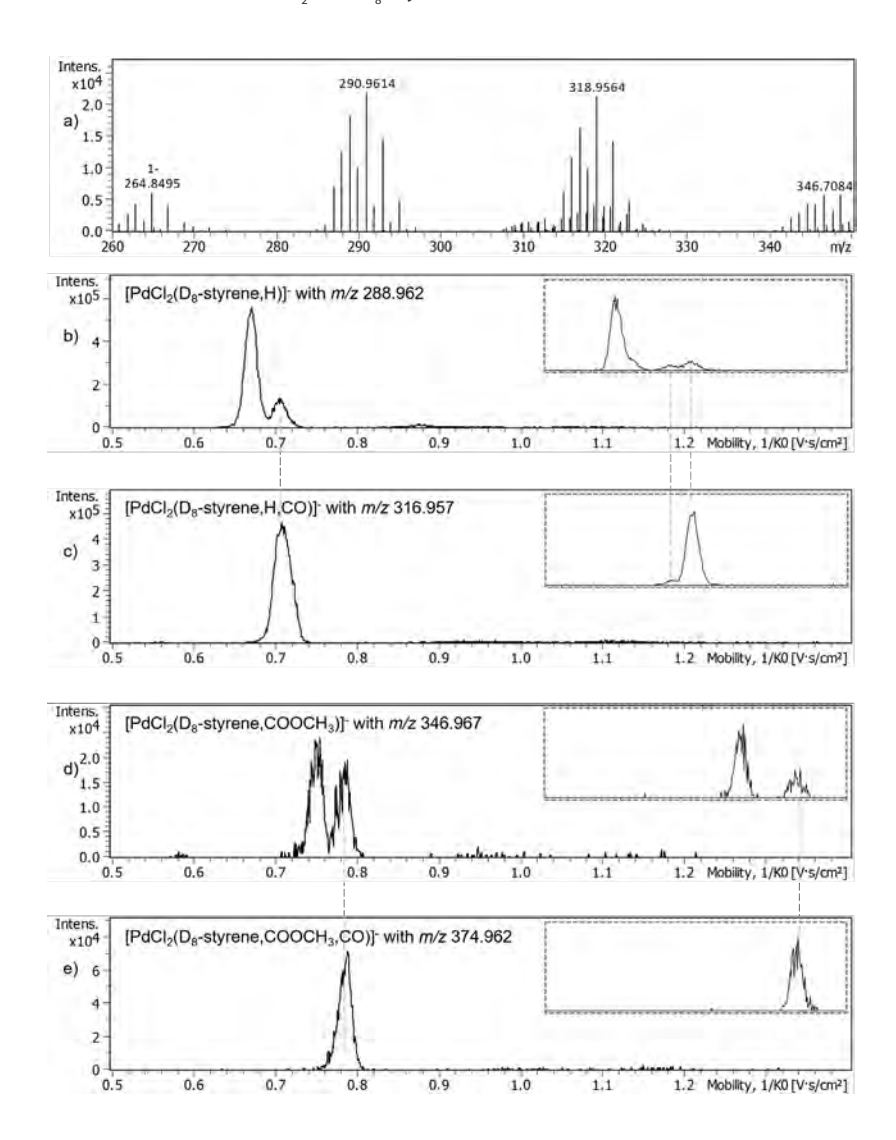


Figure S29. a) ESI-TOF spectra of the reaction mixture of excess of PdCl₂ and D₈-styrene in CH₃CN:MeOH under the CO atmosphere at 40 for 30 min, black precipitation filtered by syringe filter; b) c) d) and e) Mobilogram of specified m/z with inset showing ultra resolution mobilogram from 0.65 to 0.85 range. Dashed line indicates isomer appearing due to fragmentation.

[PdCl₂(H,D₈-styrene,CO)]⁻ (m/z 317, Figure S29 c): Ultra resolution inset graph confirms detection of 2 isomers. When compared to Figure S27 c and similar to Figure S28 c, new minor isomer with smaller reduced mobility is detected.

Collision cross section (CCS) calculation

The DFT calculations were performed using the B3LYP⁷⁴ functional with the D3 dispersion correction⁷⁵ as implemented in Gaussian 16.⁷⁶ All the calculations were done with the 6-311+G** basis set^{77,78} and SDD^{79,80} on palladium. The geometries were fully optimized by verifying that there were no imaginary frequencies.

The CCS calculations were performed using the coordinates of optimized geometries in Collidoscope⁸¹ 'trajectory method' based CCS calculator using N₂ as the collision gas. Ion mobility separation experiments were performed on Bruker timsTOF, the mass and mobilities were calibrated using standard calibration solution.82 Using the DataAnalysis and Bruker Compass mobility calculator, the experimental CCS was determined.

Table S2: Experimental and calculated CCS for [PdCl₃(H,styrene)]⁻ with m/z 281

	Experimental CCS (Ų)	Calculated CCS (Ų)	Optimized structure	Relative zero point energy difference (kJ mol ⁻¹)
(A) branched type		142.6		0
(B) linear type	140.3	145.2	. Markey &	17
(C) π type		143.9	- Alexandria	52

We note that the calculated CCS for the structure (A) and (B) is very close with only $\sim 2.6 \text{ Å}^2$ difference, If both the isomers are present then they can be separated only based on the resolution of ion mobility separation technique used. In our case, the major isomer with ~ 140 Å² was detected which we assign to structure (A). It must be noted that structure (A) is 17 kJ mol⁻¹ lower in energy when compared to structure (B).

Table S3: Experimental and calculated CCS for [PdCl₂(H,styrene,CO)]⁻ with m/z 309

	Experimental CCS (Ų)	Calculated CCS (Å ²)	Optimized structure	Relative zero point energy difference (kJ mol ⁻¹)
(A) branched type	148.5	150.7		4.4
(B) branched type'		147.1		5.6
(C)		148.7		0
(D)		161	and the same of th	4.5
(E) branched type and CO ligand on Pd		152.1		9.2
(F) linear type and CO ligand on Pd		154.3	***	25.3

Based on the comparison of experimental and calculated CCS along with the relative energies the major isomer detected is assigned to structure (C). Experiments with no oxidant in the ultra resolution also showed a minor isomer with comparatively small CCS, which could be structure (B).

Table S4: Experimental and calculated CCS for [PdCl₂(styrene,COOCH₃)]⁻ with m/z 339

	Experimental CCS (Ų)	Calculated CCS (Ų)	Optimized structure	Relative zero point energy difference (kJ mol ⁻¹)
(A) branched ester type	155.1	158.6	4	17
(B) linear ester type		164.9		0

Here, we note that the lowest energy structure has a huge difference in CCS with the experimentally obtained CCS. Based on the comparison of experimental and calculated CCS along with the relative energies, the major isomer detected is assigned structure (C).

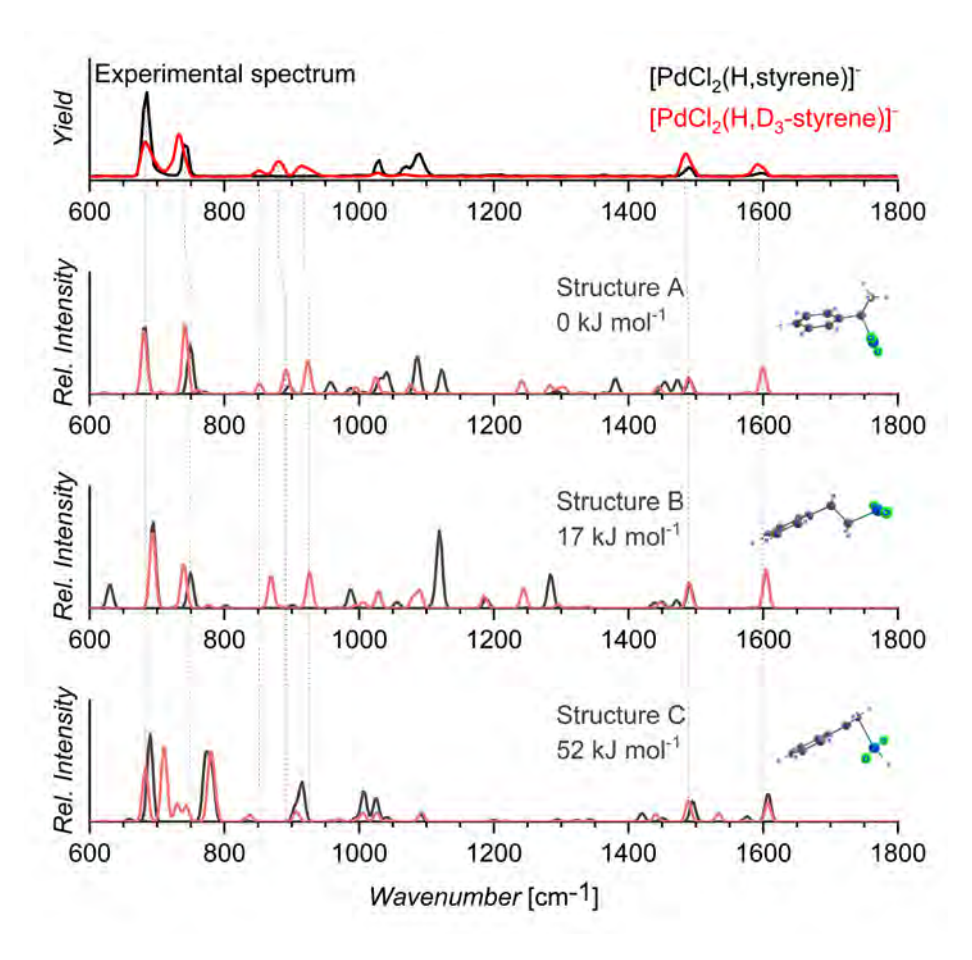


Figure S30. IRMPD of the mass-selected [PdCl₃(H,styrene)]⁻ (top experimental spectrum; black line represents m/z 281 for styrene while the red line represents corresponding complex with D₃-styrene) with the theoretical spectra of possible isomers (styrene-grey and D₃-styrene-light red).

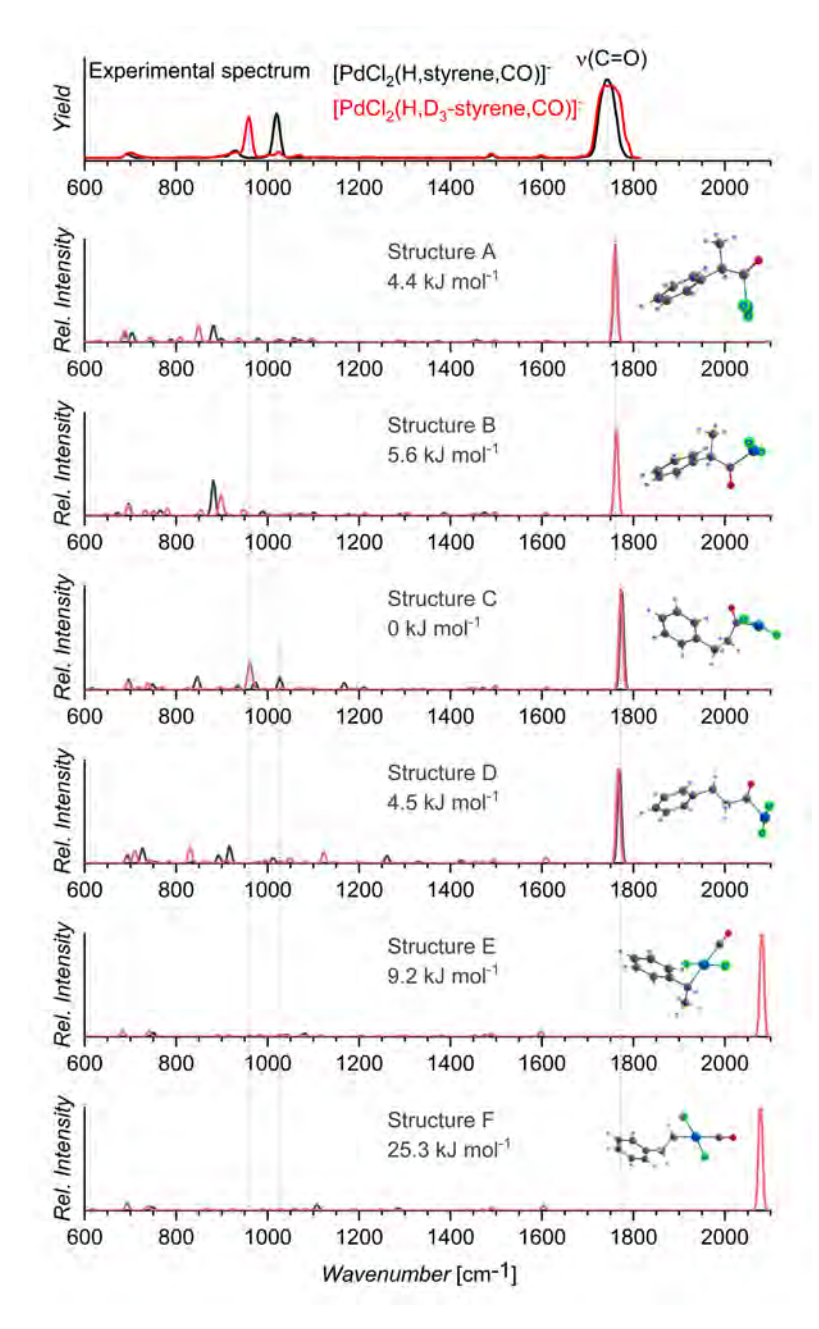


Figure S31. IRMPD of the mass-selected [PdCl₂(H,styrene,CO)]⁻ (top experimental spectrum; black line represents m/z 309 for styrene while the red line represents corresponding complex with D₃-styrene) with the theoretical spectra of possible isomers (styrene-grey and D₃-styrene-light red).

Delayed reactant labeling experiments

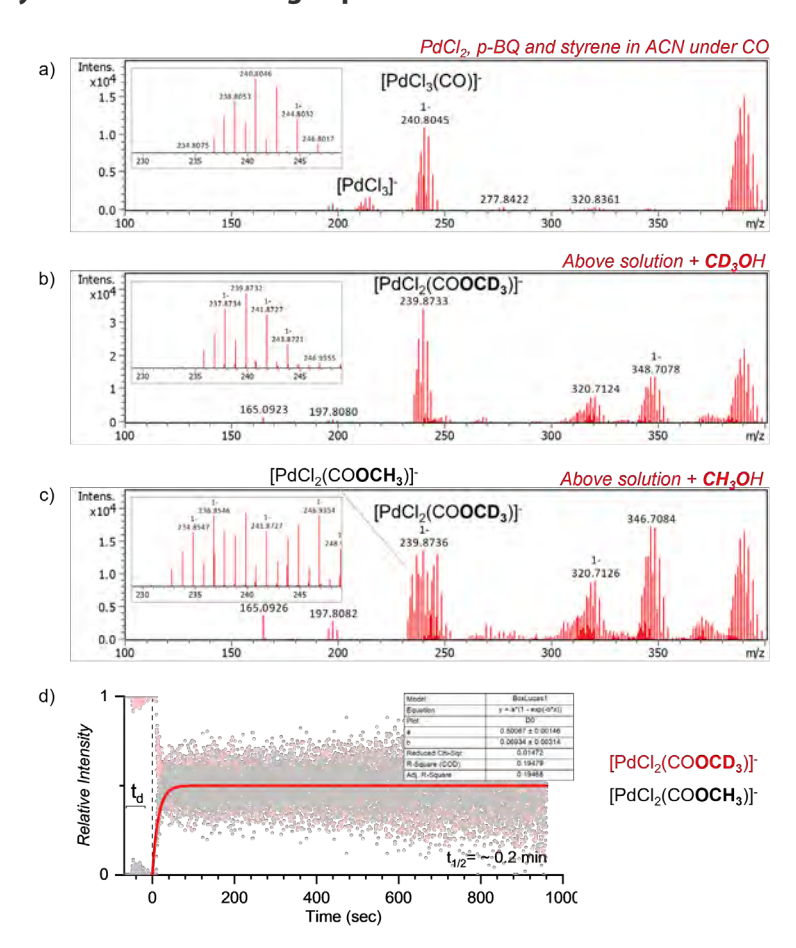


Figure S32. a) ESI-TOF spectra of the reaction mixture of PdCl₂(100 μM), p-benzoquinone (1 mM) and styrene (1 mM) in acetonitrile stirred under CO atmosphere at 40 , b) CD₃OH added, c) CH₃OH added after 1 min and d) Delayed reactant labeling plot for [PdCl,(COOCD,)] (red points) and [PdCl,(COOCH,)] (black points) showing a very fast equilibration with half-life time of ~ 0.2 min.

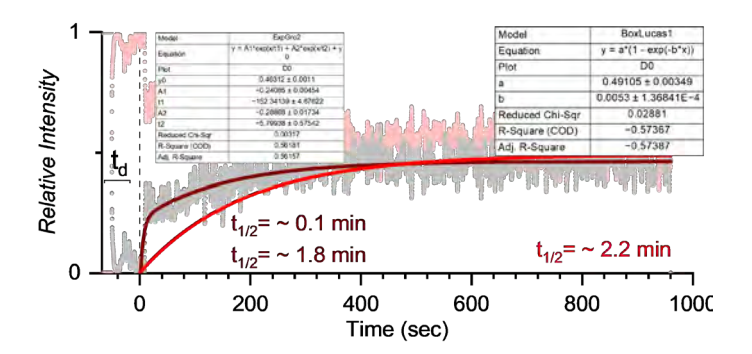


Figure S33. For the above reaction mixture, extracted delayed reactant labeling plot for [PdCl₃(styrene,COO**CD**₃)] (red points) and [PdCl₃(styrene,CO**OCH**₃)] (black points).

The DRL fitting to obtain $t_{1/2}$ in red did not fit the experimental data properly. Alternatively, using double exponential non linear curve fitting i.e. ExpGrow2 (dark red), gave 2 processes. As in this experiment the alcohol is added, this alcohol will first form Pd alkoxycarbonyl precursor and then the [PdCl₂(styrene,COO**CH**₃)] intermediate.

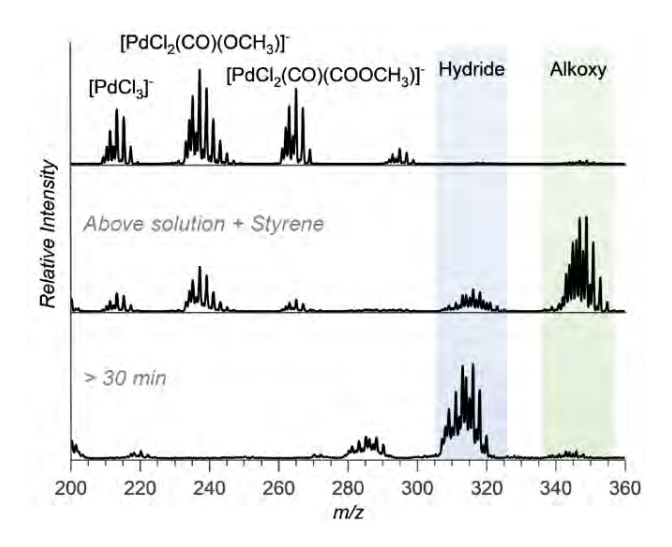


Figure S34. Snapshots of online monitoring of the reaction mixture of $PdCl_2(100 \, \mu M)$, p-benzoquinone (500 μM) and styrene (500 μM) in acetonitrile and methanol (1:1) stirred under CO atmosphere at room temperature. Initially the alkoxy intermediates are observed, followed by hydride intermediates. In the end the intermediates of hydride cycle prevails.

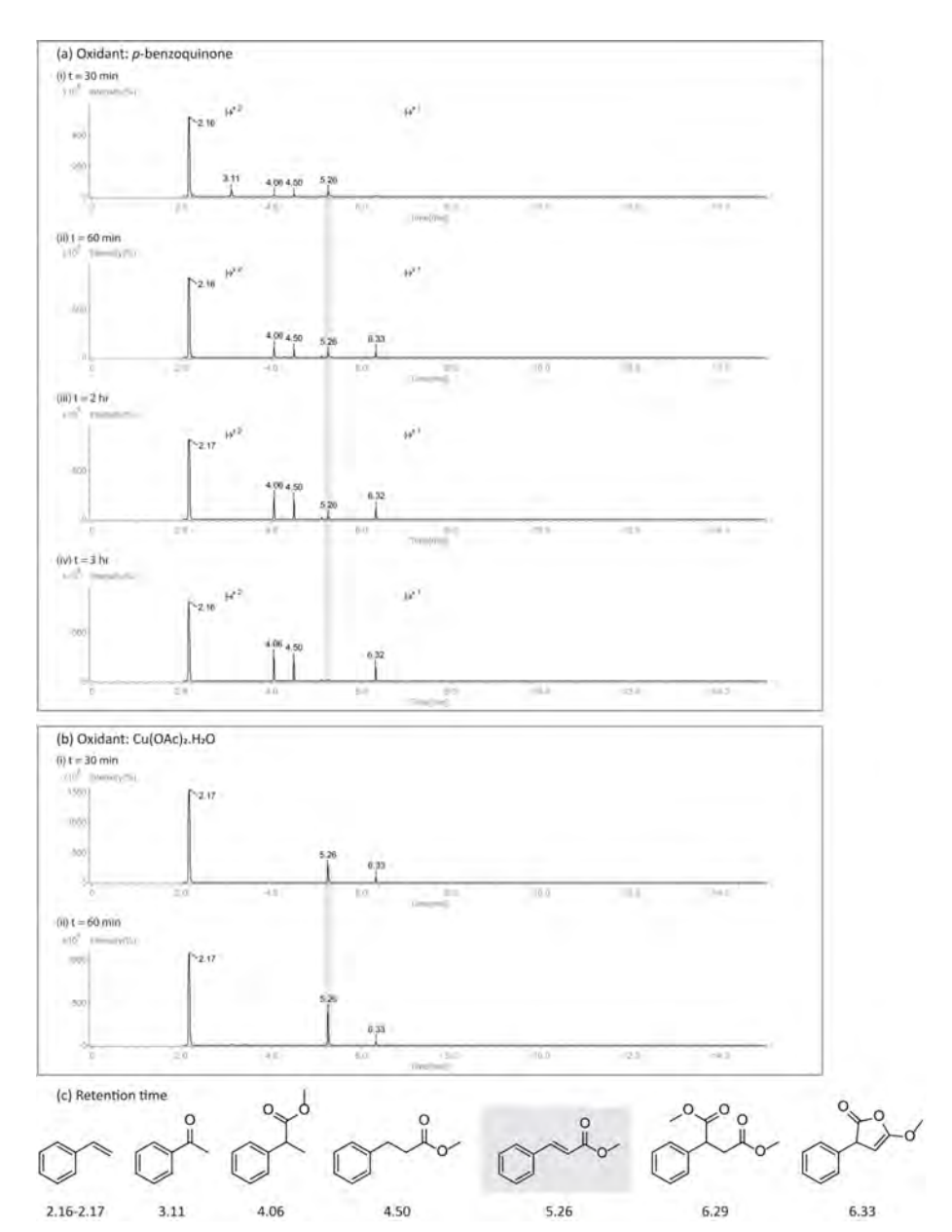


Figure S35. GC-MS chromatograms of the sample from the reaction mixture (a) PdCl₂ (10 mM), p-benzoquinone (40 mM), styrene (40 mM) in acetonitrile and CH₂OH (1:1) ratio under CO atmosphere at 40 after i) 30 minutes, ii) 60 min, iii) 2 hr and iv) 4 hr; (b) PdCl₂ (10 mM), Cu(OAc)₂.H₂O (40 mM), styrene (40 mM) in acetonitrile and CH₃OH (1:1) ratio under CO and O₂ atmosphere at 40 after i) 30 minutes and ii) 60 min; (c) Structure are assigned based on comparison of El spectrum with the NIST library.[citation] Except for the '6.33' which is not available in the NIST library and is proposed based on the m/z and fragmentation observed as a subsequent intramolecular lactonization from the dicarbonylated product.

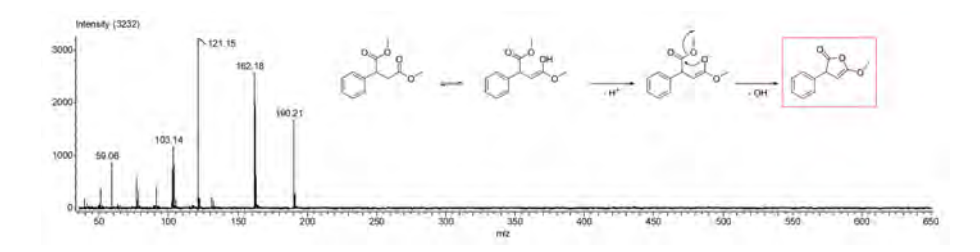


Figure S36. EI-MS spectrum of peak observed at retention time '6.33' and the proposed scheme for its formation from the dicarbonylated product.

- We observe that the reaction with p-BQ shows unsaturated oxidative carbonylation product at '5.26' at 30-60 min. When compared to other products. this unsaturated product does not grow after long time. This is in-line with our findings that the alkoxy cycle could be observed only at the start of the reaction.
- · Over long time when the pH becomes slightly acidic, then the hydride cycle becomes dominant leading to the saturated products and is reflected in the chromatogram.
- Similarly, using stoichiometric PdCl₂ with no additional oxidant showed acidic pH and resulted in the detection of the saturated carbonylated products of the hydride cycle after 2 hr at 40.

Effect of the reaction conditions on the observation of the intermediates

1,1'-Bis(diphenylphosphino)ferrocene (dppf) as the bidendate phosphine ligand

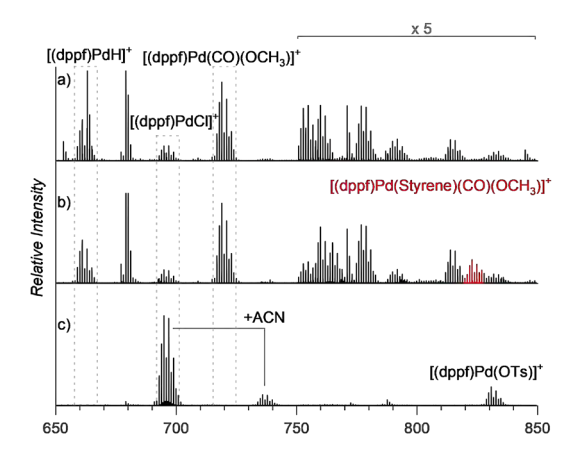


Figure S37. ESI-TOF(+) spectra, a) (dppf)PdCl₂, p-benzoquinone in CH₃CN and MeOH under CO atm, b) After styrene addition in 10min alkoxy intermediate observed and c) After acid (PTSA) addition, the alkoxy intermediate disappeared.

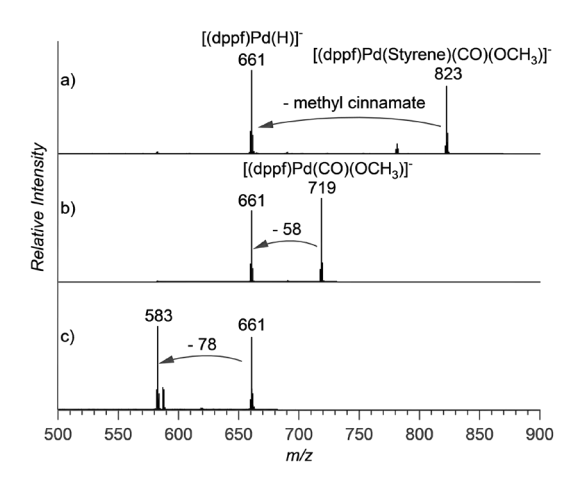


Figure S38. Collision induced dissociation (CID) spectra. a) CID of the alkoxy intermediate [(dppf) Pd(styrene,COOCH,)] $^+$ ion m/z 823, showing the loss of the product methyl cinnamate, b) CID of the Pd alkoxy precursor complex [(dppf)Pd(COOCH₂)]⁺ with m/z 719, loss of cyclic acetolactone as previously observed for negatively charged precursor complexes (see Figure S5 and S6), and c) CID spectrum of $[(dppf)Pd(H)]^+$ ion with m/z 661.

Toluene/DMSO as the solvent instead of acetonitrile

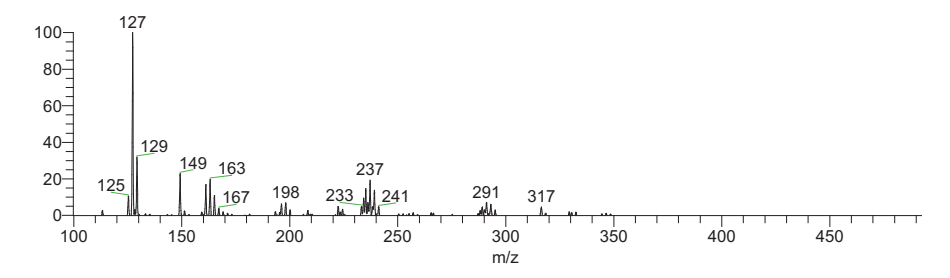


Figure S39. ESI-MS spectra of the reaction mixture of PdCl, in toluene as a solvent with 5% DMSO under CO and oxygen atmosphere.

Pd-methoxycarbonyl precursor complexes [PdCl₂(COOCH₃)]⁻ (m/z 235) was detected. Peak at m/z 289 was [PdCl₃(DMSO)]⁻.

Toluene/DMSO as the solvent instead of acetonitrile and in the presence of monodentate triphenylphosphine ligand

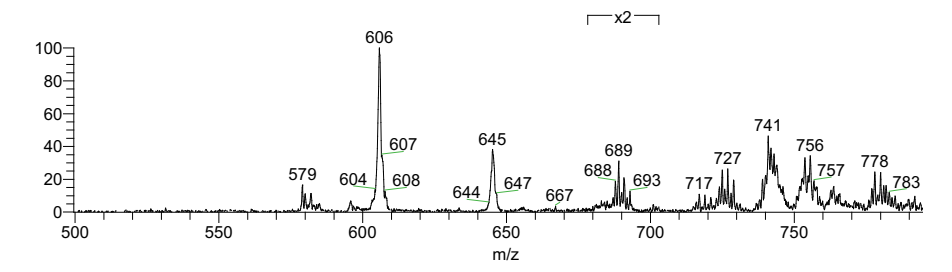


Figure S40. ESI-MS spectra of the reaction mixture of $PdCl_2(PPh_3)_2$ in toluene as solvent with 5% DMSO under CO and oxygen atmosphere.

Pd-methoxycarbonyl precursor complex with PPh₃ ligand as $[Pd(PPh_3)_2(COOCH_3)]^+$ (m/z 689) was detected.

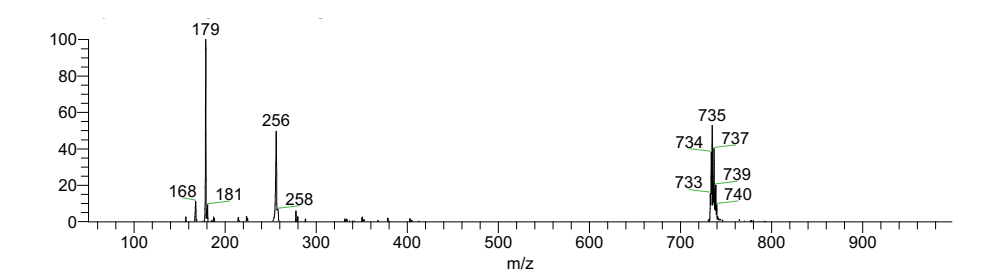


Figure S41. ESI-MS spectra of the reaction mixture of PdCl₂(PPh₃)₂, *p*-benzoquinone and styrene in toluene as solvent with 5% DMSO under CO and oxygen atmosphere.

Hydride cycle Pd-intermediate with PPh_3 ligand as $[Pd(PPh_3)_2(styrene,H)]^+$ (m/z 735) was detected.

Standard reaction with p-benzoquinone as oxidant, acetonitrile and methanol as solvent under CO, but styrene substituted to p-chloro styrene

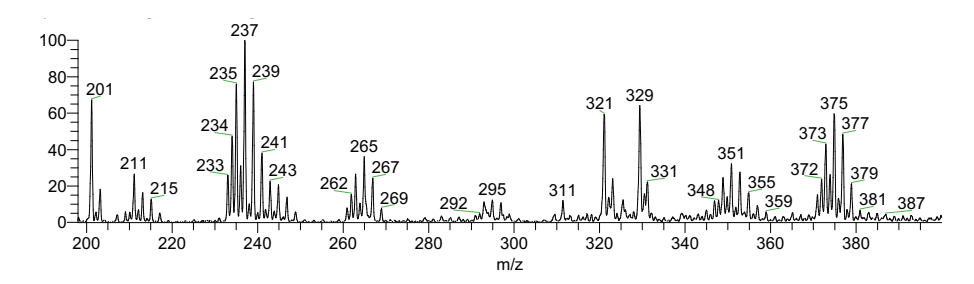


Figure S42. p-chloro styrene instead of styrene, m/z 373 is Pd alkoxy intermediate [PdCl₃(Cl-styrene,COOCH₃)]⁻.

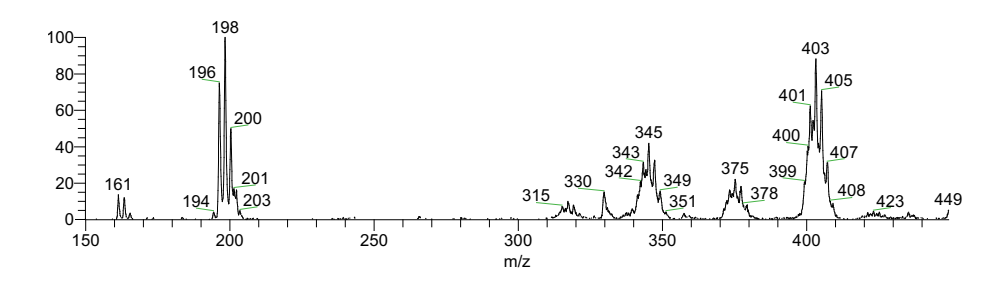


Figure S43. Chloro-styrene instead of styrene after 2 hr.

Palladium hydride intermediate m/z 343 is Pd alkoxy intermediate [PdCl₂(Clstyrene,CO,H)]⁻, Palladium alkoxy intermediate [PdCl₂(Cl-styrene,COOCH₃)]⁻ at m/z 375 and $[PdCl_{3}(Cl-styrene,COOCH_{3},CO)]^{-}$ at m/z 401.

Copper acetate monohydrate as oxidant and in the presence of tertabutyl ammonium bromide

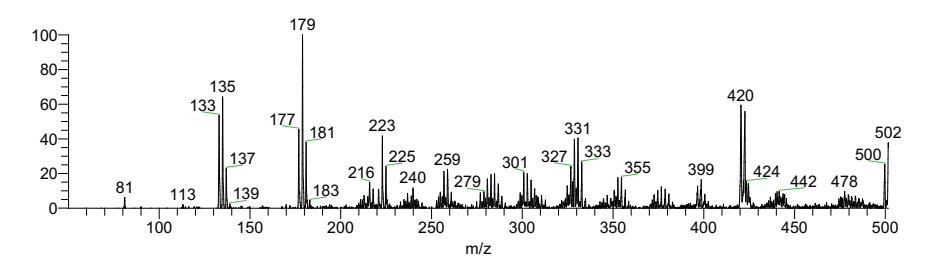


Figure S44. ESI-MS spectrum of PdCl₂, copper acetate monohydrate, tetrabutylammonium bromide in acetonitrile under CO atmosphere, showing various Pd and copper complex/clusters. This is pre-stirred mixture according to literature before styrene addition.¹⁶

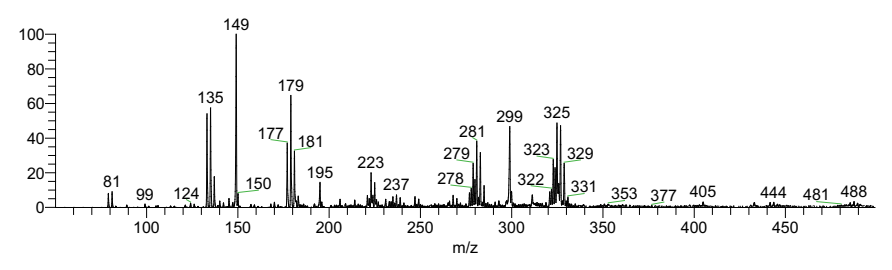


Figure S45. ESI-MS spectrum of $PdCl_2$, copper acetate monohydrate, tetrabutylammonium bromide in acetonitrile under CO atmosphere, showing various Pd and copper complex/clusters after 2 hrs. Pd alkoxy precursor complexes could be detected with bromide from TBAB exchanging with the usual chloride complex. m/z 279 is $[PdClBr(COOCH_2)]^{-1}$ and m/z 323 is $[PdBr_2(COOCH_2)]^{-1}$.

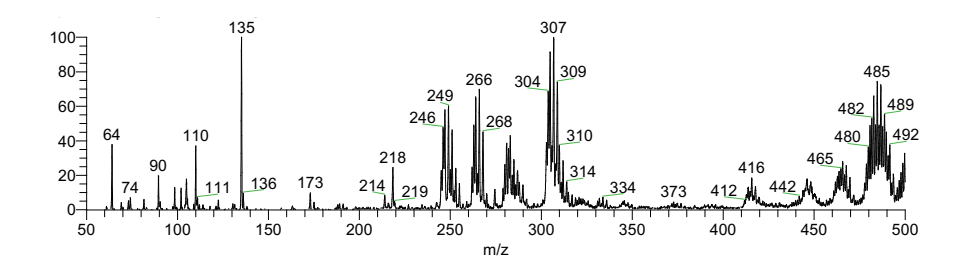


Figure S46. ESI-MS spectrum of PdCl₂, *p*-benzoquinone, styrene in acetonitrile:methanol under CO atmosphere, showing various Pd(II) complexes after 15 min. Pd complexes detected are as follows: *m/z* 247 [PdCl(H)(CH₃CN)₂]Na⁺, *m/z* 264 [PdCl(CH₃CN)₃]⁺, *m/z* 281 [PdCl₂(CH₃CN)₂]Na⁺ and *m/z* 305 is [PdCl(CH₃CN)₄]⁺.

It is important to note that -OMe containing complexes were not detected in this case when compared to oxidant copper acectate.

Palladium and copper speciation under the reaction conditions

Stock solutions of palladium chloride 2.6 mM in CH₃CN, Cu(OAc)₃.H₂O 18.7 mM in CH₂CN, styrene 144 mM in CH₂CN were prepared. The palladium chloride and copper acetate monohydrate were sonicated for 20-30 min. To 1:1 solvent mixture of CH₃CN:MeOH, 200 μM of PdCl₃ and 650 μM Cu(OAc)₃.H₃O was added. This mixture was stirred at room temperature under the balloon of carbon monoxide (CO) and oxygen. The reaction mixture was online monitored and at 1st min excess of styrene (10 mM) was added. Resulting reaction mixture was monitored for an hour on ESI-TOF.

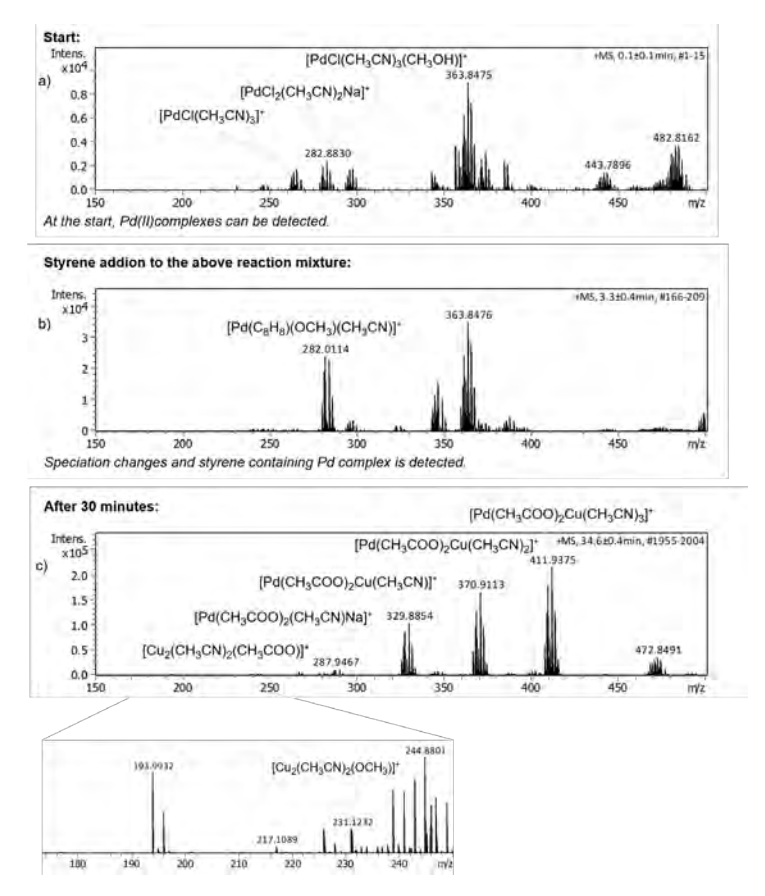


Figure S47. Snapshots of ESI-TOF online monitoring spectra of the reaction mixture of PdCl, and copper acetate monohydrate in CH₂CN:MeOH under the CO and O₂ atmosphere at room temperature a) initial spectrum, b) on addition of styrene and c) spectrum after 30 minutes, with zoomed section.

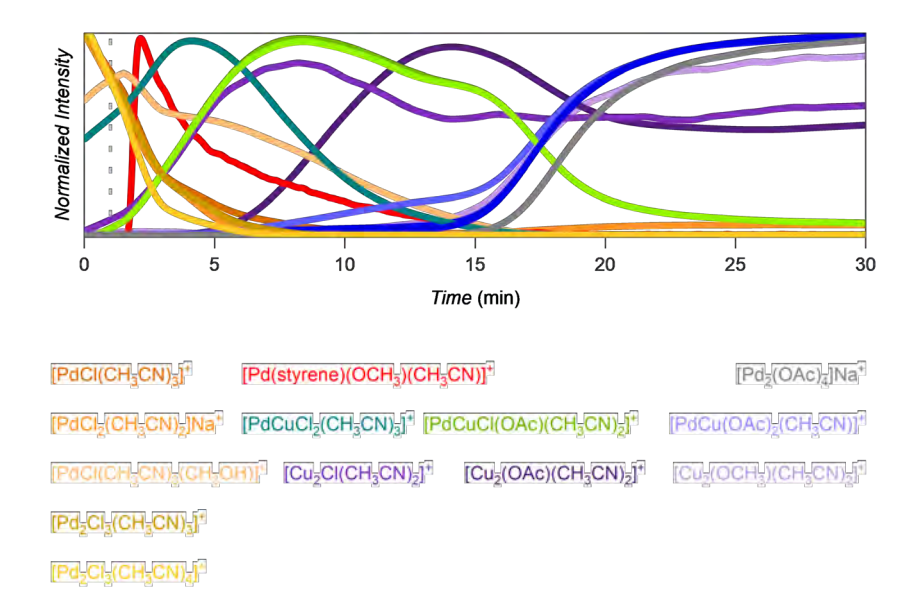


Figure \$48. Plot of normalized specified ion intensities against the time.

- At the start, we observed the Pd(II) complexes as depicted in golden yellow to orange shades.
- After styrene addition (dotted grey line indicating the addition), the red curve shows that the Pd complex containing styrene increases sharply and, over time, decreases.
- The purple shades curves indicated di copper complexes with bridging ligands. It must be noted that the dicopper complexes with methoxyl as the bridging ligand are only detected after the species containing the styrene has disappeared. During this time, the Pd(II) (grey curve) is generated simultaneously.
- Bimetallic Pd Cu complexes show the interplay of the bridging ligands. Initially, complexes with chloro bridging ligands are observed (cyan), followed by mixed choro with acetato (green), and finally, towards the end, only the complexes with the acetato bridging ligands are observed (in blue).

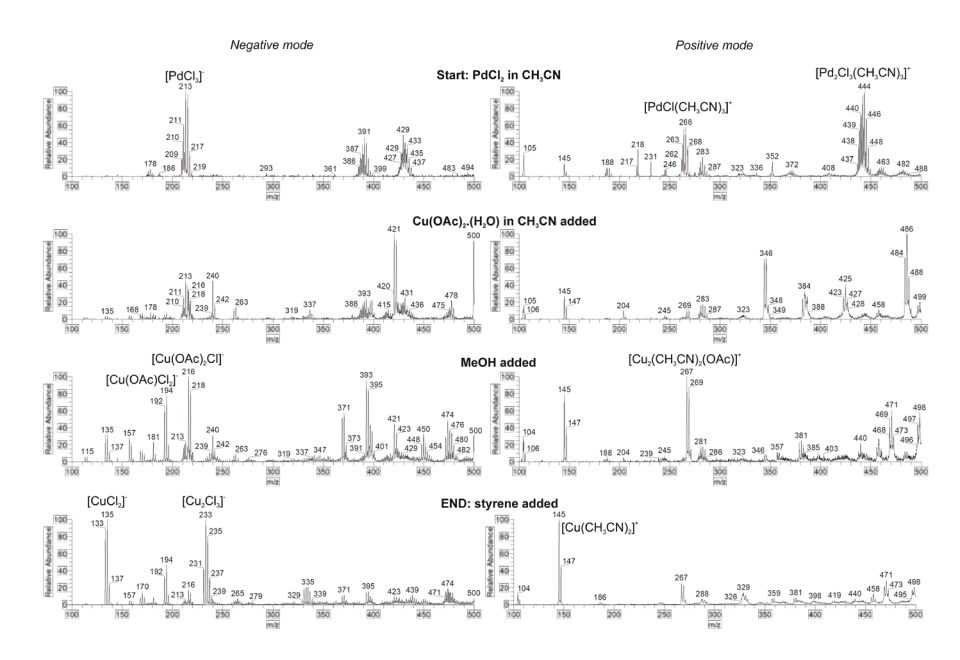


Figure S49. Plot snapshots of ESI-MS online monitoring spectra of the reaction mixture of under the O₂ atmosphere at room temperature a) initial spectrum of PdCl₂ in CH₃CN, b) on addition of copper acetate monohydrate, c) on the addition of methanol and d) spectrum after the addition of styrene in 20 minutes.

- At the start, we observed the Pd(II) complexes in both positive and negative modes.
- After the copper addition, followed by methanol, we initially observed copper(II) complexes in the negative mode.
- On the addition of styrene and as the reaction proceeds, copper(I) complexes are detected in both modes.

Control experiments in methanol

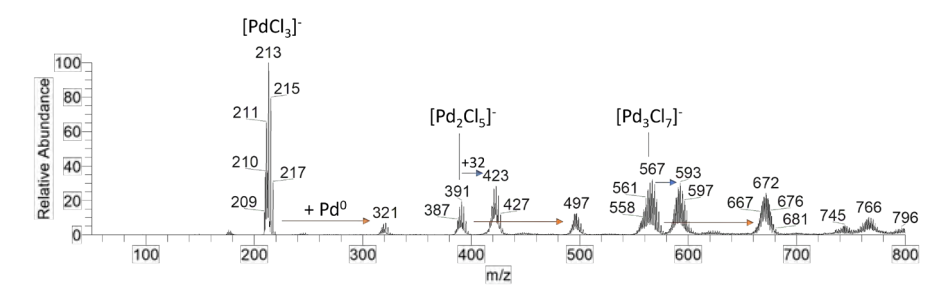


Figure S50. ESI-MS spectrum of the PdCl₂ in methanol (200 μM concentration, solution sonicated and filtered).

• We observed the $[(PdCl_2)_nCI]^-$ complexes and their adducts with Pd^0 . Because of the low solubility of $PdCl_2$ in methanol, we had to sonicate the solution for ~20 min. During this time, some palladium was reduced. Palladium(II) complex can react with the methanol ligand by β -hydrogen elimination, leading to palladium hydride and ultimately to palladium reduction.

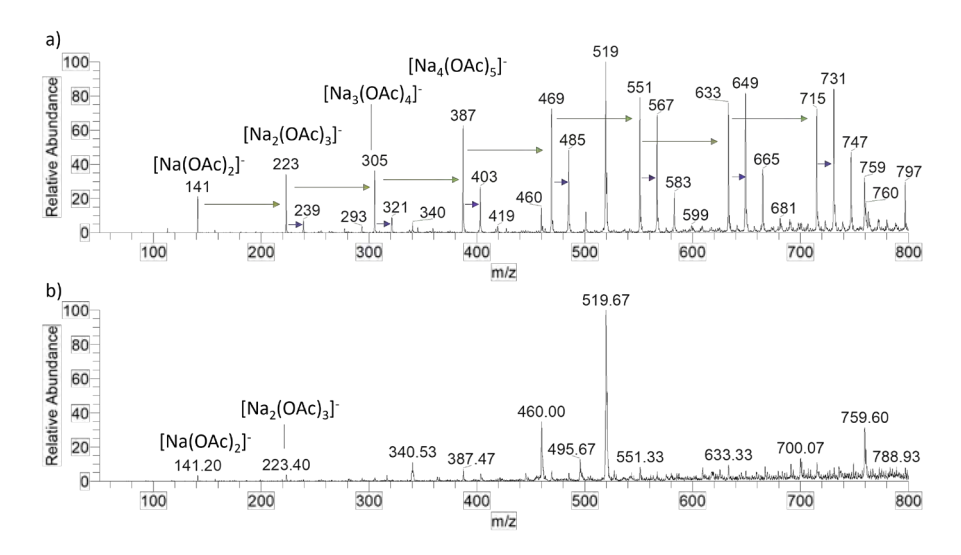


Figure S51. ESI-MS spectra a) NaOAc (200 μ M) in methanol and b) PdCl₂ in methanol + NaOAc (both 200 μ M) in methanol solutions.

We could not detect palladium complexes from the methanol solution of PdCl₂ and NaOAc. Surprisingly, even the signals of the NaOAc clusters were suppressed.



Chapter 4

Mechanistic Studies of the Palladium-Catalyzed S,O-Ligand promoted C-H Olefination of Aromatic Compounds

The work in this chapter is published: Naksomboon, K.; Gómez-Bengoa, E.; Mehara, J.; Roithová, J.; Otten, E.; Fernández-Ibáñez, M. Á. Mechanistic Studies of the Palladium-Catalyzed S,O-Ligand Promoted C–H Olefination of Aromatic Compounds. *Chem. Sci.* **2023**, *14* (11), 2943–2953.

Pd-catalyzed C-H functionalization reactions of non-directed substrates have recently emerged as an attractive alternative to the use of directing groups. Key to the success of these transformations has been the discovery of new ligands capable of increasing both the reactivity of the inert C-H bond and the selectivity of the process. Among them, a new type of an S,O-ligand has shown to be highly efficient in promoting a variety of Pd-catalyzed C-H olefination reactions of nondirected arenes. Despite the success of this type of the S,O-ligand, its role in the C-H functionalization processes is unknown. Herein, we describe a detailed mechanistic study focused on elucidating of the role of the S,O-ligand in the Pd-catalyzed C-H olefination of non-directed arenes. With this purpose, several mechanistic tools, including isolation and characterization of reactive intermediates, NMR and kinetic studies, isotope effects and DFT calculations have been employed. The data from these experiments suggest that the C-H activation is reversible and is the ratedetermining step in both cases with and without the S,O-ligand. Furthermore, the results indicate that the S,O-ligand triggers the formation of more reactive Pd cationic species, which explains the observed acceleration of the reaction. Together, these studies shed light on the role of the S,O-ligand in promoting Pd-catalyzed C-H functionalization reactions.

My specific contribution to this work centers on the mass spectrometric studies employing a charge tagging method (see Chapter 1 section 1.6), through which we successfully detected the key 'neutral' intermediate postulated in the catalytic cycle. Moreover, the mass spectrometric data further illuminated the S,O-ligand's role in catalysis, revealing the formation of more reactive Pd cationic species. Through collective efforts, a clearer understanding of the S,O-ligand's mechanistic contributions was achieved, offering valuable perspectives for future catalytic system development.

Introduction

Over the past 20 years, palladium-catalyzed C-H functionalization reactions has become a powerful synthetic tool in organic synthesis.¹ The majority of the reported methods rely on the use of directing groups to increase the reactivity and selectivity of the process.² In last few years the use of ligands in metal-catalyzed C-H functionalization reaction of non-directed substrates has emerged as an attractive alternative to the use of directing groups.³ However, to date, only few catalytic systems have shown certain generality in promoting palladium-catalyzed C-H functionalization reactions of non-directed arenes. In this context, mono-protected amino acids ligands (MPAA),⁴ pyridine based ligands⁵ or the combinations of both⁶ have been identified as efficient ligands for these transformations. Recently, we have discovered a new type of an S,O-ligand, namely thioethercarboxylic acid, that enables palladium-catalyzed C-H olefination of simple arenes, thiophenes, anisole and aniline derivatives (Scheme 1).7

Scheme 1. Pd/S,O-ligand-catalyzed C-H olefination of non-directed arenes.

The effectiveness and simplicity of the new catalytic system based on Pd/S,O-ligand has inspired other research groups to use the S,O-ligand in the functionalization of anisoles or to prepare palladium-organic frameworks containing S,O-moieties for the C-H olefination of a variety of aromatic compounds.8 Despite the potential applications of the Pd/S,O-ligand catalyst in C-H functionalization reactions, the mechanistic role of the S,O-ligand is unknown.

Herein, we describe a detail mechanistic investigation on the role of the S,O-ligand in Pd-catalyzed C-H functionalization reactions of aromatic compounds. We have isolated and characterized by X-ray diffraction analysis several complexes before and after C-H activation and evaluated their catalytic activities. NMR and kinetic studies reveal that the C-H activation is rate limiting and reversible. Moreover, these studies suggest that the S,O-ligand triggers the formation of Pd cationic species. Additionally, a cationic Pd-complex is detected by ESI-MS and its reactivity in C-H activation processes studied. DFT calculations corroborate the feasibility of the cationic pathway in the C-H activation of benzene as well as reveal the higher reactivity of cationic complexes in these processes. These investigations provide insights into the role of the S,O-ligand in promoting Pd-catalyzed C-H functionalization reactions. We expect that the finding will not only serve to guide future ligand development in the growing field of non-directed C-H functionalization reactions but also in further applications of this type of ligands in metal-catalysis.

Results and Discussion

Identification of active Pd complexes

Initially, we concentrated our efforts in the identification of Pd complexes bearing an S,O-ligand. For simplification, we performed our experiments using the 2-methyl-2-(phenylthio)propanoic acid ligand (**L2**) that shows similar performance in the C-H olefination of simple arenes as the 3-methyl-2-(phenylthio)butanoic acid (**L1**) previously used.^{7a} With this purpose, we reacted Pd(OAc)₂ with **L2** in a 1:1 ratio in CH₂Cl₂ at room temperature overnight (Scheme 2, a). From the ¹H NMR spectrum of the crude reaction mixture, several complexes were detected. Fortunately, we were able to isolate and unequivocally characterize by X-ray analysis the major Pd complex **1**-*cis* bearing two S,O-ligands in a *cis* geometry.^{7a,9} When the reaction was performed using 2 equiv of ligand **L2**, Pd-complexes **1**-*cis* and **1**-*trans* were obtained in quantitative yield in a 2:1 ratio, respectively (Scheme 2, b). In order to isolate the Pd complex with only one S,O-ligand attached, we performed the reaction in the presence of PPh₃ using a 1:1:1 ratio of Pd:**L2**:PPh₃ in CH₂Cl₂. To our delight, complex **2** bearing one S,O-ligand, one PPh₃ and one acetate ligand was isolated in 84% yield and fully characterized by X-ray analysis (Scheme 2, c).¹⁰

With these complexes in hand, we performed several experiments to evaluate their catalytic activities (Figure 1A). We executed the reaction of benzene with ethyl acrylate under the optimal reaction conditions with and without ligand **L2** (entries 1 and 2).^{7a} The reaction without ligand provided, after 2h, the olefinated product in 21% yield and in the presence of **L2**, the olefinated products **3** were obtained in 78% yield. When we performed the same reaction using 5 mol% of complex **1** instead of Pd(OAc)₂, the olefinated product was obtained in 53% yield (entry 3), indicating that complex **1** might accelerate the C-H olefination reaction. To see the effect of PPh₃ in the reaction, we tested the reaction using 5 mol% of a catalyst based on a 1:1:1 ratio of Pd:**L2**:PPh₃. This reaction provided the desired products in 79% yield which is comparable to the result of the reaction without PPh₃ (entries 2 and 4). To our delight, the reaction using 5 mol% of complex **2** gave products **3** in 77% yield

(entry 5), suggesting that this complex is involved in the catalytic reaction in the presence of PPh₃. Additionally, the kinetic profiles of the reactions using different Pd catalysts were also performed (Figure 1B). The reactions using a 1:1 ratio of Pd:L2 and complex 2 as catalyst provided comparable curves suggesting that a similar reaction mechanism is taking place with and without PPh₃. The reaction using complex 1 showed an increase in reaction rate compared with the reaction without ligand. However, the kinetic profile shows that the reaction is slower than when complex 2 or a 1:1 ratio of Pd:L2 is used.

(a)
$$Pd(OAc)_{2} + \bigvee_{SPh} OH \qquad CH_{2}CI_{2} \\ RT, overnight \\ L2 \\ (1 equiv) \qquad (1 equiv) \qquad complexes$$
(b)
$$Pd(OAc)_{2} + \bigvee_{SPh} OH \qquad CH_{2}CI_{2} \\ RT, overnight \\ L2 \qquad quantitative yield \qquad 1-cis \qquad 1-trans$$
(c)
$$Pd(OAc)_{2} + \bigvee_{SPh} OH \qquad CH_{2}CI_{2} \\ RT, overnight \\ quantitative yield \qquad 1-cis \qquad 1-trans$$
(c)
$$Pd(OAc)_{2} + \bigvee_{SPh} OH + PPh_{3} \qquad CH_{2}CI_{2} \\ RT, 1 h \qquad SPh \qquad Ph \\ RT, 1 h \qquad SPh \\ RT, 1 h \qquad$$

Scheme 2. Synthesis of Pd/S,O-ligand complexes

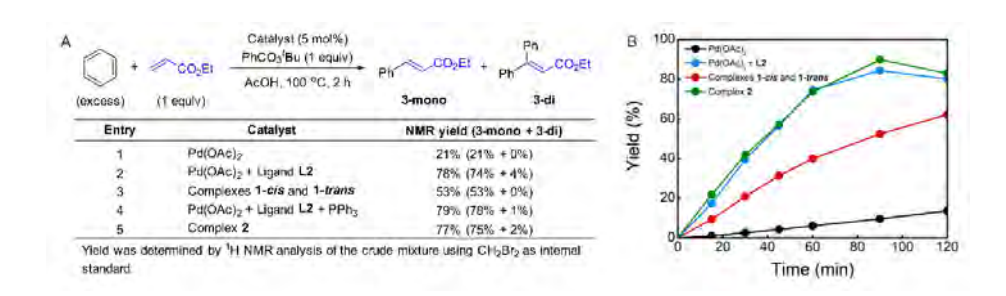


Figure 1. A) Reactivity of Pd catalyst in the C-H olefination of benzene and B) Kinetic profiles of C-H olefination of benzene.

With the intention of identifying a Pd complex after the C-H activation step, we carried out the reaction of complex 2 with benzene in a pressure tube at 100 °C for 10 min (Scheme 3, a). From the ¹H NMR spectrum of the reaction mixture, we tentatively assigned some peaks to the formation of complexes 4 and/or 4', which come after the C-H activation step, along with many other peaks that we could not identify. From the ³¹P NMR spectrum, mainly three equally intense peaks which belong to triphenylphosphine oxide, complexes 2 and 4 (or 4') were observed. Unfortunately, from the reaction mixture, we were not able to isolate complex 4 (or 4').

To confirm the formation of complex 4 (or 4'), we decided to synthesize 4' via a different synthetic route following a literature procedure.¹¹ The structure of complex 4' was confirmed by X-ray analysis where two enantiomers that differ in the configuration of the sulfur atom 4'A and 4'B were observed (see Supporting Information).¹² Then, we compared the ¹H and ³¹P NMR spectra of **4'** with the one obtained from the reaction of 2 with benzene. We found that both spectra match. confirming that 4 (or 4') was formed in the reaction of complex 2 with benzene. Next, the reaction of complex 4' with an excess of ethyl acrylate furnished the olefinated product in 90% ¹H NMR yield (Scheme 3, b). From these results, we suggest that complexes 2 and 4' (and/or 4) are active catalysts in the reaction.

Scheme 3. Reaction of (a) Pd complex 2 with benzene and (b) Pd complex 4' with ethyl acrylate.

Identification of Pd complexes during the catalytic reaction

After having several Pd complexes characterized, we attempted to identify the complexes that were formed during the catalytic reaction. The reaction was

performed in an NMR tube at 100 °C and was followed at different times by measuring the ¹H and ³¹P NMR spectra at room temperature. We performed the reaction under standard conditions but using 50 mol% of the catalyst and deuterated acetic acid as a solvent. The comparison of ¹H NMR spectra of ligand **L2**, Pd complexes 1, 2 and 4' and the reaction at different times (0, 3, 5 and 10 min) are shown in Figure 2B. Before the reaction started (0 min), ligand L2 and complex 2 were clearly identified from their characteristic peaks of the methyl groups. After 3 and 5 min, we observed mainly complex 2 in the ¹H NMR spectra. After 10 min, the reaction was completed and the signals of complex 2 were almost insignificant. After 3 min, we started to observe trace amounts of complex 1 and we did not detect any formation of complex 4' during the reaction. The ¹H NMR data were consistent with ³¹P NMR spectra as shown in Figure 2C. Mainly the peak at 27 ppm, which belongs to complex 2, was observed from 0 to 5 min and the intensity of this peak dramatically decreased after 10 min. The formation of complex 4' (31P NMR at 26 ppm) was not detected during the reaction; however, other unidentified phosphorus species were formed. These results indicate that complex 2 is the resting state of the catalyst.

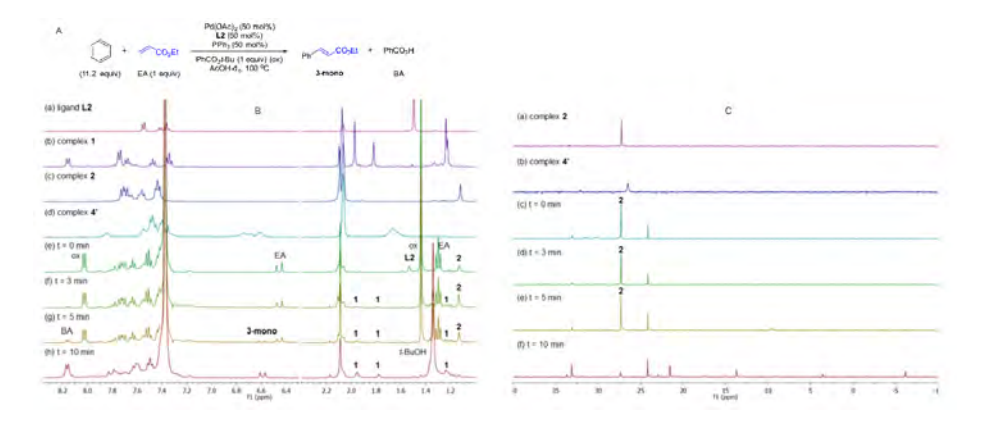


Figure 2. A) Reaction under study; B) ¹H NMR spectra of (a) ligand L2, (b) complexes 1-cis and 1-trans, (c) complex 2, (d) complex 4' in AcOH-d,. C-H Olefination of benzene and ethyl acrylate using a 1:1:1 ratio of Pd:L2:PPh, as catalyst in AcOH-d, monitored by ¹H NMR spectroscopy at (e) 0 min, (f) 3 min, (g) 5 min and (h) 10 min. ox = oxidant, EA = ethyl acrylate, BA = benzoic acid; C) ³¹P NMR spectra of (a) complex 2 and (b) complex 4' in AcOH-d_a. C-H Olefination of benzene and ethyl acrylate using a 1:1:1 ratio of Pd:L2:PPh3 as catalyst in AcOH-d4 monitored by 31P NMR spectroscopy at (c) 0 min, (d) 3 min, (e) 5 min and (f) 10 min.

Next, we examined the reaction using benzene, Pd(OAc), ligand L2 and PPh, in AcOD-d₄ in the absence of ethyl acrylate in an NMR tube at 100 °C, recording the NMR data at the indicated time at room temperature. As shown in Figure 3B, at 0 min, ligand **L2** and complex **2** were detected. After 2 and 4 min, complex **2** was the main complex observed, traces of complex **1** were detected and traces of complex **4'** (or **4**) were identified from the peaks around 6.5–7 ppm. ³¹P NMR data corroborated that complex **2** (27 ppm) was the main complex during the reaction and that traces of complex **4'** (or **4**) (26 ppm) were formed (Figure 3C).

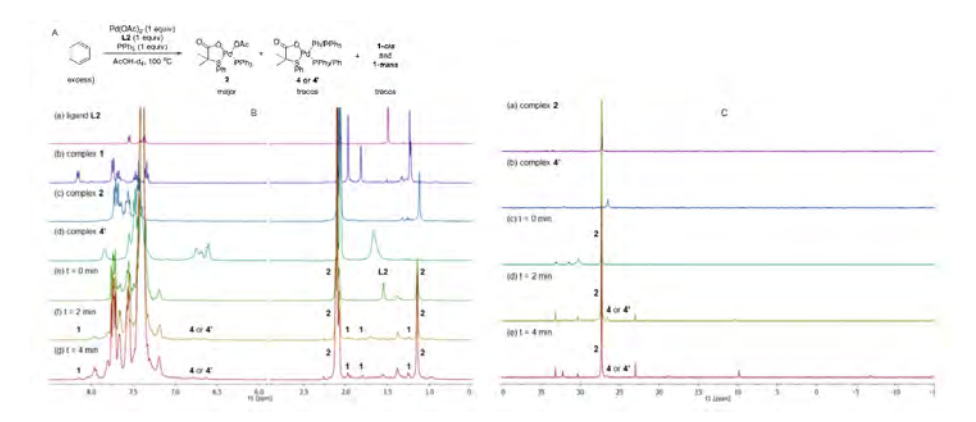


Figure 3. A) Reaction under study; B)¹H NMR spectra of (a) ligand **L2**, (b) complexes **1-***cis* and **1-***trans*, (c) complex **2** and (d) complex **4'** in AcOH-d₄. The reaction of benzene with Pd(OAc)_{2'} ligand **L2** and PPh₃ in AcOH-d₄ monitored by ¹H NMR spectroscopy at (e) 0 min, (f) 2 min and (g) 4 min; C) ³¹P NMR spectra of (a) complex **2** and (b) complex **4'** in AcOH-d₄. The reaction of benzene with Pd(OAc)_{2'}, ligand **L2** and PPh₃ in AcOH-d₄ monitored by ³¹P NMR spectroscopy at (c) 0 min, (d) 2 min and (e) 4 min.

Kinetic investigations

Order of the reaction

The order of each reagent was determined in the reaction in the presence of ligand **L1** by using the initial rate method. Figure 4A shows the plot of logarithm of the reaction rate against the concentration of the reagent. A straight line with a slope of nearly one was measured for Pd-catalyst and benzene, revealing a first order in these reagents (Figure 4A, a and b). Non-significant change in the reaction rate was observed using different concentrations of oxidant and olefin (Figure 4A, c and d), indicating that the migratory insertion and oxidation of Pd(0) occur after the RDS. Nevertheless, the small negative fractional order in both cases can be explained by the formation of off-cycle catalyst bearing these groups as neutral ligand instead of for example PPh₃. 14

Based on a previously reported observation of an inverse first-order dependence of the rate on [OAc-] in the C-H olefination of heteroarenes using a monodentate

thioether ligand, 15 we decided to determine the order of the reaction at different concentrations of NaOAc and an inverse 0.7 order dependence was found. (Figure 4A, e).¹⁶ To explain the inverse order observed, we considered two different possibilities: 1) the association of acetate to form off-cycle [Pd(L1)(OAc)_] species and 2) a reversible dissociation of acetate from LPd(L1)(OAc) to form cationic palladium species. To distinguish between these two possibilities, we added an excess of NaOAc to a 1 to 1 mixture of **L2** and Pd(OAc), in AcOD-d⁴ to investigate whether the formation of the off-cycle [Pd(S,O-L)(OAc)₂] was the cause of the inverse order on acetate. After heating the mixture at 100 °C, we observed by ¹H NMR that the relative intensity of peaks that belong to different Pd species changed but no major new Pd species were detected (see Supporting Information). Therefore, the observed inverse order with respect to NaOAc is not the result of the formation of off-cycle [Pd(S,O-L)(OAc)_] species. Taking into account these results, it seems reasonable to propose that more reactive cationic palladium species are formed during the reaction and prior the RDS. 15,17

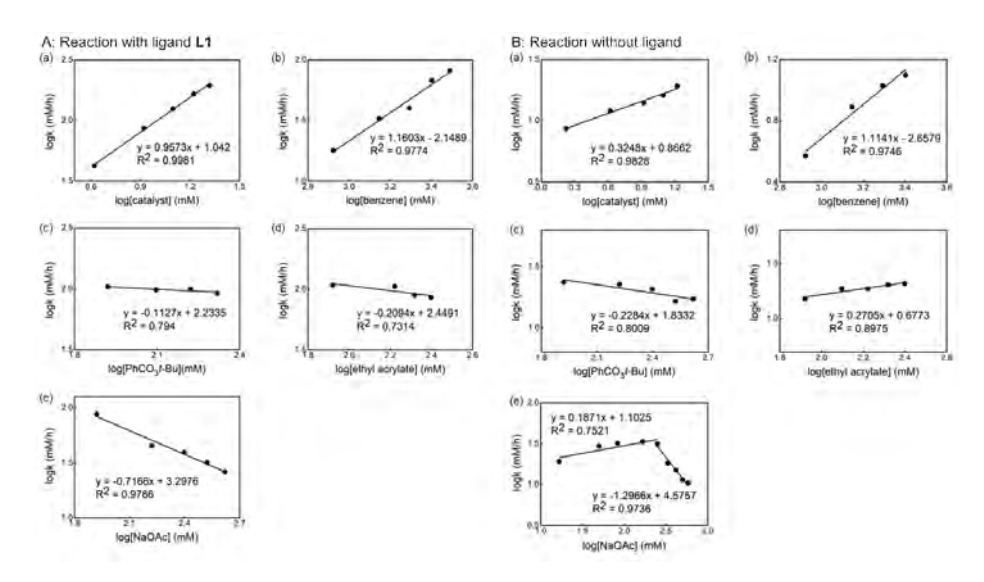


Figure 4. Dependence of the observed rate constant on the concentration of (a) catalyst, (b) benzene, (c) PhCO₂t-Bu, (d) ethyl acrylate, and (e) NaOAc in the reaction: A) with ligand L1; B) without ligand.

Next, we investigated the order of each reagent in the reaction without ligand (Figure 4B). We observed a 0.3 order in the catalyst and the first order in the benzene concentration (Figure 4B, a and b), suggesting a trimeric precatalyst and one benzene associated to the catalyst prior the RDS.¹⁸ Again, near zero order in both oxidant and olefin were observed (Figure 4B, c and d), indicating that olefin insertion and oxidation of Pd(0) occur after the RDS and that probably some off-cycle catalyst having these reagents as neutral ligands are formed. Zero order in the acetate concentration is observed at lower concentrations of NaOAc and changed to the inverse 1.2 order dependence when the concentration of acetate was increased (Figure 4B, e). We postulated that at higher concentrations of acetate the off-cycle [Pd(OAc)₃] is formed in the reaction.

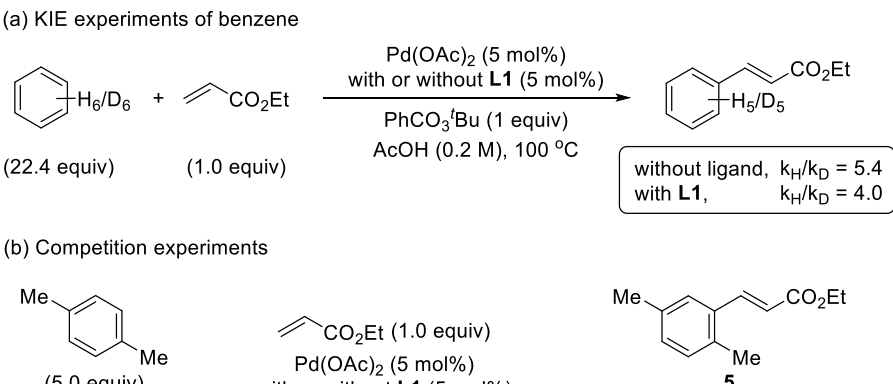
From these kinetic experiments, we suggest that the C-H activation is the RDS in both cases, with and without ligand and that the presence of the S,O-ligand triggers the formation of cationic species, which are expected to be more reactive.¹⁷ We also proposed that the reaction in the presence of the S,O-ligand occurs via catalytically active monomeric species which are the main species in solution.

KIE and H/D exchange experiments

The KIE values were examined by performing reactions with benzene and benzene-d₆ in two different reaction flasks. ¹⁹ The reaction in the presence of ligand **L1** provided a k_H/k_D ratio of 4.0 and in the absence of ligand provided a k_H/k_D ratio of 5.4 (Scheme 4, a). The observed primary KIE corroborates together with the kinetic and NMR studies that the C–H bond cleavage is the RDS in the reaction with and without the S,O-ligand. Additionally, the reversibility of the C–H activation step by performing H/D scrambling experiments using AcOD-d₄ as a deuterium source was evaluated. We used mesitylene as a diagnostic arene to facilitate the interpretation of the ¹H NMR spectra. The reaction with ligand **L1** provided the olefinated product and deuterated mesitylene in 17% after 6 h. In the reaction without ligand, by increasing the amount of the catalyst and the reaction time, the formation of 25% deuterated mesitylene was observed. Based on these experimental results, we suggest that the C–H activation is reversible in both cases, with and without the ligand.

Competition experiments

To get more insights into the mechanism of the C-H activation step, we performed one-pot intermolecular competition experiments between an electron-rich arene, *p*-xylene, and an electron-poor arene, 1,4-bis(trifluoromethyl)benzene, with and without the ligand (Scheme 4, b). We found that in both cases, electron-rich arene reacted preferentially. These results, together with the C-H bond cleavage being the RDS, are consistent with an asynchronous CMD mechanism,^{20,21} or a BIES mechanism.^{22,23}



CO₂Et
$$(1.0 \text{ equiv})$$
Pd $(OAc)_2$ $(5 \text{ mol}\%)$
with or without L1 $(5 \text{ mol}\%)$
Ph CO_3 bu (1 equiv)
AcOH (0.2 M) , 100 °C , 3 h

F₃C

CF₃
 (5.0 equiv)

F₃C

CF₃
 (5.0 equiv)

We Me

F₃C

CO₂Et

F₃C

CO₂Et

Without ligand, $(5.6 = 22\%; \text{traces})$
with L1, $(5.6 = 84\%; \text{traces})$

Scheme 4. Mechanistic studies (a) KIE experiments of benzene and (b) competition experiments.

Detection of reactive palladium complexes by ESI-MS and their reactivities in C-H activation processes

With the aim to identify cationic reactive intermediates in solution, we analyzed the system by electrospray ionization mass spectrometry (ESI-MS). Firstly, the Pd(OAc), and L2 were mixed in benzene and we detected larger palladium clusters with combination of deprotonated L2 (L2-H) and AcO ligands (Figure S1 in the Supporting Information). Upon addition of PPh₃ to the mixture, the clusters disappeared and we detected monomeric [(PPh₂)₂Pd(**L2**-H)]⁺ complex (m/z 825, Figure 5a). The activation of benzene leads to complex 4/4' that are neutral. Therefore, we repeated the experiment with an addition of the negatively charged $(PPh_{2}Ph^{SO3-})$ ligand $(Ph^{SO3-} = 3-phenylsulfonate)$. We observed the $[(PPh_{2}Ph^{SO3-})]$ Pd(L2-H)(AcO) and $[(PPh_3Ph^{SO3-})Pd(L2-H)_3]$ ions (m/z 701) and m/z 836, respectively, Figure S2). However, we were unable to detect the expected [(PPh,PhSO3-)Pd(L2-H) (Ph)] complex with this system.

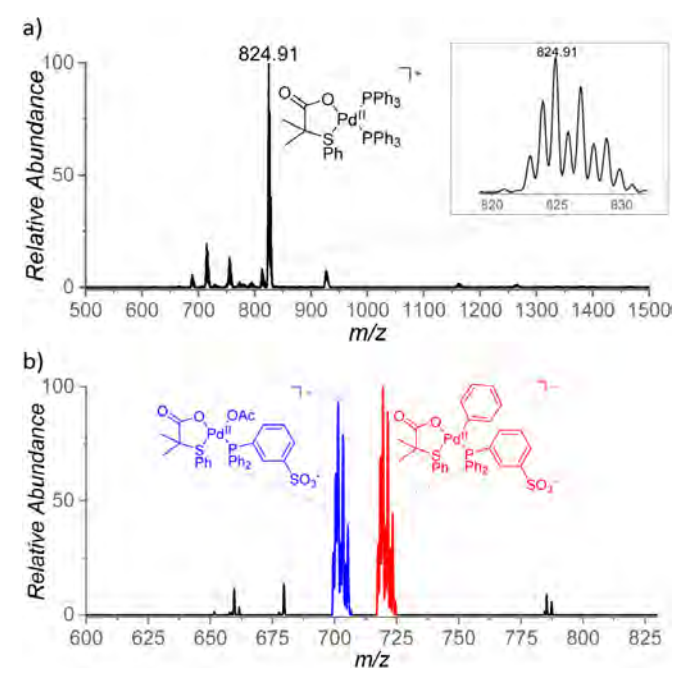


Figure 5. (a) ESI mass spectrum of a mixture of Pd(OAc)₂, **L2** and Ph₃P in benzene and (b) ESI mass spectrum of Na[(PPh₂Ph^{SO3-})Pd(**L2**-H)(AcO)] in benzene, heated for 5 min at 100 °C.

In the quest to characterize the intermediates 4/4', we synthesized the complex $[(PPh_2Ph^{SO3-})Pd(L2-H)(AcO)]Na^+$ with the charge-tagged ligand. Upon heating the complex in benzene for 5 min at 100 °C, we indeed detected the $[(PPh_2Ph^{SO3-})Pd(L2-H)(Ph)]^-$ complex (m/z 719, Figure 5b). We have confirmed this assignment by repeating the experiment in deuterated benzene and by high-resolution measurements (Figure S3 and S4).

We further explored the formation of $[(PPh_2Ph^{SO3-})Pd(\mathbf{L2}-H)(Ph)]^-$ by ion mobility studies of the mass-selected ions. The ion mobility profile is related to the shape of the ions and therefore it is expected to be different for the **4** and **4'** isomers of the $[(PPh_2Ph^{SO3})Pd(\mathbf{L2}-H)(Ph)]^-$. The ion mobility experiment indicated only one major isomer of the detected $[(PPh_2Ph^{SO3-})Pd(\mathbf{L2}-H)(X)]^-$ complexes with X = CI, OAc, and Ph. (Figure S5).

For a deeper insight into the C-H activation process itself, we explored unimolecular reactivity of the detected [(PPh₃)₂Pd(**L2**-H)]⁺ complex. This complex eliminates neutral **L2** ligand upon collisional activation (196 Da) meaning that one of the phenyl rings had been deprotonated (Figure 6a). To confirm this, we prepared

the complex with perdeuterated triphenylphosphine ligands and the main fragmentation indeed corresponded to the loss of the monodeuterated S,O-ligand L2 (197 Da) (Figure 6b). In order to determine kinetic isotope effect of this process, we prepared a mixed complex $[(PPh_2)(PPh_2-d_{1z})Pd(L2-H)]^+$ (m/z=840). From the ratio of the elimination of L2 and L2-d,, we determined the intramolecular kinetic isotopic effect as ~2 (Figure 6d). Consistently, the extrapolation of the appearance energies for the eliminations of L2 and L2-d, predicts slightly higher energy demand for the fragmentation involving D-atom transfer.

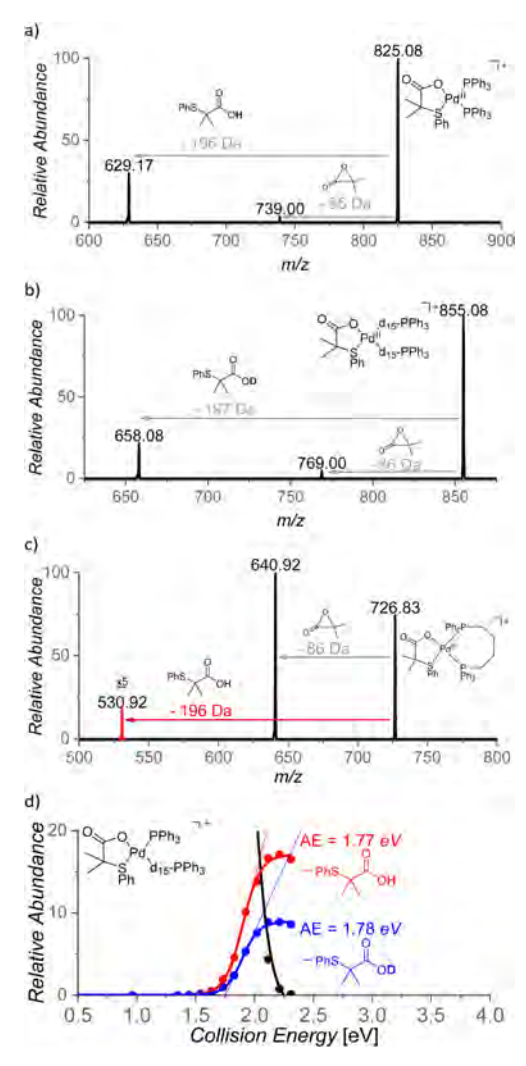


Figure 6. CID mass spectra of (a) $[(PPh_z)_2Pd(L2-H)]^+$ (m/z=825), (b) $[(P(C_zD_z)_z)_2Pd(L2-H)]^+$ (m/z=855), (c) [(dppb)Pd(**L2**-H)]⁺ (m/z=727) and (d) Energy resolved CID of mixed phosphine complex [(PPh₂) $(d_{15}-PPh_3)Pd(L2-H)]^+ (m/z=840).$

To further explore the ability of the S,O-ligand to promote intramolecular C-H activation, we studied fragmentations of four complexes bearing different diphosphine ligands: dppm [(1,1-bis(diphenylphosphino)methane], dppe [(1,1-bis(diphenylphosphino)propane] and dppb [(1,1-bis(diphenylphosphino)butane] (Figure 6c). The complexes with the dppm and dppe ligands show only a degradation of the S,O-ligand (a loss of 86 Da), whereas the larger more flexible ligands allow the activation of a phenyl bound to the phosphorus ligand evidenced by elimination of the neutral ligand **L2**. This reaction is more facile of the complex with dppb (Figure 6c) than for the complex with dppp (Figure S8(iii)). This highlights the importance of the close proximity of the C-H bond and the metal center and the S,O-ligand for the intramolecular C-H activation to occur.

From the performed experiments, the following information can be abstracted: *i*) cationic Pd-complex [(PPh₃)₂Pd(**L2**-H)]⁺ is formed when mixing Pd(OAc)₂, **L2**, PPh₃ in benzene; *ii*) related **2** complex [(PPh₂Ph^{SO3-})Pd(**L2**-H)(AcO)]⁻ is detected by ESI-MS and its reaction with benzene, forming the related **4/4'** isomers [(PPh₂Ph^{SO3}) Pd(**L2**-H)(Ph)]⁻, is confirmed and, *iii*) the carboxylate group of the **L2**-H ligand is capable of acting as internal base when the C-H bond is in close proximity.

DFT Calculations

Density functional theory calculations were also carried out to get more insight into the species involved in the mechanism and the reactivity difference between cationic and neutral Pd-complexes. Following our previous discussion about the formation of cationic species during the reaction and considering that 1-cis is an active precatalyst, we took its protonated form (complex I) as the initial point for the calculations (G=0). From there, several complexes were evaluated by substitution or partial decoordination of one of the S,O-ligands, introducing also benzene as a necessary element prior to its C-H activation. Among the computed complexes (see Supporting Information), the most relevant structures are shown in Figure 7, where the substitution of one S,O-ligand by PPh₃ and benzene units is exothermic (II-P, $\Delta G = -3.4 \text{ kcal/mol}$), while the partial substitution of the S,O-ligand by a molecule of benzene is endothermic (II-S, $\Delta G = +9.9 \text{ kcal/mol}$), but affordable in the experimental conditions.

Figure 7. Relative computed energies (in kcal/mol) of I and benzene containing structures II

From these intermediates (II-P and II-S), a series of changes in the coordination sphere lead to the direct precursors of the C-H activation, IV-P and IV-S. The necessary steps are the decoordination of the S atom and the n¹-coordination of the acetate anion, prior to the C-H cleavage during the transition states TS-P and TS-S (Figure 8). Significantly, the activation energies of the C-H activation are 27.4 and 23.9 kcal/mol respectively, which are accessible barriers in the reaction conditions.

Figure 8. Computed transformation of the cationic complexes II into the transition structures.

Although the previous scheme confirms the feasibility of the cationic pathway, the absolute values are not especially low, and do not show any distinctive feature with respect to other previously computed neutral systems.²⁵ For that reason, we decided to compare directly the C-H functionalization of very similar systems, like those solely differentiated by the presence/absence of just one proton (Figure 9). To our delight, the activation energies are up to 3 kcal/mol lower for the cationic systems than for the neutral ones. The values in the Figure represent the barrier between IV-P and **TS-P** ($\Delta\Delta G^{\dagger}=7.3$ kcal/mol) and its comparison with the deprotonated system (**TSP'**, $\Delta\Delta G^{\dagger}=10.6$ kcal/mol). For the couple **TS-S** and **TS-S'**, a similar difference was also found (10.6 vs 13.8 kcal/mol). This direct comparison confirms the better performance of cationic species with respect to very similar neutral species with an energy difference of roughly two orders of magnitude in reaction rate. We believe that this finding further supports the idea that the efficiency of our ligands rests in their ability to promote the formation of more reactive cationic catalytic systems.

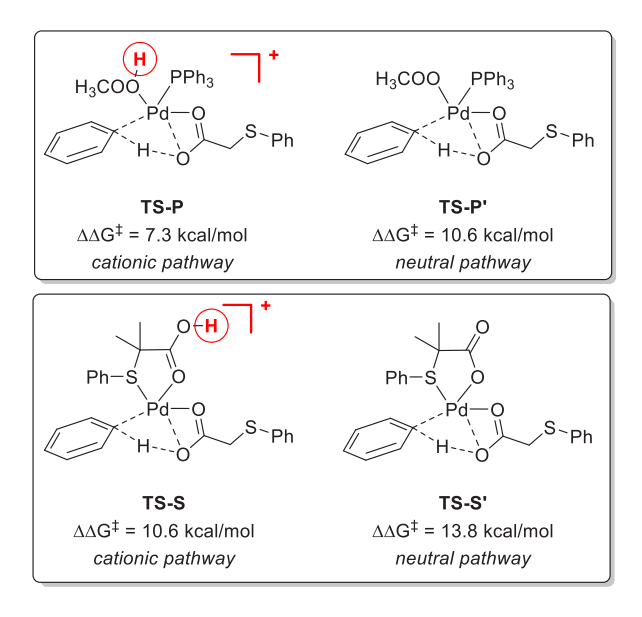


Figure 9. Computed relative activation energies between cationic and neutral transition states.

Proposed catalytic cycle in the presence of S,O-ligand

By combining all the experimental data we have, we propose the mechanism outlined in Scheme 5 for the C-H olefination of arenes in the presence of the S,O-ligand. We draw the intermediates with PPh₃ as ligand since we isolated and identified many of these complexes in the catalytic reaction and similar mechanism is expected to occur with and without PPh₃. Nevertheless, in the case of performing the reaction without PPh₃, complexes bearing an innocent ligand () or the formation of polymeric species might be formed. First, Pd(OAc)₂ reacts with ligand **L2** and PPh₃ forming Pd complex **2**, which we isolated and demonstrated that is catalytically active. We observed by NMR that complex **2** is the catalyst resting state, indicating that C-H activation is the RDS. This is in agreement with the order of the reaction and the large KIE values observed. After the reversible C-H activation step, complex **4** is formed. We propose that the C-H activation takes place *via*

cationic monomeric palladium species 7, which are formed from complex 2 after losing an OAc⁻ ligand. The formation of cationic species is supported by the inverse order in OAc⁻ observed. Additionally, a monomeric cationic [(PPh₂)₂Pd(**L2**-H)]⁺ complex, which matches with the structure of palladium species 7, was detected by ESI-MS and its reactivity in intramolecular C-H activation processes proved. DFT calculations corroborate the feasibility of the cationic pathway in the C-H activation of benzene. Complex 4 reacts with ethyl acrylate providing complex 9 which then undergoes β-H elimination to provide the olefinated compound and Pd(0) species. The oxidation of these species by an oxidant completes the catalytic cycle.

From the comparison of the experiments performed with and without ligand, we propose that the S,O-ligand triggers the formation of cationic palladium species that are more reactive than the neutral species in the C-H activation step, which is in both cases the RDS.

Scheme 5. Proposed catalytic cycle

Conclusion

This article describes a detailed mechanistic study on the role of the S,O-ligand in the Pd-catalyzed C-H olefination reactions of non-directed arenes. Several monomeric Pd/S,O-ligand complexes before and after the C-H activation step have been isolated and fully characterized and their reactivities have been evaluated. NMR and kinetics studies, and KIE values indicate that the C-H activation step is RDS and reversible in both cases with and without S,O-ligand. Moreover, these studies suggest that the S,O-ligand triggers the formation of Pd cationic species. Additionally, a cationic Pd-complex has been detected by ESI-MS and its reactivity in C-H activation processes studied. DFT calculations corroborate the feasibility of the cationic pathway in the C-H activation of benzene as well as reveal the higher reactivity of cationic complexes in these processes. Together, these studies shed light on the role of the S,O-ligand in promoting Pd-catalyzed C-H functionalization reactions.

References

- For general review of C-H activation reaction, see: (a) Godula, K.; Sames, D., C-H Bond Functionalization in Complex Organic Synthesis. Science 2006, 312, 67-72; (b) Bergman, R. G., C-H Activation. Nature 2007, 446, 391-393; (c) Chen, X.; Engle, K. M.; Wang, D.-H.; Yu, J.-Q., Palladium(II)-Catalyzed C-H Activation/C-C Cross-Coupling Reactions: Versatility and Practicality. Angew. Chem. Int. Ed. **2009**, 48, 5094-5115; (d) Yu, J.-Q.; Shi, Z., C-H Activation. Springer: 2010; Vol. 292; (e) Hartwig, J. F., Evolution of C-H Bond Functionalization from Methane to Methodology. J. Am. Chem. Soc. 2016, 138, 2-24; (f) Dixneuf, P. H.; Doucet, H., C-H Bond Activation and Catalytic Functionalization I. Springer: 2016. For selected examples of C-H olefination reaction, see: (g) Jia, C.; Lu, W.; Kitamura, T.; Fujiwara, Y., Highly Efficient Pd-Catalyzed Coupling of Arenes with Olefins in the Presence of tert-Butyl Hydroperoxide as Oxidant. Org. Lett. 1999, 1, 2097-2100; (h) Jia, C.; Piao, D.; Oyamada, J.; Lu, W.; Kitamura, T.; Fujiwara, Y., Efficient Activation of Aromatic C-H Bonds for Addition to C-C Multiple Bonds. Science 2000, 287, 1992-1995; (i) Dams, M.; De Vos, D. E.; Celen, S.; Jacobs, P. A., Toward Waste-Free Production of Heck Products with a Catalytic Palladium System under Oxygen. Angew. Chem. Int. Ed. 2003, 42, 3512-3515; (j) Grimster, N. P.; Gauntlett, C.; Godfrey, C. R.; Gaunt, M. J., Palladium-Catalyzed Intermolecular Alkenylation of Indoles by Solvent-Controlled Regioselective C-H Functionalization. Angew. Chem. Int. Ed. 2005, 44, 3125-3129; (k) Beck, E. M.; Grimster, N. P.; Hatley, R.; Gaunt, M. J., Mild aerobic oxidative palladium (II) catalyzed C-H bond functionalization: regioselective and switchable C-H alkenylation and annulation of pyrroles. J. Am. Chem. Soc. 2006, 128, 2528-2529; (I) Beck, E. M.; Hatley, R.; Gaunt, M. J., Synthesis of rhazinicine by a metal-catalyzed C-H bond functionalization strategy. Angew. Chem. Int. Ed. 2008, 47, 3004-3007; (m) Obora, Y.; Okabe, Y.; Ishii, Y., Direct oxidative coupling of benzenes with acrylonitriles to cinnamonitriles catalyzed by Pd (OAc) 2/HPMoV/O 2 system. Org. Biomol. Chem. 2010, 8, 4071-4073; (n) Le Bras, J.; Muzart, J., Intermolecular dehydrogenative Heck reactions. Chem. Rev. 2011, 111, 1170-1214.
- (a) Chen, Z.; Wang, B.; Zhang, J.; Yu, W.; Liu, Z.; Zhang, Y., Transition metal-catalyzed C-H bond functionalizations by the use of diverse directing groups. Org. Chem. Front. 2015, 2, 1107-1295; (b) Pototschnig, G.; Maulide, N.; Schnürch, M., Direct functionalization of C-H bonds by iron, nickel, and cobalt catalysis. Chem. Eur. J. 2017, 23, 9206-9232; (c) Ma, W.; Gandeepan, P.; Li, J.; Ackermann, L., Recent advances in positional-selective alkenylations: removable guidance for twofold C-H activation. Org. Chem. Front. 2017, 4, 1435-1467; (d) Sambiagio, C.; Schönbauer, D.; Blieck, R.; Dao-Huy, T.; Pototschnig, G.; Schaaf, P.; Wiesinger, T.; Zia, M. F.; Wencel-Delord, J.; Besset, T., A comprehensive overview of directing groups applied in metal-catalysed C-H functionalisation chemistry. Chem. Soc. Rev. 2018, 47, 6603-6743.
- (a) Lyons, T. W.; Sanford, M. S., Palladium-catalyzed ligand-directed C-H functionalization reactions. Chem. Rev. 2010, 110, 1147-1169; (b) Kuhl, N.; Hopkinson, M. N.; Wencel-Delord, J.; Glorius, F., Beyond Directing Groups: Transition-Metal-Catalyzed C-H Activation of Simple Arenes. Angew. Chem. Int. Ed. 2012, 51, 10236-10254; (c) Engle, K. M.; Yu, J.-Q., Developing ligands for palladium (II)-catalyzed C-H functionalization: intimate dialogue between ligand and substrate. J. Org. Chem. 2013, 78, 8927-8955; (d) Wedi, P.; van Gemmeren, M., Arene-Limited Nondirected C-H Activation of Arenes. Angew. Chem. Int. Ed. 2018, 57, 13016-13027; (e) Wang, D.; Weinstein, A. B.; White, P. B.; Stahl, S. S., Ligand-promoted palladium-catalyzed aerobic oxidation reactions. Chem. Rev. 2018, 118, 2636-2679.
- For selected examples of C-H functionalization reactions of directed arenes using MPAA as ligand, see: (a) Shi, B. F.; Maugel, N.; Zhang, Y. H.; Yu, J. Q., Pdll-Catalyzed Enantioselective Activation of C (sp2)—H and C (sp3)—H Bonds Using Monoprotected Amino Acids as Chiral Ligands. Angew. Chem. Int. Ed. 2008, 47, 4882-4886; (b) Novák, P.; Correa, A.; Gallardo-Donaire, J.; Martin, R., Synergistic

Palladium-Catalyzed C(sp3)-H Activation/C(sp3)-O Bond Formation: A Direct, Step-Economical Route to Benzolactones. Angew. Chem. Int. Ed. 2011, 50, 12236-12239; (c) Cheng, X.-F.; Li, Y.; Su, Y.-M.; Yin, F.; Wang, J.-Y.; Sheng, J.; Vora, H. U.; Wang, X.-S.; Yu, J.-Q., Pd (II)-catalyzed enantioselective C-H activation/C-O bond formation: Synthesis of chiral benzofuranones. J. Am. Chem. Soc. 2013, 135, 1236-1239; (d) Li, G.; Leow, D.; Wan, L.; Yu, J.-Q., Ether-Directed ortho-C-H Olefination with a Palladium(II)/Monoprotected Amino Acid Catalyst. Angew. Chem. Int. Ed. 2013, 52, 1245-1247; (e) Chu, L.; Xiao, K.-J.; Yu, J.-Q., Room-temperature enantioselective C-H iodination via kinetic resolution. Science 2014, 346, 451-455; (f) Zhu, C.; Zhang, Y.; Kan, J.; Zhao, H.; Su, W., Ambienttemperature ortho C-H arylation of benzoic acids with aryl iodides with ligand-supported palladium catalyst. Org. Lett. 2015, 17, 3418-3421. For selected examples of C-H functionalization reactions of non-directed arenes using MPAA as ligand, see:(g) Cong, X.; Tang, H.; Wu, C.; Zeng, X., Role of Mono-N-protected Amino Acid Ligands in Palladium(II)-Catalyzed Dehydrogenative Heck Reactions of Electron-Deficient (Hetero)arenes: Experimental and Computational Studies. Organometallics 2013, 32, 6565-6575; (h) Huang, Q.; Zhang, X.; Qiu, L.; Wu, J.; Xiao, H.; Zhang, X.; Lin, S., Palladium-Catalyzed Olefination and Arylation of Polyfluoroarenes Using Molecular Oxygen as the Sole Oxidant. Adv. Synth. Catal. 2015, 357, 3753-3757; (i) Zhuang, Z.; Herron, A. N.; Liu, S.; Yu, J.-Q., Rapid Construction of Tetralin, Chromane, and Indane Motifs via Cyclative C-H/C-H Coupling: Four-Step Total Synthesis of (±)-Russujaponol F. J. Am. Chem. Soc. 2021, 143, 687-692.

For selected examples of C-H functionalization reactions of directed arenes using pyridine-based ligands, see: (a) Wang, C.; Rakshit, S.; Glorius, F., Palladium-catalyzed intermolecular decarboxylative coupling of 2-phenylbenzoic acids with alkynes via C-H and C-C bond activation. J. Am. Chem. Soc. 2010, 132, 14006-14008; (b) Xu, H.; Shang, M.; Dai, H.-X.; Yu, J.-Q., Ligand-controlled paraselective C-H arylation of monosubstituted arenes. Org. Lett. 2015, 17, 3830-3833; (c) Zhu, D.; Yang, G.; He, J.; Chu, L.; Chen, G.; Gong, W.; Chen, K.; Eastgate, M. D.; Yu, J.-Q., Ligand-Promoted ortho-C-H Amination with Pd Catalysts. Angew. Chem. Int. Ed. 2015, 54, 2497-2500; (d) Lu, M.-Z.; Chen, X.-R.; Xu, H.; Dai, H.-X.; Yu, J.-Q., Ligand-enabled ortho-C-H olefination of phenylacetic amides with unactivated alkenes. Chem. Sci. 2018, 9, 1311-1316. For selected examples of C-H functionalization reactions of non-directed arenes using pyridine-based ligands, see: (e) Ishiyama, T.; Takagi, J.; Ishida, K.; Miyaura, N.; Anastasi, N. R.; Hartwig, J. F., Mild Iridium-Catalyzed Borylation of Arenes. High Turnover Numbers, Room Temperature Reactions, and Isolation of a Potential Intermediate. J. Am. Chem. Soc. 2002, 124, 390-391; (f) Ferreira, E. M.; Stoltz, B. M., Catalytic C-H bond functionalization with palladium (II): aerobic oxidative annulations of indoles. J. Am. Chem. Soc. 2003, 125, 9578-9579; (g) Murphy, J. M.; Liao, X.; Hartwig, J. F., Meta Halogenation of 1,3-Disubstituted Arenes via Iridium-Catalyzed Arene Borylation. J. Am. Chem. Soc. 2007, 129, 15434-15435; (h) Izawa, Y.; Stahl, S. S., Aerobic Oxidative Coupling of o-Xylene: Discovery of 2-Fluoropyridine as a Ligand to Support Selective Pd-Catalyzed C-H Functionalization, Adv. Synth, Catal. 2010, 352, 3223-3229; (i) Ye. M.; Gao, G.-L.; Yu, J.-Q., Ligand-promoted C-3 selective C-H olefination of pyridines with Pd catalysts. J. Am. Chem. Soc. 2011, 133, 6964-6967; (j) Emmert, M. H.; Cook, A. K.; Xie, Y. J.; Sanford, M. S., Remarkably High Reactivity of Pd (OAc)2/Pyridine Catalysts: Nondirected C-H Oxygenation of Arenes. Angew. Chem. Int. Ed. 2011, 50, 9409-9412; (k) Cook, A. K.; Emmert, M. H.; Sanford, M. S., Steric control of site selectivity in the Pd-catalyzed C-H acetoxylation of simple arenes. Org. Lett. 2013, 15, 5428-5431; (I) Gary, J. B.; Cook, A. K.; Sanford, M. S., Palladium Catalysts Containing Pyridinium-Substituted Pyridine Ligands for the C-H Oxygenation of Benzene with K2S2O8. ACS Catal. 2013, 3, 700-703; (m) Cheng, C.; Hartwig, J. F., Iridium-Catalyzed Silylation of Aryl C-H Bonds. J. Am. Chem. Soc. 2015, 137, 592-595; (n) Valderas, C.; Naksomboon, K.; Fernández-Ibáñez, M. Á., Ligand-Promoted Palladium-Catalyzed C-H Acetoxylation of Simple Arenes. ChemCatChem 2016, 8, 3213-3217; (o) Wang, P.; Verma, P.; Xia, G.; Shi, J.; Qiao, J. X.; Tao, S.; Cheng, P. T.; Poss, M. A.; Farmer, M. E.; Yeung, K.-S., Ligand-accelerated non-directed C-H functionalization of arenes. Nature 2017, 551, 489-493; (p) Álvarez-Casao, Y.; van Slagmaat, C. A.; Verzijl, G. K.; Lefort, L.; Alsters, P. L.; Fernández-Ibáñez, M. Á., Palladium-catalyzed cross-dehydrogenative coupling of o-xylene: evidence of a new rate-limiting

- step in the search for industrially relevant conditions. ChemCatChem 2018, 10, 2620-2626; (g) Karmel, C.; Chen, Z.; Hartwig, J. F., Iridium-Catalyzed Silylation of C-H Bonds in Unactivated Arenes: A Sterically Encumbered Phenanthroline Ligand Accelerates Catalysis. J. Am. Chem. Soc. 2019, 141, 7063-7072; (r) Liu, L.-Y.; Qiao, J. X.; Yeung, K.-S.; Ewing, W. R.; Yu, J.-Q., meta-Selective C-H Arylation of Fluoroarenes and Simple Arenes. Angew. Chem. Int. Ed. 2020, 59,13831-13939.
- For selected examples of C-H functionalization reactions using pyridine derivative and MPAA as ligands, see: (a) Chen, H.; Wedi, P.; Meyer, T.; Tavakoli, G.; van Gemmeren, M., Dual Ligand-Enabled Nondirected C-H Olefination of Arenes. Angew. Chem. Int. Ed. 2018, 57, 2497-2501; (b) Zhao, D.; Xu, P.; Ritter, T., Palladium-catalyzed late-stage direct arene cyanation. Chem. 2019, 5, 97-107; (c) Mondal, A.; Chen, H.; Flämig, L.; Wedi, P.; van Gemmeren, M., Sterically controlled late-stage C-H alkynylation of arenes. J. Am. Chem. Soc. 2019, 141, 18662-18667; (d) Chen, H.; Mondal, A.; Wedi, P.; van Gemmeren, M., Dual Ligand-Enabled Nondirected C-H Cyanation of Arenes. ACS Catal. 2019, 9, 1979-1984; (e) Chen, H.; Farizyan, M.; Ghiringhelli, F.; van Gemmeren, M., Sterically Controlled C-H Olefination of Heteroarenes. Angew. Chem. Int. Ed. 2020, 59, 12213-12220; (f) Mondal, A.; van Gemmeren, M., Catalyst-Controlled Regiodivergent C–H Alkynylation of Thiophenes. Angew. Chem. Int. Ed. 2021, 60, 742-746.
- (a) Naksomboon, K.; Valderas, C.; Gómez-Martínez, M.; Álvarez-Casao, Y.; Fernández-Ibáñez, M. A., S,O-Ligand-promoted palladium-catalyzed C-H functionalization reactions of nondirected arenes. ACS Catal. 2017, 7, 6342-6346; (b) Naksomboon, K.; Álvarez-Casao, Y.; Uiterweerd, M.; Westerveld, N.; Maciá, B.; Fernández-Ibáñez, M. Á., S,O-ligand-promoted palladium-catalyzed C-H olefination of arenes with allylic substrates. Tetrahedron Lett. 2018, 59, 379-382; (c) Álvarez-Casao, Y.; Fernández-Ibáñez, M. Á., S,O-Ligand-Promoted Pd-Catalyzed C-H Olefination of Thiophenes. Eur. J. Org. Chem. 2019, 1842-1845; (d) Naksomboon, K.; Poater, J.; Bickelhaupt, F. M.; Fernández-Ibáñez, M. Á., para-Selective C-H Olefination of Aniline Derivatives via Pd/S,O-Ligand Catalysis. J. Am. Chem. Soc. 2019, 141, 6719-6725; (e) Jia, W.-L.; Westerveld, N.; Wong, K. M.; Morsch, T.; Hakkennes, M.; Naksomboon, K.; Fernández-Ibáñez, M. Á., Selective C-H Olefination of Indolines (C5) and Tetrahydroquinolines (C6) by Pd/S,O-Ligand Catalysis. Org. Lett. 2019, 21, 9339-9342; (f) Sukowski, V.; Jia, W.-L.; van Diest, R.; van Borselen, M.; Fernández-Ibáñez, M. Á., S,O-Ligand-Promoted Pd-Catalyzed C-H Olefination of Anisole Derivatives. Eur. J. Org. Chem. 2021, 4132-4135.
- (a) Van Velthoven, N.; Wang, Y.; Van Hees, H.; Henrion, M.; Bugaev, A. L.; Gracy, G.; Amro, K.; Soldatov, A. V.; Alauzun, J. G.; Mutin, P. H.; De Vos, D. E., Heterogeneous Single-Site Catalysts for C-H Activation Reactions: Pd(II)-Loaded S,O-Functionalized Metal Oxide-Bisphosphonates. ACS Appl. Mater. Interfaces 2020, 12, 47457-47466; (b) Van Velthoven, N.; Henrion, M.; Dallenes, J.; Krainc, A.; Bugaev, A. L.; Liu, P.; Bals, S.; Soldatov, A. V.; Mali, G.; De Vos, D. E., S,O-Functionalized Metal-Organic Frameworks as Heterogeneous Single-Site Catalysts for the Oxidative Alkenylation of Arenes via C-H activation. ACS Catal. 2020, 10, 5077-5085; (c) Yin, B.; Fu, M.; Wang, L.; Liu, J.; Zhu, Q., Dual ligand-promoted palladium-catalyzed nondirected C-H alkenylation of aryl ethers. Chem. Commun. 2020, 56, 3293-3296.
- 9. CCDC 1567101 contains the supplementary crystallographic data for Pd complex 1-cis.
- 10. CCDC 1969711 contains the supplementary crystallographic data for Pd complex 2.
- 11. (a) Grushin, V. V.; Alper, H., Alkali-induced disproportionation of palladium(II) tertiary phosphine complexes, [L2PdCl2], to LO and palladium(O). Key intermediates in the biphasic carbonylation of ArX catalyzed by [L2PdCl2]. Organometallics 1993, 12, 1890-1901; (b) Perego, L. A.; Grimaud, L.; Bellina, F., Mechanistic Studies on the Palladium-Catalyzed Direct C-5 Arylation of Imidazoles: The Fundamental Role of the Azole as a Ligand for Palladium. Adv. Synth. Catal. 2016, 358, 597-609.
- 12. CCDC 1969712 and CCDC 1969713 contains the supplementary crystallographic data for Pd
- 13. Espenson, J. H., Chemical kinetics and reaction mechanisms (2nd ed.). McGraw Hill: 1987.

- 14. (a) Cook, A. K.; Sanford, M. S., Mechanism of the Palladium-Catalyzed Arene C–H Acetoxylation: A Comparison of Catalysts and Ligand Effects. J. Am. Chem. Soc. 2015, 137, 3109-3118; (b) Blackmond, D. G., Kinetic Profiling of Catalytic Organic Reactions as a Mechanistic Tool. J. Am. Chem. Soc. 2015, 137, 10852-10866; (c) Wedi, P.; Farizyan, M.; Bergander, K.; Mück-Lichtenfeld, C.; van Gemmeren, M., Mechanism of the Arene-Limited Nondirected C–H Activation of Arenes with Palladium, Angew. Chem. Int. Ed. 2021, 60, 15641-15649.
- Gorsline, B. J.; Wang, L.; Ren, P.; Carrow, B. P., C–H Alkenylation of Heteroarenes: Mechanism, Rate, and Selectivity Changes Enabled by Thioether Ligands. J. Am. Chem. Soc. 2017, 139, 9605-9614.
- Deprez, N. R.; Sanford, M. S., Synthetic and Mechanistic Studies of Pd-Catalyzed C–H Arylation with Diaryliodonium Salts: Evidence for a Bimetallic High Oxidation State Pd Intermediate. J. Am. Chem. Soc. 2009, 131, 11234-11241.
- 17. (a) Boele, M. D. K.; van Strijdonck, G. P. F.; de Vries, A. H. M.; Kamer, P. C. J.; de Vries, J. G.; van Leeuwen, P. W. N. M., Selective Pd-Catalyzed Oxidative Coupling of Anilides with Olefins through C–H Bond Activation at Room Temperature. *J. Am. Chem. Soc.* **2002**, *124*, 1586-1587; (b) Nishikata, T.; Lipshutz, B. H., Cationic Pd(II)-Catalyzed Fujiwara–Moritani Reactions at Room Temperature in Water. *Org. Lett.* **2010**, *12*, 1972-1975; (c) Nishikata, T.; Abela, A. R.; Lipshutz, B. H., Room Temperature C–H Activation and Cross-Coupling of Aryl Ureas in Water. **2010**, *49*, 781-784.
- Vana, J.; Lang, J.; Soltesova, M.; Hanusek, J.; Ruzicka, A.; Sedlak, M.; Roithova, J., The role of trinuclear species in a palladium acetate/trifluoroacetic acid catalytic system. *Dalton Trans.*, 2017, 46, 16269-16275.
- (a) Gómez-Gallego, M.; Sierra, M. A., Kinetic Isotope Effects in the Study of Organometallic Reaction Mechanisms. Chem. Rev. 2011, 111, 4857-4963; (b) Simmons, E. M.; Hartwig, J. F., On the Interpretation of Deuterium Kinetic Isotope Effects in C–H Bond Functionalizations by Transition-Metal Complexes. Angew. Chem. Int. Ed. 2012, 51, 3066-3072.
- 20. For selected examples of C-H activation reaction that proceed through a CMD/AMLA mechanism, see: (a) Lafrance, M.; Rowley, C. N.; Woo, T. K.; Fagnou, K., Catalytic Intermolecular Direct Arylation of Perfluorobenzenes. J. Am. Chem. Soc. 2006, 128, 8754-8756; (b) García-Cuadrado, D.; Braga, A. A. C.; Maseras, F.; Echavarren, A. M., Proton Abstraction Mechanism for the Palladium-Catalyzed Intramolecular Arylation. J. Am. Chem. Soc. 2006, 128, 1066-1067; (c) Lafrance, M.; Fagnou, K., Palladium-Catalyzed Benzene Arylation: Incorporation of Catalytic Pivalic Acid as a Proton Shuttle and a Key Element in Catalyst Design. J. Am. Chem. Soc. 2006, 128, 16496-16497; (d) García-Cuadrado, D.; de Mendoza, P.; Braga, A. A. C.; Maseras, F.; Echavarren, A. M., Proton-Abstraction Mechanism in the Palladium-Catalyzed Intramolecular Arylation: Substituent Effects. J. Am. Chem. Soc. 2007, 129, 6880-6886; (e) Gorelsky, S. I.; Lapointe, D.; Fagnou, K., Analysis of the Concerted Metalation-Deprotonation Mechanism in Palladium-Catalyzed Direct Arylation Across a Broad Range of Aromatic Substrates. J. Am. Chem. Soc. 2008, 130, 10848-10849; (f) Ackermann, L.; Vicente, R.; Althammer, A., Assisted Ruthenium-Catalyzed C-H Bond Activation: Carboxylic Acids as Cocatalysts for Generally Applicable Direct Arylations in Apolar Solvents. Org. Lett. 2008, 10, 2299-2302; (g) Sun, H.-Y.; Gorelsky, S. I.; Stuart, D. R.; Campeau, L.-C.; Fagnou, K., Mechanistic Analysis of Azine N-Oxide Direct Arylation: Evidence for a Critical Role of Acetate in the Pd(OAc), Precatalyst. J. Org. Chem. 2010, 75, 8180-8189; (h) Wedi, P.; Farizyan, M.; Bergander, K.; Mück-Lichtenfeld, C.; van Gemmeren, M, Mechanism of the Arene-Limited Nondirected C-H Activation of Arenes with Palladium. Angew. Chem. Int. Ed. 2021, 60, 15641-15649. For a selected example of C-H activation reaction that proceed through a IES mechanism, see: (i) Oxgaard, J.; Tenn, W. J.; Nielsen, R. J.; Periana, R. A.; Goddard, W. A., Mechanistic Analysis of Iridium Heteroatom C-H Activation: Evidence for an Internal Electrophilic Substitution Mechanism. Organometallics 2007, 26, 1565-1567. For a selected example of C-H activation reaction that proceed through an eCMD mechanism, see: (j) Wang, L.; Carrow, B. P., Oligothiophene Synthesis by a General C-H Activation Mechanism: Electrophilic Concerted Metalation-Deprotonation (eCMD). ACS Catal. 2019, 9, 6821-6836.

- 21. Recently, Macgregor and Davies observed that electronic subsituent effects depend on whether the reaction is under kinetic or thermodynamic control. Under kinetic control, electron-rich arenes react faster and under thermodynamic control the products with electron withdrawing substituents are preferred. In our competitions experiments, we found the same electronic substituent effect independently of the conditions used. Alharis, R. A.; McMullin, C. L.; Davies, D. L.; Singh, K.; Macgregor, S. A., The Importance of Kinetic and Thermodynamic Control when Assessing Mechanisms of Carboxylate-Assisted C-H Activation. J. Am. Chem. Soc. 2019, 141, 8896-8906.
- 22. For selected examples of C-H activation reaction that proceed through a BIES mechanism, see: (a) Ma, W.; Mei, R.; Tenti, G.; Ackermann, L., Ruthenium(II)-Catalyzed Oxidative C-H Alkenylations of Sulfonic Acids, Sulfonyl Chlorides and Sulfonamides. Chem. Eur. J. 2014, 20, 15248-15251; (b) Liu, W.; Richter, S. C.; Zhang, Y.; Ackermann, L., Manganese(I)-Catalyzed Substitutive C-H Allylation. Angew. Chem. Int. Ed. 2016, 55, 7747-7750; (c) Zell, D.; Bursch, M.; Müller, V.; Grimme, S.; Ackermann, L., Full Selectivity Control in Cobalt(III)-Catalyzed C-H Alkylations by Switching of the C-H Activation Mechanism. Angew. Chem. Int. Ed. 2017, 56, 10378-10382; (d) Raghuvanshi, K.; Zell, D.; Ackermann, L., Ruthenium(II)-Catalyzed C-H Oxygenations of Reusable Sulfoximine Benzamides. Org. Lett. 2017, 19, 1278-1281; (e) Bu, Q.; Rogge, T.; Kotek, V.; Ackermann, L., Distal Weak Coordination of Acetamides in Ruthenium(II)-Catalyzed C-H Activation Processes. Angew. Chem. Int. Ed. 2018, 57, 765-768; (f) Liang, Y.-F.; Yang, L.; Rogge, T.; Ackermann, L., Ruthenium(IV) Intermediates in C-H Activation/Annulation by Weak O-Coordination. Chem. Eur. J. 2018, 24, 16548-16552; (g) Ma, W.; Weng, Z.; Rogge, T.; Gu, L.; Lin, J.; Peng, A.; Luo, X.; Gou, X.; Ackermann, L., Ruthenium(II)-Catalyzed C-H Chalcogenation of Anilides. Adv. Synth. Catal. 2018, 360, 704-710; (h) Sk, M. R.; Bera, S. S.; Maji, M. S., Cp*Co(III)-Catalyzed C-H Alkenylation of Aromatic Ketones with Alkenes. Adv. Synth. Catal. 2019, 361, 585-590.
- 23. For examples of electrophilic aromatic substitution reaction that provide small KIE, see and references therein: (a) Zollinger, H., Hydrogen Isotope Effects in Aromatic Substitution Reactions. In Adv. Phys. Org. Chem., Gold, V., Ed. Academic Press: 1964; Vol. 2, pp 163-200. For a selected example of C–H activation reaction that proceed through an electrophilic aromatic metalation mechanism with a small KIE, see: (b) Park, C.-H.; Ryabova, V.; Seregin, I. V.; Sromek, A. W.; Gevorgyan, V., Palladium-Catalyzed Arylation and Heteroarylation of Indolizines. Org. Lett. 2004, 6, 1159-1162. For selected examples of C-H activation reaction that proceed through an electrophilic aromatic metalation mechanism with large KIE, see: (c) Engle, K. M.; Wang, D.-H.; Yu, J.-Q., Ligand-Accelerated C-H Activation Reactions: Evidence for a Switch of Mechanism. J. Am. Chem. Soc. 2010, 132, 14137-14151; and ref 17a.
- 24. The DFT calculations were carried out with the Gaussian16 software, using M06IEFPCM/ def2tzvpp energies on B3LYP/6-31G(d,p)(Pd,SDD) optimized structures. For more details, see SI.
- 25. (a) Haies, B. E.; Berry, J. F.; Yu, J. Q.; Musaev, D. G. Factors Controlling Stability and Reactivity of Dimeric Pd(II) Complexes in C-H Functionalization Catalysis ACS Catal. 2016, 6, 829-839; (b) Yang, Y.-F.; Hong, X.; Yu, J.-Q.; Houk, K. N. Experimental-Computational Synergy for Selective Pd(II)-Catalyzed C-H Activation of Aryl and Alkyl Groups Acc. Chem. Res. 2017, 60, 2853-2860; (c) Gair, J. J.; Haines, B. E.; Filatov, A. S.; Musaev, D. G.; Lewis, J. C. Mono-N-protected amino acid ligands stabilize dimeric palladium(II) complexes of importance to C-H functionalization Chem. Sci. 2017, 8, 5746-5756; (d) Davies, D. L.; Macgregor, S. A.; McMullin, C. L. Computational Studies of Carboxylate Assisted C–H Activation and Functionalization at Group 8-10 Transition Metal Centers. Chem. Rev. 2017, 117, 8649-8709.
- 26. Zhang, Z.; Wang, Z. Diatomite-Supported Pd Nanoparticles: An Efficient Catalyst for Heck and Suzuki Reactions. J. Org. Chem. 2006, 71 (19), 7485-7487.
- 27. Kubota, A.; Emmert, M. H.; Sanford, M. S. Pyridine Ligands as Promoters in Pd II/0 -Catalyzed C-H Olefination Reactions. Org. Lett. 2012, 14 (7), 1760-1763.

Appendices

For detailed supplementary information: Naksomboon, K.; Gómez-Bengoa, E.; Mehara, J.; Roithová, J.; Otten, E.; Fernández-Ibáñez, M. Á. Mechanistic Studies of the Palladium-Catalyzed S,O-Ligand Promoted C–H Olefination of Aromatic Compounds. *Chem. Sci.* **2023**, *14* (11), 2943–2953.

It can be accessed via https://doi.org/10.34973/pdan-6826 upon request of the promotor or the IMM data steward.

Mass spectrometric measurements

The mass spectra were recorded on a linear ion trap (LTQ) instrument with an electrospray ionization (ESI) source. General conditions used were as follows: 4 to 5 kV spray voltage, 200 to 275 °C capillary temperature and 1 to 20 psi sheath gas. For positive mode, 0 to 20 V capillary voltage and 25 to 70 V tube lens while for the negative mode 0 to -20 V capillary voltage and -25 to -75 V tube lens.

Energy resolved collision induced dissociation (CID) experiments were performed on LCQ Deca mass spectrometer with an ESI source. The calibration was performed using the thermometer ions using the Schroder's method to correlate the collision energy and the appearance energies of the ions.

In general, 1 mM fresh stock solution was prepared in the desired solvent (sonication used if turbidity observed followed by filtration, filtrate used). From these stock solutions after mixing/addition, by appropriate dilution with the desired solvent final concentration of 50 to 200 μ M was injected directly into the ESI–MS inlet with the help of a silica capillary using the nitrogen overpressure in the vial.

[Pd(L-H)(PPh₂Ph^{so3})OAc]Na i.e. the negatively charge tagged analog of 'complex 2' was synthesized according to the "Procedure for the synthesis of complex 2" described above with the exception that instead of triphenylphosphine, 3-(Diphenylphosphino)benzenesulfonic acid sodium salt i.e. PPh₂Ph^{so3}Na was used and dark yellowish solid of [Pd(L-H)(PPh₂Ph^{so3})OAc]Na was obtained. This was then used further for mass spectrometry analysis.

High resolution mass spectra were recorded with a timsTOF instrument from Bruker Daltonik (Bremen, Germany) equipped with ESI source. Calibration was performed using Agilent ESI low concentration tune mix before the experiment. The sample and the calibrant solutions were injected in the timsTOF using a glass syringe

pump with 0.5 mL volume and flow rate of 0.3 µL. The timsTOF was operated in the negative ion mode in a mass range of m/z 50 to 1500 with spray voltage of 4.5 kV. The end plate offset of -500 V with a N₂ nebulizer pressure of 0.3 bar and a dry gas flow of 1.5 L min⁻¹ at 275 °C.

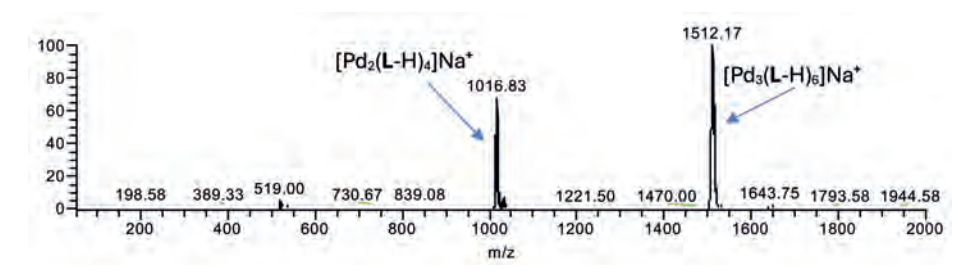


Figure S1. ESI mass spectrum (positive mode) of a mixture of Pd(OAc), and L2 in benzene and ethyl acetate.

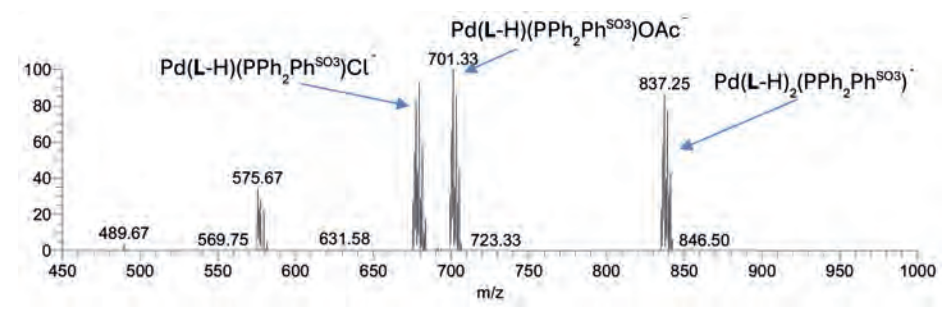


Figure S2. ESI mass spectrum (negative mode) of a mixture of Pd(OAc)₂, L2, (PPh₂Ph^{5O3-})Na and acetic acid in benzene and deuterated benzene.

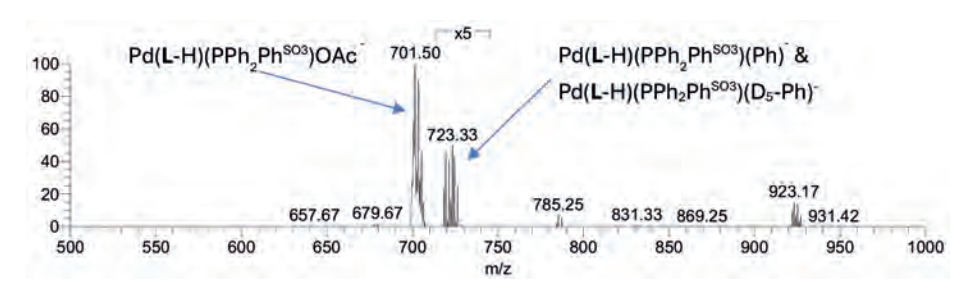


Figure S3. ESI mass spectrum (negative mode) of [Pd(L-H)(PPh,PhSO3)OAc]Na in benzene and deuterated benzene (heated for 5min at 80°C and filtered, filtrate injected).

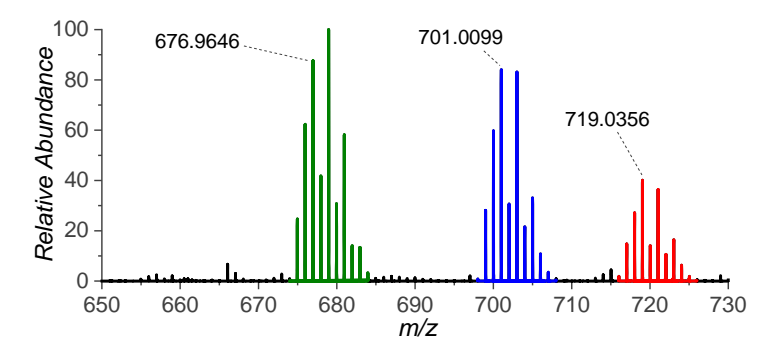


Figure S4. High resolution mass spectrum (negative mode) of $[Pd(L-H)(PPh_2Ph^{SO3})OAc]Na$ in benzene and DCM (heated for 5min at 60°C and filtered, filtrate injected); $[(PPh_2Ph^{SO3})Pd(L2-H)(X)]^-$ ions highlighted, where X = CI (m/z 677, green), AcO (m/z 701, blue), or Ph (m/z 719, red).

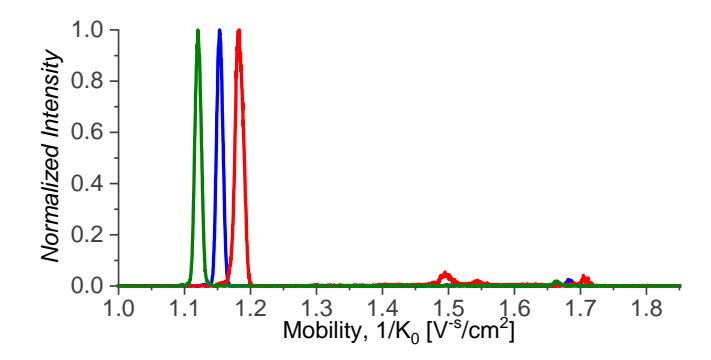


Figure S5. Mobilogram of $[(PPh_2Ph^{SO3-})Pd(L2-H)(X)]^-$, where X = CI (m/z 677, green), AcO (m/z 701, blue), or Ph (m/z 719, red). Note that the minor peaks at the higher values of mobility originate from fragmentations of larger clusters; i.e., they do not correspond to isomers of the monopalladium complexes.

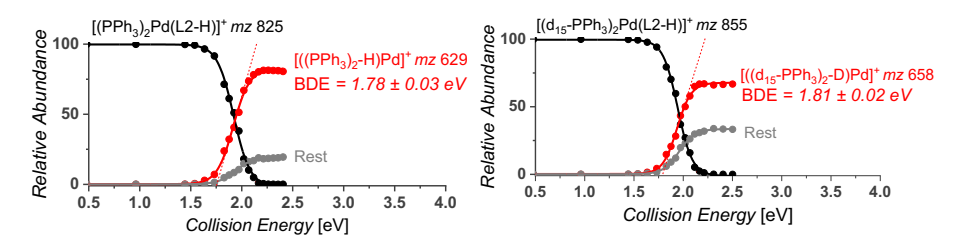


Figure S6. Energy resolved CID of $[(PPh_z)_2Pd(L2-H)]^+$ m/z=825 (left) and $[(P(C_5D_5)_3)_2Pd(L2-H)]^+$ *m/z*=855 (right).

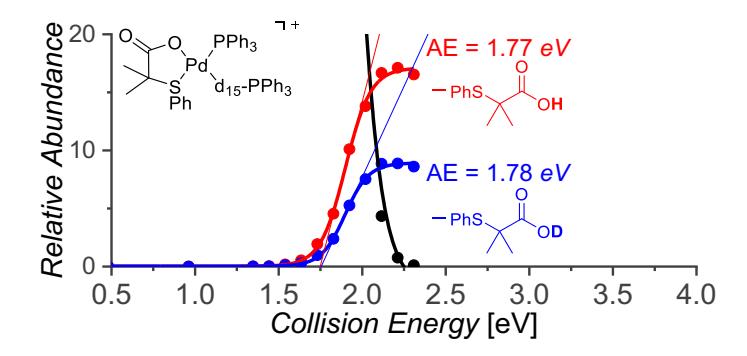


Figure S7. Energy resolved CID of $[(PPh_3)(d_{15}-PPh_3)Pd(L2-H)]^+ (m/z=840)$.

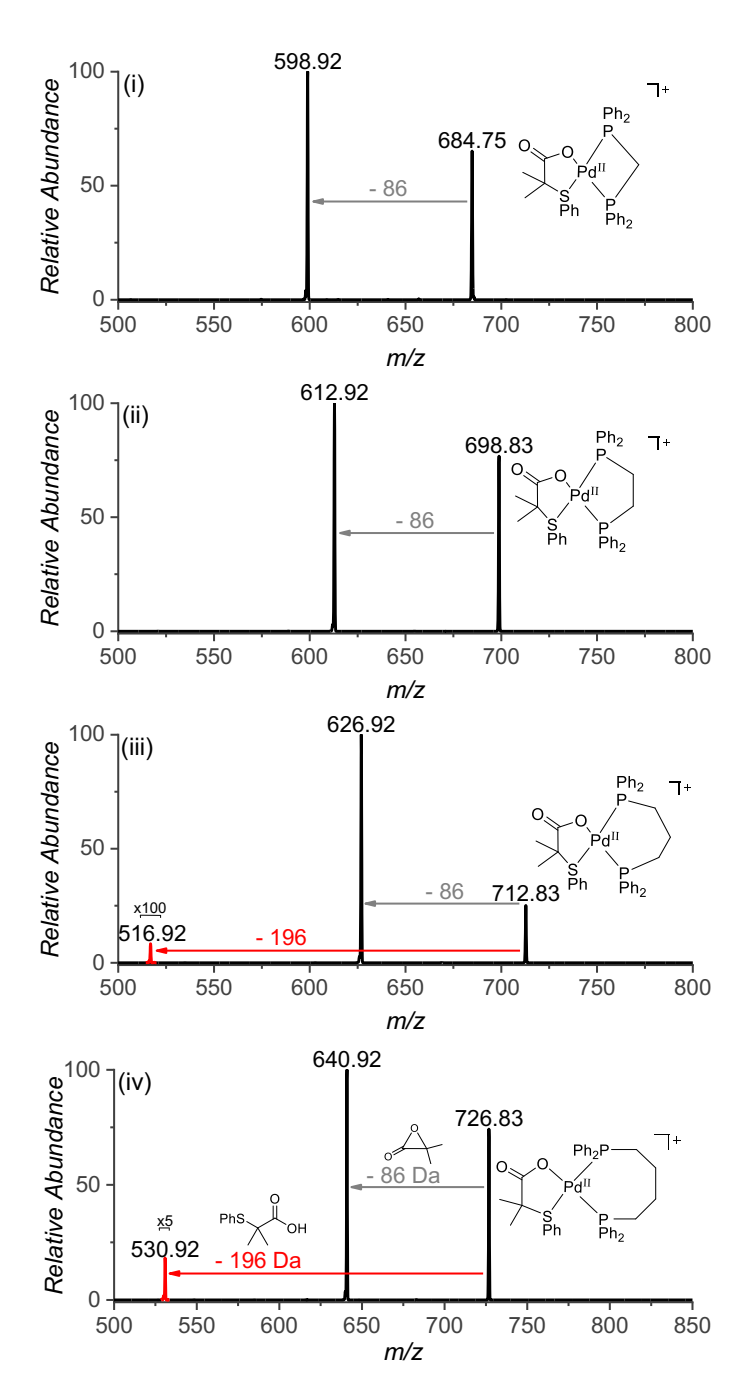


Figure S8. CID mass spectra of (i) $[(dppm)Pd(L2-H)]^+$ (m/z=685), (ii) $[(dppe)Pd(L2-H)]^+$ (m/z=699), (iii) $[(dppp)Pd(L2-H)]^+$ (m/z=713) and (iv) $[(dppb)Pd(L2-H)]^+$ (m/z=727).



Chapter 5

Cationic Gold(II) Complexes: Experimental and Theoretical Study

The work in this chapter is published: <u>Mehara, J.</u>; Koovakattil Surendran, A.; van Wieringen, T.; Setia, D.; Foroutan-Nejad, C.; Straka, M.; Rulíšek, L.; Roithová, J. Cationic Gold(II) Complexes: Experimental and Theoretical Study**. *Chem. – A Eur. J.* **2022**, *28* (60), e202201794.

Mass spectrometric, Electrochemical and Ion Spectroscopic studies.

Gold(II) complexes are rare, and their application to the catalysis of chemical transformations is underexplored. The limited application of gold(II) complexes in catalysis is primarily attributed to their facile oxidation or reduction processes, resulting in the formation of more stable gold(III) or gold(I) complexes, respectively. This chapter delves into the exploration of the formation of [Au^{II}(L)(X)]⁺ complexes (L=ligand, X=halogen) from the corresponding gold(III) precursors and investigated their stability and spectral properties in the IR and visible range in the gas phase. The results show that the best ancillary ligands L for stabilizing gaseous [Au^{II}(L)(X)]⁺ complexes are bidentate and tridentate ligands with nitrogen donor atoms. The electronic structure and spectral properties of the investigated gold(II) complexes were correlated with quantum chemical calculations. The results show that the molecular and electronic structure of the gold(II) complexes as well as their spectroscopic properties are very similar to those of analogous stable copper(II) complexes.

Introduction

Gold(I) and gold(III) complexes have an important place in the field of metal catalysis.¹⁻⁹ Gold(I) complexes are mainly used for the activation of multiple bonds towards additions and subsequent cascade reactions¹⁰, whereas gold(III) complexes have been utilized as catalysts in various coupling reactions.^{11–15} Conversely, reports on gold(II) chemistry are sparse. 16-22 The gold(II) complexes are usually unstable and tend to disproportionate to the gold(I) and gold(III) complexes.²³ The destabilization of the gold(II) oxidation state is due to the relativistic effects^{24,25} which are responsible for an expansion and energy destabilization of the 5d shell and contraction of the 6s electron shell.^{24,26} As a result, the contribution of the 5d electrons to the valence shell increases. The ionization of 5d electrons is then associated with the Jahn-Teller distortion, leading to a large energy splitting of the d_{z2} and $d_{x2\cdot y2}$ energy levels. Thus, gold is easily ionized to the gold(III) state with all electrons paired.27

Heinze and co-workers reported a series of stable monomeric gold(II) complexes supported by porphyrin ligands.^{20,28,29} The preparation of the gold(II) complexes relied on the reduction of the corresponding gold(III) precursors. In order to avoid the subsequent reduction to gold(I), the authors used cobaltocene ($E_{\nu} = -1.3 \text{ V } vs$ Fc/Fc⁺ couple) which matched the redox potential for the first reduction potential of the gold(III) porphyrin complex.²⁰ The only reactivity of prepared gold(II) complexes studied so far was based on electron transfer processes.²⁰ However, they were suggested as intermediates in several reactions involving radical chemistry. 15,30 The reactions beyond the electron transfer require a labile coordination site at the gold(II) complexes that could coordinate reactive molecules or radicals. Therefore, we aimed at exploring the generation and properties of gold(II) complexes with bidentate and tridentate ligands.

Previous electrochemical experiments with analogous complexes showed that the reduction of gold(III) complexes often leads directly to the gold(I) complexes or that the $Au^{II} \rightarrow Au^{I}$ and $Au^{I} \rightarrow Au^{I}$ potentials are very close and therefore the steps are difficult to separate.31-34 In such a situation, where the properties of reactive complexes cannot be properly studied in solution, isolation of these species in the gas phase can extend their lifetime and thus allow a detailed study albeit in vacuum.^{35,36} This approach permitted an exploration of the chemistry of metal complexes in unusual oxidation states or even in the oxidation states that cannot be prepared in a condensed phase.³⁷ In addition, previous DFT calculations suggested that the gold(II) complexes are more stable in the gas phase than in the solution.²³

Herein, we present a gas-phase study of the intrinsic properties of gaseous gold(II) complexes with bidentate and tridentate ligands. We generated the gold(II) complexes from their gold(III) precursors and explored how various common ligands stabilize the unusual oxidation state. We have characterized the generated gold(II) complexes with gas-phase ion spectroscopy. Benchmarked to the experiment, we have also investigated their structure and spectroscopic properties by DFT calculations.

Table 1. Fragmentation of [Au^{III}(Ligand)(X)₂]⁺ complexes.^{a,b}

Branching of fragmenta	ation	s pathways ^b		
		Reaction 1	Reaction 2	Reaction 3
Ligand	Χ	$[Au^{II}(L)(X)]^{+} + X^{\bullet}$	$[Au^{l}(L)]^{+} + X_{2}$	$[Au^{II}(L-H)(X)]^+ + HX$
Pyridine	Cl	-	18%	66%
Pyridine	Br	-	94%	-
TMEDA	Cl	13%	-	8%
TMEDA	Br	98%	-	2%
2,2'-bipyridine	Cl	93%	6%	-
2,2'-bipyridine	Br	100%	-	-
2,2'-bipyridine	1	99%	-	-
1,10-phenanthroline	Cl	93%	7%	-
1,10-phenanthroline	Br	100%	-	-
2,2':6',2"-terpyridine	Cl	85%	14%	-
2,2':6',2"-terpyridine	Br	96%	2%	-
PPh ₃	Cl	Precursor comp	lex [Au ^{III} (PPh ₃) ₂ (0	Cl) ₂] ⁺ not observed
PPh ₃	Br	Precursor comp	lex [Au ^{III} (PPh ₃) ₂ (I	Br) ₂] ⁺ not observed
Ph ₂ P-(CH ₂)-PPh ₂ (dppm)	Cl	Precursor comp	lex [Au ^{III} (dppm)	(CI) ₂] ⁺ not observed
Ph ₂ P-(CH ₂)-PPh ₂ (dppm)	Br	Precursor comp	lex [Au ^{III} (dppm)	(Br) ₂] ⁺ not observed
Ph ₂ P-(CH ₂) ₂ -PPh ₂ (dppe)	Cl	-	-	2%
Ph ₂ P-(CH ₂) ₂ -PPh ₂ (dppe)	Br	63%	-	-
Ph ₂ P-(CH ₂) ₃ -PPh ₂ (dppp)	Cl	-	-	5%
Ph ₂ P-(CH ₂) ₃ -PPh ₂ (dppp)	Br	8%	16%	-
Ph ₂ P-(CH ₂) ₄ -PPh ₂ (dppb)	Cl	-	-	15%
Ph ₂ P-(CH ₂) ₄ -PPh ₂ (dppb)	Br	Precursor comp	lex [Au ^{III} (dppb)(l	Br) ₂]+ not observed
Phenylpyridine	Cl	Precursor compl [Au ^{III} (phenylpyri		nylpyridine) ₂ (Br) ₂]+ or ot observed
Thiophene	Br	Precursor comp	lex [Au ^{III} (thioph	ene) ₂ (Br) ₂] ⁺ not observed
2,2'-Bithiophene	Br	Precursor comp	lex [Au ^{III} (2,2'-thi	ophene)(Br),] ⁺ not observed

[[]a] The complexes were generated from an acetonitrile and dichloromethane solution of the AuX₃ salt (0.1 mM) and the ligand (0.1 mM), achieving a final concentration of 100 µM.

[[]b] The fragmentations were investigated at collision energies of 1.9 – 3.9 eV

Other
 (specification of the fragment(s))
16% (X ₂ ;pyridine loss) : complex reduced to gold(I)
6%
79% ([Au(H)(Cl) ₂] loss)
-
1%
-
1%
-
-
1%
2%
98% (loss of PhCl & subsequent ligand degradation)
37% (loss of PhBr & subsequent ligand degradation)
95% (subsequent ligand degradation)
76% (subsequent ligand degradation)
85% (loss of 2x HCl & subsequent ligand degradation)

Results

Generation of the gaseous complexes

Our aim has been to explore the properties in terms of thermodynamic stability and spectral properties in IR/VIS range of cationic gold(II) complexes in the gas phase. We envisaged that the easiest general way of generation of these complexes could start from the $[Au^{()}(L)_{\alpha}(X)_{\alpha}]^{+}$ precursors (n = 1 for bidentate ligands and n = 2)for monodentate ligands such as pyridine and PPh₂) that might be prone to lose a halogen radical and thereby form the desired $[Au^{II}(L)_{,x}(X)]^{+}$ complexes (Reaction 1). In the study of the gold(III) complexes, we indeed observed this reaction path. However, we also observed competing reactions leading to the reduction of the complex to gold(I) (Reaction 2) or to the degradation of the gold(III) complex (Reaction 3).

$$[Au^{||}(L)(X)_{2}]^{+} \rightarrow [Au^{||}(L)(X)]^{+} + X^{*}$$
 (1)

$$[Au^{|||}(L)(X)_{2}]^{+} \rightarrow [Au^{||}(L)]^{+} + X_{2}$$
 (2)

$$[Au^{|||}(L)(X)_{2}]^{+} \rightarrow [Au^{|||}(LH)(X)]^{+} + HX$$
 (3)

We have tested the fragmentations of $[Au^{\parallel}(L)_{\alpha}(X)_{\alpha}]^{+}$ with a series of monodentate-, bidentate- and tridentate ligands with N, P, and S coordinating atoms (Table 1). The monodentate ligands do not support the desired formation of gold(II) complexes. The reason stems from the coordination flexibility of the monodentate ligands in the coordination sphere of the gold atom. The gold(III) precursors were formed in a square planar geometry 14,38,39 with the $[Au^{III}(\eta^1-ligand)_2(X)_2]^+$ speciation. These complexes can easily eliminate the dihalogen molecule (X₂) because the resulting [Au^I(η¹-ligand)₂]⁺ can attain the favoured linear arrangement of the two n¹-ligands and thereby make Reaction 2 favoured.33,40-44 Dicationic gold(II) complexes with neutral monodentate ligands can be generated in the gas phase by reaction of gold atoms with neutral ligands and subsequent electron ionization of the complex. Properties of the $[Au^{\parallel}(\eta^{1}-ligand)_{n}]^{2+}$ generated in this way were studied previously.45,46

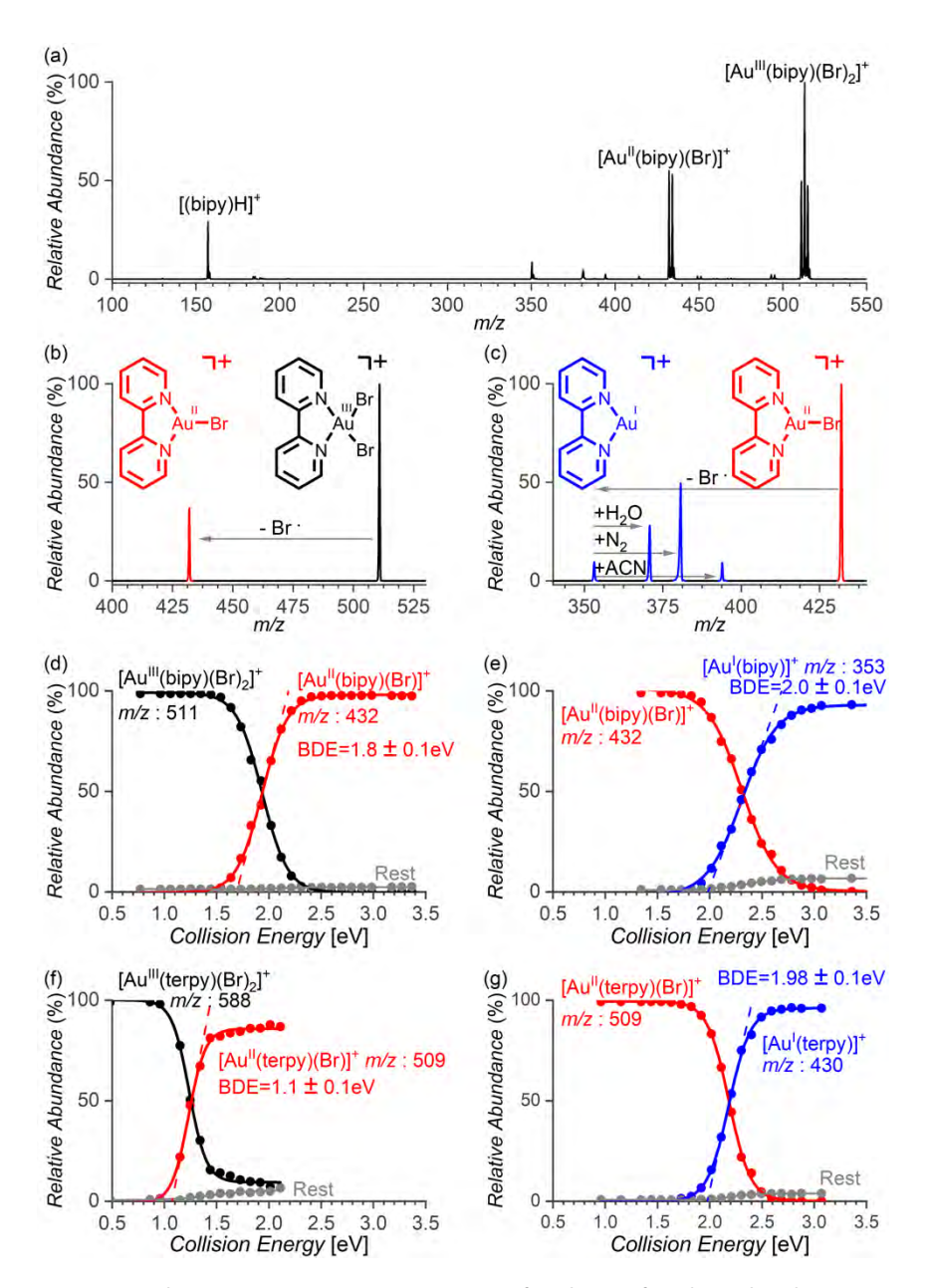


Figure 1. (a) Electrospray ionization mass spectrum of a solution of 2,2'-bipyridine (bipy, 100 µM) and AuBr₃ (100 μM) in ACN. (b) Collision induced dissociation (CID) spectrum of mass-selected [Au^{III}(bipy) (Br),]+ (m/z 511) at the collision energy of 1.9 eV. (c) CID spectrum of mass-selected [Au^{II}(bipy)(Br)]+ (m/z 432) at the collision energy of 2.4 eV. (d,e) Integrated abundances of the peaks in the energyresolved CID spectra of the ions with m/z 511 and m/z 432, respectively. (f,q) Integrated abundances of the peaks in the energy-resolved CID spectra of [Au^{III}(terpy)(Br)]⁺ (m/z 588) and [Au^{II}(terpy)(Br)]⁺ (m/z 509), respectively. The extrapolation of the onset of the fragmentation provides the bond dissociation energy (BDE) for the given fragmentation.

On the contrary, the bidentate ligands do support the formation of gold(II) complexes. The gold(III) precursors were formed with the [Au^{III}(n²-Ligand)(X)_a]⁺ speciation.⁴⁷ Fragmentation of the gold(III) precursors with N,N'-bidentate ligands led almost exclusively to the elimination of a halogen radical and thus to the formation of the desired [Au^{II}(n²-ligand)(X)]⁺ complexes (Reaction 1, Figure 1b). In comparison, phosphine-based ligands are less suitable for the generation of gold(II) complexes because they get easily oxidised in the presence of the gold(III) salts. Accordingly, next to the desired gold(III) precursors with the bis-phosphine ligands (P,P'-Ligands), we have always observed gold(I) complexes with the bis-phosphineoxide ligands. Nevertheless, we have detected a fraction of the desired [Au^{III}(P,P'-Ligand)(X)_a]⁺ precursors with the bis-diphenylphosphine ethylene (dppe) and propylene (dppp) ligands and therefore we could explore the possibility to form the gold(II) complexes.⁴⁸ The desired reaction 1 occurred only for complexes with X = Br; hence, we observed the formation of [Au^{II}(dppe)(Br)]⁺ and [Au^{II}(dppp)(Br)]⁺. The competing reactions led generally to the reduction of the complexes to the gold(I) state and to a degradation of the ligands (see Table 1). The bis(diphenylphosphino) methane (dppm) ligand with a smaller bite angle provided directly just gold(I) complexes. We also tested sulphur-based ligands but were unable to prepare the desired gold(III) precursor complexes.

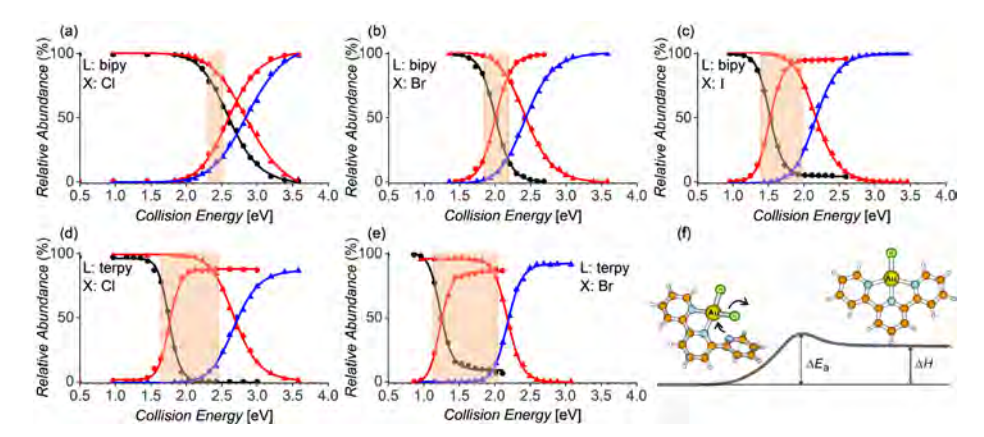


Figure 2. Energy-resolved CID curves for dissociation of $[Au^{III}(L)(X)_2]^+$ (black) to $[Au^{II}(L)(X)]^+$ (red) and $[Au^{II}(L)(X)]^+$ (red) to $[Au^{II}(L)]^+$ (blue); L = bipy (a to c) and terpy (d,e); X = CI (a,d), Br (b,e) and I (c). The orange region depicts the energy window for the possible generation of the gold(II) complexes. The window starts when 20% of the gold(III) complexes fragmented to the gold(II) complexes and stops when 20% of the gold(II) complexes fragmented to the gold(I) complexes. (f) Schematic potential energy profile for elimination of CI from $[Au^{III}(terpy)CI_2]^+$; the depicted structures are optimized at the B3LYP-D3BJ/6-311* $G^{**}/SDD(Au)$ level of theory.

	-				-	11	
		[Au ^{III} (L)(X) ₂]+	[Au"(L)(X)]+ X	[Au ^{II} (L)(X)]+-	→ [Au¹(L)]+ + X·		
X	L	BDE _{exp} [a] [kJ mol ⁻¹]	BDE _{theor} [b] [kJ mol ⁻¹]	BDE _{exp} [a] [kJ mol ⁻¹]	BDE _{theor} [b] [kJ mol ⁻¹]	Δ <i>BDE</i> _{exp} [kJ mol ⁻¹]	Δ <i>BDE</i> _{theor} [kJ mol ⁻¹]
Cl	bipy	213 ± 1	225	229 ± 2	244	16	19
Br	bipy	169 ± 5	199	196 ± 4	231	27	32
1	bipy	128 ± 2	174	177 ± 2	221	49	47
Cl	terpy	155 ± 3	131	226 ± 1	232	71	101
Br	terpy	108 ± 6	113	191 ± 1	210	83	97
		$[Au^{\scriptscriptstyle{ }}(L)(X)]^{\scriptscriptstyle{2+}}\!\rightarrow$	$[Au^{II}(L)]^{2+} + X^{\cdot}$				
Cl	terpy	185 ± 4	259				
Br	terpy	165 ± 4	237				

Table 2. Experimental^a and theoretical^b bond dissociation energies of [Au(L)(X)] + complexes (n = 1 or 2).

Finally, we tested the same approach with a N,N',N"-tridentate ligand (1²,2²:2⁶,3²-terpyridine, terpy in the following). The precursor gold(III) complexes had a [Au^{III}(terpy)(X)]⁺ speciation. As the gold(III) complexes prefer square planar coordination and the complex retains two halogen ligands, the terpy ligand initially coordinates probably only as a bidentate ligand. The complex easily eliminates one of the halogen atoms and forms [Au"(terpy)(X)]⁺. Presumably, the ligand changes the coordination mode and fills in the vacant coordination site after the elimination of X. For more detailed information, we studied bond dissociation energies (BDEs) for the halogen eliminations.

Energetics of gold(II) complex formations and fragmentations

A comparison of the results for various complexes suggests that the bromido ligands are more suitable for the generation of the gold(II) complexes than the chlorido ligands. We have investigated this in a more detail using complexes with the 2,2'-bipyridine ligand and we have also included the iodido precursors. The aim was to determine the span of the energies that are sufficient to induce the reduction from $[Au^{\parallel}(bipy)(X)_{3}]^{+}$ to $[Au^{\parallel}(bipy)(X)]^{+}$, but insufficient to induce the second reduction step from [Au^{II}(bipy)(X)]⁺ to [Au^I(bipy)]⁺ (Figure 2, Table 2). Note that the gold(III) iodine complexes easily undergo a disproportionation reaction.^{49,50} Therefore, we had to generate the [Au(bipy)(I)₃]⁺ complexes in situ by the Finkelstein reaction^{51,52} from the corresponding chloride complex and sodium iodide.

[[]a] The experimental values were determined from energy-resolved CID experiments.

[[]b] The theoretical values were calculated by Gaussian 16: B3LYP-D3BJ/6-311+G** level with SDD/SDD-ECP on Au and 6-311G** on I. See also Table S1 for results obtained at the PBE0-D3/def2TZVPP level of theory. These results show the same trend, but overestimate the binding energies even more.

The energy demands for the reduction reactions were determined from energy-resolved collision induced dissociation experiments with mass-selected [Au^{III}(bipy) $(X)_2$]⁺ and [Au^{III}(bipy)(X)]⁺ (Figure 1 and Figure 2). The extrapolation of the energy-dependent relative fragmentation cross-section for the elimination of the halogen atom provides the experimental Au-X bond-dissociation energy (see the Experimental Details). The energy difference between the energy demands for the Au^{III} \rightarrow Au^{II} and Au^{III} \rightarrow Au^{II} reductions decrease in the order of X: I > Br > CI (Table 2). Hence, the iodido complexes provide the largest interval of energies that allow the formation of the gold(II) complexes from their gold(III) precursors. However, with respect to the low stability of the gold(III) iodido precursors, the bromido complexes are probably the best candidates for studying gold(II) complexes in the gas phase.

We have also studied *BDEs* for the complexes with the tridentate ligand terpy and X = CI and Br. The dominant gold(III) complexes detected from the solution correspond to the $[Au^{III}(terpy)(X)]^{2+}$ dications. The energy required for the formation of $[Au^{III}(terpy)]^{2+}$ is slightly smaller than that for the formation of $[Au^{III}(terpy)]^{2+}$ (the bottom of Table 2). This attests that a pyridine type ligand better stabilizes the +II oxidation state of gold than the chlorido ligand. Interestingly, this trend is not caught by the DFT calculations (see also below).

The gold(III) complexes with the terpy ligand and two chlorido ligands, [Au^{III}(terpy) $(X)_2$]⁺, can have two possible structures. The first structure can have a square planar arrangement of the halogen ligands and two pyridine units (N-N-X-X, see Figure 2f). The alternative structure can have one halogen and three pyridine units coordinated to the gold centre in the plane (N-N-N-X) and the remaining halogen above the plane. According to DFT calculations, the latter structure lies ~48 kJ mol⁻¹ higher in energy for $[Au^{III}(terpy)(CI)_2]^+$ and could not have been localized for $[Au^{III}(terpy)(Br)_2]^+$ (see Figure S29). Hence, we conclude that the recombination of $[Au^{III}(terpy)(X)]^{2+}$ and X^- during the transfer to the gas phase proceeds via a pyridine-to- X^- replacement in the square planar arrangement.

The analysis of the fragmentation energetics shows that the binding energies of the halogens in the $[Au^{III}(terpy)(X)_2]^+$ complexes are more than 60 kJ mol⁻¹ smaller than in $[Au^{III}(bipy)(X)_2]^+$. The reason probably stems from the assistance of one of the pyridine units in the elimination of the halogen radical (see Figure 2f). The binding energies of the halogen atoms in the gold(II) complexes $[Au^{II}(terpy)(X)]^+$ remain very close to those in $[Au^{II}(bipy)(X)]^+$. Table 2 shows a comparison of the experimental *BDE*s and the computed values (B3LYP-D3BJ/6-311+G**, SDD/SDD ECP on Au and 6-311G** on I). The theoretical calculations overestimate the bond

dissociation energies. In the exploratory calculations, we have found out that the overestimation is even larger if we use larger basis sets and if we (correctly) include the spin-orbit coupling and non-scalar relativity (X2C). We will investigate the origin of this peculiar effect in a large benchmarking study of the theoretical methods in future. For the purpose of this study, we will evaluate the relative trends (1st vs 2nd dissociation; CI/Br/I ligands) that are reasonably reproduced irrespective of various methodological ingredients.

The theoretical results show in agreement with the experiment that the gold(II) complexes are better stabilized with heavier halogen ligands and that the tridentate ligand stabilizes the complex better than the bidentate ligand. The formation of the gold(II) complexes from $[Au^{III}(terpy)(X)_{3}]^{+}$ is about 60 kJ mol⁻¹ less energy-demanding than that from [Au^{III}(bipy)(X)₂]+. In theoretical calculations, this value is even higher and reaches 80 – 90 kJ mol⁻¹. The discrepancy is caused by the fact that we measure ΔE_{a} in the experiment, whereas we calculate ΔH in the theory (see Figure 2f). Typically, the simple bond cleavages are quazi-barrierless endothermic processes and therefore the measured activation energy corresponds to the reaction enthalpy of the bond cleavage process, i.e., to the bond dissociation energy (BDE). In the case of $[Au^{III}(terpy)(X)_{\alpha}]^+$, the starting complex has a pseudo square planar geometry around the gold centre formed by two pyridine units and the two halogen atoms (see the initial structure in Figure 2f). The third pyridine unit interacts only weakly with the gold ion. The X elimination proceeds via a transition structure in which the initially loosely bound pyridine unit coordinates to the gold centre. The measured activation energy thus corresponds to the barrier height of this process.

Electrochemistry experiments

The experiments determining bond dissociation energies of the gaseous complexes show that the window of the stability of the gold(II) complexes is rather narrow. It is sufficient to generate these complexes in the gas phase, but it remains a question, whether these complexes could be also studied in solution. In order to test this possibility, we have prepared the [Au(bipy)X₂]PF₆ and [Au(terpy)X](PF₆)₂ complexes and performed cyclic voltammetry (CV) experiments in dichloromethane (DCM) and dimethylformamide (DMF) solutions. We have selected DCM, because it is non-polar non-coordinating solvent and thus the conditions are closest to the gas phase experiments (Figure S14 & S16). Unfortunately, the terpy complexes were not soluble in DCM and therefore the comparison of all complexes was done in DMF.

Figure 3 shows a comparison of the reduction waves of the $[Au(bipy)(X)_2]PF_6$ and $[Au(terpy)(X)](PF_6)_2$ (X = CI or Br) complexes (X = CI or Br) in DMF under the same conditions. We show the range of the CVs with the reduction waves corresponding to the reduction of gold(III) to gold(I) complexes. This 2e-reduction process has been studied and discussed in detail for analogous complexes^{33,53,54} with the bipy and terpy type ligands previously. The whole range of the CV experiments with the assignment of the $Au^{III} \rightarrow Au^I$ and $Au^I \rightarrow Au^I$ transitions is in the Supporting Information (Figures S13, S15, S17- S23).

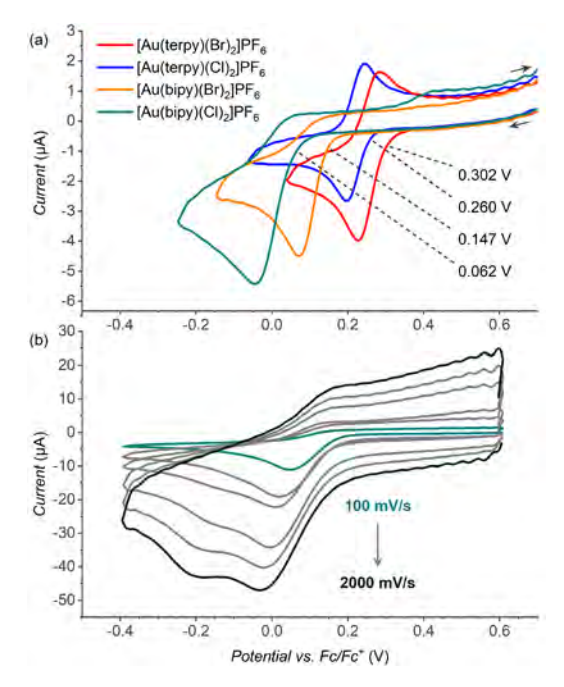


Figure 3. (a) Cyclic voltammogram of $[Au(bipy)(X)_2]PF_6$ and $[Au(terpy)(X)](PF_6)_2$ (X = Cl or Br) in dimethylformamide (0.25 mM) in the range of the $Au^{III} \rightarrow Au^{II}$ reduction potential (scan rate 100 mV s⁻¹). (b) Cyclic voltammogram of $[Au(bipy)(CI)_2]PF_6$ in dichloromethane (0.5 mM) at various scan rates (100, 300, 500, 1000, 1500 and 2000 mV s⁻¹).

The comparison of the $Au^{III} \rightarrow Au^I$ reductions waves for the studied complexes shows the trend of the shifts to more positive potentials in the order $[Au(terpy)(Br)]^{2+} > [Au(terpy)(CI)]^{2+}$ and $[Au(bipy)(Br)_2]^+ > [Au(bipy)(CI)_2]^+$. The reduction of the complexes with the terpy ligand is reversible, whereas the reduction of the complexes with the bipy ligand is irreversible. We have further tested, whether we could separate the 2e-reduction wave to the two one-electron reduction steps by increasing the CV scanning rate. The only successful separation was achieved for the [Au(bipy)]

(Cl)₂]+ complex (in DCM - Figure 3b and in DMF - Figure S20). With the increasing scanning rate, the reduction became partially reversible. This result suggests that the irreversibility is associated with the decomposition of the complex that is fast. We did not succeed in separation of the reduction steps for the bromide complexes which suggest that they decompose even faster than the chloride complexes.

Vibrational photodissociation spectra

Next, we investigated the spectroscopic properties in the infrared region for the $[Au^{II}(bipv)(X)]^+$ complexes (X = Cl and Br) in the gas phase and compared them with the analogous complexes of copper(II). While 2,2'-Bipyridine is usually not acting as a redox-active ligand, ⁵⁶ it can be redox active in some complexes. ^{57,58} In addition, some metals can activate a C-H bond of 2.2'-Bipyridine in a roll-over mechanism. 59,60 We have assumed that if the C-H activation reactivity or the redox reactivity would be important for the gold(II) complexes, then we should detect distinct signatures by vibrational and electronic spectroscopy of the mass-selected complexes. ^{61–64} For an easier interpretation, we compared all spectral features with those of analogous copper complexes.

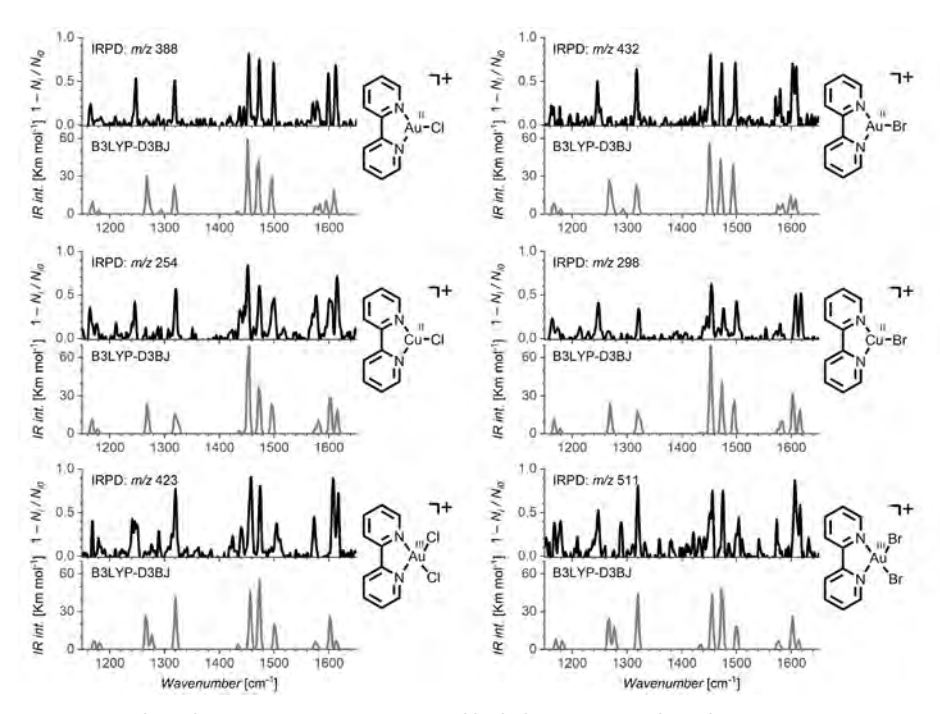


Figure 4. IR photodissociation spectra (measured by helium tagging photodissociation spectroscopy) of Au(III), Au(II) and Cu(II) complexes (black lines) and their comparison with theoretically predicted IR spectra (grey lines, calculated by B3LYP-D3BJ/6-311+G**(SDD on Au/Cu/Br), scaling factor: 0.98).

We measured IR spectra by helium tagging photodissociation method.⁶⁵ In the range of our OPO IR light source, the spectra show mostly only the vibrations of the bipy ligand (Figure 4). The comparison of gold and copper (M = Au or Cu) analogues of [M"(bipy)(Cl)]* and [M"(bipy)(Br)]* reveals that both metals interact with the ligand in the same way (compare the top IRPD spectra in both columns in Figure 4). The spectra do not reveal any significant differences. We also measured IR spectra of the gold(III) precursors (bottom IRPD spectra in Figure 4). The gold(III) complexes show a very similar fingerprint of the bipy ligands as the respective gold(II) complexes. The comparison of the experimental spectra with the IR spectra predicted by DFT (B3LYP-D3BJ⁶⁶ - the most frequently used functional in ion spectroscopy⁶⁷⁻⁶⁹ - in grey in Figure 4) shows a very good agreement. The agreement suggests that the DFT method describes well the interaction between gold(II) and the ligand as well as the overall geometry of the complex. The assignment of the vibrational bands is shown in Figure S26.

We have further measured the IRPD spectra of [Au(terpy)(Cl)₂]⁺ and [Au(terpy)(Cl)]²⁺ (Figures S29 and S31). They are very similar to the spectra of the bipy complexes. The spectra show the vibrations of the terpy ligand that are similar to those of the bipy ligand. The experimental spectrum of [Au(terpy)(CI)₂]⁺ better agrees with the theoretical spectrum of the more stable isomer of [Au(terpy)(Cl)₂]⁺ with the N-N-Cl-CI planar arrangement of the ligands, but the IR spectrum of the alternative highenergy isomer with the N-N-N-Cl arrangement of the ligands is rather similar (see Figure S29).

Electronic photodissociation spectra

Next, we have characterized the newly generated gold(II) complexes [Au^{II}(bipy)(X)]⁺ (X = Cl or Br) by measuring their absorption spectra in the visible range using the helium tagging photodissociation method. For the comparison, we measured also the spectra of the stable copper(II) analogs [Cu^{II}(bipy)(Cl)]⁺ and [Cu^{II}(bipy)(Br)]⁺. The copper chlorido complex has an absorption band below 450 nm. We could detect only the onset of this band, because of the working range of our laser (Figure 5a). The absorption maximum for [Cu^{II}(bipy)(Br)]⁺ is red shifted to 544 nm (Figure 5c). For the gold complexes, we detect a band at 637 nm for [Au^{II}(bipy)(Cl)]⁺ (Figure 5b) and two bands at 494 nm and 663 nm for [Au^{II}(bipy)(Br)]⁺ (Figure 5d). In order to explain the spectra and get a deeper insight into the properties of gold(II) complexes, we have performed quantum chemical calculations.

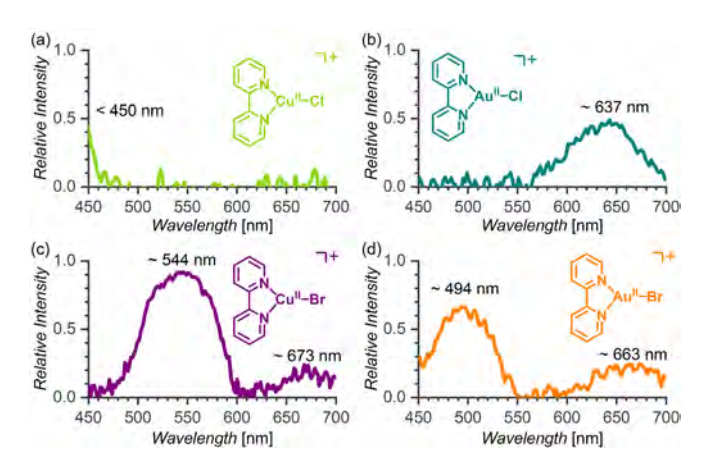


Figure 5. Helium-tagging photodissociation spectra in the visible range (visPD) of Cu(II) and Au(II) complexes at 3K.

Computed electronic spectra

To provide an interpretation and computational support of the experimental absorption spectra (Figure 5), we employed the CAM-B3LYP/aug-cc-pVTZ/Au(PP) density functional theory method. The equilibrium geometries were obtained at the PBE0/def2-TZVPP/PP(Au)^{70,71} level. This combination provided a good agreement between the computed and experimental data and afforded their straightforward interpretation, though it partly relies on error cancellation, see SI. A comparison of the DFT functionals, basis set requirements, subtle structural effects on the computed spectra, as well and the spin-orbit effects are given in the SI, including the full set of the calibration data, Tables S2-S5.

The calculations clearly reveal the origin of two transitions responsible for the spectral features that are common to all four studied complexes. The transitions are illustrated in Figure 6. It can be seen that the experimental band near 650 nm (Figure 5) arises from LP(X) > π (M–X)* a_1 (LP: lone pair, a' in the C_2 symmetry, vide infra) excitation (Figure 6a) whereas the experimental band near 500 nm (Figure 5) arises from the $\sigma(M-X) > \pi(M-X)^* b_1(a'' \text{ in } C_s)$ excitation (Figure 6b). These common features are calculated at all tested levels, DFT and ab initio, see Tables S2-S5.

Comparison of theoretical and experimental data shown in Table 3 reveals that for $X = Br, i.e., for the [Cu(bipy)(Br)]^+ and [Au(bipy)(Br)]^+ complexes, both transitions are$ experimentally observed and the calculations are in a good agreement with the experimental values (to within 220 nm). For $[Cu(bipy)(Cl)]^+$, the predicted $\lambda_{calc}(b_2) =$ 455 nm seems to correspond to the experimental band appearing at the end of the

short-wave-length of the experimental spectra (~ 450 nm) whereas the predicted $\lambda_{\rm calc}(a_1)$ at 684 nm seems to be hidden in noise on the other end of the experimental spectra (Figure 5a). For [Au(bipy)(Cl)]⁺, the predicted $\lambda_{\rm calc}(b_2)=416$ nm in the $C_{\rm 2v}$ geometry and $\lambda_{\rm calc}(a'')=433$ nm in the $C_{\rm 5}$ minimum (see discussion below) is clearly outside the experimental window ($\lambda_{\rm min}\sim 450$ nm). This explains the missing b_2 band in the spectrum of [Au(bipy)(Cl)]⁺ (Figure 5b).

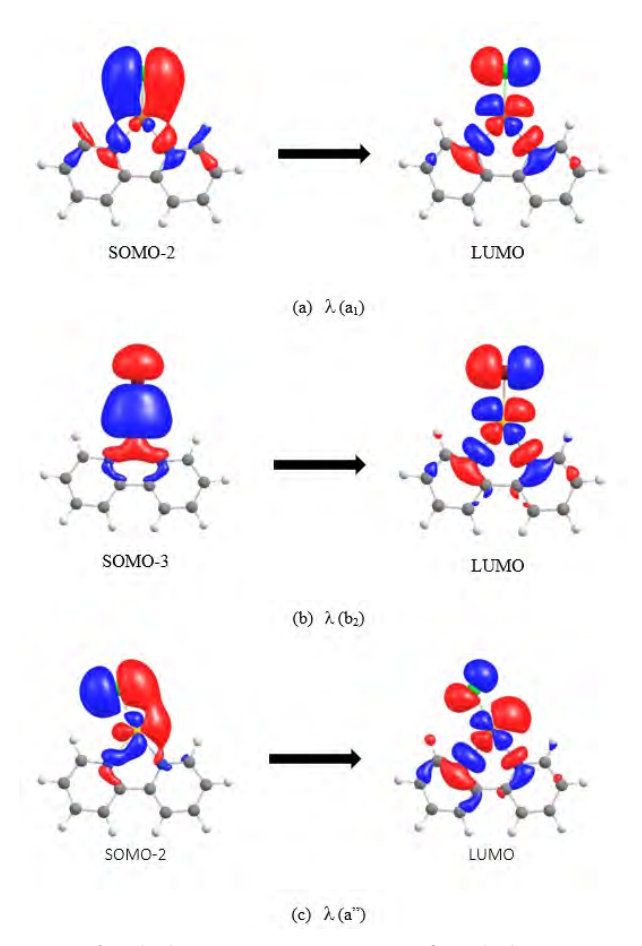


Figure 6. The MO origin of studied excitations. (a) a_1 excitation from the b_2 LP(X) SOMO-2 to b_2 π (M–X)* LUMO; in the C_{2v} geometry. (b) b_2 excitation from a_1 σ (M–X) SOMO-3 to b_2 π (M–X)* LUMO; in the C_{2v} geometry. (c) a^2 excitation from the a^n LP(X) SOMO-2 to a^n π (M–X)* LUMO in the C_2 geometry.

As for the computed intensities of the two peaks, the computed value of the oscillator strength for the a_1 excitation ($f \approx 14\cdot10^4$, Figure 6b, Table 3) at the C_{2v} minima is rather low. We assumed that it was caused by neglecting of the vibronic coupling. To further elaborate on this assumption, the in-plane bending mode

(Figure 7) of the halogen atom in the [M(bipy)(X)]⁺ complex is associated with a very low vibrational frequency of a few tens of cm¹. In energy terms, this corresponds to a computed deformation energy of 2 – 4 kJ.mol¹ (vide infra).

Interestingly, in the case of [Au(bipy)(CI)]+ complex, the equilibrium geometry at the PBEO/de2TZVPP/Au(PP) level corresponds to the C_s minimum (Figure 7a); whereas the C_{24} structure lies ~ 2 kJ.mol¹ above (Figure 7b). In fact, the latter (C_{2n}) is a transition state with an imaginary mode of i30 cm⁻¹, whereas the lowest vibrational mode in the C_e minimum (30 cm⁻¹) corresponds to soft in-plane ligandgold-chlorine bending. More importantly, for the C_{ς} minimum of $[Au(bipy)(CI)]^+$ the computations predict ~ 100 times higher oscillator strength for the $\lambda_{calc}(a')$ excitation in comparison with the $\lambda_{calc}(a_1)$ in the C_{2v} geometry (f=0.0103 vs 0.0001, c.f. Table 3). The predicted wavelength of the $\lambda_{\rm calc}(a')$ transition raises from 639 to 665 nm (1.94 to 1.86 eV), which is admittedly away from the experimental value of 637 nm (1.95 eV).

Similar arguments can be applied for [Au(bipy)(Br)]+. The equilibrium geometry of $[Au(bipy)(Br)]^+$ at all tested levels – corresponds to a C_{2v} minimum, for which the calculated oscillator strength of the b_2 transition is also very low, $f \approx 10^4$ (Table 3). However, a relaxed scan of the N1-Au-Br tilt angle reveals that the energy of the system changes only very little (< 2 kJ.mol¹ for 20 degrees), while the intensity of the a' transition strongly raises, by ~100 times for the same (20 degrees) tilt, c.f. Table S6. The $\lambda_{\rm calc}$ (a) calculated then raises to 754 nm (1.64 eV), relatively far from the experimental value of 663 nm (1.87 eV). Inclusion of spin-orbit coupling in calculations may decrease the predicted value by few tens of nm as shown in Table S2. All in all, we qualitatively demonstrated the sensitivity of the computed intensities on the small structural changes of the studied complexes.

Table 3. Comparison of theoretical and experimental absorption resonances for [M(bipy)(X)]⁺ M=Cu, Au; X=CI, Br systems. In nm. Calculated oscillator strengths are in parentheses. CAM-B3LYP/aug-ccpVTZ/Au(PP)//PBE0/def2TZVPP/Au(PP) level.

, ,		, ,			
Molecule	Sym.	$\lambda_{calc}(b_2)$	$\lambda_{exp}(b_2)$	$\lambda_{\text{calc}}(a_1)$	$\lambda_{exp}(a_1)$
[Cu(bipy)(Cl)] ⁺	C_{2v}	455(0.12)	<450	684(4x10 ⁻⁴)	-
[Au(bipy)(Cl)] ⁺	C_{2v}	416(0.17)	-	639(1x10 ⁻⁴)	637
[Cu(bipy)(Br)] ⁺	C_{2v}	545(0.12)	544	694(4x10 ⁻⁴)	673
[Au(bipy)(Br)] ⁺	C_{2v}	495(0.17)	494	664(1x10 ⁻⁴)	663
[Au(bipy)(Cl)] ⁺	C _s	433(0.01) [a]	-	665(0.01) ^[a]	637

[a] C_s -symmetry. λ_{calc} (a") and λ_{calc} (a')

It can be thus concluded that the ratio between the computed intensities of the two peaks is between 1:10 and 1:100. This still seems to be somewhat in disagreement with the experimental spectrum (Figure 5c) for which the ratio 1:3 can be inferred from the visual inspection of the figure. However, the band intensities in the visPD spectra depend on the laser power that varies with the wavelength. In addition, the spectra were measured with large attenuations (close to the saturation regime) with the aim to detect also less intense bands. In a linear regime, the ratio between the bands would be larger, making the agreement between experimental and theoretical results qualitatively correct.

As mentioned above, the a_1 band is either missing or hidden in the noise in the spectra of [Cu(bipy)(Cl)]⁺ system, Figure 5a. Calculations of C_s -symmetric [Cu(bipy) (Cl)]⁺ with Cl artificially bent by 20 degrees from the C_{2v} minimum give λ_{calc} (a_1) = 679 nm with oscillator strength ~ 0.003 that is only ca 10x higher than in the C_{2v} minimum. Apparently, the vibronic coupling is much weaker in [Cu(bipy)(Cl)]⁺ and the corresponding band is not well observed in the spectrum.

Oxidation state and electronic configuration of the metal

To check the unusual oxidation state II of the gold ion in the studied complexes, QTAIM (Quantum Theory of Atoms in Molecules) analysis 72 of the electronic structure has been carried out employing the *localization index*, $\lambda(A)$ as the central property. The oxidation state of an electropositive element in contact with elements that are more electronegative can be defined as the difference between its atomic number and its $\lambda(A)$. This quantity is consistent with the IUPAC definition of the oxidation state that is atomic charge after "ionic approximation" of the heteronuclear bonds. The QTAIM analysis of $[M(bipy)(X)]^+$ (M = Cu, Au; X = CI, Br, I) complexes in Table 4 shows that while the atomic charges of M vary from 0.4 for $[Au(bipy)(I)]^+$ to 1.0 for $[Cu(bipy)(CI)]^+$, the $\lambda(A)$ index remains rather constant among all species, confirming the II oxidation state of the metal. The differences between the $\lambda(A)$ and atomic numbers for copper and gold complexes are similar to each other, which is consistent with their similar oxidation numbers.

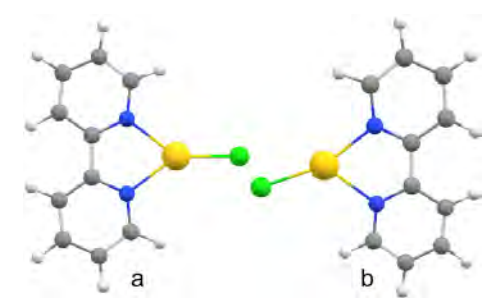


Figure 7. (a) C_s and (b) C_s structures of the [Au(bipy)Cl]⁺ systems.

The bonding between Au(II) and the other atoms in the molecule can be described by the delocalization index, DI, that expresses the level of electron sharing, i.e., covalency, between two atoms. The results in Table 4 point to the covalent M-X bonds with DI_{M.Y} values varying between 1.1 ([Cu(bipy)(Br)]⁺) and 1.5 ([Au(bipy) (CI)]+). The DI_{M.Y.} higher than 1 denotes multiple bonding, see NBO analysis below. Dative bonds are predicted between M and nitrogen atoms, with DI_{M.N} about 0.5-0.7 for each nitrogen in Table 4. It is worth noting that as the covalent character of M-X in both copper and gold complexes increases, spin density on the metal centres decreases. This is compensated by an increase of the spin density at the halide atoms. Visualizing the spin density in 2D and 3D plots, Figures S34-S36, shows that the unpaired electron is placed in the d-orbitals of the gold atom with some contribution of the X and nitrogen atoms. The calculated spin densities are listed in Table 4.

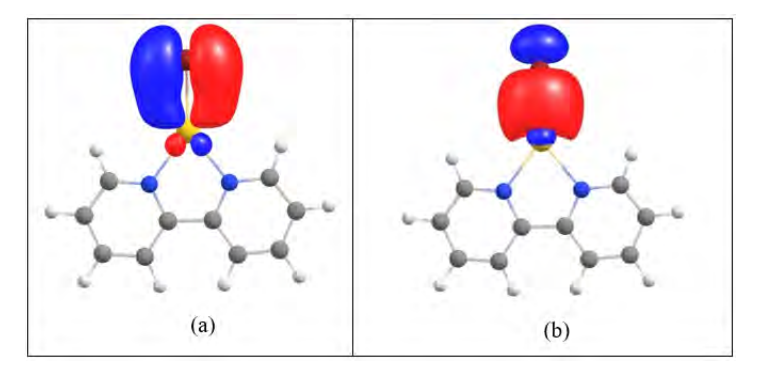


Figure 8. M-X bonding NBOs found in [Au(bipy)(Br)]+ system. (a) Single occupied alpha NBO corresponding to one-electron $LP_{-}(X)>d_{-}^{*}(M)$ interaction, and, (b) NBO that corresponds to $\sigma(M-X)$ bond. Here, in fact, two NBOs, one alpha and one beta single occupied NBO share similar spatial shape, so only one is shown.

and metal and nitrogen atoms. Spin densities at metal, halogen and nitrogen atoms; atomic properties of the nitrogen atoms in the asymmetric structures are Table 4. The atomic charges, Q, on metal, halogen, and nitrogen atoms, localization index of the metals (LI) and delocalization index (DI) between metal and halogen, reported for N1 and N2 as marked in Figure 7, respectively. Calculated at TPSS/def2TZVP level.

Molecules	Q	ď	ď		OS(rounded) DI _{MX}	D	۵	SD _M	SD _x	SD
[Au(bipy)(CI)] ⁺	0.65	-0.28	0	76.89	+2	1.33		0.43	0.27	0.13
$[Au(bipy)(CI)]^{+[a]}$	0.72	-0.36	-1.20/-1.19 ^[a]	76.82	+2	1.26	0.71/0.69 ^[a]	0.53	0.17	0.05/0.22 ^[a]
[Au(bipy)(Br)]+	0.56	-0.16	-1.10	76.97	+2	1.40	0.65	0.40	0.32	0.12
[Au(bipy)(I)]+	0.41	0.02	-1.10	77.10	+2	1.51	0.62	0.35	0.41	0.10
[Cu(bipy)(Cl)]+	0.94	-0.42	-1.16	26.80	+2	1.13	0.59	0.50	0.28	0.10
[Cu(bipy)(Br)]+	0.87	-0.34	-1.15	26.86	+2	1.19	0.58	0.47	0.33	60:0
[Cu(bipy)(I)]+	0.75	-0.18	-1.15	26.94	+2	1.29	0.56	0.42	0.42	0.07

[a] C, minimum.

The multiple bonding character of M–X bonds (DI $_{\text{M-X}}$ >1 in Table 4) is reflected in the NBO analysis of ([Au(bipy)(Br)]+) that finds three one-electron bonding NBOs between Au and X. Two of these one-electron bonds share similar spatial shape but one host an alpha- the other host a beta electron (Figure 8b) which basically corresponds to a two-electron $\sigma(M-X)$ bond. The third M-X bonding NBO corresponds to one-electron LP π (X) donation to $d_{\pi}^*(M)$, Figure 8a. The Au-N interactions are also observed in all systems. The NBO procedure finds LP(N) NBOs that strongly interact with the M-X antibonding NBOs.

Discussion

The isolation of ions in the gas phase allowed us to study properties of gold(II) complexes with the $[Au^{\parallel}(L)(X)]^+$ speciation (L = bidentate or tridentate ligand, X = halogen) in detail. The gold(II) complexes can be prepared by reduction of gold(III) precursors. The challenge in this preparation is a possibility of an easy direct reduction of gold(III) complexes to gold(I) complexes. We have explored the possibility to generate the gold(II) complexes by sequential eliminations of halogen radicals from the $[Au^{(1)}(L)(X)_{\alpha}]^+$ precursors in the gas phase for various L and X combinations. The experiments clearly showed that the ligands L that stabilize gold(I) complexes do not favour the formation of the desired gold(II) complexes. This includes all monodentate ligands that easily support favourable linear coordination of gold(I) complexes and ligands with "soft" donor atoms (especially P-based). The most favourable ligands for the formation of gold(II) halido complexes were N,N'bidentate and *N,N',N''*-tridentate ligands.

Knowing the ligands that can stabilize gold(II) halido complexes, we have attempted to prepare the respective gold(II) complexes also in solution by electrochemical reduction. Unfortunately, the electrochemical reaction led always to the twoelectron reduction and the formation of gold(I) complexes. Nevertheless, we have observed the trend in the onset potential for the reduction of the gold(III) complexes that correlates well with the gas-phase halogen bond dissociation energies from the respective $[Au^{((L)}(X)_3]^+$ ions (Figure 9b). For the tridentate ligand terpy, the reduction is reversible and the ions are speciated as [Au^{III}(terpy)(X)]²⁺ in solution (Figures S11 and S12).^{74–76} Accordingly, the dications are also the dominant complexes detected by electrospray ionization mass spectrometry (Figure S7 & S8). The [Au^{III}(terpy)(X)]²⁺ complexes can accept 2 electrons without forming an unstable species (Reaction 5 in Figure 9a). On contrary, the bidentate ligand will support the [Au^{III}(bipy)(X)₃]⁺ speciation. Electrochemical reduction of these

complexes was always irreversible. Likely, the [Au^{III}(bipy)(X)₂]+ complexes accept 2 electrons and then spontaneously dissociate to form linear [Au(X)_a]⁻ and the free ligand. Alternatively, the complexes could dimerize. 32,33,77 Interestingly, a correlation between the BDEs of the gold-halogen bonds in [Au^{III}(L)(X)_a]⁺ and the reduction onset potentials (blue points in Figure 9) suggests that the energy of the gas-phase homolytic M-X bond cleavage to a certain degree predict the redox potential of the metal M. The fact that we see a better correlation with the BDE values measured for [Au^{III}(terpy)(X)_a]⁺ than with those for the solution-relevant [Au^{III}(terpy)(X)]²⁺ complexes is most probably because of the charge. The double charge increases the BDEs in the gas-phase. Hence, the additional chlorido ligands in [Au^{III}(terpy) (X)₂]⁺ compensate this effect and allow the rough correlation even in a family of different ligands.

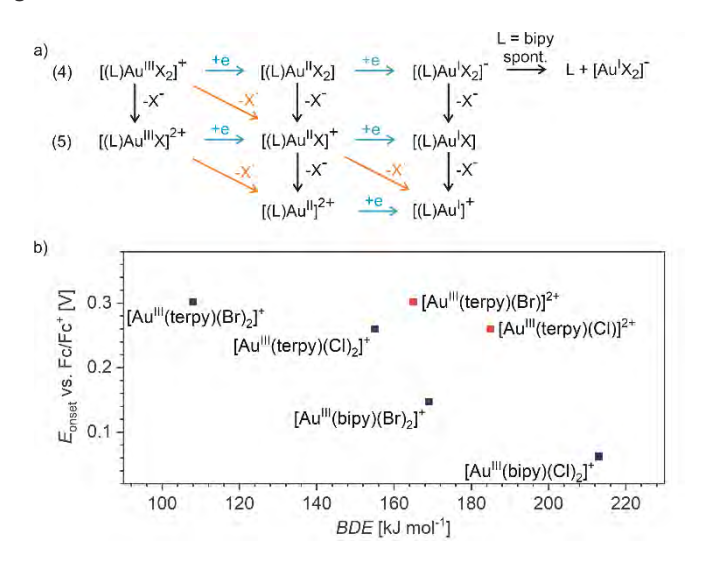


Figure 9. a) The possible processes in solution (one-electron reductions are indicated by blue arrows, ligand dissociations are indicated by black arrows) and the processes studied by collision induced dissociation experiments (radical cleavages indicated by orange arrows). b) Correlation between E_{onset} of the $Au^{III} \rightarrow Au^{II}$ redox potentials and the bond dissociation energies of the $[Au^{III}(L)(X)_{-}]^+$ complexes (blue symbols) and $[Au^{III}(terpy)(X)]^{2+}$ (red symbols; L = terpy or bipy, X = Br or CI).

The possibility to generate the gold(II) halido complexes in the gas phase allowed us to characterize their spectroscopic properties. Using infrared photodissociation spectroscopy, we could show that gold(II) has a very similar electronic interaction with the auxiliary ligands as copper(II). The IR spectra showing the vibrations of bipy ligand do not suggest any unpaired electron delocalization at the ligand. The gold(II) complexes absorb also in the visible range. In comparison to the analogous copper(II) complexes, their absorption maxima are slightly blue shifted. The spectra

suggest the orange-red color for [Au"(bipy)(Br)]+ and cyan for [Au"(bipy)(Cl)]+. The theoretical analysis of the spectra showed that the excitations are metal-centered and also demonstrated how subtle structural variations and vibronic coupling dramatically change the intensities of peaks and also shift non-negligibly the positions of the absorption peaks.

QTAIM calculations confirm that both gold and copper are in oxidation state M^{II} in calculated [(bipy)M"X]⁺ systems, with the calculated M-X bond order between 1 and 1.5 (multiple bonding) and with the M-N bond orders near 0.7 (dative bonding). The NBO analysis reveals a strong interaction of the in-plane LP(X) with the halfempty d orbital at the gold(II) center.

Conclusions

We have shown that gold(II) complexes with bidentate and tridentate ligands can be generated in the gas phase by eliminations of halogen radicals from the gold(III) halogen precursors. We have further explored spectroscopic and electronic properties of the [Au^{II}(bipy)(X)]⁺ complexes in detail, because these complexes are not fully coordinatively saturated and thus offer a possibility to study reactivity of gold(II) complexes in future. The results show that the interaction of gold(II) with the ancillary ligand bipy is analogous to that of copper(II). Also, electronic spectra of the gold(II) complexes are similar to those of the analogous copper(II) complexes. The absorption maxima in the spectra are blue-shifted for the gold complexes suggesting that the color of [Au^{II}(bipy)(Br)]⁺ should be orange-red and that of [Au^{II}(bipy)(CI)]⁺ should be cyan.

Experimental Section

Mass spectrometry

Mass spectrometric (MS) experiments were carried out using the Thermo Scientific LTQ XL linear ion trap mass spectrometer with electrospray ionization (ESI) source.⁷⁸ Energy-resolved collision-induced dissociation spectra were measured with an LCQ Deca XP ion trap mass spectrometer.⁷⁹ In the collision-induced dissociation (CID) experiments, bond dissociation energies (BDE) can be determined from the dependence of the relative cross-section of the given dissociation on the collision energy.80 The linear extrapolation of the rise of the sigmoid fit of the cross-section energy dependence gives the appearance energy of the given

Infrared and UV-VIS photodissociation spectroscopy

The IR and Vis spectra of mass-selected ions were measured with a helium tagging photodissociation method using the ISORI instrument.⁶⁵ The ions were generated by the electrospray ionization, mass selected by a quadrupole, and transferred to a wire quadrupole trap operated at 3 K. The ions were trapped and cooled down using the helium buffer gas. The relaxed ions attached a helium atom. The helium complexes then served for the spectroscopic experiments. The complexes were irradiated with the OPO/OPA system from LaserVision pumped by Nd:YAG laser Surelite EX from Continuum (tuning range 700-4700 cm⁻¹, FWHM ~1.5 cm⁻¹, 10 ns pulse length) or with supercontinuum laser NKT Photonics SuperK Extreme (430-700 nm range using acusto-optic tunable filter SuperK Select).⁸⁴ The spectra are constructed as $(1 - N_i/N_{i0})$, where N_i and N_{i0} are numbers of helium complexes with and without laser irradiation.^{85,86}

Electrochemistry. The gold(III) complexes were prepared according to the literature.⁸⁷ The NMR spectra of the solutions of the complexes in CD₃CN on comparison with the literature indicate that the complexes are present as [Au(bipy) Cl₂]⁺, [Au(bipy)Br₂]⁺, [Au(terpy)Cl]²⁺ and [Au(terpy)Br]²⁺ (see SI, Figures S9-S12).^{74-76,87} We note that overtime these complexes especially the terpy based gold(III) complexes decomposed in solution as precipitation was observed. The speciation can depend on the solvent, but the results are consistent with the dominant speciation detected by NMR. Cyclic voltammetry (CV) experiments were performed using a Metrohm potentiostat (Autolab PGSTAT204) at room temperature in a solution of 0.25 or 0.5 mM of the respective gold complex (freshly prepared), 0.1 M of the supporting electrolyte (tertabutyl ammonium hexafluorophosphate) either

in DMF or in DCM. Glassy carbon working electrode, Pt counter electrode and a double junction non-aqueous Aq/AqCl reference electrode filled with 2 M LiCl in ethanol as the inner electrolyte was used. Prior to the measurements the electrolyte was deoxygenated by argon bubbling, and during the measurement electrolyte was kept under the argon atmosphere. Reference electrode was calibrated against ferrocene redox couple before measurements.

DFT calculations. All quantum chemical calculations were carried out using Gaussian 16,66 and Turbomole 7.5.1. programs.88 Density functional theory (DFT) has been mostly used throughout. A set of density functionals, including pure generalized-gradient approximation (GGA),89 meta-GGA and hybrids were employed: B3LYP, PBE, TPSS, and PBEO, Basis sets of triple-zeta quality 6-311+G**, and def2-TZVP(P) used throughout are considered as sufficiently large to report the converged DFT values. For gold and iodine core Stuttgart-Dresden (SDD) pseudopotentials (ECP's) were used. 90-96 The electronic excitation spectra were mostly calculated by employing time-dependent (TD-) DFT theory as implemented in Gaussian 16. For comparison, the ab initio CC2 and ADC2 calculations were performed using the Turbomole 7.5.1 code. The spin-orbit SO-ZORA excitations we obtained in the ADF 2021 program suite.97-100 The particular method used for computations is always denoted in the following by employing the standard notation: Method A/basis set A//method B/basis set B. This describes the level of theory at which the geometry was optimized (method B/basis set B) and the final single-point energy (method A/basis set A) calculated. Zero-point vibrational energy (and entropic and thermal contributions, if needed) were obtained employing the standard normal-mode analysis.

Quantum Theory of Atoms in Molecules (QTAIM) and NBO analysis. To investigate chemical bonding and to determine the oxidation states of metal in the studied complexes, quantum theory of atoms in molecules, QTAIM, 101 was employed. All QTAIM computations were performed by the AIMAII suite of programs. 102 Natural bond orbital analysis 103-107 used program NBO 7.0103,108 linked to the Gaussian 16 code.66

References

- (1) Hashmi, A. S. K. Gold-Catalyzed Organic Reactions. Chem. Rev. 2007, 107 (7), 3180–3211.
- (2) Echavarren, A. M.; Hashmi, A. S. K.; Toste, F. D. Gold Catalysis Steadily Increasing in Importance. *Adv. Synth. Catal.* **2016**, *358* (9), 1347.
- (3) Quach, R.; Furkert, D. P.; Brimble, M. A. Gold Catalysis: Synthesis of Spiro, Bridged, and Fused Ketal Natural Products. *Org. Biomol. Chem.* **2017**, *15* (15), 3098–3104.
- (4) Zi, W.; Dean Toste, F. Recent Advances in Enantioselective Gold Catalysis. *Chem. Soc. Rev.* **2016**, *45* (16), 4567–4589.
- (5) Fricke, C.; Reid, W. B.; Schoenebeck, F. A Review on Oxidative Gold-Catalyzed C-H Arylation of Arenes – Challenges and Opportunities. *European J. Org. Chem.* 2020, 2020 (46), 7119–7130.
- (6) Kramer, S. Homogeneous Gold-Catalyzed Aryl–Aryl Coupling Reactions. Synthesis (Stuttg). 2020, 52 (14), 2017–2030.
- (7) Huang, L.; Rudolph, M.; Rominger, F.; Hashmi, A. S. K. Photosensitizer-Free Visible-Light-Mediated Gold-Catalyzed 1,2-Difunctionalization of Alkynes. *Angew. Chemie - Int. Ed.* 2016, 55 (15), 4808–4813.
- (8) Winston, M. S.; Wolf, W. J.; Toste, F. D. Photoinitiated Oxidative Addition of CF3I to Gold(I) and Facile Aryl-CF3 Reductive Elimination. *J. Am. Chem. Soc.* **2014**, *136* (21), 7777–7782.
- (9) Tlahuext-Aca, A.; Hopkinson, M. N.; Sahoo, B.; Glorius, F. Dual Gold/Photoredox-Catalyzed C(Sp)-H Arylation of Terminal Alkynes with Diazonium Salts. Chem. Sci. 2016, 7 (1), 89–93.
- (10) Dorel, R.; Echavarren, A. M. Gold(I)-Catalyzed Activation of Alkynes for the Construction of Molecular Complexity. Chem. Rev. 2015, 115 (17), 9028–9072.
- (11) Kumar, R.; Linden, A.; Nevado, C. Evidence for Direct Transmetalation of Au III –F with Boronic Acids. *J. Am. Chem. Soc.* **2016**, *138* (42), 13790–13793.
- (12) Rocchigiani, L.; Bochmann, M. Recent Advances in Gold(III) Chemistry: Structure, Bonding, Reactivity, and Role in Homogeneous Catalysis. *Chem. Rev.* **2021**, *121* (14), 8364–8451.
- (13) Kim, S.; Toste, F. D. Mechanism of Photoredox-Initiated C–C and C–N Bond Formation by Arylation of IPrAu(I)–CF 3 and IPrAu(I)–Succinimide. *J. Am. Chem. Soc.* **2019**, *141* (10), 4308–4315.
- (14) Wu, C. Y.; Horibe, T.; Jacobsen, C. B.; Toste, F. D. Stable Gold(III) Catalysts by Oxidative Addition of a Carbon-Carbon Bond. *Nature* **2015**, *517* (7535), 449–454.
- (15) Pintus, A.; Rocchigiani, L.; Fernandez-Cestau, J.; Budzelaar, P. H. M.; Bochmann, M. Stereo- and Regioselective Alkyne Hydrometallation with Gold(III) Hydrides. *Angew. Chemie Int. Ed.* **2016**, *55* (40), 12321–12324.
- (16) Laguna, A.; Laguna, M. Coordination Chemistry of Gold(II) Complexes. *Coord. Chem. Rev.* **1999**, 193–195, 837–856.
- (17) Seidel, S.; Seppelt, K. Xenon as a Complex Ligand: The Tetra Xenono Gold(II) Cation in AuXe 4 2+ (Sb 2 F 11) 2. Science (80-.). **2000**, 290 (5489), 117–118.
- (18) Blake, A. J.; Greig, J. A.; Holder, A. J.; Hyde, T. I.; Taylor, A.; Schröder, M. Bis(1,4,7-trithiacyclononane) Gold Dication: A Paramagnetic, Mononuclear Aull Complex. *Angew. Chemie Int. Ed. English* **1990**, 29 (2), 197–198.
- (19) Gencheva, G.; Tsekova, D.; Gochev, G.; Mehandjiev, D.; Bontchev, P. R. Monomeric Au(II) Complex with Hematoporphyrin IX. *Inorg. Chem. Commun.* **2003**, *6* (3), 325–328.
- (20) Preiß, S.; Förster, C.; Otto, S.; Bauer, M.; Müller, P.; Hinderberger, D.; Hashemi Haeri, H.; Carella, L.; Heinze, K. Structure and Reactivity of a Mononuclear Gold(II) Complex. *Nat. Chem.* **2017**, *9* (12), 1249–1255.

- (21) Bava, M.; Pérez-Bitrián, A.; Martínez-Salvador, S.; Martín, A.; Casas, J. M.; Menión, B.; Orduna, J. Gold(II) Trihalide Complexes from Organogold(III) Precursors. Chem. - A Eur. J. 2018, 24 (7), 1514–1517.
- (22) Veit, P.; Volkert, C.; Förster, C.; Ksenofontov, V.; Schlicher, S.; Bauer, M.; Heinze, K. Gold(Ii) in Redox-Switchable Gold(i) Catalysis. Chem. Commun. 2019, 55 (32), 4615-4618.
- (23) Barakat, K. A.; Cundari, T. R.; Rabaâ, H.; Omary, M. A. Disproportionation of Gold(II) Complexes. A Density Functional Study of Ligand and Solvent Effects. J. Phys. Chem. B 2006, 110 (30), 14645–14651.
- (24) Pyykkö, P. Theoretical Chemistry of Gold. Angew. Chemie Int. Ed. 2004, 43 (34), 4412–4456.
- (25) Pyykkö, P. Theoretical Chemistry of Gold. II. Inorganica Chim. Acta 2005, 358 (14), 4113–4130.
- (26) Schmidbaur, H.; Cronie, S.; Diordievic, B.; Schuster, O. Understanding Gold Chemistry through Relativity. Chem. Phys. 2005, 311 (1-2 SPEC.ISS.), 151-161.
- (27) Hargittai, M.; Schulz, A.; Réffy, B.; Kolonits, M. Molecular Structure, Bonding, and Jahn-Teller Effect in Gold Chlorides: Quantum Chemical Study of AuCl 3, Au 2 Cl 6, AuCl 4 -, AuCl, and Au 2 Cl 2 and Electron Diffraction Study of Au 2 Cl 6. J. Am. Chem. Soc. 2001, 123 (7), 1449-1458.
- (28) Heinze, K. The Quest for Mononuclear Gold(II) and Its Potential Role in Photocatalysis and Drug Action. Angew. Chemie - Int. Ed. 2017, 56 (51), 16126-16134.
- (29) Preiß, S.; Päpcke, A.; Burkhardt, L.; Großmann, L.; Lochbrunner, S.; Bauer, M.; Opatz, T.; Heinze, K. Gold(II) Porphyrins in Photoinduced Electron Transfer Reactions. Chem. - A Eur. J. 2019, 25 (23), 5940-5949.
- (30) Di Terlizzi, L.; Scaringi, S.; Raviola, C.; Pedrazzani, R.; Bandini, M.; Fagnoni, M.; Protti, S. Visible Light-Driven, Gold(I)-Catalyzed Preparation of Symmetrical (Hetero)Biaryls by Homocoupling of Arylazo Sulfones. J. Org. Chem. 2022, 87 (7), 4863-4872.
- (31) Koelle, U.; Laguna, A. Electrochemistry of Au-Complexes. Inorganica Chim. Acta 1999, 290 (1),
- (32) Roașca, D. A.; Smith, D. A.; Hughes, D. L.; Bochmann, M. A Thermally Stable Gold(III) Hydride: Synthesis, Reactivity, and Reductive Condensation as a Route to Gold(II) Complexes. Angew. Chemie - Int. Ed. 2012, 51 (42), 10643-10646.
- (33) Gimeno, M. C.; López-de-Luzuriaga, J. M.; Manso, E.; Monge, M.; Olmos, M. E.; Rodríguez-Castillo, M.; Tena, M.-T.; Day, D. P.; Lawrence, E. J.; Wildgoose, G. G. Synthesis, Photochemical, and Redox Properties of Gold(I) and Gold(III) Pincer Complexes Incorporating a 2,2':6',2'-Terpyridine Ligand Framework. Inorg. Chem. 2015, 54 (22), 10667–10677.
- (34) Preiß, S.; Melomedov, J.; Wünsche Von Leupoldt, A.; Heinze, K. Gold(III) Tetraarylporphyrin Amino Acid Derivatives: Ligand or Metal Centred Redox Chemistry? Chem. Sci. 2016, 7 (1), 596-610.
- (35) Andris, E.; Jašík, J.; Gómez, L.; Costas, M.; Roithová, J. Spectroscopic Characterization and Reactivity of Triplet and Quintet Iron(IV) Oxo Complexes in the Gas Phase. Angew. Chemie - Int. Ed. **2016**, *55* (11), 3637–3641.
- (36) Andris, E.; Navrátil, R.; Jašík, J.; Puri, M.; Costas, M.; Que, L.; Roithovaá, J. Trapping Iron(III)-Oxo Species at the Boundary of the "Oxo Wall": Insights into the Nature of the Fe(III)-O Bond. J. Am. Chem. Soc. 2019, 140 (43), 14391-14400.
- (37) De Kler, N. R. M.; Roithová, J. Copper Arylnitrene Intermediates: Formation, Structure and Reactivity. Chem. Commun. 2020, 56 (84), 12721-12724.
- (38) Langseth, E.; Görbitz, C. H.; Heyn, R. H.; Tilset, M. Versatile Methods for Preparation of New Cyclometalated Gold(III) Complexes. Organometallics 2012, 31 (18), 6567–6571.

- (39) Huang, L.; Rominger, F.; Rudolph, M.; Hashmi, A. S. K. A General Access to Organogold(III) Complexes by Oxidative Addition of Diazonium Salts. Chem. Commun. 2016, 52 (38), 6435–6438.
- (40) Xiong, X.-G.; Wang, Y.-L.; Xu, C.-Q.; Qiu, Y.-H.; Wang, L.-S.; Li, J. On the Gold–Ligand Covalency in Linear [AuX 2] Complexes. *Dalt. Trans.* **2015**, *44* (12), 5535–5546.
- (41) Parker, D.; Roy, P. S.; Ferguson, G.; Hunt, M. M. Crystal and Molecular Structure of Chloro-1,4, 7-Trithiacyclononane Gold(I): Adoption of a Strained [225] Conformation by the Macrocyclic Ligand. *Inorganica Chim. Acta* **1989**, *155* (2), 227–230.
- (42) Collado, A.; Nelson, D. J.; Nolan, S. P. Optimizing Catalyst and Reaction Conditions in Gold(I) Catalysis–Ligand Development. Chem. Rev. 2021, 121 (14), 8559–8612.
- (43) Nahra, F.; Tzouras, N. V.; Collado, A.; Nolan, S. P. Synthesis of N-Heterocyclic Carbene Gold(I) Complexes. Nat. Protoc. 2021, 16 (3), 1476–1493.
- (44) Zuccarello, G.; Zanini, M.; Echavarren, A. M. Buchwald-Type Ligands on Gold(I) Catalysis. *Isr. J. Chem.* **2020**, *60* (3–4), 360–372.
- (45) Walker, N. R.; Wright, R. R.; Barran, P. E.; Murrell, J. N.; Stace, A. J. Comparisons in the Behavior of Stable Copper(II), Silver(II), and Gold(II) Complexes in the Gas Phase: Are There Implications for Condensed-Phase Chemistry? J. Am. Chem. Soc. 2001, 123 (18), 4223–4227.
- (46) Walker, N. R.; Wright, R. R.; Barran, P. E.; Stace, A. J. Stable Gold(II) Complexes in the Gas Phase. Organometallics 1999, 18 (18), 3569–3571.
- (47) Ferraz de Paiva, R. E.; Nakahata, D. H.; Corbi, P. P. Synthesis and Crystal Structure of Dichlorido(1,10-Phenanthroline-κ 2 N, N ')Gold(III) Hexafluoridophosphate. Acta Crystallogr. Sect. E Crystallogr. Commun. 2017, 73 (7), 1048–1051.
- (48) Dierkes, P.; van Leeuwen, P. W. N. M. The Bite Angle Makes the Difference: A Practical Ligand Parameter for Diphosphine Ligands. *J. Chem. Soc. Dalt. Trans.* **1999**, No. 10, 1519–1530.
- (49) Söhnel, T.; Brown, R.; Kloo, L.; Schwerdtfeger, P. The Stability of Gold lodides in the Gas Phase and the Solid State. *Chem. A Eur. J.* **2001**, *7* (14), 3167–3173.
- (50) Schulz, A.; Hargittai, M. Structural Variations and Bonding in Gold Halides: A Quantum Chemical. *Chem. A Eur. J.* **2001**, *7*, 3657–3670.
- (51) Finkelstein, H. Darstellung Organischer Jodide Aus Den Entsprechenden Bromiden Und Chloriden. *Berichte der Dtsch. Chem. Gesellschaft* **1910**, *43* (2), 1528–1532.
- (52) Jin, X.; Davies, R. P. Copper-Catalysed Aromatic-Finkelstein Reactions with Amine-Based Ligand Systems. *Catal. Sci. Technol.* **2017**, *7* (10), 2110–2117.
- (53) Amani, V.; Abedi, A.; Ghabeshi, S.; Khavasi, H. R.; Hosseini, S. M.; Safari, N. Synthesis and Characterization of a Series of Gold(III) Complexes with the 4,4'-Dimethyl-2,2'-Bipyridine Ligand: Counterion Influence on the Cytotoxicity of Gold(III) Complexes. *Polyhedron* 2014, 79, 104–115.
- (54) Bortoluzzi, M.; De Faveri, E.; Daniele, S.; Pitteri, B. Synthesis of a New Tetrakis(2-Pyridinyl)Pyrazine Complex of Gold(III) and Its Computational, Spectroscopic and Electrochemical Characterization. Eur. J. Inorg. Chem. 2006, 2 (17), 3393–3399.
- (55) Pierce, D. T.; Geiger, W. E. Electrochemical Kinetic Discrimination of the Single-Electron-Transfer Events of a Two-Electron-Transfer Reaction: Cyclic Voltammetry of the Reduction of the Bis(Hexamethylbenzene)Ruthenium Dication. J. Am. Chem. Soc. 1992, 114 (15), 6063–6073.
- (56) Groom, C. R.; Bruno, I. J.; Lightfoot, M. P.; Ward, S. C. The Cambridge Structural Database. Acta Crystallogr. Sect. B Struct. Sci. Cryst. Eng. Mater. 2016, 72 (2), 171–179.
- (57) Scarborough, C. C.; Wieghardt, K. Electronic Structure of 2,2'-Bipyridine Organotransition-Metal Complexes. Establishing the Ligand Oxidation Level by Density Functional Theoretical Calculations. *Inorg. Chem.* 2011, 50 (20), 9773–9793.

- (58) Wang, M.; England, J.; Weyhermüller, T.; Wieghardt, K. Electronic Structures of "Low-Valent" Neutral Complexes [NiL 2] 0 (S = 0; L = Bpy, Phen, Tpy) – An Experimental and DFT Computational Study. Eur. J. Inorg. Chem. 2015, 2015 (9), 1511-1523.
- (59) Butschke, B.; Schlangen, M.; Schröder, D.; Schwarz, H. "Roll-over" Cyclometalation of 2,2'-Bipyridine Platinum(II) Complexes in the Gas Phase: A Combined Experimental and Computational Study. Chem. - A Eur. J. 2008, 14 (35), 11050-11060.
- (60) Butschke, B.; Schwarz, H. Mechanistic Study on the Gas-Phase Generation of "Rollover"-Cyclometalated [M(Bipy - H)]+ (M = Ni, Pd, Pt). Organometallics 2010, 29 (22), 6002-6011.
- (61) Yassaghi, G.; Jašíková, L.; Roithová, J. Gas-Phase Study of Metal Complexes with Redox-Active Ligands. Int. J. Mass Spectrom. 2016, 407, 92-100.
- (62) Milko, P.; Roithová, J. Redox Processes in the Iron(III)/9,10-Phenanthraguinone System. Inorg. Chem. 2009, 48 (24), 11734-11742.
- (63) Rezabal, E.; Duch, L.; Milko, P.; Holthausen, M. C.; Roithov, J.; Goethe-universit, J. W.; Pho, L.; Oh, C. H.; Pho, C.; Phoh, L. Ligand Effects on the [Cu (PhO) (PhOH)] b Redox Active Complex. 2010, No. 23, 8421-8429.
- (64) Milko, P.; Roithová, J.; Tsierkezos, N.; Schröder, D. The C-O Stretch as an Unprecedently Large Spectral Marker for the Electron Transfer between Copper(II) and a Phenolate Anion. J. Am. Chem. Soc. 2008, 130 (23), 7186-7187.
- (65) Jašík, J.; Žabka, J.; Roithová, J.; Gerlich, D. Infrared Spectroscopy of Trapped Molecular Dications below 4 K Dedicated to the Memory of Detlef Schröder. Int. J. Mass Spectrom. 2013, 354-355, 204-210.
- (66) Frisch, M. J.; Trucks, G. W.; Schlegel, H. B.; Scuseria, G. E.; Robb, M. a.; Cheeseman, J. R.; Scalmani, G.; Barone, V.; Petersson, G. a.; Nakatsuji, H.; Li, X.; Caricato, M.; Marenich, a. V.; Bloino, J.; Janesko, B. G.; Gomperts, R.; Mennucci, B.; Hratchian, H. P.; Ortiz, J. V.; Izmaylov, a. F.; Sonnenberg, J. L.; Williams; Ding, F.; Lipparini, F.; Egidi, F.; Goings, J.; Peng, B.; Petrone, A.; Henderson, T.; Ranasinghe, D.; Zakrzewski, V. G.; Gao, J.; Rega, N.; Zheng, G.; Liang, W.; Hada, M.; Ehara, M.; Toyota, K.; Fukuda, R.; Hasegawa, J.; Ishida, M.; Nakajima, T.; Honda, Y.; Kitao, O.; Nakai, H.; Vreven, T.; Throssell, K.; Montgomery Jr., J. a.; Peralta, J. E.; Ogliaro, F.; Bearpark, M. J.; Heyd, J. J.; Brothers, E. N.; Kudin, K. N.; Staroverov, V. N.; Keith, T. a.; Kobayashi, R.; Normand, J.; Raghavachari, K.; Rendell, a. P.; Burant, J. C.; Iyengar, S. S.; Tomasi, J.; Cossi, M.; Millam, J. M.; Klene, M.; Adamo, C.; Cammi, R.; Ochterski, J. W.; Martin, R. L.; Morokuma, K.; Farkas, O.; Foresman, J. B.; Fox, D. J. G16_C01. 2016, p Gaussian 16, Revision C.01, Gaussian, Inc., Wallin.
- (67) Andris, E.; Navrátil, R.; Jašík, J.; Sabenya, G.; Costas, M.; Srnec, M.; Roithová, J. Detection of Indistinct Fe-N Stretching Bands in Iron(V) Nitrides by Photodissociation Spectroscopy. Chem. - A Eur. J. 2018, 24 (20), 5078-5081.
- (68) Corinti, D.; Crestoni, M. E.; Chiavarino, B.; Fornarini, S.; Scuderi, D.; Salpin, J.-Y. Insights into Cisplatin Binding to Uracil and Thiouracils from IRMPD Spectroscopy and Tandem Mass Spectrometry. J. Am. Soc. Mass Spectrom. 2020, 31 (4), 946-960.
- (69) Martens, J.; van Outersterp, R. E.; Vreeken, R. J.; Cuyckens, F.; Coene, K. L. M.; Engelke, U. F.; Kluijtmans, L. A. J.; Wevers, R. A.; Buydens, L. M. C.; Redlich, B.; Berden, G.; Oomens, J. Infrared Ion Spectroscopy: New Opportunities for Small-Molecule Identification in Mass Spectrometry - A Tutorial Perspective. Anal. Chim. Acta 2020, 1093, 1–15.
- (70) Vícha, J.; Patzschke, M.; Marek, R. A Relativistic DFT Methodology for Calculating the Structures and NMR Chemical Shifts of Octahedral Platinum and Iridium Complexes. Phys. Chem. Chem. Phys. 2013, 15 (20), 7740.

- (71) Vícha, J.; Novotný, J.; Straka, M.; Repisky, M.; Ruud, K.; Komorovsky, S.; Marek, R. Structure, Solvent, and Relativistic Effects on the NMR Chemical Shifts in Square-Planar Transition-Metal Complexes: Assessment of DFT Approaches. *Phys. Chem. Chem. Phys.* 2015, 17 (38), 24944–24955.
- (72) IUPAC. Compendium of Chemical Terminology, 2nd ed. (the "Gold Book"). Compiled by A. D. McNaught and A. Wilkinson. Blackwell Scientific Publications, Oxford (1997). Online version (2019-) created by S. J. Chalk.
- (73) Day, C. S.; Do, C. D.; Odena, C.; Benet-Buchholz, J.; Xu, L.; Foroutan-Nejad, C.; Hopmann, K. H.; Martin, R. Room-Temperature-Stable Magnesium Electride via Ni(II) Reduction. *J. Am. Chem. Soc.* **2022**, *144* (29), 13109–13117.
- (74) Pitteri, B.; Marangoni, G.; Visentin, F.; Bobbo, T.; Bertolasi, V.; Gilli, P. Equilibrium and Kinetic Studies of (2,2':6',2'-Terpyridine)Gold(III) Complexes. Preparation and Crystal Structure of [Au(Terpy)(OH)] [ClO4]2. J. Chem. Soc. Dalt. Trans. 1999, No. 5, 677–682.
- (75) Czerwińska, K.; Golec, M.; Skonieczna, M.; Palion-Gazda, J.; Zygadło, D.; Szlapa-Kula, A.; Krompiec, S.; Machura, B.; Szurko, A. Cytotoxic Gold(Iii) Complexes Incorporating a 2,2':6',2"-Terpyridine Ligand Framework-the Impact of the Substituent in the 4'-Position of a Terpy Ring. *Dalt. Trans.* 2017, 46 (10), 3381–3392.
- (76) Peng, K.; Friedrich, A.; Schatzschneider, U. 2,2':c',2"-Terpyridine Switches from Tridentate to Monodentate Coordination in a Gold(Iii) Terpy Complex upon Reaction with Sodium Azide. Chem. Commun. 2019, 55 (56), 8142–8145.
- (77) Dann, T.; Roşca, D. A.; Wright, J. A.; Wildgoose, G. G.; Bochmann, M. Electrochemistry of Aull and AullIpincer Complexes: Determination of the Aull-Aull Bond Energy. *Chem. Commun.* 2013, 49 (86), 10169–10171.
- (78) Anania, M.; Jašíková, L.; Zelenka, J.; Shcherbachenko, E.; Jašík, J.; Roithová, J. Monoaurated: Vs. Diaurated Intermediates: Causality or Independence? *Chem. Sci.* **2020**, *11* (4), 980–988.
- (79) Škríba, A.; Schulz, J.; Roithová, J. Monitoring of Reaction Intermediates in the Gas Phase: Ruthenium-Catalyzed C-C Coupling. *Organometallics* **2014**, *33* (23), 6868–6878.
- (80) Zins, E.-L.; Pepe, C.; Schröder, D. Energy-Dependent Dissociation of Benzylpyridinium lons in an lon-Trap Mass Spectrometer. *J. Mass Spectrom.* **2010**, *45* (11), 1253–1260.
- (81) Morsa, D.; Gabelica, V.; Rosu, F.; Oomens, J.; De Pauw, E. Dissociation Pathways of Benzylpyridinium "Thermometer" lons Depend on the Activation Regime: An IRMPD Spectroscopy Study. *J. Phys. Chem. Lett.* **2014**, *5* (21), 3787–3791.
- (82) Carpenter, J. E.; McNary, C. P.; Furin, A.; Sweeney, A. F.; Armentrout, P. B. How Hot Are Your lons Really? A Threshold Collision-Induced Dissociation Study of Substituted Benzylpyridinium "Thermometer" lons. J. Am. Soc. Mass Spectrom. **2017**, *28* (9), 1876–1888.
- (83) Rahrt, R.; Auth, T.; Demireva, M.; Armentrout, P. B.; Koszinowski, K. Benzhydrylpyridinium Ions: A New Class of Thermometer Ions for the Characterization of Electrospray-Ionization Mass Spectrometers. Anal. Chem. 2019, 91 (18), 11703–11711.
- (84) Andris, E.; Segers, K.; Mehara, J.; Rulíšek, L.; Roithová, J. Closed Shell Iron(IV) Oxo Complex with an Fe–O Triple Bond: Computational Design, Synthesis, and Reactivity. *Angew. Chemie Int. Ed.* **2020**, *59* (51), 23137–23144.
- (85) Roithová, J.; Gray, A.; Andris, E.; Jašík, J.; Gerlich, D. Helium Tagging Infrared Photodissociation Spectroscopy of Reactive Ions. *Acc. Chem. Res.* **2016**, *49* (2), 223–230.
- (86) Jašík, J.; Navrátil, R.; Němec, I.; Roithová, J. Infrared and Visible Photodissociation Spectra of Rhodamine lons at 3 K in the Gas Phase. *J. Phys. Chem. A* **2015**, *119* (51), 12648–12655.

- (87) Casini, A.; Diawara, M. C.; Scopelliti, R.; Zakeeruddin, S. M.; Grätzel, M.; Dyson, P. J. Synthesis, Characterisation and Biological Properties of Gold(Iii) Compounds with Modified Bipyridine and Bipyridylamine Ligands. J. Chem. Soc. Dalt. Trans. 2010, 39 (9), 2239–2245.
- (88) Balasubramani, S. G.; Chen, G. P.; Coriani, S.; Diedenhofen, M.; Frank, M. S.; Franzke, Y. J.; Furche, F.; Grotjahn, R.; Harding, M. E.; Hättig, C.; Hellweg, A.; Helmich-Paris, B.; Holzer, C.; Huniar, U.; Kaupp, M.; Marefat Khah, A.; Karbalaei Khani, S.; Müller, T.; Mack, F.; Nguyen, B. D.; Parker, S. M.; Perlt, E.; Rappoport, D.; Reiter, K.; Roy, S.; Rückert, M.; Schmitz, G.; Sierka, M.; Tapavicza, E.; Tew, D. P.; van Wüllen, C.; Voora, V. K.; Weigend, F.; Wodyński, A.; Yu, J. M. TURBOMOLE: Modular Program Suite for Ab Initio Quantum-Chemical and Condensed-Matter Simulations. J. Chem. Phys. 2020, 152 (18), 184107.
- (89) Perdew, J. P.; Burke, K.; Ernzerhof, M. Generalized Gradient Approximation Made Simple. Phys. Rev. Lett. 1996, 77 (18), 3865-3868.
- (90) Pritchard, B. P.; Altarawy, D.; Didier, B.; Gibson, T. D.; Windus, T. L. New Basis Set Exchange: An Open, Up-to-Date Resource for the Molecular Sciences Community. J. Chem. Inf. Model. 2019, 59 (11), 4814-4820.
- (91) Feller, D. The Role of Databases in Support of Computational Chemistry Calculations. J. Comput. Chem. 1996, 17 (13), 1571-1586.
- (92) Schuchardt, K. L.; Didier, B. T.; Elsethagen, T.; Sun, L.; Gurumoorthi, V.; Chase, J.; Li, J.; Windus, T. L. Basis Set Exchange: A Community Database for Computational Sciences. J. Chem. Inf. Model. **2007**, 47 (3), 1045–1052.
- (93) Clark, T.; Chandrasekhar, J.; Spitznagel, G. W.; Schleyer, P. V. R. Efficient Diffuse Function-Augmented Basis Sets for Anion Calculations. III. The 3-21+G Basis Set for First-Row Elements, Li-F. J. Comput. Chem. 1983, 4 (3), 294-301.
- (94) Krishnan, R.; Binkley, J. S.; Seeger, R.; Pople, J. A. Self-consistent Molecular Orbital Methods. XX. A Basis Set for Correlated Wave Functions. J. Chem. Phys. 1980, 72 (1), 650-654.
- (95) Dolg, M.; Wedig, U.; Stoll, H.; Preuss, H. Energy-adjusted a binitio Pseudopotentials for the First Row Transition Elements. J. Chem. Phys. 1987, 86 (2), 866-872.
- (96) Schwerdtfeger, P.; Dolg, M.; Schwarz, W. H. E.; Bowmaker, G. A.; Boyd, P. D. W. Relativistic Effects in Gold Chemistry. I. Diatomic Gold Compounds. J. Chem. Phys. 1989, 91 (3), 1762–1774.
- (97) te Velde, G.; Bickelhaupt, F. M.; Baerends, E. J.; Fonseca Guerra, C.; van Gisbergen, S. J. A.; Snijders, J. G.; Ziegler, T. Chemistry with ADF. J. Comput. Chem. 2001, 22 (9), 931–967.
- (98) Lenthe, E. van; Baerends, E. J.; Snijders, J. G. Relativistic Regular Two-component Hamiltonians. J. Chem. Phys. 1993, 99 (6), 4597-4610.
- (99) van Lenthe, E.; Baerends, E. J.; Snijders, J. G. Relativistic Total Energy Using Regular Approximations. J. Chem. Phys. 1994, 101 (11), 9783-9792.
- (100) van Lenthe, E.; Ehlers, A.; Baerends, E.-J. Geometry Optimizations in the Zero Order Regular Approximation for Relativistic Effects. J. Chem. Phys. 1999, 110 (18), 8943–8953.
- (101) Bader, R. F. W. Atoms in Molecules: A Quantum Theory; Clarendon Press, Oxford; New York, 1990.
- (102) Keith, T. A. AIMAII; TK Gristmill Software, Overland Park KS, USA, 2019.
- (103) Glendening, E. D.; Badenhoop, J. K.; Reed, A. E.; Carpenter, J. E.; Bohmann, J. A.; Morales, C. M.; Karafiloglou, P.; Landis, C. R.; Weinhold, F. NBO 7.0. Theoretical Chemistry Institute, University of Wisconsin, Madison.
- (104) Carpenter, J. E.; Weinhold, F. Analysis of the Geometry of the Hydroxymethyl Radical by the "Different Hybrids for Different Spins" Natural Bond Orbital Procedure. J. Mol. Struct. THEOCHEM **1988**, *169*, 41–62.
- (105) Foster, J. P.; Weinhold, F. Natural Hybrid Orbitals. J. Am. Chem. Soc. 1980, 102 (24), 7211–7218.

- (106) Reed, A. E.; Weinhold, F. Natural Bond Orbital Analysis of Near-Hartree–Fock Water Dimer. *J. Chem. Phys.* **1983**, *78* (6), 4066–4073.
- (107) Reed, A. E.; Weinstock, R. B.; Weinhold, F. Natural Population Analysis. *J. Chem. Phys.* **1985**, *83* (2), 735–746.
- (108) Glendening, E. D.; Landis, C. R.; Weinhold, F. NBO 7.0: New Vistas in Localized and Delocalized Chemical Bonding Theory. *J. Comput. Chem.* **2019**, *40* (25), 2234–2241.
- (109) Motloch, P.; Jašík, J.; Roithová, J. Gold(I) and Silver(I) π -Complexes with Unsaturated Hydrocarbons. *Organometallics* **2021**, *40* (10), 1492–1502.
- (110) Rezsnyak, C. E.; Autschbach, J.; Atwood, J. D.; Moncho, S. Reactions of Gold(III) Complexes with Alkenes in Aqueous Media: Generation of Bis-(β -Hydroxyalkyl)Gold(III) Complexes. *J. Coord. Chem.* **2013**, *66* (7), 1153–1165.

Appendices

For detailed supplementary information: Mehara, J.; Koovakattil Surendran, A.; van Wieringen, T.; Setia, D.; Foroutan-Nejad, C.; Straka, M.; Rulíšek, L.; Roithová, J. Cationic Gold(II) Complexes: Experimental and Theoretical Study**. Chem. – A Eur. J. **2022**, 28 (60), e202201794.

It can be accessed via https://doi.org/10.34973/pdan-6826 upon request of the promotor or the IMM data steward.

Mass spectrometric studies:

The experiments were performed on either Thermo Scientific LTO XL linear trap or Finnigan LCQ Deca XP mass spectrometer equipped with an electrospray ionization (ESI) source. 109 General conditions were as follows: sheath gas 5-40 arbitrary unit, auxiliary gas 0-5 arbitrary unit, capillary temperature 150-220 °C, spray voltage 2-5 kV, capillary voltage 0-50 V and tube lens 0-150 V.

Helium tagging photodissociation method was used to measure the IR spectra of the mass selected complexes on the ISORI instrument equipped with ESI source.85 The ISORI instrument features a wire quadrupole trap operated at 3-5K, trapped ions are cooled down because of the helium buffer gas. These cooled ions then attach a helium atom, the helium complexes on irradiation with the IR laser undergo helium detachment and the IR spectra is constructed as $(1 - N_i/N_{i0})$, where N_i and N_{i0} are numbers of helium complexes with and without laser irradiation. For irradiation OPO/OPA system from LaserVision was used.

The energy resolved collision induced dissociation (CID) experiments were performed on LCQ Deca mass spectrometer with an ESI source. The collision energies in the LCQ ion trap was calibrated based on the measurements of dissociation energies of series of thermometer ion consisting of benzylpyridinium and benzhydrylpyridinium thermometer ions using Schroder's method.80,82,83 The complexes were measured for 2-4 times to calculate the standard deviation.

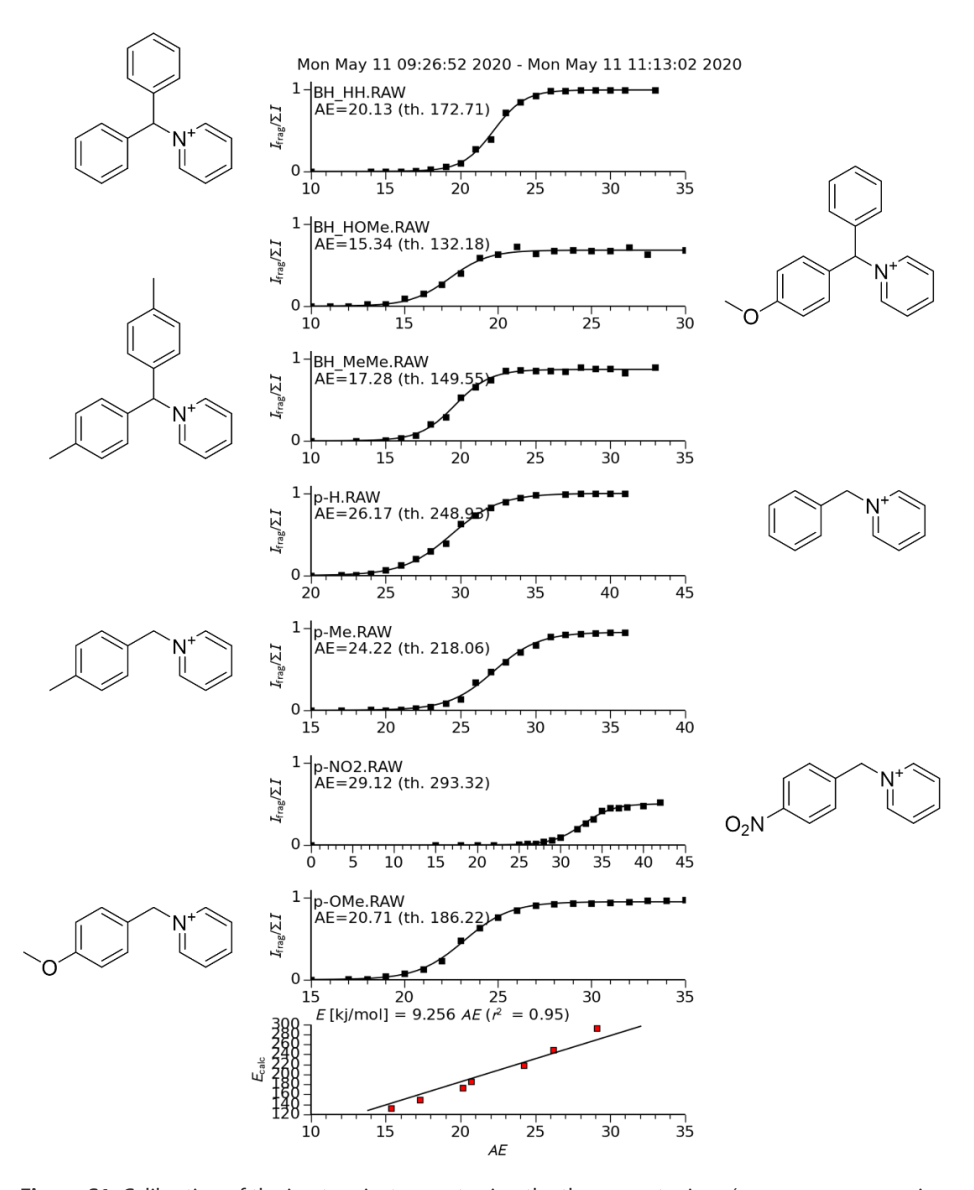


Figure S1. Calibration of the ion trap instrument using the thermometer ions (appearance energy i.e. AE for a set of thermometer ions is plotted against the known bond dissociation energy).

ESI spectrum of various ligands from Table 1 with AuX, (Source spectrum, CIDs and(/or) energy resolved CIDs)

2,2'-bipyridine with AuCl, 1)

Sample preparation: 100 μ L of 1 mM AuCl₃ in Acetonitrile (ACN) + 100 μ L of 1 mM bipyridine (bipy) in dichloromethane (DCM) + 0.8 mL DCM.

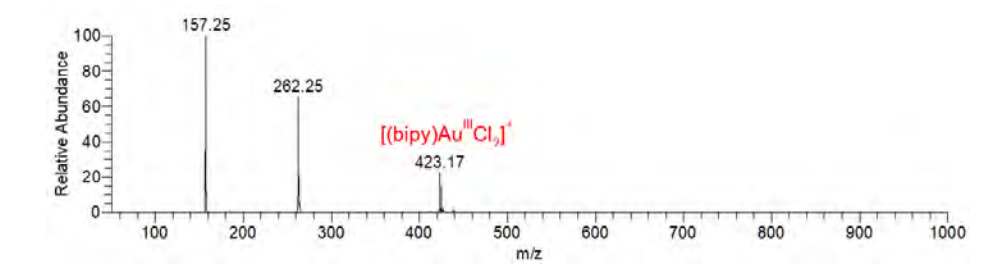


Figure S2. Source spectrum of 2,2'-bipyridine with AuCl,

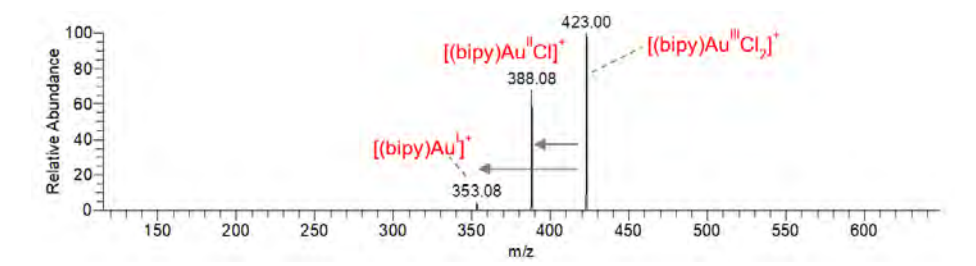


Figure S3. CID of m/z 423 at C.E = 16.5%

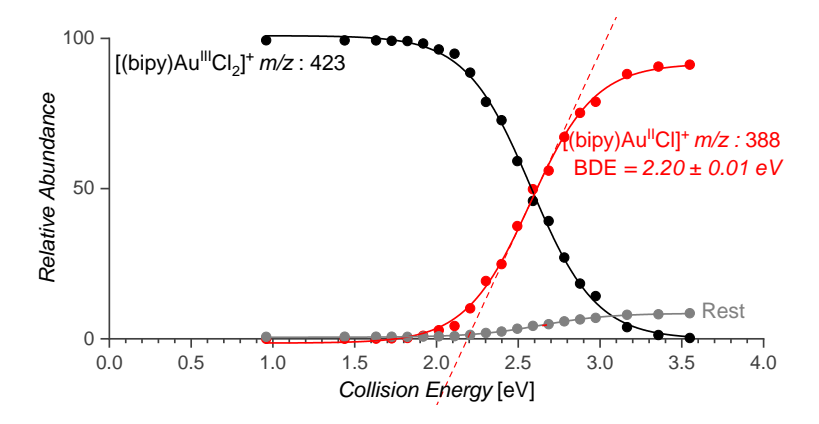


Figure S4. Energy Resolved CID of m/z 423

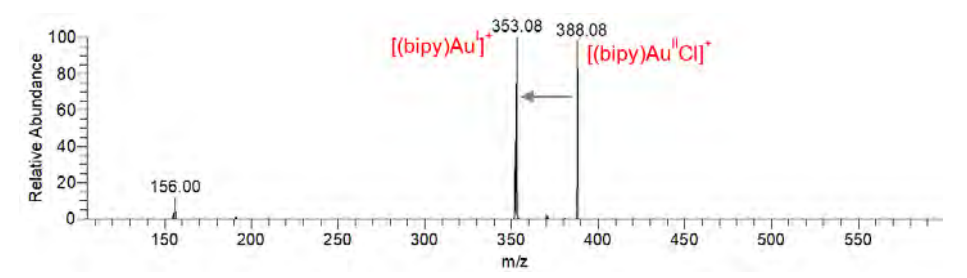


Figure S5. CID of m/z 388 at C.E = 29%

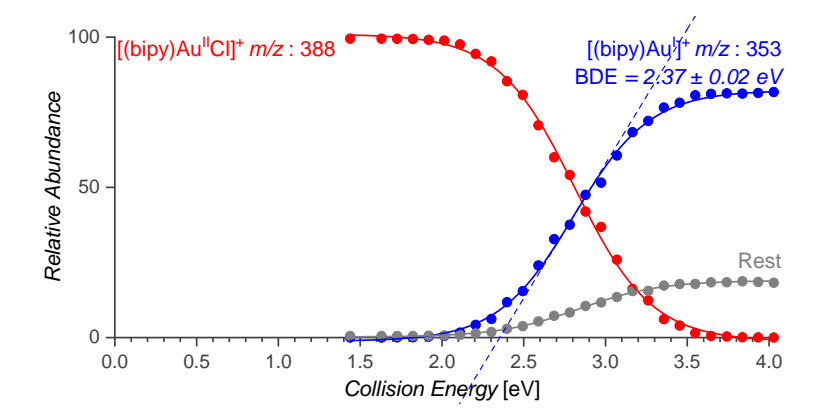


Figure S6. Energy Resolved CID of m/z 388

Similarly source spectra and energy resolved collision induced dissociation datasets for all other ligands and metals can be accessed via https://doi.org/10.34973/pdan-6826 upon request of the promotor or the IMM data steward.

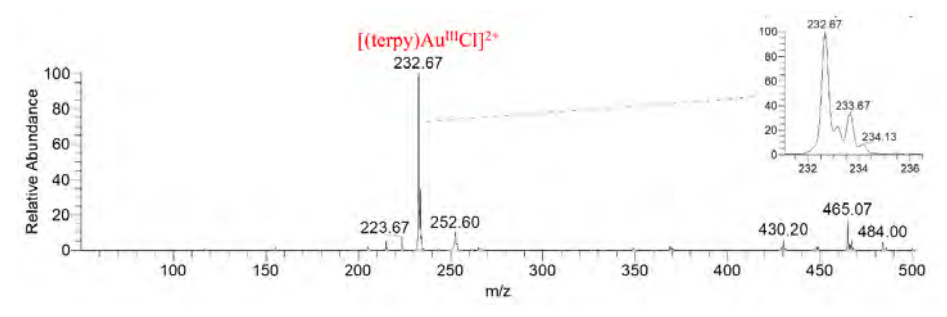


Figure S7. [Au(terpy)(CI)](PF₆)₂ dissolved in acetonitrile

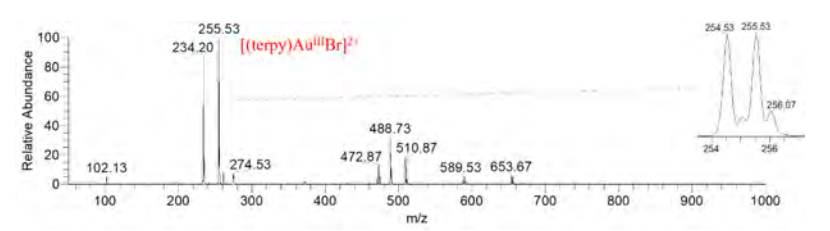


Figure S8. [Au(terpy)(Br)](PF₆), dissolved in acetonitrile

Synthesis of gold(III) complexes

Using the synthesis procedure described by Casini et al., gold(III) complexes of bipyridine, phenanthroline and terpyridine with CI or Br and PF₆ as counterion were prepared.⁸⁷ To 1 eq. of the ligand in acetonitrile, aqueous solution of 1 eq. of KAuX₄ or AuX₃ was added and the mixture refluxed for 12-24 hrs. Followed by addition of 3 eq. of KPF₆ and refluxed for another 2-3 hours. The solution was cooled to room temperature and the precipitate was filtered, washed with cold water (3X) and dried under vacuum. These complexes were used for electrochemical studies.

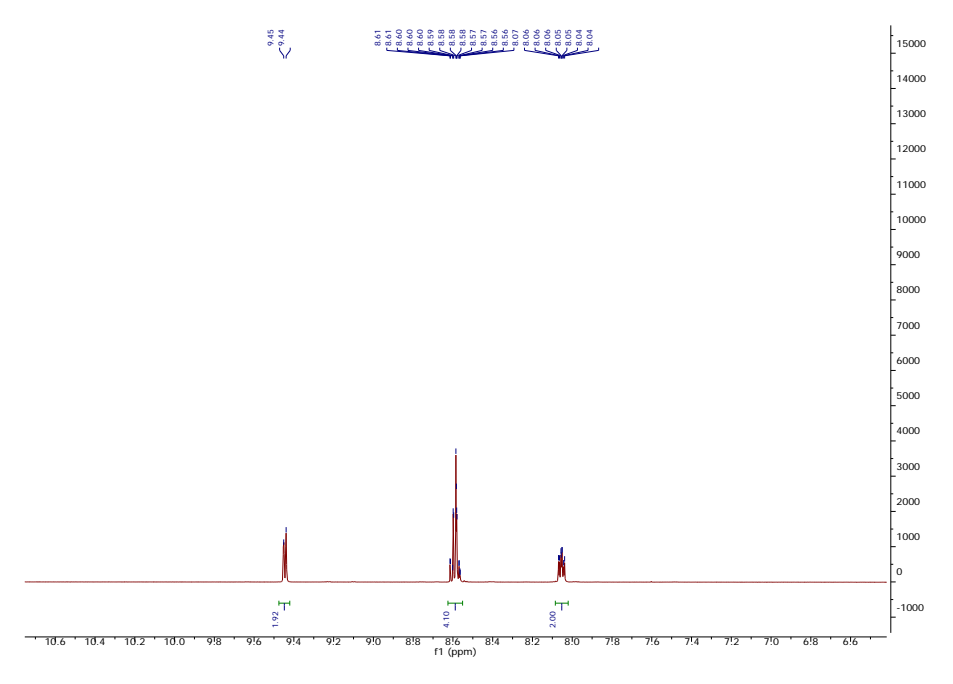
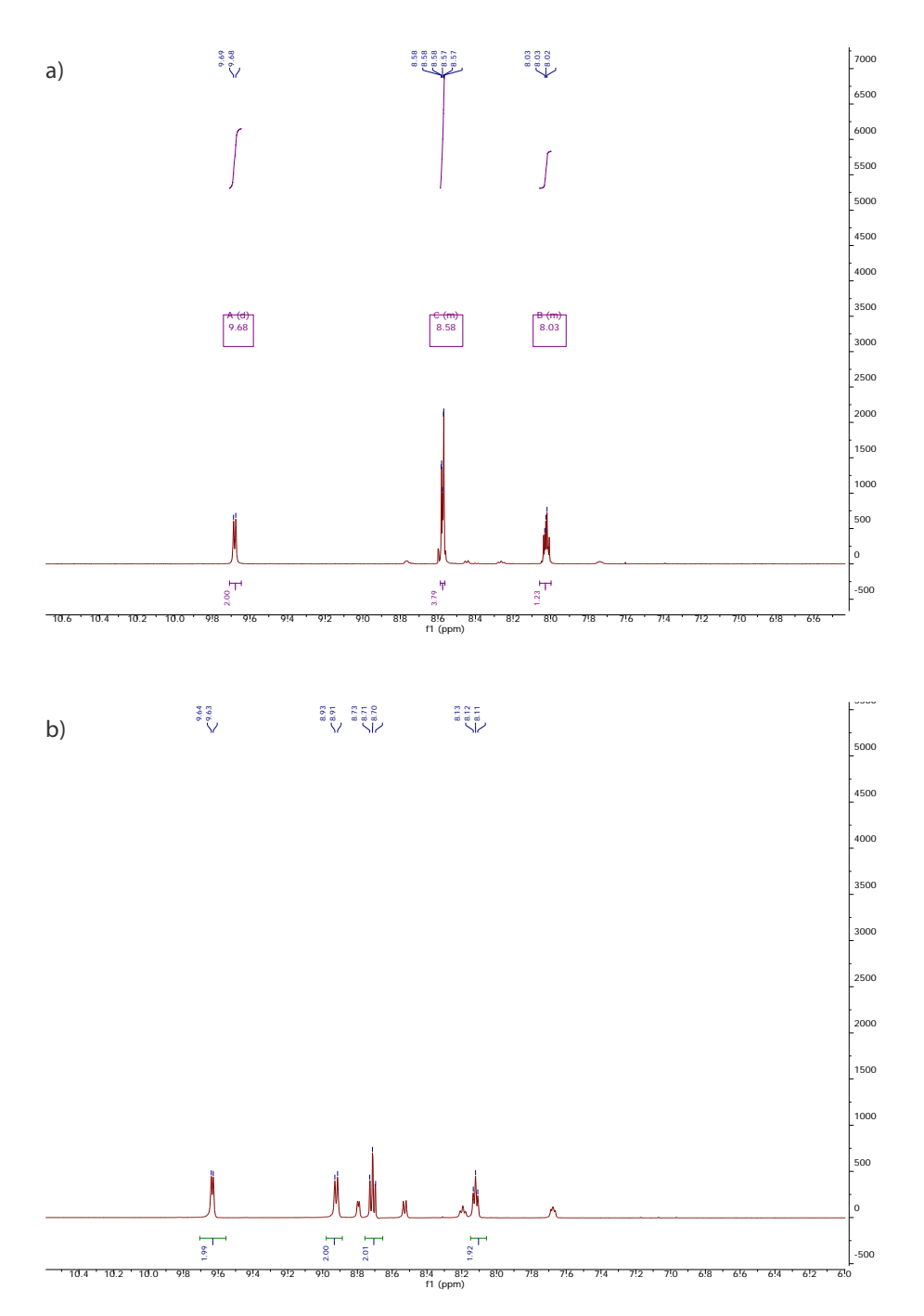


Figure S9. 1H NMR in CD₃CN of gold(III) complex prepared with bipy, gold(III) chloride with PF₆ counterion [Au(bipy)Cl₂]PF₆

¹H NMR (500 MHz, CD₃CN) δ 9.47 – 9.42 (d, 2H), 8.63 – 8.55 (m, 4H), 8.10 – 8.01 (td, 2H). NMR matches with the literature values of the complex. 110



 $\textbf{Figure $10.} \ ^{1}\text{H NMR of gold(III) complex prepared with bipy, gold(III) bromide with PF}_{6} \ counterion \ [\text{Au(bipy)Br}_{2}]\text{PF}_{6}-\text{a) CD}_{3}\text{CN and b) DMSO-d}_{6}$

¹H NMR (500 MHz, CD₃CN) δ 9.68 (d, J = 6.0 Hz, 2H), 8.59 – 8.54 (m, 4H), 8.09 – 7.98 (m, 1H).

1H NMR (500 MHz, DMSO) δ 9.64 – 9.63 (d, 2H), 8.93 – 8.91 (d, 2H), 8.73 – 8.70 (t, 2H), 8.13 - 8.11 (t, 2H).

As noted in the literature for similar gold(III) complexes, the low intensity signals are due to the degradation of the complex in DMSO-d_s.75

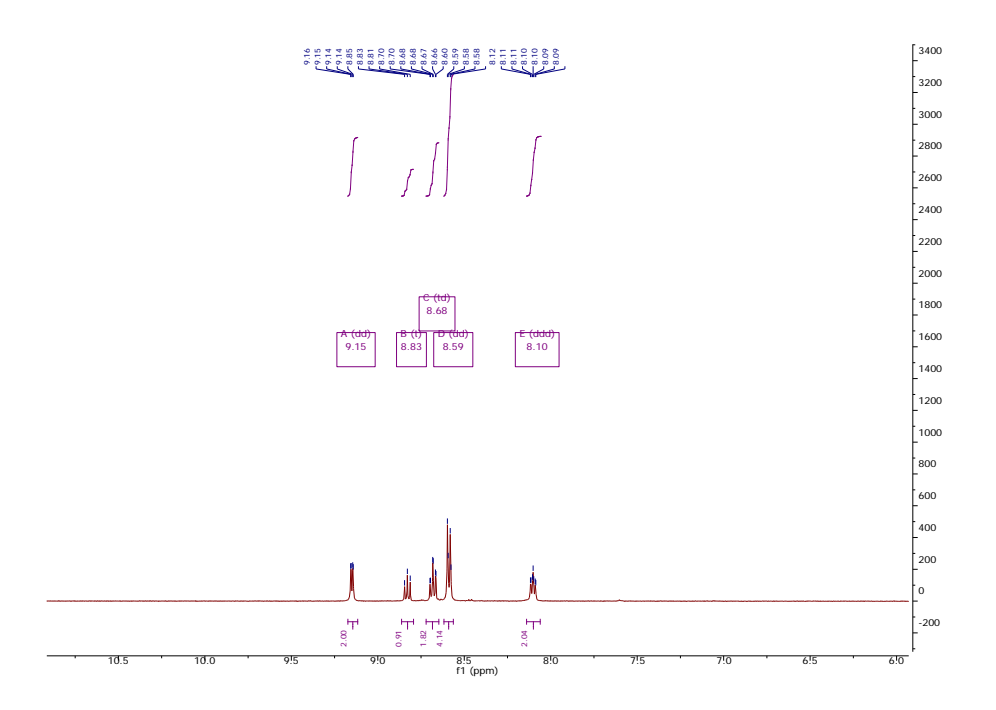


Figure S11. 1H NMR in CD₃CN of gold(III) complex prepared with terpy, gold(III) chloride with PF₆ counterion [Au(terpy)CI](PF₆),

 1 H NMR (500 MHz, CD $_{3}$ CN) δ 9.15 (dd, J = 6.0, 1.5 Hz, 2H), 8.83 (t, J = 8.2 Hz, 1H), 8.68 (td, J = 7.9, 1.5 Hz, 2H), 8.59 (dd, J = 8.1, 2.2 Hz, 4H), 8.10 (ddd, J = 7.7, 6.0, 1.6 Hz, 2H).

NMR compares well with the literature values of the same complex (shifts observed because of different solvents used).75

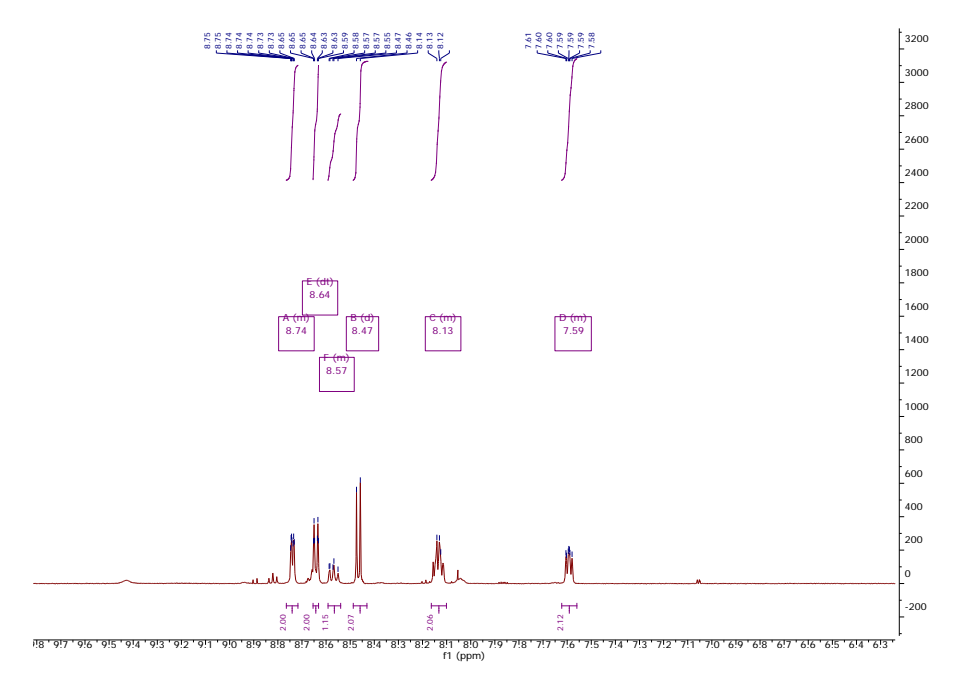
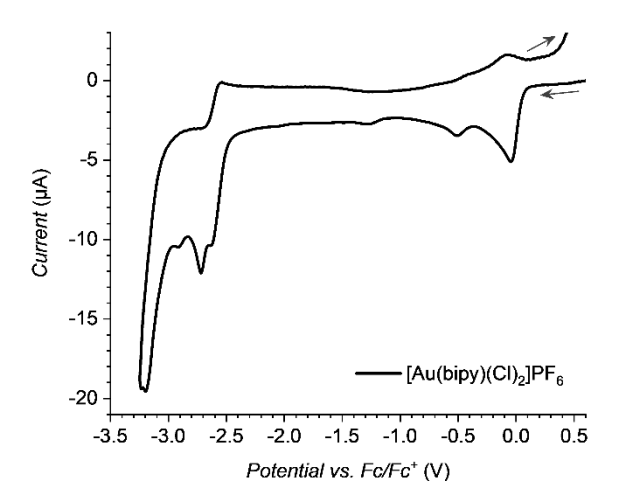


Figure S12. ¹H NMR in CD_3CN of gold(III) complex prepared with bipy, gold(III) bromide with PF_6 counterion [Au(terpy)Br](PF_6)₂

¹H NMR (500 MHz, CD_3CN) δ 8.76 – 8.72 (m, 2H), 8.64 (dt, J = 8.0, 1.1 Hz, 2H), 8.59 – 8.54 (m, 1H), 8.47 (d, J = 7.9 Hz, 2H), 8.16 – 8.10 (m, 2H), 7.62 – 7.56 (m, 2H).

As noted in the literature for similar gold(III) complexes, the low intensity signals are due to the degradation of the complex; we have also observed a precipitation overtime.⁷⁵

Electrochemistry experiments



 $\textbf{Figure S13.} \ \, \textbf{Cyclic voltammogram (CV) of } \, [\textbf{Au(bipy)(Cl)}_2] \textbf{PF}_6 \ \, \textbf{(0.25mM) measured in TBAPF}_6 \ \, \textbf{(0.1M) in}$ DMF with a scan rate of 100 mV/s.

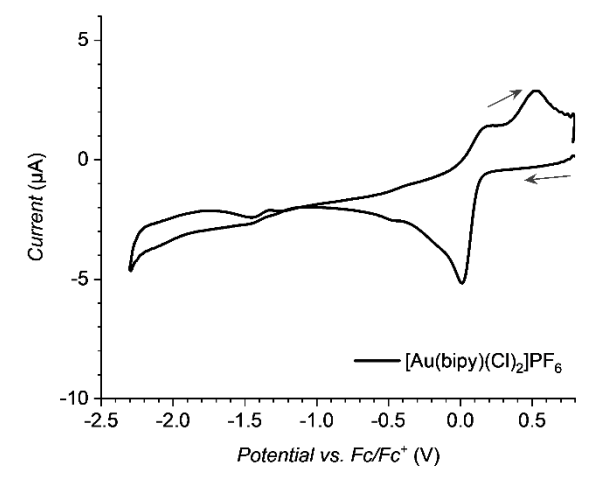


Figure S14. Cyclic voltammogram (CV) of $[Au(bipy)(CI)_2]PF_6$ (0.25mM) measured in TBAPF $_6$ (0.1M) in DCM with a scan rate of 100 mV/s.

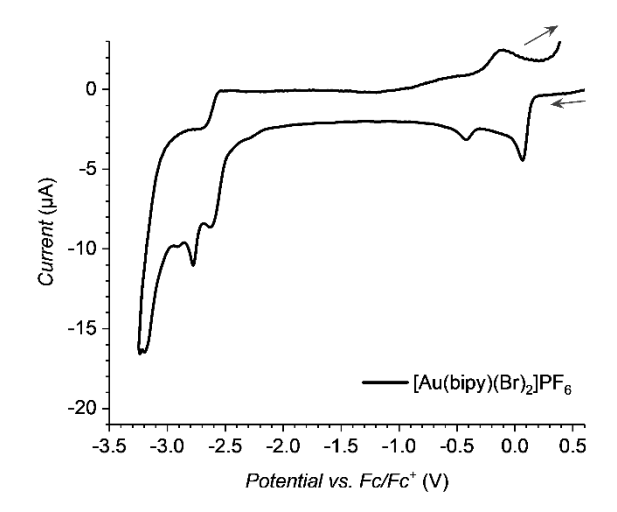


Figure S15. Cyclic voltammogram (CV) of $[Au(bipy)(Br)_2]PF_6$ (0.25mM) measured in TBAPF $_6$ (0.1M) in DMF with a scan rate of 100 mV/s.

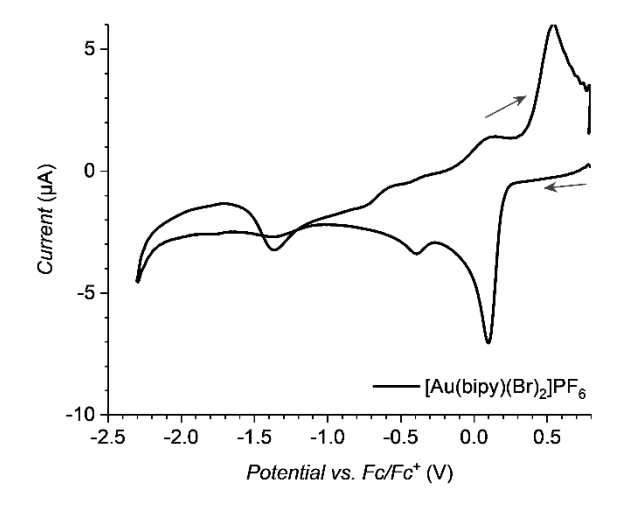


Figure S16. Cyclic voltammogram (CV) of $[Au(bipy)(Br)_2]PF_6$ (0.25mM) measured in TBAPF $_6$ (0.1M) in DCM with a scan rate of 100 mV/s.

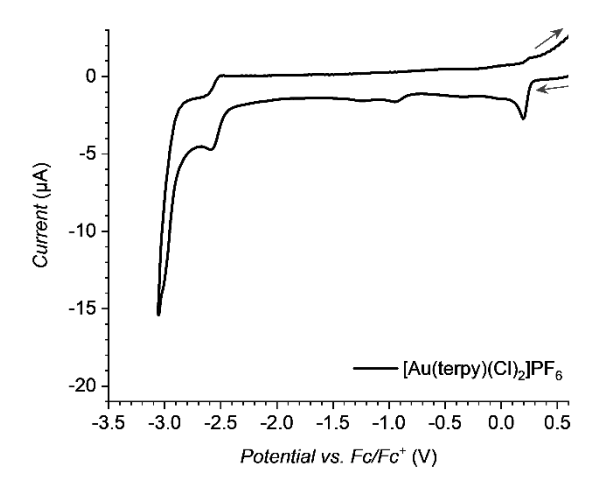
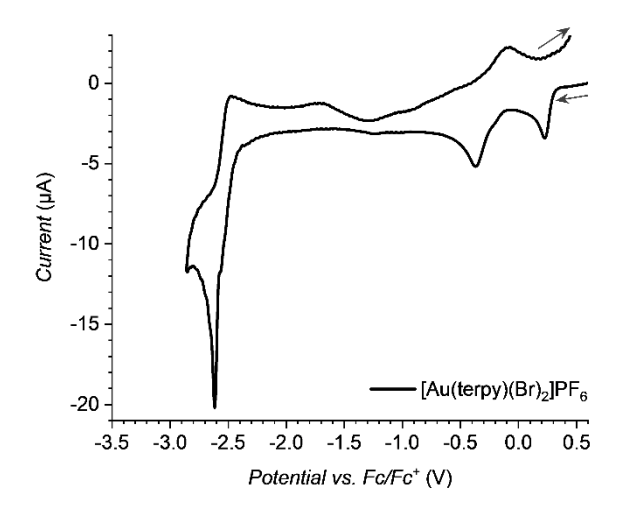


Figure S17. Cyclic voltammogram (CV) of [Au(terpy)(Cl)](PF₆)₂ (0.25mM) measured in TBAPF₆ (0.1M) in DMF with a scan rate of 100 mV/s.



 $\textbf{Figure S18.} \ \text{Cyclic voltammogram (CV) of } [\text{Au(terpy)(Br)}] (\text{PF}_6)_2 (0.25 \text{mM}) \ \text{measured in TBAPF}_6 \ (0.1 \text{M}) \ \text{in}$ DMF with a scan rate of 100 mV/s.

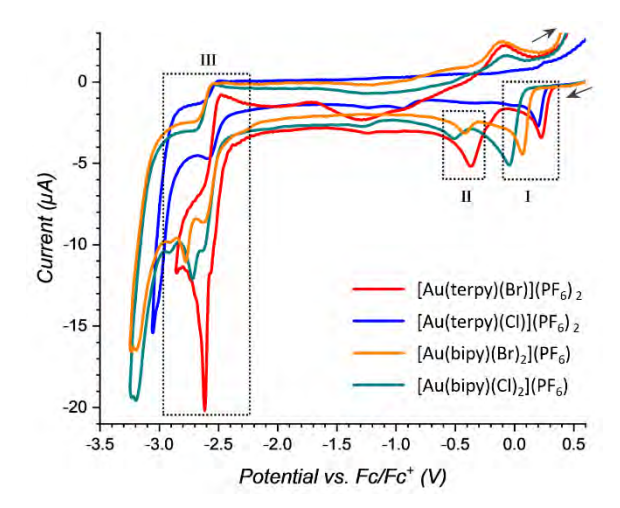


Figure S19. Overlaid cyclic voltammogram (CV) of $[Au(bipy)(Cl)_2]PF_6$ (dark cyan), $[Au(bipy)(Br)_2]PF_6$ (orange), $[Au(terpy)(Cl)](PF_6)_2$ (dark blue) and $[Au(terpy)(Br)]PF_6)_2$ (red) (0.25mM) measured in TBAPF_6 (0.1M) in DMF with a scan rate of 100 mV/s. Region I corresponds to the reduction of $Au(III) \rightarrow Au(I)$ of the corresponding gold(III) complexes.^{31,33} The region II corresponds to the reduction of free Au(III) salt present in the complex, this is further confirmed by performing CV experiments with $AuCl_3$ and $AuBr_3$ salts (Figure S21). Region III includes the reduction of $Au(II) \rightarrow Au(0)$ and the ligand reduction (the ligand reduction is shown in the figure S21).

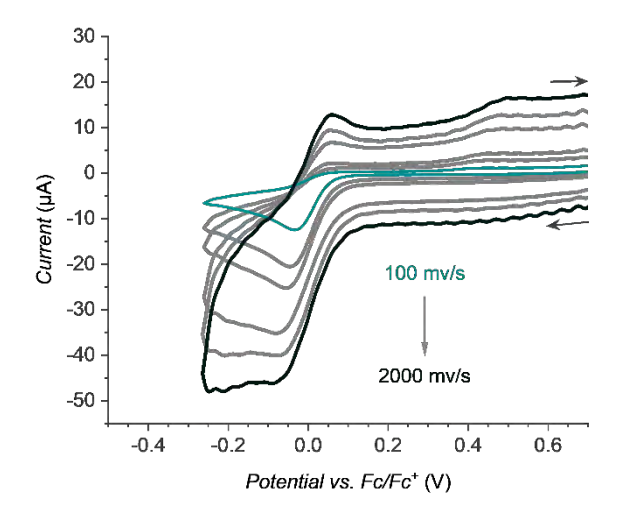


Figure S20. Cyclic voltammogram of [Au(bipy)(CI)₂]PF₆ in DMF (0.5 mM) at various scan rates (100, 300, 500, 1000, 1500 and 2000 mV/s) in the range of the Au^{III} → Au^I reduction potential

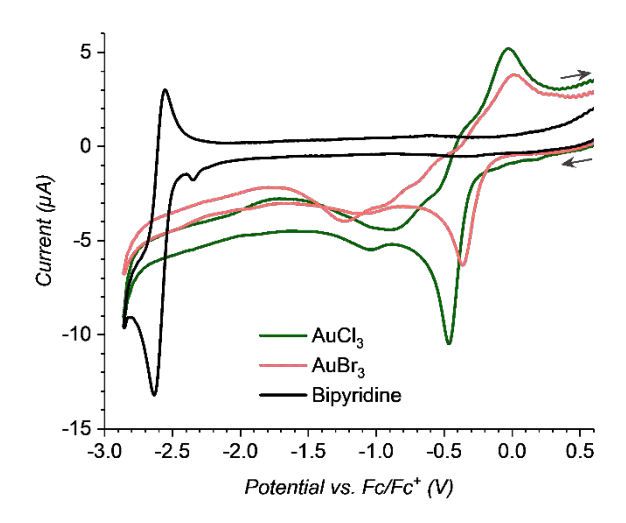


Figure S21. Cyclic voltammogram of gold salts AuCl₃, AuBr₃ and 2,2'-bipyridine ligand in DMF (0.5 mM) at a scan rate of 100 mV/s.

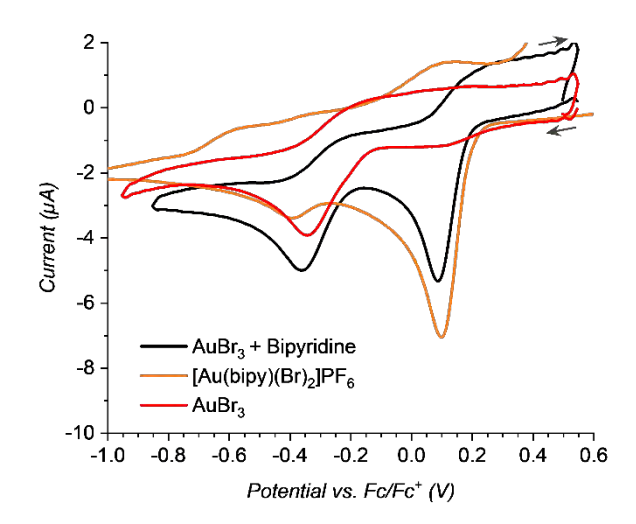


Figure S22. Cyclic voltammogram of AuBr₃ salt mixed with 2,2'-bipyridine (black), the synthesized complex [Au(bipy)(Br)₂]PF₆ (orange), and AuBr₃ salt (red) in DMF at a scan rate of 100 mV/s. The mixing of AuBr₃ with bipyridine also shows the same reduction peak of [Au(bipy)(Br)₂]PF₆ (synthesized separately) indicative of the formation same gold(III) complex.

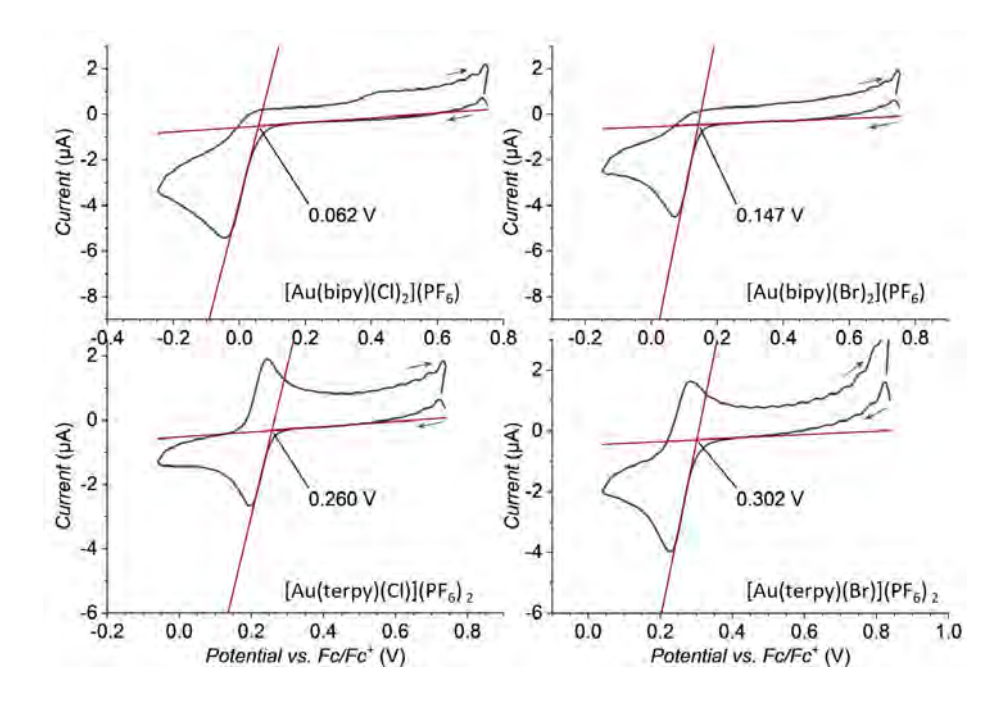


Figure S23. Calculation of the onset potentials using tangent line intersection from the cyclic voltammogram for gold(III) complexes in DMF (0.25 mM) at a scan rate of 100 mV/s.

IRPD and Vis spectra

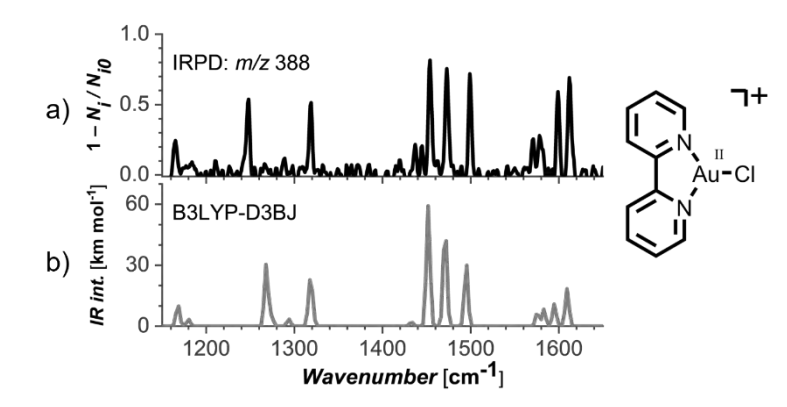


Figure 524. a) The experimental IR spectra of [Au(bipy)(CI)]+ measured by helium tagging photodissociation spectroscopy and b) Theoretically predicted IR spectra of [Au(bipy)(CI)]+ calculated by B3LYP-D3BJ/SDD, scaling factor: 0.98.

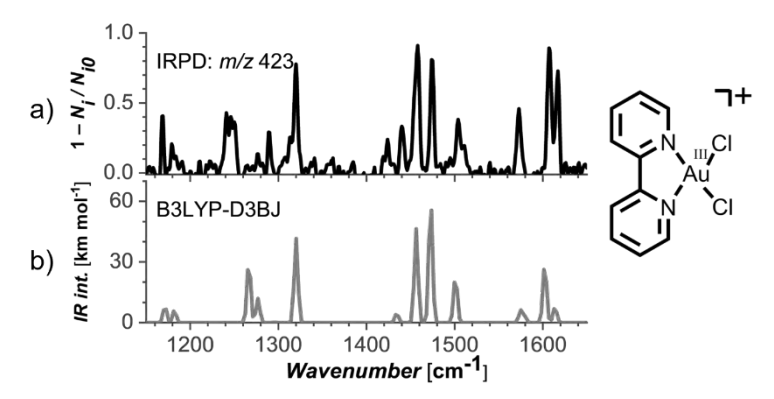


Figure S25. a) The experimental IR spectra of [Au(bipy)(CI),]+ measured by helium tagging photodissociation spectroscopy and b) Theoretically predicted IR spectra of [Au(bipy)(CI),]+calculated by B3LYP-D3BJ/SDD, scaling factor: 0.98.

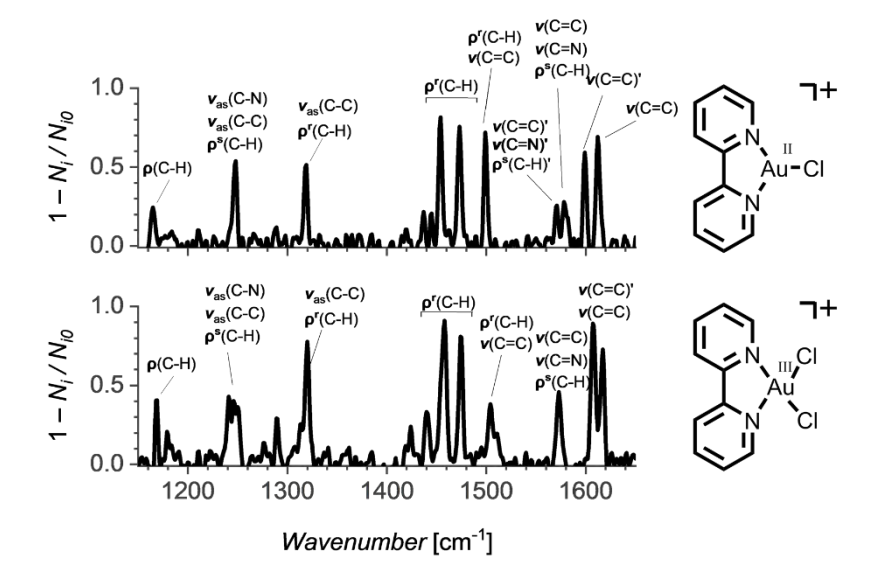


Figure S26. Experimental IR spectra comparison of the [Au^{III}(bipy)Cl]⁺ and [Au^{III}(bipy)Cl₂]⁺ with tentative assignment of the vibration modes. Note: is a stretching vibration, as is an asymmetric stretching vibration, is a general in-plane vibration, 'is a rocking vibration and 's is a scissoring vibration.

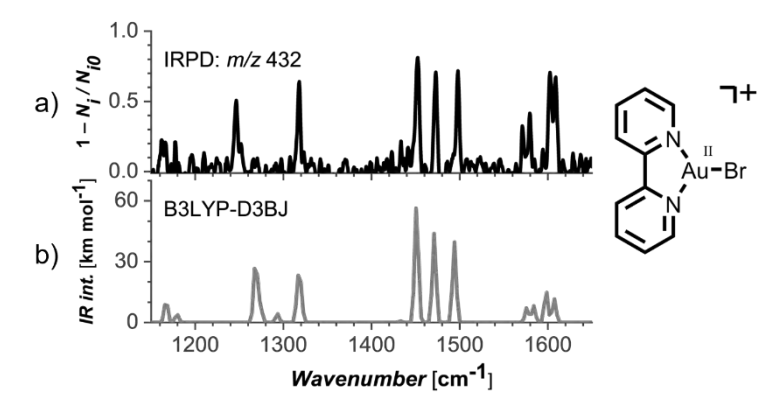


Figure S27. a) The experimental IR spectra of [Au(bipy)(Br)]⁺ measured by helium tagging photodissociation spectroscopy. b) Theoretically predicted IR spectra of [Au(bipy)(Br)]⁺ calculated by B3LYP-D3BJ/SDD, scaling factor: 0.98.

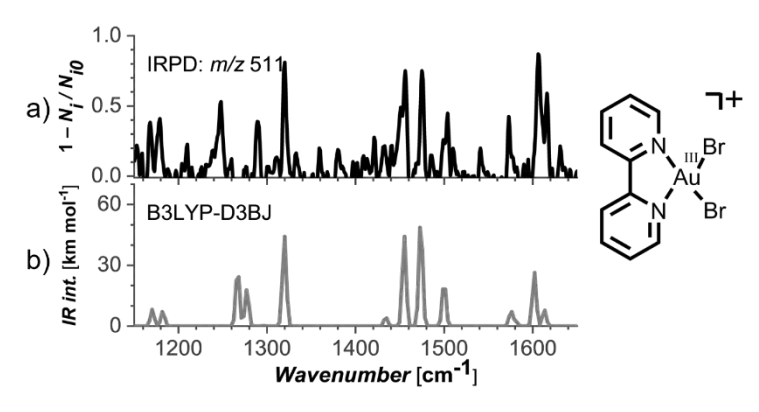


Figure S28. a) The experimental IR spectra of [Au(bipy)(Br)₂]⁺ measured by helium tagging photodissociation spectroscopy. b) Theoretically predicted IR spectra of [Au(bipy)(Br)₂]⁺ calculated by B3LYP-D3BJ/SDD, scaling factor: 0.98.

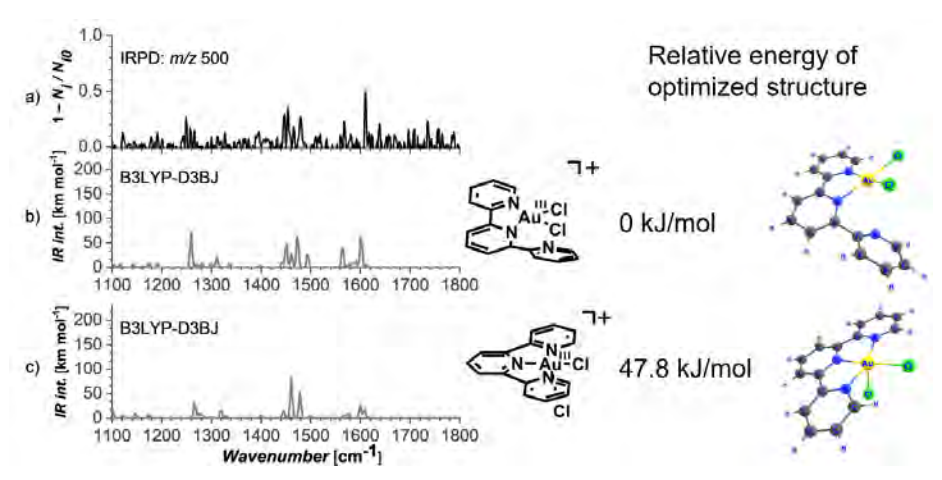


Figure S29. a) The experimental IR spectra of [Au(terpy)(CI),]+ measured by helium tagging photodissociation spectroscopy. b) Theoretically predicted IR spectra of [Au(terpy)(CI),]+calculated by B3LYP-D3BJ/SDD, scaling factor: 0.98. c) Theoretically predicted IR spectra of [Au(terpy)(Cl),]+calculated by B3LYP-D3BJ/SDD, scaling factor: 0.98.

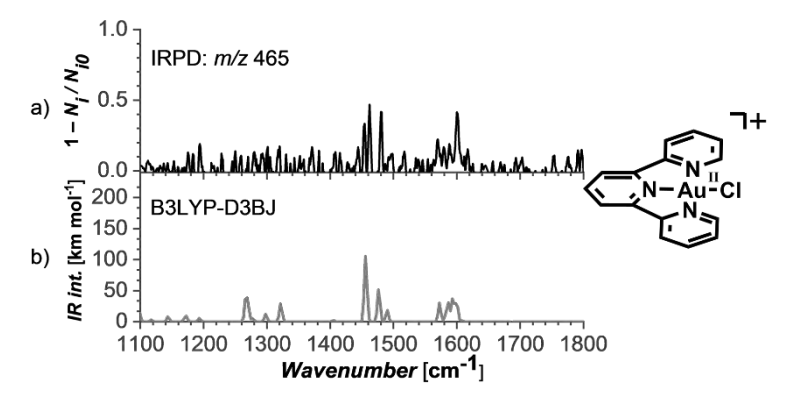


Figure S30. a) The experimental IR spectra of [Au(terpy)(CI)]+ measured by helium tagging photodissociation spectroscopy. b) Theoretically predicted IR spectra of [Au(terpy)(Cl)]⁺ calculated by B3LYP-D3BJ/SDD, scaling factor: 0.98.

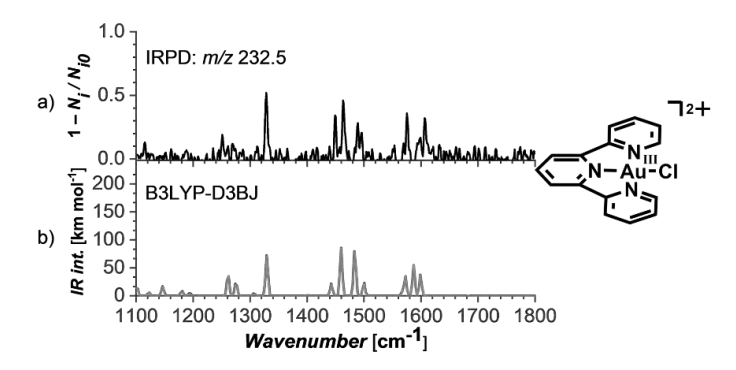


Figure S31. a) The experimental IR spectra of [Au(terpy)(Cl)]²⁺ measured by helium tagging photodissociation spectroscopy. b) Theoretically predicted IR spectra of [Au(terpy)(Cl)]²⁺ calculated by B3LYP-D3BJ/SDD, scaling factor: 0.98.

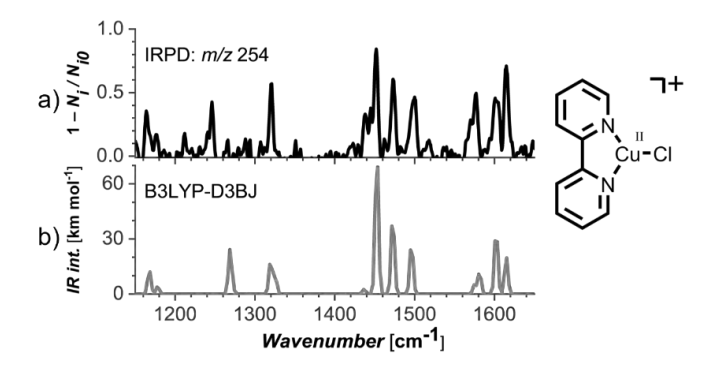


Figure S32. a) The experimental IR spectra of [Cu(bipy)(Cl)]⁺ measured by helium tagging photodissociation spectroscopy and b) Theoretically predicted IR spectra of [Cu(bipy)(Cl)]⁺ calculated by B3LYP-D3BJ/SDD, scaling factor: 0.98.

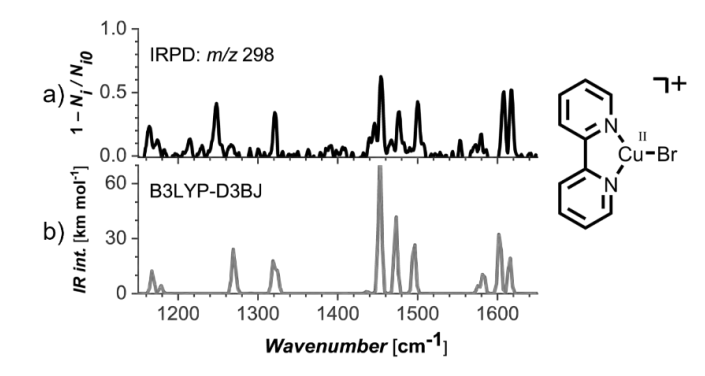


Figure S33. a) The experimental IR spectra of [Cu(bipy)(Br)]⁺ measured by helium tagging photodissociation spectroscopy and b) Theoretically predicted IR spectra of [Cu(bipy)(Br)]⁺ calculated by B3LYP-D3BJ/SDD, scaling factor: 0.98.

Theoretical Details

Table S1. Overview of experimental and theoretical bond dissociation energies of [Au(Lig)(X)_]+ complexes (n = 1 or 2).

Reaction	action BDE _{expt} [kJ BDE _{theo} [kJ mol ⁻¹] mol ⁻¹]		B3LYP-D3/6-311+G**SDD on Au, Br and I	
		B3LYP-D3BJ/ Def2VTZPP	B3LYP-D3/6- 311+G**Def2TZVPD on Au	[Au ^{III} (bipy)(Cl) ₂] ⁺ [rechts] [Au ^{II} (bipy)(Cl)] ⁺ + Cl·
213 ± 1	215	246	226	$[Au^{II}(bipy)(CI)]^{+} \rightarrow$ $[Au^{I}(bipy)]^{+} + CI^{-}$
228 ± 2	235	266	246	$[Au^{\parallel}(bipy)(Br)_{2}]^{+} \rightarrow$ $[Au^{\parallel}(bipy)(Br)]^{+} + Br$
169 ± 5	172	214	197	$[Au^{II}(bipy)(Br)]^{+} \rightarrow$ $[Au^{I}(bipy)]^{+} + Br$
196 ± 4	203	247	231	$[Au^{\parallel}(bipy)(I)_{2}]^{+} \rightarrow$ $[Au^{\parallel}(bipy)(I)]^{+} + I^{-}$
128 ± 2	146	123		$[Au''(bipy)(I)]^+ \rightarrow [Au'(bipy)]^+ + I^-$
178 ± 2	197	230		$[Au^{\parallel}(terpy)(Cl)_{2}]^{+} \rightarrow$ $[Au^{\parallel}(terpy)(Cl)]^{+} + Cl^{-}$
155 ± 3	125		136	$[Au''(terpy)(Cl)]^+ \rightarrow [Au'(terpy)]^+ + Cl^-$
226 ± 1	224		232	$[Au^{\parallel}(terpy)(Br)_2]^+ \rightarrow$ $[Au^{\parallel}(terpy)(Br)]^+ + Br$
108 ± 6	86		114	$[Au''(terpy)(Br)]^{+} \rightarrow \\ [Au'(terpy)]^{+} + Br$
191 ± 1	188		209	

Method calibration for electronic spectra

In here, we tested performance of several functionals, ab initio methods, different basis sets, ECPs, role of the optimized structure, and spin-orbit effects in the calculations of electronic spectra of studied systems. Optimized structure is an important factor here. For example, the calculated $\lambda(a_1)$ in $[Au(bipy)(Br)]^+$ covers a relatively broad range of wavelengths, 639723 nm (1.721.94 eV) depending on the method used for the geometry optimization. The expected dependence on DFT is mild. The tested functionals (B3LYP, CAM-B3LYP, PBE0, wB97DX) predict results from 440 nm to 464 nm (2.672.82 eV; **Table S2**) for $\lambda(a_1)$ in [Au(bipy)(Br)]⁺. The aug-cc-pVTZ quality basis sets with the corresponding pseudopotentials (PP) provide results that converge within a few nm (Table S3) and are affordable for studied systems. Inclusion of scalar relativistic effects via ECP (effective core pseudopotential) is a necessity for Au atom but has only marginal effect for Br atom (Table S2). Using ECP on Cu atom may to lead to larger deviations and problems, **Table S3**. The effect of spin-orbit (SO) coupling can be relatively large, several tens of nm, Tables S2 and S5. For the qualitative analysis in the main text, we decided to use PBEO/def2TZVPP/PP(Au) for geometry and CAM-B3LYP/aug-cc-pVTZ/Au(PP) for excitation energies.

Table S2. Comparison of theoretical and experimental excitation bands for [Au(bipy)(Br)]⁺.

Geometry	Functional	Basis set and ECP	$\lambda(b_2)/\text{nm}$	$\lambda(a_1)/\text{nm}$
B3LYP/6-311+G**/SDD(Au)	B3LYP	aug-cc-pVTZ/PP(Au,Br)	530	713
B3LYP/6-311+G**/SDD(Au,Br)		aug-cc-pVTZ/PP(Au,Br)	558	723
TPSS/def2-TZVP/PP(Au)		aug-cc-pVTZ/PP(Au,Br)	497	667
PBE0/def2-TZVPP/PP(Au)		aug-cc-pVTZ/SDD(Au,Br)	475	639
		6-311+G*/SDD(Au, Br)	476	647
		aug-cc-pVTZ/PP(Au,Br)	480	638
	B3LYP	aug-cc-pVTZ/PP(Au)	477	637
	CAM-B3LYP	aug-cc-pVTZ/PP(Au)	495	664
	PBE0	aug-cc-pVTZ/PP(Au)	482	638
	wB79xD	aug-cc-pVTZ/PP(Au)	500	672
	CAM-B3LYP	ZORA/TZP	479	634
	CAM-B3LYP	SO-ZORA/TZP	434	621
TPSS/def2-TZVP/Au(PP)	ADC(2)	def2-TZVP	554	713
TPSS/def2-TZVP/Au(PP)	CC2	def2-TZVP	510	646
Experiment			494	663

Table S3. Comparison of theoretical and experimental excitation bands for [Cu(bipy)(Cl)]⁺.

Geometry	Functional	Basis set and ECP	$\lambda(b_2)/\text{nm}$	$\lambda(a_1)/\text{nm}$
B3LYP/6-311G**	B3LYP	aug-cc-pVTZ	484	681
PBE0/def2-TZVPP		auc-cc-pVTZ	464	658
		6-311+G**	487	697
		auc-cc-pVTZ	464	658
		aug-cc-pVQZ	464	654
		aug-cc-pVTZ/SDD(Cu)	333	409
PBE0/def2-TZVPP	B3LYP	aug-cc-pVTZ/PP(Cu) 435		654
	CAM-B3LYP	aug-cc-pVTZ/PP(Cu)	413	674
	CAM-B3LYP	aug-cc-pVTZ	455	684
	PBE0	aug-cc-pVTZ	443	686
	wB79XD	aug-cc-pVTZ	440	692
TPSS/def2TZVP ADC(2)		def2-TZVP	556	898
TPSS/def2TZVP CC2		def2-TZVP	558	617
Experiment			<450	-

Table S4. Comparison of theoretical and experimental excitation bands for [Cu(bipy)(Br)]⁺.

Geometry	Functional	Basis set and ECP	$\lambda(b_2)/\text{nm}$	$\lambda(a_1)/\text{nm}$
B3LYP/6-311G**	B3LYP	aug-cc-pVTZ		
B3LYP/6-311G**/ SDD(Cu)		aug-cc-pVTZ		
PBE0/def2-TZVPP		auc-cc-pVTZ	532	680
PBE0/def2-TZVPP		6-311+G**		
		auc-cc-pVTZ		
		aug-cc-pVQZ	532	669
		aug-cc-pVTZ/SDD(Cu)	413	1095
	B3LYP	aug-cc-pVTZ/PP(Cu)		
	CAM-B3LYP	aug-cc-pVTZ/PP(Cu)	497	691
	CAM-B3LYP	aug-cc-pVTZ	545	694
	PBE0	aug-cc-pVTZ	520	699
	wB79XD	aug-cc-pVTZ	534	699
	M06-2X	aug-cc-pVTZ/PP(Au)	368	991
TPSS/def2-TZVP	ADC(2)	def2-TZVP	785	968
TPSS/def2-TZVP	CC2	def2-TZVP	681	1097
Experiment			544	673

Table S5. Comparison of theoretical and experimental excitation bands for [Au(bipy)(Cl)]⁺ using the C_{structure}.

Structure	Functional	Basis set and ECP	λ(<i>a</i> ")/nm	$\lambda(a')/\text{nm}$
B3LYP/6-311+G**/SDD(Au)	B3LYP	aug-cc-pVTZ/PP(Au)	515	750
PBE0/def2-TZVPP/PP(Au)		aug-cc-pVTZ/PP(Au)	457	693
		6311+G**/SDD(Au)	472	717
		aug-cc-pVTZ/SDD(Au)	464	705
	B3LYP	aug-cc-pVTZ/PP(Au)	457	693
	CAM-B3LYP	aug-cc-pVTZ/PP(Au)	469	665
	PBE0	aug-cc-pVTZ/PP(Au)	451	677
	wB97DX	aug-cc-pVTZ/PP(Au)	469	674
	M06-2X	aug-cc-pVTZ/PP(Au)	485	767
	CAM-B3LYP	ZORA/TZP	464	708
	CAM-B3LYP	SO-ZORA/TZP	408	646
TPSS/def2-TZVP/Au(PP)	ADC(2)	def2-TZVP	461	697
TPSS/def2-TZVP/Au(PP)	CC2	def2-TZVP	440	633
Experiment			-	637

Table S6. Dependence of electronic energy and calculated excitation energies (intensities in parenthesis) on N-Au-Br in-plane bending in [Au(bipy)(Br)]+.

N-Au-Br(deg)	E(kJ/mol)	λ (<i>a</i> ")/nm	λ (<i>a</i> ′)/nm
147	0		664(0.0001)
137	0.04	514(0.1468)	706(0.0047)
127	0.63	512(0.0707)	754(0.0194)
117	2.21	508(0.0320)	809(0.0200)

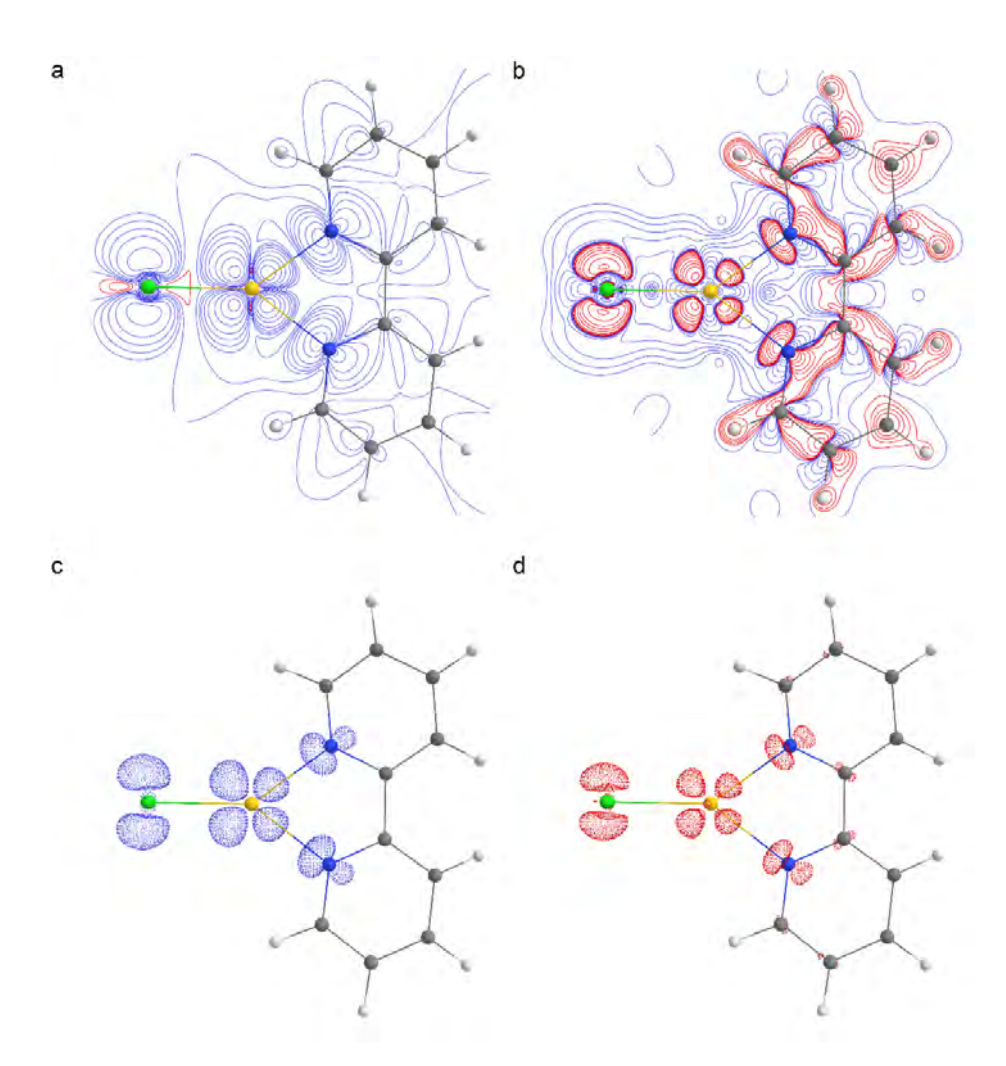


Figure S34. Profiles of (a) the spin density and (b) the Laplacian of the spin density on the plane of the [Au(bipy)(Cl)]⁺ complex. (c) The isosurfaces of (c) the spin density at 0.01 and (d) the Laplacian of the spin density at -0.05 au. Positive and negative values are presented by blue and red in all maps. Negative values in the Laplacian plots denote regions in with spin density is more concentrated.

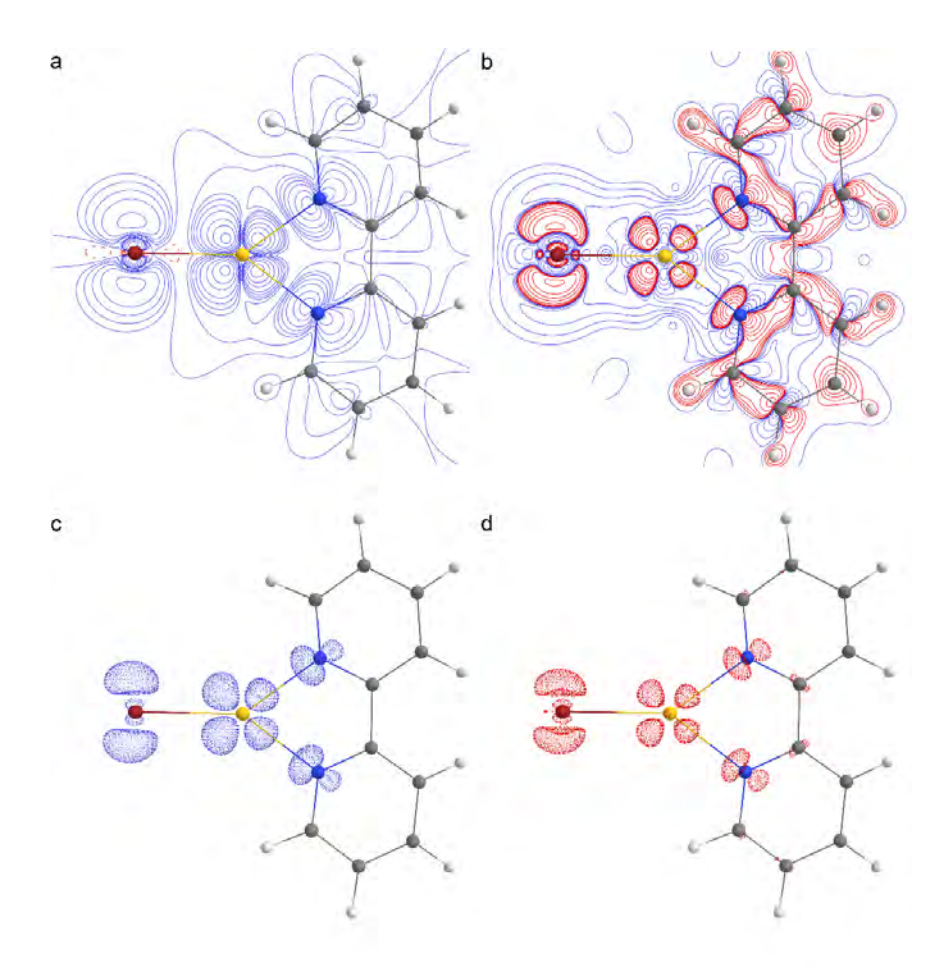


Figure S35. Profiles of (a) the spin density and (b) the Laplacian of the spin density on the plane of the [Au(bipy)(Br)]⁺ complex. (c) The isosurfaces of (c) the spin density at 0.01 and (d) the Laplacian of the spin density at -0.05 au. Positive and negative values are presented by blue and red in all maps. Negative values in the Laplacian plots denote regions in with spin density is more concentrated.

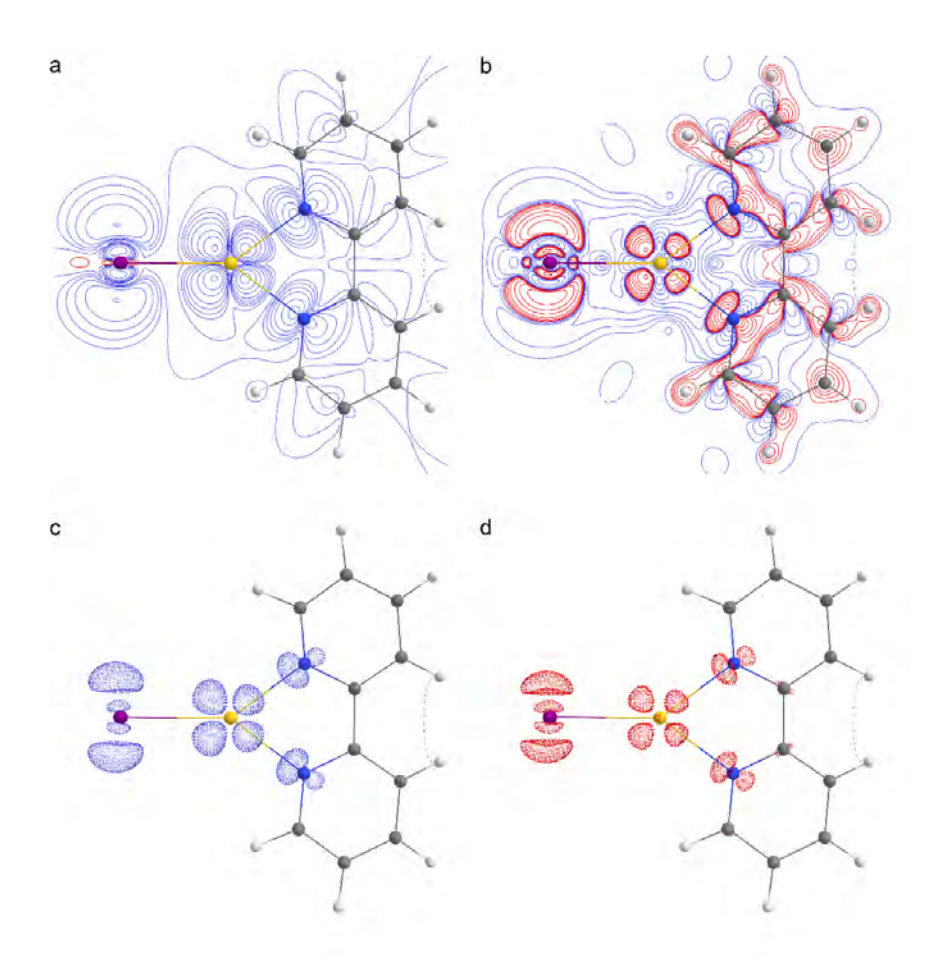


Figure S36. Profiles of (a) the spin density and (b) the Laplacian of the spin density on the plane of the [Au(bipy)(I)]+ complex. (c) The isosurfaces of (c) the spin density at 0.01 and (d) the Laplacian of the spin density at -0.05 au. Positive and negative values are presented by blue and red in all maps. Negative values in the Laplacian plots denote regions in with spin density is more concentrated.



Chapter 6

Binding interactions in copper, silver, and gold π -complexes

The work in this chapter is published: <u>Mehara, J.</u>; Watson, B. T.; Noonikara-Poyil, A.; Zacharias, A. O.; Roithová, J.; Rasika Dias, H. V. Binding Interactions in Copper, Silver and Gold Π-Complexes. *Chem. – A Eur. J.* **2022**, *28* (13).

Mehara, J.; Roithová, J.: Mass spectrometric and Ion Spectroscopic studies.

Watson, B. T.; Noonikara-Poyil, A.; Zacharias, A. O; Rasika Dias, H. V.: NMR and XRD studies.

This chapter investigates the interactions of copper(I), silver(I), and gold(I) metals with π -ligands, emphasizing on the σ -bonding and π -back-bonding mechanisms. We investigated these interactions using bidentate ancillary ligands with electron donating and withdrawing substituents. The π -ligands span from ethylene to larger terminal and internal alkenes and alkynes. By means of X-ray crystallography, NMR, and IR spectroscopy and gas phase experiments, we show that the binding energies increase in the order Ag < Cu < Au and the binding energies are slightly higher for alkynes than for alkenes. By modulating the electron density at the metal using substituents on the ancillary ligands, we show that the π -back bonding interaction plays a dominant role for the binding in the copper and gold complexes.

Introduction

Coinage metals (Cu, Ag, and Au) play critical roles in the chemical transformations of small unsaturated hydrocarbons such as olefins and alkynes.¹ For example, copper(I) salts and complexes are often employed as catalysts in azide-alkyne cycloadditions,² cyclopropanation of alkenes,³ and cyclopropenation of alkynes.⁴ Copper(I) salts supported by alumina are also involved in the oxychlorination of ethylene.⁵ Silver(I) is used industrially for the epoxidation of ethylene to ethylene oxide.⁶ and also has found use in numerous alkyne transformations.⁷ Likewise, gold catalyzes the hydrochlorination of acetylene to give vinyl chloride,8 another industrially important chemical, and many processes involving various alkenes and alkynes.⁹ Recently, Hashmi reported a bimetallic gold/silver catalyzed alkynylation of cyclopropenes.9c

Polydentate ligands comprised of N-containing heterocycles have had a longstanding use in stabilizing isolable coinage metal complexes of small hydrocarbon molecules.^{1c} Poly(pyrazolyl)borates are particularly attractive in this regard due to their high degree of steric and electronic tunability through variations of substituents on the pyrazolyl moieties. The tris(pyrazolyl)borate $[HB(3,5-(CH_3),Pz)_2]Cu(C_3H_4)$ (1) is the first structurally authenticated copper-ethylene complex.10 The highly fluorinated tris(pyrazolyl)borate ligand analog [HB(3,5- $(CF_3)_2Pz)_3$ enabled the isolation of $[HB(3,5-(CF_3)_2Pz)_3]M(C_3H_4)$ (M = Cu (2), Ag (3), Au (4)), which represents the first complete series of structurally characterized coinage metal (group 11) ethylene complexes. 11 The silver(I) adduct [HB(3,5-(CF $_{_2}$) $_{_2}$ Pz) $_{_2}$] Ag(C₂H₂) is a rare isolable complex featuring a silver-acetylene bond.^{11b} [HB(3,5-(CF₂)₂Pz)₂]Cu(C₂H₄) (2) has been utilized in ethylene sensing applications, ¹² while the bis(pyrazolyl)borate analog [H₂B(3,5-(CF₃)₂Pz)₂]Cu is a very effective material for the separation of ethylene from ethane.¹³ Furthermore, bis- and tris-(pyrazolyl)borate copper complexes [H₂B(3,5-(CF₃)₂Pz)₂]CuNCMe and [HB(3,5-(CF₃)₂Pz)₃]CuNCMe are excellent catalysts for the cyclopropenation of alkynes, 4a while [Ph_B(3-(CF_2)_Pz)_] Cu(C₂H₄) mediates alkene cyclopropanation chemistry.¹⁴ The copper complexes such as [HB(3,5-(CH₂)₂Pz)₂]Cu(C₂H₄) with non-fluorinated tris(pyrazolyl)borate ligand (Figure 1) supports are also proven to be good catalysts for the cyclopropanation of alkenes, cyclopropenation of alkynes, and aziridination of alkenes. 15

Figure 1. Tris(pyrazolyl)borate coinage metal complexes of ethylene (1-4), and bis(pyrazolyl) borate (5) and bis(pyrazolyl)methane (6) supporting ligands.

In contrast to the anionic, poly(pyrazolyl)borates (e.g. [HB(3,5-(CH₂)₂Pz)₃]², [H₂B(3,5-(CH₂)₂Pz)₃]⁻ (**5**)), the closely related neutral poly(pyrazolyl)methanes (e.g., HC(3,5- $(CH_3)_2Pz)_3$, $H_2C(3.5-(CH_3)_2Pz)_2$ (6)) have been less thoroughly explored. ^{1c,16}To date, very few bis(pyrazolyl)methane supported olefin complexes have been reported, despite having a similar degree of tunability to their anionic counterparts. For example, in 2006, Pampaloni and coworkers prepared the electron-rich bis(pyrazolyl)methane (H₂C(3,5-(CH₃)₂Pz)₂ (5)) supported copper(I) complexes of cyclooctene, norbornene, and p-vinyl anisole.¹⁷ The following year the same group prepared electron poor bis(pyrazolyl)methane (H₂C(3,5-(CF₃)₂Pz)₃) and H₂C(3-CF₃Pz)₃) copper(I) and silver(I) complexes of cyclooctene.¹⁸ However, only [H₂C(3,5-(CH₂)₃Pz)₂Cu(cyclooctene)] [OTf] was characterized using X-ray crystallography. Recently, Sumby and Doonan prepared Mn(II) based MOF using bis[4-carboxyphenyl-(3,5-dimethylpyrazol-1-yl)]methane to trap and characterize copper(I) complexes of CO, ethylene, norbornadiene (NBD) and phenyl acetylene.19 They also managed to obtained X-ray structural data of the copper ethylene complex, **MnMOF-1**•[Cu(C,H_a)][BF_a], and the related NBD and phenyl acetylene adducts. Other reported copper and silver complexes of bis(pyrazolyl)methane are typically the homoleptic compounds with two bis(pyrazolyl)methane ligands on metals^{16,20} or dimers^{17,18,21} which feature bridging bis(pyrazolyl)methane ligands. In addition, there are also quite a few computational studies involving coinage metal complexes of alkenes and alkynes.²² Overall, isolable and structurally authenticated molecules of copper, silver and gold alkenes and alkynes supported by bis(pyrazolyl)methane ligands are quite rare as evident from the above account.

Figure 2. Metal complexes (M = Cu, Ag, Au) with ligands L, (H₂C(3,5-(CH₂)₂Pz)₃, 6), L₂(H₂C(3-(CF₂)Pz)₂), and L₂ (H₂C(3,5-(CF₂),Pz)₂). The π -ligands were various alkenes (ethylene displayed here) and alkynes.

Furthermore, despite the importance of coinage metals in alkene and alkyne chemistry, there is little experimental evidence on how changing the nature of the ancillary ligand on coinage metal ions and substituents on alkenes and alkynes effect the binding energies of the two components. Previously, we have investigated binding energies of unsaturated hydrocarbons to phosphinogold(I) and phospinosilver(I) ions.²³ The binding energies to alkenes and alkynes were in the range of 1.8 – 1.9 eV for $[Au(PMe_2)(\pi-ligand)]^+$ and in the range of 1.6 – 1.8 for $[Au(PPh_a)(\pi-ligand)]^{+.24}$ In general, the binding energies were always about 0.1 eV higher for alkynes than for alkenes. In the silver complexes $[Ag(PPh_2)(\pi-ligand)]^+$, the binding energies dropped to the 1.3-1.6 eV range.

In this work, we present results from a systematic study on synthesis, structures, and binding energies involving coinage metal ions and alkenes and alkynes supported by bis(pyrazolyl)methanes. This includes the first X-ray structural data and detailed study of isoleptic, {[H₂C(3,5-(CH₃)₂Pz)₂]M(C₂H₄)}⁺ series involving the coinage metals, M = Cu, Ag, Au. We also probed the effects of supporting ligand fluorination (and therefore the donor features) on the chemistry of such species. Being a neutral ligand, bis(pyrazolyl)methanes make it an ideal platform for performing mass spectrometric studies to investigate these effects since the complexes of M(I) supported by such ligands are cationic species.

Results

Synthesis and spectroscopic data of alkene and alkyne complexes.

The first part of this work involves the isolation of $[LM(\pi-ligand)]^+$ complexes where L represents bidentate, bis(pyrazolyl)methane ligand scaffolds and M was copper, silver, and gold (Figure 2). The properties, spectroscopic, and structural studies of such species were the focus. For this purpose, ethylene complexes [L,M(C,H,)][SbF,]

Scheme 1. Synthesis of Cu(I), Ag(I) and Au(I) ethylene complexes supported by ligands L_1 ($H_2C(3,5-(CH_1),Pz)_1$), L_2 ($H_2C(3-(CF_1),Pz)_2$) and L_3 ($H_3C(3,5-(CF_3),Pz)_3$).

The 1-pentene complex $[L_1Cu(1-pentene)][SbF_6]$ (12) was also obtained via a similar route^[26] using an in-situ generated $Cu[SbF_6]$ sample in the presence of excess 1-pentene followed by the addition of L_1 (Scheme 2). The $[L_1Cu(1-pentyne)][SbF_6]$ (13) was synthesized by generating the ethylene complex 7 *in situ*, followed by the addition of excess alkyne (Scheme 2). The related 2-pentyne complex of copper(I) was prepared via an analogous method to that of 13. Attempts to prepare these

copper(I) alkyne complexes using the route utilized for 12 and alkynes instead of alkenes were unsuccessful. The solid products of 12 and 13 were obtained by removing the solvent using a nitrogen stream rather than reduced pressure to prevent π -ligand dissociation.

$$\begin{array}{c|c} Cu[SbF_6] \\ \hline N & N \\ \hline \end{array}$$

$$\begin{array}{c|c} Cu[SbF_6] \\ \hline \end{array}$$

$$\begin{array}{c|c} Cu \\ \end{array}$$

Scheme 2. Synthesis of pentene and pentyne complexes of copper(I) supported by ligands $L_1(H_2C(3,5-(CH_3)_2Pz)_2).$

These complexes were characterized by several analytical techniques including ¹H and ¹³C NMR spectroscopy. The key NMR spectroscopic features of olefinic and alkyne moieties bound to the coinage metal ions are summarized in Table 1. In comparison to the free ethylene, the ¹H and ¹³C NMR spectra of copper(I) complex 7 show coordination induced upfield shifts of 0.92 ppm and 35.6 ppm for the ethylene protons and carbons, respectively, while the analogous silver(I) complex 8 shows a 0.18 ppm downfield shift of the ethylene proton signals and a 11.6 ppm upfield shift of the carbon resonance (Table 1). The gold(I) complex 9 displayed a noticeably large upfield shift of the ethylene proton and carbon signals (1.70 ppm

(¹H) and 66.3 ppm (¹³C)). The *N,N'*-bis(8-(3,5-dichlorophenyl)-1-naphthyl)butane-2,3-diimine (Nap′₂Diimine) ligand supported, cationic coinage metal mono-ethylene adducts, [(Nap′₂Diimine)M(C₂H₄)][SbF₆] reported by Daugulis and co-workers²⁷ provide a good comparison, and show their ethylene ¹³C shifts at δ 88.0, 105.4, and 65.4 ppm for M = Cu, Ag and Au, respectively. The group trends are consistent between **7-9** and [(Nap′₂Diimine)M(C₂H₄)][SbF₆], as well as with neutral coinage metal ethylene complexes supported by tris(pyrazolyl)borate ligands including the [PhB(3-(C₂F₅)Pz)₃]M(C₂H₄) series (i.e., the gold and silver complexes displaying the highest and lowest upfield ethylene carbon shifts, respectively, as a result of metal ion coordination).¹c,¹¹¹,²²²</sup> The relative magnitude of the upfield shifts in ethylene carbons due to coordination reflects the σ-acceptor and π-donor abilities of the coinage metal atom (e.g., d¹⁰→d¹⁰s¹ electron affinity of Cu(I), Ag(I) and Au(I) ions are -7.72, -7.57 and -9.22 eV, respectively, and d¹⁰→d⁰p¹ promotional energies of Cu(I), Ag(I) and Au(I) ions are 8.25, 9.94 and 7.83 eV, respectively),²⁰ and the extent of M-ethylene π-back bonding believed to exist in these molecules.²²8b,³⁰

Table 1. Selected peaks from 1H and ^{13}C NMR for complexes **7-13** and the chemical shift ($\Delta\delta$) from corresponding free π -ligand ($\Delta\delta$ = δ (metal complex) - δ (free ligand)), $L_1 = H_2C(3,5-(CH_3)_2Pz)_2$) and $L_3 = H_2C(3,5-(CF_3)_2Pz)_2$. For comparison, free ethylene has chemical shifts of δ 5.40 (1H) and 123.1 (^{13}C) ppm in CDCl₃, 5.40 (1H) and 123.2 (^{13}C) in CD₃Cl₃, and 5.38 (1H) and 123.5 (^{13}C) in acetone-d₄.

compound	1 H NMR H_{2} C=CHR or H C≡CR (ppm)	Δδ (ppm)	¹³ C NMR H ₂ C=CHR or HC≡CR (ppm)	Δδ (ppm)
$[L_1Cu(C_2H_4)][SbF_6]$ (7)	4.48 ^[a]	-0.92	87.9 ^[c]	-35.6
$[L_1Ag(C_2H_4)][SbF_6]$ (8)	5.56 ^[c]	+0.18	111.9 ^[c]	-11.6
$[L_1Au(C_2H_4)][SbF_6]$ (9)	3.70 ^[b]	-1.70	56.9 ^[b]	-66.3
$[L_3Cu(C_2H_4)][SbF_6]$ (10)	4.82 ^[c]	-0.56	93.4 ^[c]	-30.1
$[L_3Ag(C_2H_4)][SbF_6]$ (11)	5.78 ^[b]	+0.38	113.6 ^[b]	-9.6
$[L_1Cu(1-pentene)][SbF_6]$ (12)	4.76, 4.71 ^[c]	-0.21, -0.22	119.4, 94.9 ^[c]	-19.6, -19.5
$[L_1Cu(1-pentyne)][SbF_6]$ (13)	4.62 ^[b]	+2.67	98.1, 75.8 ^[b]	+13.6, +7.6

[[]a]CDCl₃, [b]CD₂Cl₂, [c]acetone-d₆

Compared to L_1 ($H_2C(3,5-(CH_3)_2Pz)_2$), the highly fluorinated L_3 ($H_2C(3,5-(CF_3)_2Pz)_2$) is a weaker donor and should make the metal sites supported by this ligand relatively electron poor. The copper(I) and silver(I) ethylene complexes **10** and **11**, indeed show relatively smaller upfield shifts of the ethylene ^{13}C signal due to metal ion coordination, suggesting somewhat lower level of metal—ethylene backbonding relatively to the related **7** and **8**. 28b,30 The olefinic proton and carbon signals in ^{1}H and ^{13}C NMR spectra

of the 1-pentene complex of copper 12 in acetone-d_s also shows upfield shifts relative to the corresponding signals of the free 1-pentene, indicating the existence of this adduct in solution. In contrast to the M(olefin) complexes, the 1-pentyne complex 13 displayed large downfield shifts of 2.67 ppm (1H) and 13.6, 7.6 ppm (13C) in its spectra for the HC≡ proton and alkyne carbons. The IR spectrum of 13 displayed bands at 1937 and 3199 cm⁻¹, which can be assigned to the C \equiv C and \equiv C-H stretch. These bands were observed in the free 1-pentyne at 2120 and 3307 cm⁻¹, respectively, and thus show red shifts of 183 and 108 cm⁻¹, respectively.

The copper(I)-olefin complexes are moderately air stable, colorless solids, but slowly oxidize to green, presumably copper(II) decomposition products. However, solutions of these olefin complexes are significantly more sensitive to air, and easily produce dark green solutions. The copper(I) complexes of ethylene (7, 10) show poor solubility, except in highly polar solvents such as acetone, tetrahydrofuran, and methanol. Thus, we had to synthesize $[L,Cu(C,H_a)]^+$ with a different counter ion [n-BuBF₂] to obtain suitable crystals of [L,Cu(C₂H₄)][n-BuBF₂] (**14**) for X-ray crystallographic studies. The gold(I) ethylene complex 9 is somewhat light sensitive and best kept in the dark under an ethylene atmosphere at -20 °C. In solution, we observed partial loss of ethylene from 9 to produce [L,Au]+ species. It is possible to minimize this ethylene dissociation at lower temperatures. The silver and gold complexes 8 and 9 dissociate and binds ethylene reversibly in solutions when purged with nitrogen gas or ethylene gas as evident from the data from NMR experiments. Remarkably, the 1-pentyne complex 13 was quite shelf stable, even after 6 months of storage.

X-ray crystallographic study.

The copper, silver, and gold ethylene complexes, [L₁Cu(C₂H₄)][n-BuBF₂] (**14**), $[L_1Ag(C_2H_4)][SbF_6]$ (8), and $[L_1Au(C_2H_4)][SbF_6]$ (9) were isolated using weakly coordinating hexafluoroantimonate and n-butyl trifluoroborate anions in order to get a more accurate understanding of the metal- π -ligand interaction between the coinage metal ion and ethylene without significant interference from a coordinating anion. They were characterized by X-ray crystallography and represent a rare, complete series of closely related cationic coinage metal-ethylene complexes with structural data from group trend studies. The coinage metal monoethylene adducts, [(Nap',Diimine)Cu(C,H,)][OTf], [(Nap',Diimine)Ag(C,H,)][BF,] and [(Nap',Diimine)Au(C,Ha)][SbF6] reported by Daugulis and co-workers,27 and the trisethylene complexes $[M(C_2H_4)_3][SbF_6]^{25}$ and $[M(C_2H_4)_3][Al\{OC(CF_3)_3\}_4]$ (M = Cu, Ag and Au)³¹ represent the only other complete series of cationic coinage metal ethylene complexes with X-ray structural data to our knowledge.

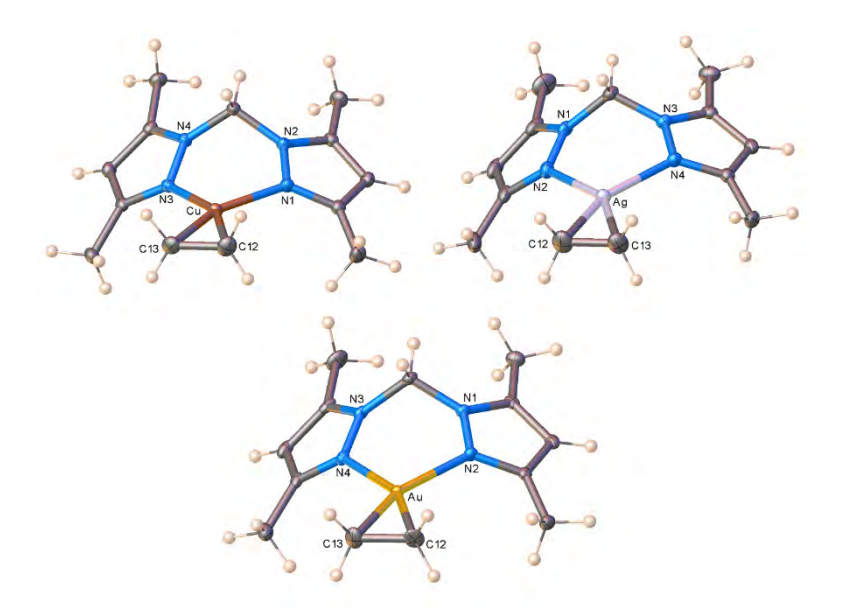


Figure 3. Molecular structures of $[L_1Cu(C_2H_4)][n-BuBF_3]$ (14), $[L_1Ag(C_2H_4)][SbF_6]$ (8), and $[L_1Au(C_2H_4)][SbF_6]$ (9) (clockwise from top to bottom). Anions have been omitted for clarity. $L_1 = H_2C(3,5-(CH_4),Pz)$, (6)

Figure 3 depicts the molecular structures of the cationic moieties $[L_1M(C_2H_4)]^+$. They are three-coordinate metal complexes with κ^2 -bound $H_2C(3,5\text{-}(CH_3)_2Pz)_2$ ligands. The ethylene coordinates to metal in a familiar η^2 -fashion. The cyclic CN_4M core adopts a flattened boat conformation. Table 2 summarizes selected structural parameters. The sum of angles about the metal center in **8**, **9** and **14** is 360°, indicating the trigonal-planer geometry at the metal site. One of the fluorine atoms of $[n\text{-BuBF}_3]$ in $[L_1Cu(C_2H_4)][n\text{-BuBF}_3]$ (**14**) sits near Cu at 2.5825(10) Å, which is within the van der Waals contact separation of Cu and F atoms (3.84 Å) but this interaction is not significant to distort the planar geometry at copper. Furthermore, Cu(I) complexes of terminal fluoride ligands usually have much shorter Cu-F distances, e.g., $[(t\text{-Bu})_2\text{phen}]\text{CuF}$ (1.870(8) Å), 32 (PPh $_3$) $_3$ CuF (2.062(6) Å). 33

Table 2. Selected bond lengths and angles of bis(pyrazolyl)methane complexes of Cu, Ag and Au and those of several related complexes for comparisons.

compound	π-ligand C=C (Å)	C-M-C (°)	N-M-N (°)	M-N (Å)	C-M (Å)	Σ angles at M (°) involving N and centroid of C=C
$[L_1 Cu(C_2 H_4)]$ $[n-BuBF_3]$ (14)	1.361(2)	39.44(6)	94.45(4)	1.9885(11), 1.9896(11)	2.0153(13), 2.0181(13)	360
$[L_1Ag(C_2H_4)]$ $[SbF_6]$ (8)	1.350(5)	34.96(12)	88.96(9)	2.223(2), 2.232(2)	2.243(3), 2.253(3)	360
$[L_1Au(C_2H_4)]$ $[SbF_6]$ (9)	1.401(3)	39.04(10)	87.37(7)	2.1720(19), 2.1733(18)	2.098(2), 2.094(2)	360
$[PhB(3-(C_{2}F_{5})$ $Pz)_{3}]Cu(C_{2}H_{4})^{28a}$	1.354(7)	38.96(19)	93.76(13)	2.008(3), 2.009(3)	2.027(4), 2.033(4)	360
$[PhB(3-(C_{2}F_{5})$ $Pz)_{3}]Ag(C_{2}H_{4})^{28a}$	1.311(5)	33.38(14)	86.02(7)	2.279(2), 2.286(2)	2.286(3), 2.279(3)	360
$[PhB(3-(C_{2}F_{5})$ $Pz)_{3}]Au(C_{2}H_{4})^{28a}$	1.366(12)	38.0(3)	84.7(2)	2.213(6), 2.216(6)	2.089(8), 2.105(7)	360
[L ₃ Ag(C ₂ H ₄)] [SbF ₆] (11) ^[a]	1.340(4); 1.340(4)	33.67(11); 33.69(11)	86.44(6); 86.49(6)	2.3306(18), 2.3328(18); 2.3330(18), 2.3293(18)	2.309(3), 2.319(3); 2.312(3), 2.313(3)	359.7; 359.8
[L ₁ Cu(1- pentene)] [SbF ₆] (12)	1.364(3)	39.14(8)	95.69(6)	1.9816(14), 1.9936(14)	2.0194(18), 2.0512(17)	359.0
[L ₁ Cu(coe)] [OTf] ¹⁷ (15)	1.362(3)	38.57(9)	94.57(9)	2.007(2), 2.009(2)	2.072(2), 2.050(2)	354.2 ^[b]
[L ₁ Cu(1- pentyne)] [SbF ₆] (13)	1.241(2) ^[c]	36.64(6)	91.93(5)	1.9787(11), 1.9856(12)	1.9540(14), 1.9927(14)	359.8 ^[d]

[a]two molecules in the asymmetric unit, [b]triflate counterion excluded in the calculation of sum of angles, [c]C \equiv C length, [d]involving centroid of C \equiv C

The N-M-N and C-M-C planes are nearly coplanar with torsion angles of 1.85°, 5.67°, and 2.12° for $[L_1M(C_2H_4)]^+$ (M = Cu, Ag and Au, respectively), with the silver adduct showing the largest twist perhaps suggesting the weakest M-ethylene π -back bonding. The Cu-N<Au-N<Ag-N bond length follows the covalent radii, as silver is bigger than both gold and copper.³⁴ The M-C bond lengths also follow this trend, and they compare well with the previously reported tris(pyrazolyl)borate ligand supported coinage metal ethylene complexes^{1c,11c,28} and copper and silver dipyridyl amine systems involving larger olefins.35 The ethylene C=C bond is longest for $[L_1Au(C_2H_A)]^+$, followed by $[L_1Cu(C_2H_A)]^+$ and $[L_1Ag(C_2H_A)]^+$ with bond lengths of 1.401(3), 1.361(2), and 1.350(5) Å, respectively, but the difference in the latter two numbers is not significant at the 3σ limit of estimated standard deviations (for comparison, the C=C bond length for free gaseous ethylene is 1.3305(10) Å while the corresponding distance from X-ray data is 1.313 Å).³⁶ Apart from the MOF complex **MnMOF-1·**[Cu(C_2H_4)]BF₄,¹⁹ there are no structurally characterized bis(pyrazolyl)methane adducts of Cu, Ag or Au with ethylene to our knowledge. The M-N, M-C, and C=C bond lengths of [L₁M(C_2H_4)]⁺ are however, consistent with the structural data on molecules supported by various other supporting ligands, which suggests that gold interacts strongest with ethylene, followed by copper while silver having the weakest interaction with ethylene.^{27-28,37}

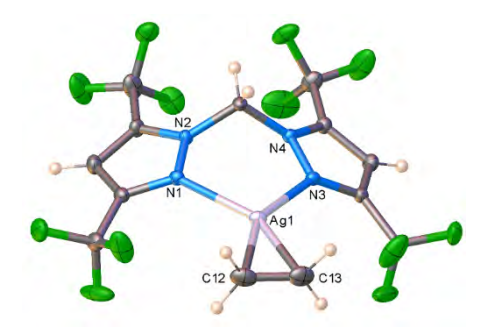


Figure 4. Molecular structure of $[L_3Ag(C_2H_4)][SbF_6]$ (11). The anion has been omitted for clarity. $L_3 = H_2C(3,5-(CF_3)_2Pz)_2$

We have also managed to crystallize and characterize [L₃Ag(C₂H₄)][SbF₆] (11) that has a highly fluorinated bis(pyrazolyl)methane supporting ligand, H₂C(3,5-(CF₂)₂Pz)₃ using single crystal X-ray crystallography (Figure 4). Basic structural features are similar between $[L_1Ag(C_2H_\lambda)][SbF_a]$ and $[L_3Ag(C_2H_\lambda)][SbF_a]$. The $[L_3Ag(C_2H_\lambda)][SbF_a]$ is also a three-coordinate, trigonal planar metal complex. The Ag-N and Ag-C distances are significantly longer in the [L₃Ag(C₂H₄)][SbF₆] compared to those of the [L,Ag(C,Ha)][SbF6] pointing to the relatively weakly coordinating nature of $H_2C(3,5-(CF_3)_2Pz)_2$ in comparison to $H_2C(3,5-(CH_3)_2Pz)_2$ (Table 2). This observation is in agreement with the NMR data presented above for the two adducts (i.e., $[L_1Ag(C_2H_4)][SbF_6]$ and $[L_2Ag(C_2H_4)][SbF_6]$ display chemical shifts of 5.56 and 5.78 ppm in their ¹H spectra and 111.9 and 113.6 ppm in their ¹³C spectra for the ethylene moiety). However, the C=C distance is not significantly different between the two complexes, which is not unusual, 28b,38 considering typically smaller changes in the distances are often overshadowed by the relatively high estimated standard deviations (esds) associated with the measurement, libration effects and anisotropy of the electron density.

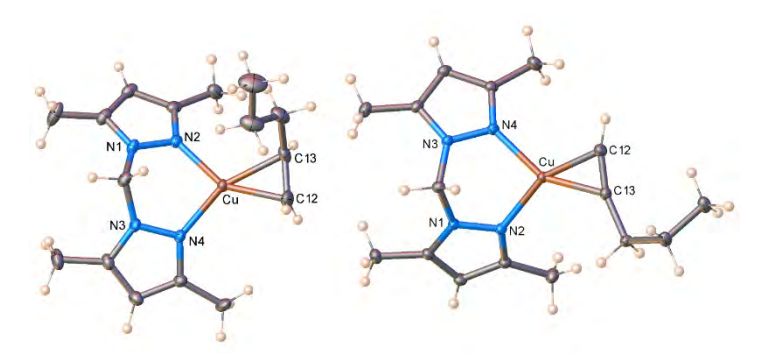


Figure 5. Molecular structures of [L,Cu(1-pentene)][SbF_e] (12, left) and [L,Cu(1-pentyne)][SbF_e] (13, right). The anions were omitted for clarity. $L_1 = H_2C(3,5-(CH_2),PZ)$

We have also investigated the 1-pentene and 1-pentyne complexes, [L,Cu(1pentene)][SbF₂] (12) and [L,Cu(1-pentyne)][SbF₂] (13) using X-ray crystallography. The molecular structures are illustrated in Figure 5. They are three-coordinate metal complexes with κ^2 -bound H₂C(3,5-(CH₂)₂Pz)₃ ligands. Pentene and pentyne coordinate to copper in the typical η^2 -fashion. The cyclic CN₂Cu core in these molecules adopts a flattened boat conformation. The N-M-N and C-M-C planes are not strictly coplanar with torsion angles of 9.63° and 5.20° for [L,Cu(1-pentene)] [SbF₆] and [L₁Cu(1-pentyne)][SbF₆], respectively.

The C=C bond length of 1.364(3) Å of [L,Cu(1-pentene)][SbF₂] is similar to the corresponding distance observed in the ethylene complex 14 (1.361(2) Å). The bending back angle between the CuC₁C₂ plane and the C₁C₂C₃ plane of 1-pentene is 9.9° deviated from the idealized 90°, illustrating the effect of σ/π -interaction between the copper(I) to 1-pentene in 12. A copper(I)-cyclooctene complex, [L,Cu(coe)][OTf]¹⁷ (15) supported by L, is known, but this molecule features a short TfO—Cu contact leading to a pseudo-tetrahedral copper site (Table 2). The Cu-C and Cu-N distances of 15 are slightly longer than the corresponding distances observed for 12.

The C \equiv C bond length of [L,Cu(1-pentyne)][SbF,] (1.241(2) Å) is at the upper end of the few reported three-coordinate, terminal copper(I) alkynes of the type N_2 Cu(alkyne) in the literature.³⁹ The C \equiv C-C bond angle of 160.85(14)° is typical^{2c} and shows a significant deviation from linearity as a result of the copper-coordination. For comparison, the neutral copper(I)-hexyne complex, [N{(C₃F₇)C(Dipp)N}₂] Cu(EtC≡CEt) has C≡C-C bond angles of 156.5(2)° and 156.3(2)°.40 Packing diagrams of 8, 9, 11-14 show contacts between some fluorine atoms of the anion and some hydrogen atoms of the cationic moieties, as well as between the Cu site and one of the fluorines in compound **14**.

Mass spectroscopic studies.

Next, we investigated bond dissociation energies in mass-selected cationic [LM(π -ligand)]⁺ complexes with L = L₁, L₂, and L₃ (Tables 3 – 5 and Figure 6). Despite all efforts, it was impossible to generate gaseous complexes with ethylene or acetylene. However, we could prepare a series of [L₁M(π -ligand)]⁺ complexes with larger terminal and internal alkenes and alkynes. We were not able to generate all complexes with the more electron-deficient ligands L₂ and L₃, therefore we will discuss the general trends for the complexes with the L₁ ligand first.

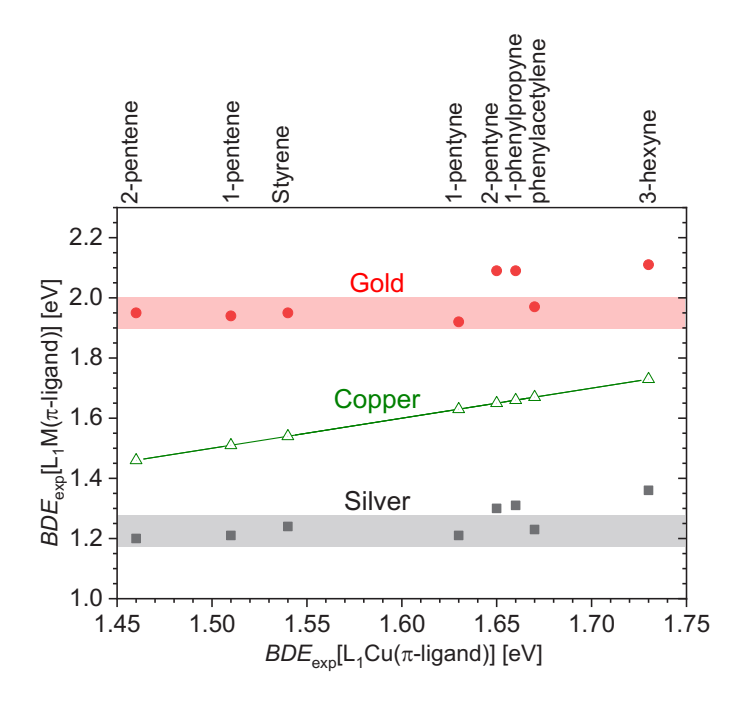


Figure 6. The relation between the experimental *BDEs* of π -ligands in [L₁Ag(π -ligand)]⁺ and [L₁Au(π -ligand)]⁺ (Table 3). L₁= H₂C(3,5-(CH₃)₂Pz)₂

In the series of the metal complexes, the binding energies to the π ligands increase going from the silver to the copper and finally to the gold complexes (Table 3). This observation is consistent with the data from spectroscopic and structural studies described above. The copper complex binds with a larger energy to the alkynes than to the alkenes (see distribution along x-axis in Figure 6). Silver and gold complexes

bind with a similar binding energy to alkenes and terminal alkynes (~1.2 eV in $[L,Ag(\pi-ligand)]^+$ and ~1.9 eV in $[L,Au(\pi-ligand)]^+$, see the color-highlighted stripes in Figure 6). The internal alkynes have about 0.1 – 0.2 eV larger binding energies in both, silver, and gold complexes (see the point above the color-highlighted stripes in Figure 6). For all the investigated complexes, the symmetrical 3-hexyne has the largest binding energy. Interestingly, Widenhoefer has also observed such unusual binding involving 3-hexyne with phosphine supported gold (I).⁴¹ An easily isolable, isoleptic series $[N\{(C_2F_7)C(Dipp)N\}_2]M(EtC\equiv CEt)$ (M = Cu, Ag and Au) is also known with 3-hexvne.40

Table 3. Bond dissociation energies of π -ligands from [L.M(π -ligand)]⁺, L.= H₂C(3,5-(CH₂)₂Pz)₂

π-Ligand	[L₁Cu(π-liga	nd)] ⁺	[L ₁ Ag(π-liga	nd)] ⁺	[L ₁ Au(π-liga	nd)] ⁺
	BDE _{exp} [eV]	BDE _{theor} [eV]	BDE _{exp} [eV]	BDE _{theor} [eV]	BDE _{exp} [eV]	BDE _{theor} [eV]
1-Pentene	1.51 ± 0.02	1.40	1.21 ± 0.01	1.16	1.94 ± 0.01	1.95
2-Pentene	1.46 ± 0.01	1.33	1.20 ± 0.04	1.12	1.95 ± 0.04	1.90
1-Pentyne	1.63 ± 0.02	1.48	1.21 ± 0.03	1.16	1.92 ± 0.04	1.96
2-Pentyne	1.65 ± 0.02	1.52	1.30 ± 0.02	1.21	2.09 ± 0.04	2.02
3-Hexyne	1.73 ± 0.03	1.58	1.36 ± 0.01	1.27	2.11 ± 0.04	2.09
Styrene	1.54 ± 0.01	1.51	1.24 ± 0.04	1.21	1.95 ± 0.01	1.97
Phenylacetylene	1.67 ± 0.01	1.54	1.23 ± 0.01	1.22	1.97 ± 0.01	1.99
1-Phenylpropyne	1.66 ± 0.02	1.57	1.31 ± 0.02	1.27	2.09 ± 0.01	2.05

We have further calculated the bond dissociation energies of the π -ligands in the $[L,M(\pi-ligand)]^+$ complexes using DFT theory (B3LYP-D3/def2TZVPP). In a rough approximation, the experimental data correlate well with the theory (see the solid points in Figure 7 and their grouping around the dashed correlation lines). We find the best agreement between the theoretical and experimental values of the gold complexes. In the case of the silver and copper complexes, the values correlate well, but the theoretical bonding energies are underestimated by about 0.05 eV for the silver complexes and by about 0.1 eV for the copper complexes. However, in a more detailed inspection of individual metal complexes series, the trend of the BDEs of different π -ligands correlates well only for the copper complexes except for the BDEs for styrene and 1-phenylpropyne (see Figure S3). The prediction of the BDE trend in the silver (Figure S4) and gold complexes (Figure S5) is less precise.

Next, we have compared the binding energies in complexes with modified ligands $L_1 - L_2$ (Figure 7, Tables 3 – 5). The electron deficient ligands could be expected to promote a stronger σ-bonding associated with the electron density transfer from the π -ligands to the metal centers but should have a weaker π -back bonding interaction. The experiments show that the *BDE*s of the given π -ligands slightly decreased when the ancillary ligand was more electron deficient (see the y-values of the connected points in Figure 7; for details see Figures S6 – S8) pointing to the importance of the π -back bonding. That trend is in agreement with the reported DFT data on three-coordinate, gold tris(pyrazolyl)borate complexes. ⁴² Note that the formation of the complexes with the electron deficient ligands L_2 and L_3 was difficult and therefore we couldn't measure whole series of the complexes. The gold complexes with L_3 were not formed at all.

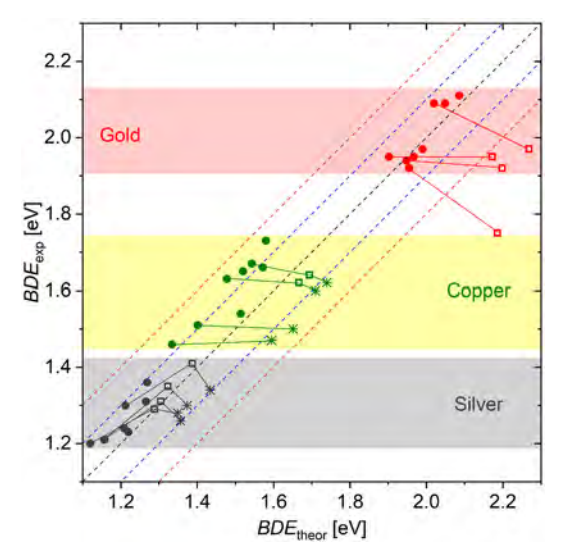


Figure 7. The relation between theoretically calculated *BDEs* of π-ligands in copper, silver, and gold complexes (green, black, and red, respectively) $[L_1M(\pi-ligand)]^+$ (solid circles), $[L_2M(\pi-ligand)]^+$ (open squares), $[L_3M(\pi-ligand)]^+$ (stars) (listed in Tables 3 – 5). The color-coded lines connect points corresponding to the complexes with the same π -ligand, but different L. $L_1 = H_2C(3,5-(CH_3)_2Pz)_2$, $L_2 = H_2C(3-(CF_3)Pz)_2$ and $L_3 = H_2C(3,5-(CF_3)_2Pz)_2$.

Table 4. Bond dissociation energies of π -ligands from [L₂M(π -ligand)]⁺. L₂ = H₂C(3-(CF₂)Pz)₂

π-Ligand	[L₂Cu(π-ligar	nd)] ⁺	[L₂Ag(π-ligar	nd)] ⁺	[L₂Au(π-ligar	nd)]†
	BDE _{exp} [eV]	BDE _{theor} [eV]	BDE _{exp} [eV]	BDE _{theor} [eV]	BDE _{exp} [eV]	BDE _{theor} [eV]
1-Pentene		1.60	1.31 ± 0.03	1.31	1.92 ± 0.01	2.20
2-Pentene		1.54	1.29 ± 0.07	1.29	1.95 ± 0.01	2.17
1-Pentyne	1.62 ± 0.01	1.67	1.35 ± 0.02	1.32	1.75 ± 0.08	2.19
2-Pentyne	1.64 ± 0.01	1.69	1.41 ± 0.02	1.39	1.97 ± 0.03	2.27

		3	- 3	3 3	2	1.7 .7
π-Ligand	[L₃Cu(π-liga	nd)] ⁺	[L₃Ag(π-liga	nd)] ⁺	[L₃Au(π-liga	nd)] ⁺
	BDE _{exp} [eV]	BDE _{theor} [eV]	BDE _{exp} [eV]	BDE _{theor} [eV]	BDE _{exp} [eV]	BDE _{theor} [eV]
1-Pentene	1.50	1.65	1.26 ± 0.02	1.36		2.24
2-Pentene	1.47	1.60	1.28 ± 0.04	1.35		2.24
1-Pentyne	1.60 ± 0.02	1.71	1.30 ± 0.01	1.37		2.19
2-Pentyne	1.62 ± 0.03	1.74	1.34 ± 0.04	1.43		2.30

Table 5. Bond dissociation energies of π -ligands from $[L_xM(\pi-\text{ligand})]^+$, $L_x = H_xC(3,5-(CF_x)^2PZ)_x$

Ion spectroscopy

In order to confirm the trend of the binding energies, we have also measured IR photodissociation spectra of selected gaseous complexes. The focus was on complexes with 1-pentyne as they show a prominent C \equiv C stretching vibration. The spectral shifts of this vibration can also be related to the effect of the metal binding on the C \equiv C bond. The v_{cc} of free 1-pentyne is 2120 cm⁻¹.⁴³ We have first compared the C≡C stretching vibrations in copper, silver, and gold complexes with the L. ligand (Figure 8). In agreement with the predicted trend of binding energies, we observed the smallest red shift for the silver complex ($v_{cc} = 2024 \text{ cm}^{-1}$), followed by the copper complex ($v_{cc} = 1947 \text{ cm}^{-1}$) and by the gold complex with the largest red shift ($v_{cc} = 1862 \text{ cm}^{-1}$). The stretching frequency of the $L_1Cu(1-pentyne)^+$ agreed well with the isolated solid complex ($v_{cc} = 1937 \text{ cm}^{-1}$ in both the Raman and infrared). The remaining part of the fingerprint spectra nicely correspond to the theoretically predicted bands (see Figures S9 - S11).

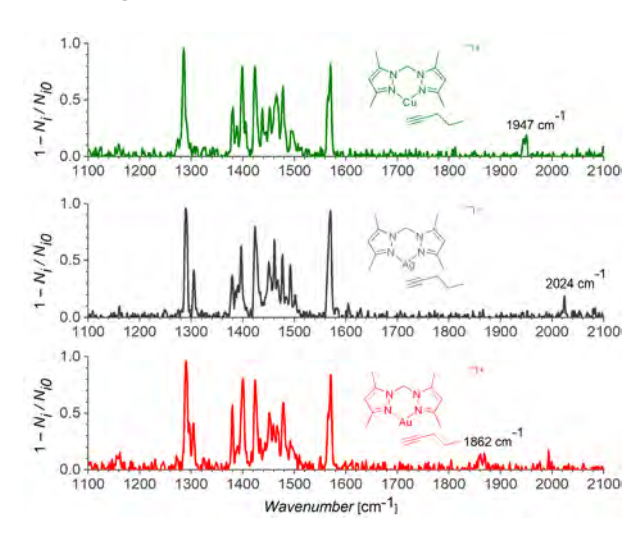


Figure 8. Helium tagging photodissociation spectra of [L,Cu(1-pentyne)]+(top, green), [L,Ag(1-pentyne)]+(top, green), [L,Ag(1pentyne)]+ (middle, grey), and[L,Au(1-pentyne)]+ (bottom, red). The fingerprint IR spectrum agrees with the theoretically predicted spectra (Figures S9 – S11). $L_1 = H_2C(3.5-(CH_3)_2Pz)_3$.

Next, we investigated series of copper complexes with 1-pentyne and the ligands L_1 , L_2 , and L_3 (Figure 9). The IR photodissociation spectra clearly show that the red shift of the C \equiv C stretching vibration is slightly smaller for the complexes with electron deficient ligands (L_1 : 1947 cm $^{-1}$, L_2 : 1977 cm $^{-1}$, L_3 : 1980 cm $^{-1}$). Similarly, we could compare the IR spectra of silver complexes with L_1 and L_3 and the trend (L_1 : 2024 cm $^{-1}$, L_3 : 2035 cm $^{-1}$) again clearly showed a weaker interaction of the alkyne with the complex bearing the electron deficient ligand L_3 . These spectroscopic data thus fully support the experimental binding energies and show that the more electron deficient ancillary ligands do not support a stronger interaction between the coinage metals and the π -ligands.

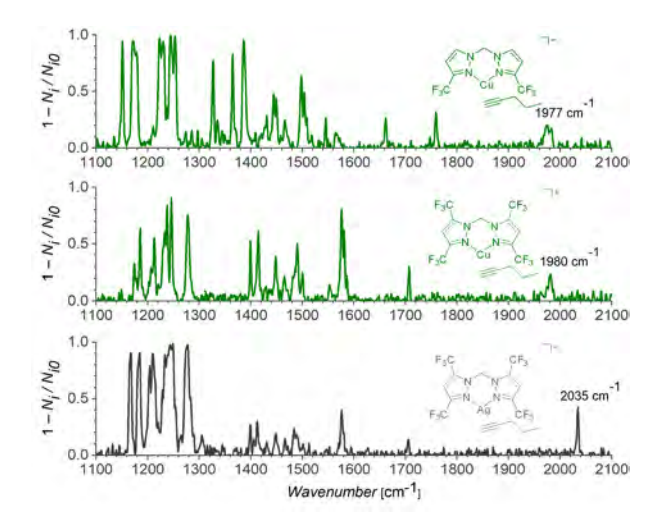


Figure 9. Helium tagging photodissociation spectra of $[L_2Cu(1-pentyne)]^+$ and $[L_3Cu(1-pentyne)]^+$ (top and middle, both green) and $[L_3Ag(1-pentyne)]^+$ (bottom, grey). The fingerprint IR spectrum agrees well with the theoretically predicted spectra (Figures S12 – S14). $L_2 = H_2C(3-(CF_3)Pz)_2$ and $L_3 = H_2C(3-(CF_3)Pz)_2$.

Discussion

We have reported a series of π -complexes with copper(I), silver(I), and gold(I) having bidentate ancillary ligands. The binding energies of the π -ligands increase in the complexes in the order of Ag < Cu < Au (Table 3). This trend correlates with the increasing C-C bond distances of the π -bonds of the ligands in the corresponding crystal structures (Table 2). In solution, the increasing binding energy correlates with the increasing up-field NMR shifts of the carbon atoms of the coordinated multiple bond as well as with the up-field NMR shifts of the hydrogen atoms

attached to those carbon atoms (Table 1). The effect on the NMR shifts is almost negligible for the silver complexes but increases for the copper- and even more for the gold complexes. These results suggest that the binding between the coinage metals Cu^{\dagger} and Au^{\dagger} and the π -ligands leads to an increase of electron density at the π -bond and thus is dominantly mediated by π -back bonding in these complexes. This finding is in agreement with recent computational analysis of three-coordinate coinage metal complexes bearing nitrogen-based supporting ligands. 14,42,44 Interestingly, the computational data of the coinage metal ethylene and acetylene complexes without supporting ligands predict the presence of more dominant σ -bonding interaction over π -back bonding.⁴⁵

The importance of the π -back bonding for the interactions in the reported complexes is further highlighted by a neutral- or a negative effect of electronwithdrawing substituents at the ancillary ligands on the binding energies between the metals and π -ligands. The electron-withdrawing substitution at the ancillary ligands decreases electron density at the metals. Therefore, it should support σ -bonding interaction between the π -ligands and the metals but should weaken the π -back bonding. The experimental data show that upon the reducing of the electron density at the metal, the binding energies slightly grow for silver complexes, stay about the same for copper complexes and decrease for the gold complexes. The trend suggests that the role of the π -back bonding grows in the series Ag < Cu < Au and is probably the dominating interaction for the gold π -complexes.⁴²

Finally, a comparison of the experimental BDE data with non-relativistic DFT calculations presented above (Figure 7) shows that DFT does not correctly describe the effects of electron-withdrawing substituents at the ancillary ligands on metal- π -ligand moiety. This is probably due to an insufficient description of the π -back bonding at the nonrelativistic level. 46a Accordingly, the agreement for the gold complexes is the worst. The relativistic effects destabilize the 5d electrons that are therefore high in energy and thus can more efficiently participate in the binding interactions with π ligands. 46b If this relativistic effect is insufficiently included in the calculations, the participation of the d-electrons in the binding will be underestimated leading to a wrong description of the π -back bonding.

Conclusions

The bis(pyrazolyl)methane ligands enabled a detailed investigation of coinage metal alkene and alkyne complexes including the solid state structural data on a rare isoleptic series $[L_1M(C_2H_4)]^+$ (M=Cu, Ag, Au). The interaction between these transition metals and π -ligands is a combination of σ bonding and π -back bonding. Consistent with NMR spectroscopic and X-ray structural data, and in agreement with previous studies, this shows that the binding energies of π -ligands in the coinage metal complexes increase in the series Ag < Cu < Au.⁴⁷ It is often believed that the σ bonding contribution for the d¹0 coinage metal complexes prevails over the π -back bonding contribution. However, the experimental trend of binding energies and geometry parameters does not support this hypothesis. On contrary, the π -ligand binding energies for copper and gold complexes decrease with the electron withdrawing substitution on the ancillary ligands. This suggest that the π -back bonding interaction play a significant role in this type of complexes, even though they are cationic, closed-shell d¹0 metal systems.

References

- a) Echavarren, A. M.; Jiao, N.; Gevorgyan, V. Coinage Metals in Organic Synthesis. Chem. Soc. Rev. 2016, 45 (16), 4445-4447; b) Díaz-Requejo, M. M.; Pérez, P. J. Coinage Metal Catalyzed C-H Bond Functionalization of Hydrocarbons. Chem. Rev. 2008, 108 (8), 3379-3394; c) Corinti, D.; Crestoni, M. E.; Chiavarino, B.; Fornarini, S.; Scuderi, D.; Salpin, J.-Y. Insights into Cisplatin Binding to Uracil and Thiouracils from IRMPD Spectroscopy and Tandem Mass Spectrometry. J. Am. Soc. Mass Spectrom. 2020, 31 (4), 946–960; d) Jordan, A. J.; Lalic, G.; Sadighi, J. P. Coinage Metal Hydrides: Synthesis, Characterization, and Reactivity. Chem. Rev. 2016, 116 (15), 8318–8372; e) Hashmi, A. S. K. Introduction: Gold Chemistry. Chem. Rev. 2021, 121 (14), 8309–8310; f) Dyker, G. An Eldorado for Homogeneous Catalysis? Angew. Chemie - Int. Ed. 2000, 39, 4237.
- a) Hein, J. E.; Fokin, V. V. Copper-Catalyzed Azide-Alkyne Cycloaddition (CuAAC) and beyond: New 2. Reactivity of Copper(i) Acetylides. Chem. Soc. Rev. 2010, 39 (4), 1302; b) Haldón, E.; Nicasio, M. C.; Pérez, P. J. Copper-Catalysed Azide-Alkyne Cycloadditions (CuAAC): An Update. Org. Biomol. Chem. 2015, 13 (37), 9528-9550; c) Parasar, D.; Ponduru, T. T.; Noonikara-Poyil, A.; Jayaratna, N. B.; Dias, H. V. R. Acetylene and Terminal Alkyne Complexes of Copper(I) Supported by Fluorinated Pyrazolates: Syntheses, Structures, and Transformations. Dalt. Trans. 2019, 48 (42), 15782–15794.
- a) Angulo, B.: Herrerías, C. I.: Hormigón, Z.: Mayoral, J. A.: Salvatella, L. Copper-Catalyzed Cyclopropanation Reaction of but-2-Ene. J. Mol. Model. 2018, 24 (8), 195; b) Lyle, M. P. A.; Draper, N. D.; Wilson, P. D. Synthesis and Evaluation of New Chiral Nonracemic C2-Symmetric and Unsymmetric 2,2'-Bipyridyl Ligands. Org. Biomol. Chem. 2006, 4 (5), 877; c) Handy, S. T.; Ivanow, A. In Situ Generated Polypyrazolylborate-Copper Complexes as Cyclopropanation Catalysts. Inorganica Chim. Acta 2009, 362 (12), 4468-4471; d) Martín, C.; Muñoz-Molina, J. M.; Locati, A.; Alvarez, E.; Maseras, F.; Belderrain, T. R.; Pérez, P. J. Copper(I)-Olefin Complexes: The Effect of the Trispyrazolylborate Ancillary Ligand in Structure and Reactivity. Organometallics 2010, 29 (16), 3481-3489.
- a) Noonikara-Poyil, A.; Ridlen, S. G.; Dias, H. V. R. Isolable Copper(I) n 2 -Cyclopropene Complexes. Inorg. Chem. 2020, No. I, acs.inorgchem.0c02886; b) Díaz-Requejo, M. M.; Mairena, M. A.; Belderrain, T. R.; Nicasio, M. C.; Pérez, P. J.; Trofimenko, S. A Family of Highly Active Copper(i)-Homoscorpionate Catalysts for the Alkyne Cyclopropenation Reaction. Chem. Commun. 2001, No. 18, 1804–1805; c) Rodríguez, P.; Caballero, A.; Díaz-Reguejo, M. M.; Nicasio, M. C.; Pérez, P. J. Very Efficient, Reusable Copper Catalyst for Carbene Transfer Reactions under Biphasic Conditions Using Ionic Liquids. Org. Lett. 2006, 8 (4), 557-560; d) Pérez, J.; Morales, D.; García-Escudero, L. A.; Martínez-García, H.; Miguel, D.; Bernad, P. Synthesis of New Copper(I) Complexes with Tris(2-Pyridyl) Ligands. Applications to Carbene and Nitrene Transfer Reactions. Dalt. Trans. 2009, No. 2, 375-382; e) Martínez-García, H.; Morales, D.; Pérez, J.; Puerto, M.; Miguel, D. 1,3,5-Tris(Thiocyanatomethyl)Mesitylene as a Ligand. Pseudooctahedral Molybdenum, Manganese, and Rhenium Carbonyl Complexes and Copper and Silver Dimers. Copper-Catalyzed Carbene- and Nitrene-Transfer Reactions. Inorg. Chem. 2010, 49 (15), 6974-6985; f) Martín, C.; Sierra, M.; Alvarez, E.; Belderrain, T. R.; Pérez, P. J. Hydrotris(3-Mesitylpyrazolyl)Borato-Copper(i) Alkyne Complexes: Synthesis, Structural Characterization and Rationalization of Their Activities as Alkyne Cyclopropenation Catalysts. Dalt. Trans. 2012, 41 (17), 5319; q) Maestre, L.; Ozkal, E.; Ayats, C.; Beltrán, Á.; Díaz-Requejo, M. M.; Pérez, P. J.; Pericàs, M. A. A Fully Recyclable Heterogenized Cu Catalyst for the General Carbene Transfer Reaction in Batch and Flow. Chem. Sci. 2015, 6 (2), 1510-1515.
- Lamberti, C.; Prestipino, C.; Capello, L.; Bordiga, S.; Zecchina, A.; Spoto, G.; Moreno, S.; Marsella, A.; Cremaschi, B.; Garilli, M.; Vidotto, S.; Leofanti, G. The CuCl2/Al2O3 Catalyst Investigated in Interaction with Reagents. Int. J. Mol. Sci. 2001, 2 (5), 230-245.

- 6. a) Plischke, J. K.; Benesi, A. J.; Vannice, A. M. A 13C NMR Study of Ethylene Adsorbed on Reduced and Oxygen-Covered Ag Surfaces. J. Catal. 1992, 138 (1), 223–239; b) Dias, H. V. R.; Wang, Z. Ethylene Oxide and Propylene Sulfide Complexes of Silver(I): Synthesis and Characterization of [HB(3,5-(CF 3) 2 Pz) 3]Ag(SC 3 H 6). Inorg. Chem. 2000, 39 (16), 3724–3727; c) Böcklein, S.; Günther, S.; Reichelt, R.; Wyrwich, R.; Joas, M.; Hettstedt, C.; Ehrensperger, M.; Sicklinger, J.; Wintterlin, J. Detection and Quantification of Steady-State Ethylene Oxide Formation over an Ag(111) Single Crystal. J. Catal. 2013, 299, 129–136; d) Roithová, J.; Schröder, D. Gas-Phase Models for Catalysis: Alkane Activation and Olefin Epoxidation by the Triatomic Cation Ag 2 O +. J. Am. Chem. Soc. 2007, 129 (49), 15311–15318.
- Fang, G.; Bi, X. Silver-Catalysed Reactions of Alkynes: Recent Advances. Chem. Soc. Rev. 2015, 44
 (22), 8124–8173.
- a) Li, Y.; Zhang, C.; Zhang, H.; Li, L.; Zhang, J.; Oh, R.; Yao, L.; Cai, M.; Li, J.; Zhang, M.; Li, F. Effects of N-, P-, or O-Containing Ligands on Gold-Based Complex Catalysts for Acetylene Hydrochlorination. Appl. Catal. A Gen. 2021, 612, 118015; b) Chen, Z.; Chen, Y.; Chao, S.; Dong, X.; Chen, W.; Luo, J.; Liu, C.; Wang, D.; Chen, C.; Li, W.; Li, J.; Li, Y. Single-Atom Au I – N 3 Site for Acetylene Hydrochlorination Reaction. ACS Catal. 2020, 10 (3), 1865–1870.
- a) Hashmi, A. S. K. Gold-Catalyzed Organic Reactions. *Chem. Rev.* 2007, 107 (7), 3180–3211; b)
 Li, Z.; Brouwer, C.; He, C. Gold-Catalyzed Organic Transformations. *Chem. Rev.* 2008, 108 (8), 3239–3265; c) Yang, Y.; Antoni, P.; Zimmer, M.; Sekine, K.; Mulks, F. F.; Hu, L.; Zhang, L.; Rudolph, M.; Rominger, F.; Hashmi, A. S. K. Dual Gold/Silver Catalysis Involving Alkynylgold(III) Intermediates Formed by Oxidative Addition and Silver-Catalyzed C–H Activation for the Direct Alkynylation of Cyclopropenes. *Angew. Chemie Int. Ed.* 2019, 58 (15), 5129–5133.
- 10. Thompson, J. S.; Harlow, R. L.; Whitney, J. F. Copper(I)-Olefin Complexes. Support for the Proposed Role of Copper in the Ethylene Effect in Plants. J. Am. Chem. Soc. 1983, 105 (11), 3522–3527.
- a) Dias, H. V. R.; Lu, H.-L.; Kim, H.-J.; Polach, S. A.; Goh, T. K. H. H.; Browning, R. G.; Lovely, C. J. Copper(I) Ethylene Adducts and Aziridination Catalysts Based on Fluorinated Tris(Pyrazolyl) Borates [HB(3-(CF3),5-(R)Pz)3] (Where R = CF 3, C 6 H 5, H; Pz = Pyrazolyl). Organometallics 2002, 21 (7), 1466–1473; b) Dias, H. V. R.; Wang, Z.; Jin, W. Synthesis and Chemistry of [Hydrotris(3,5-Bis(Trifluoromethyl)Pyrazolyl)Borato]Silver(I) Complexes. Inorg. Chem. 1997, 36 (27), 6205–6215; c) Dias, H. V. R.; Wu, J. Thermally Stable Gold(I) Ethylene Adducts: [(HB{3,5-(CF 3) 2 Pz} 3)Au(CH 2 = CH 2)] and [(HB{3-(CF 3),5-(Ph)Pz} 3)Au(CH 2=CH 2)]. Angew. Chemie Int. Ed. 2007, 46 (41), 7814–7816.
- Esser, B.; Swager, T. M. Detection of Ethylene Gas by Fluorescence Turn-On of a Conjugated Polymer. Angew. Chemie 2010, 122 (47), 9056–9059; b) Esser, B.; Schnorr, J. M.; Swager, T. M. Selective Detection of Ethylene Gas Using Carbon Nanotube-based Devices: Utility in Determination of Fruit Ripeness. Angew. Chemie Int. Ed. 2012, 51 (23), 5752–5756.
- 13. Noonikara-Poyil, A.; Cui, H.; Yakovenko, A. A.; Stephens, P. W.; Lin, R.; Wang, B.; Chen, B.; Dias, H. V. R. A Molecular Compound for Highly Selective Purification of Ethylene. *Angew. Chemie Int. Ed.* **2021**, *60* (52), 27184–27188.
- Noonikara-Poyil, A.; Muñoz-Castro, A.; Boretskyi, A.; Mykhailiuk, P. K.; Dias, H. V. R. When SF 5 Outplays CF 3: Effects of Pentafluorosulfanyl Decorated Scorpionates on Copper. *Chem. Sci.* 2021, 12 (43), 14618–14623.
- a) Perez, P. J.; Brookhart, M.; Templeton, J. L. A Copper(I) Catalyst for Carbene and Nitrene Transfer to Form Cyclopropanes, Cyclopropenes, and Aziridines. Organometallics 1993, 12 (2), 261–262; b) Muñoz-Molina, J. M.; Belderrain, T. R.; Pérez, P. J. Trispyrazolylborate Coinage Metals Complexes: Structural Features and Catalytic Transformations. Coord. Chem. Rev. 2019, 390, 171–189.
- Fujisawa, K.; Noguchi, Y.; Miyashita, Y.; Okamoto, K.; Lehnert, N. Mononuclear and Binuclear Copper(I) Complexes Ligated by Bis(3,5-Diisopropyl-1-Pyrazolyl)Methane: Insight into the

- Fundamental Coordination Chemistry of Three-Coordinate Copper(I) Complexes with a Neutral Coligand. Inorg. Chem. 2007, 46 (25), 10607-10623.
- 17. Boni, A.; Pampaloni, G.; Peloso, R.; Belletti, D.; Graiff, C.; Tiripicchio, A. Synthesis of Copper(I) Bis(3,5-Dimethylpyrazolyl)Methane Olefin Complexes and Their Reactivity towards Carbon Monoxide. J. Organomet. Chem. 2006, 691 (26), 5602-5609.
- 18. Pampaloni, G.; Pelosos, R.; Belletti, D.; Graiff, C.; Tiripicchio, A. Trifluoromethyl-Substituted Bis(Pyrazolyl)Methanes as Ligands for Copper and Silver: Synthesis and Spectroscopic and Structural Characterization. Organometallics 2007, 26 (17), 4278-4286.
- 19. Peralta, R. A.; Huxley, M. T.; Albalad, J.; Sumby, C. J.; Doonan, C. J. Single-Crystal-to-Single-Crystal Transformations of Metal-Organic-Framework-Supported, Site-Isolated Trigonal-Planar Cu(I) Complexes with Labile Ligands. Inorg. Chem. 2021, 60 (16), 11775–11783.
- 20. a) Chou, C.-C.; Liu, H.-J.; Su, C.-C. The First Stereochemically Nonrigid Monomeric Two-Coordinate Copper(i) Complexes with Homoleptic and Heteroleptic "N2" Donor Set. Dalt. Trans. 2008, No. 25, 3358; b) Chou, C.-C.; Su, C.-C.; Tsai, H.-L.; Lii, K.-H. First Example of a 2:1 Cocrystal of Mixed Cu(I)/Cu(II) Complexes and a Novel Ferromagnetic Bis(µ-Hydroxo)Dicopper(II) Complex with a Bis(Pyrazol-1-YI)Methane Bidentate Ligand. Inorg. Chem. 2005, 44 (3), 628–632.
- 21. a) Bassanetti, I.; Mattarozzi, M.; Delferro, M.; Marks, T. J.; Marchiò, L. Silver(I) Bis(Pyrazolyl)Methane Complexes and Their Implementation as Precursors for Metallic Silver Deposition. Eur. J. Inorg. Chem. 2016, 2016 (15-16), 2626-2633; b) José Calhorda, M.; Costa, P. J.; Crespo, O.; Gimeno, M. C.; Jones, P. G.; Laguna, A.; Naranjo, M.; Quintal, S.; Shi, Y.-J.; Villacampa, M. D. Group 11 Complexes with the Bis(3,5-Dimethylpyrazol-1-Yl)Methane Ligand. How Secondary Bonds Can Influence the Coordination Environment of Aq(I): The Role of Coordinated Water in [Aq_(u-L)_(OH_)_](OTf)_. Dalt. Trans. 2006, No. 34, 4104–4113; c) Fujisawa, K.; Kanda, R.; Miyashita, Y.; Okamoto, K. Copper(II) Complexes with Neutral Bis(Pyrazolyl)Methane Ligands: The Influence of Steric Hindrance on Their Structures and Properties. Polyhedron 2008, 27 (5), 1432-1446.
- 22. a) Lin, Y.-C.; Sundholm, D.; Jusélius, J.; Cui, L.-F.; Li, X.; Zhai, H.-J.; Wang, L.-S. Experimental and Computational Studies of Alkali-Metal Coinage-Metal Clusters. J. Phys. Chem. A 2006, 110 (12), 4244–4250; b) Tsipis, A. C. Unveiling the Nature of Binding Interactions of Acetylene and Ethylene with Triangular Coinage Metal Clusters: A DFT Computational Study. Organometallics 2010, 29 (2), 354–363; c) Jover, J.; Maseras, F. Computational Characterization of the Mechanism for Coinage-Metal-Catalyzed Carboxylation of Terminal Alkynes. J. Org. Chem. 2014, 79 (24), 11981-11987; d) Besora, M.; Braga, A. A. C.; Sameera, W. M. C.; Urbano, J.; Fructos, M. R.; Pérez, P. J.; Maseras, F. A Computational View on the Reactions of Hydrocarbons with Coinage Metal Complexes. J. Organomet. Chem. **2015**, 784, 2–12.
- 23. Motloch, P.; Jašík, J.; Roithová, J. Gold(I) and Silver(I) π-Complexes with Unsaturated Hydrocarbons. Organometallics 2021, 40 (10), 1492-1502.
- 24. Jašíková, L.; Roithová, J. Interaction of the Gold(I) Cation Au(PMe 3) + with Unsaturated Hydrocarbons. Organometallics 2012, 31 (5), 1935–1942.
- 25. a) Fianchini, M.; Campana, C. F.; Chilukuri, B.; Cundari, T. R.; Petricek, V.; Dias, H. V. R. Use of [SbF6]to Isolate Cationic Copper and Silver Adducts with More than One Ethylene on the Metal Center. Organometallics 2013, 32 (10), 3034–3041; b) Dias, H. V. R.; Fianchini, M.; Cundari, T. R.; Campana, C. F. Synthesis and Characterization of the Gold(I) Tris(Ethylene) Complex [Au(C 2 H 4) 3][SbF 6]. Angew. Chemie Int. Ed. 2008, 47 (3), 556-559.
- 26. Fianchini, M.; Dai, H.; Dias, H. V. R. Organometallic Wheels Based on Coinage Metal Ions and Norbornene: Syntheses and Structural Characterization of [M(Norbornene)3][SbF6] (M = Au, Ag, Cu). Chem. Commun. 2009, No. 42, 6373-6375.
- 27. Klimovica, K.; Kirschbaum, K.; Daugulis, O. Synthesis and Properties of "Sandwich" Diimine-Coinage Metal Ethylene Complexes. Organometallics 2016, 35 (17), 2938–2943.

- a) Dias, H. V. R.; Wu, J. Structurally Similar, Thermally Stable Copper(I), Silver(I), and Gold(I) Ethylene Complexes Supported by a Fluorinated Scorpionate. *Organometallics* 2012, 31 (4), 1511–1517; b)
 Dias, H. V. R.; Wu, J. Structurally Characterized Coinage-Metal-Ethylene Complexes. *Eur. J. Inorg. Chem.* 2008, 2008 (4), 509–522.
- 29. a) Nyholm, R.S. Electron Configuration and Structure of Transition-Metal Complexes. Proc. Chem. Soc. **1961**, 273–296; b) C. Elschenbroich, *Organometallics, 3rd, Completely Revised and Extended Edition*, 3rd ed., Wiley, Weinheim, **2006**.
- 30. a) Oguadinma, P. O.; Schaper, F. π Back-Bonding in Dibenzyl-β-Diketiminato Copper Olefin Complexes. *Organometallics* **2009**, *28* (23), 6721–6731; b) van Dijkman, T. F.; Siegler, M. A.; Bouwman, E. Highly Tunable Fluorinated Trispyrazolylborates [HB(3-CF 3 -5-{4-RPh}pz) 3] (R = NO 2, CF 3, Cl, F, H, OMe and NMe 2) and Their Copper(i) Complexes. *Dalt. Trans.* **2015**, *44* (48), 21109–21123; c) Munakata, M.; Kitagawa, S.; Kosome, S.; Asahara, A. Studies of Copper(l) Olefin Complexes. Formation Constants of Copper Olefin Complexes with 2,2'-Bipyridine, 1,10-Phenanthroline, and Their Derivatives. *Inorg. Chem.* **1986**, *25* (15), 2622–2627; d) Kazi, A. B.; Rasika Dias, H. V.; Tekarli, S. M.; Morello, G. R.; Cundari, T. R. Coinage Metal–Ethylene Complexes Supported by Tris(Pyrazolyl)Borates: A Computational Study. *Organometallics* **2009**, *28* (6), 1826–1831.
- 31. a) Santiso-Quiñones, G.; Reisinger, A.; Slattery, J.; Krossing, I. Homoleptic Cu–Phosphorus and Cu–Ethene Complexes. Chem. Commun. 2007, No. 47, 5046; b) Krossing, I.; Reisinger, A. A Stable Salt of the Tris(Ethene)Silver Cation: Structure and Characterization of [Ag(n²-C₂H₄)₃]*[Al{OC(CF₃)₃}₄]⁻. Angew. Chemie Int. Ed. 2003, 42 (46), 5725–5728; c) Schaefer, J.; Himmel, D.; Krossing, I. [Au(n²-C₂ H₄)₃]*[Al(OR^F)₄]⁻ a Stable Homoleptic (Ethene)Gold Complex. Eur. J. Inorg. Chem. 2013, 2013 (15), 2712–2717.
- 32. Liu, Y.; Chen, C.; Li, H.; Huang, K.-W.; Tan, J.; Weng, Z. Efficient S N 2 Fluorination of Primary and Secondary Alkyl Bromides by Copper(I) Fluoride Complexes. *Organometallics* **2013**, *32* (21), 6587–6592.
- 33. Gulliver, D. J.; Levason, W.; Webster, M. Coordination Stabilised Copper(I) Flouride. Crystal and Molecular Structure of Fluorotris(Triphenylphosphine)Copper(I)-ethanol (1/2), Cu(PPh3)3, P-2EtOH. *Inorganica Chim. Acta* **1981**, *52*, 153–159.
- 34. a) Bayler, A.; Schier, A.; Bowmaker, G. A.; Schmidbaur, H. Gold Is Smaller than Silver. Crystal Structures of [Bis(Trimesitylphosphine)Gold(I)] and [Bis(Trimesitylphosphine)Silver(I)] Tetrafluoroborate. *J. Am. Chem. Soc.* **1996**, *118* (29), 7006–7007; b) Omary, M. A.; Rawashdeh-Omary, M. A.; Gonser, M. W. A.; Elbjeirami, O.; Grimes, T.; Cundari, T. R.; Diyabalanage, H. V. K.; Gamage, C. S. P.; Dias, H. V. R. Metal Effect on the Supramolecular Structure, Photophysics, and Acid–Base Character of Trinuclear Pyrazolato Coinage Metal Complexes. *Inorg. Chem.* **2005**, *44* (23), 8200–8210.
- 35. a) Thompson, J. S.; Whitney, J. F. Copper(I) Complexes with Unsaturated Small Molecules. Preparation and Structural Characterization of Copper(I)-Di-2-Pyridylamine Complexes with Olefins, Acetylene, and Carbon Monoxide. *Inorg. Chem.* 1984, 23 (18), 2813–2819; b) Allen, J. J.; Barron, A. R. Synthesis and Structural Characterization of [Ag(H-Dpa) (H2-Styrene)]BF4: Comparing Silver and Copper for Olefin Binding. *J. Chem. Crystallogr.* 2009, 39 (12), 935–939; c) Allen, J. J.; Barron, A. R. Olefin Coordination in Copper(I) Complexes of Bis(2-PyridyI)Amine. *Dalt. Trans.* 2009, No. 5, 878–890.
- 36. a) Craig, N. C.; Groner, P.; McKean, D. C. Equilibrium Structures for Butadiene and Ethylene: Compelling Evidence for Π-Electron Delocalization in Butadiene. J. Phys. Chem. A 2006, 110 (23), 7461–7469; b) van Nes, G. J. H.; van Bolhuis, F. Single-Crystal Structures and Electron Density Distributions of Ethane, Ethylene and Acetylene. II. Single-Crystal X-Ray Structure Determination

- of Acetylene at 141 K. Acta Crystallogr. Sect. B Struct. Crystallogr. Cryst. Chem. 1979, 35 (11), 2580-2593.
- 37. Ridlen, S. G.; Wu, J.; Kulkarni, N. V.; Dias, H. V. R. Isolable Ethylene Complexes of Copper(I), Silver(I), and Gold(I) Supported by Fluorinated Scorpionates [HB{3-(CF3),5-(CH3)Pz}3] – and [HB{3-(CF3),5-(Ph)Pz}3]-. Eur. J. Inorg. Chem. 2016, 2016 (15-16), 2573-2580.
- 38. Reisinger, A.; Trapp, N.; Knapp, C.; Himmel, D.; Breher, F.; Rüegger, H.; Krossing, I. Silver-Ethene Complexes $[Ag(\eta 2 - C 2 H 4) n][Al(OR F) 4]$ with n = 1, 2, 3 (R F = Fluorine-Substituted Group). Chem. - A Eur. J. 2009, 15 (37), 9505-9520.
- 39. Groom, C. R.; Bruno, I. J.; Lightfoot, M. P.; Ward, S. C. The Cambridge Structural Database. Acta Crystallogr. Sect. B Struct. Sci. Cryst. Eng. Mater. 2016, 72 (2), 171–179.
- 40. Dias, H. V. R.; Flores, J. A.; Wu, J.; Kroll, P. Monomeric Copper(I), Silver(I), and Gold(I) Alkyne Complexes and the Coinage Metal Family Group Trends. J. Am. Chem. Soc. 2009, 131 (31), 11249-11255.
- 41. Brown, T. J.; Widenhoefer, R. A. Synthesis and Equilibrium Binding Studies of Cationic, Two-Coordinate Gold(I) π-Alkyne Complexes. J. Organomet. Chem. 2011, 696 (6), 1216–1220.
- 42. Wu, J.; Noonikara-Poyil, A.; Muñoz-Castro, A.; Dias, H. V. R. Gold(i) Ethylene Complexes Supported by Electron-Rich Scorpionates. Chem. Commun. 2021, 57 (8), 978-981.
- 43. NIST Chemistry WebBook, SRD 69, Gas Phase IR Spectrum of 1-Pentyne. https://webbook.nist. gov/cgi/cbook.cgi?ID=C627190&Units=SI&Mask=80#Refs (accessed 8/25/2021).
- 44. a) Geri, J. B.; Pernicone, N. C.; York, J. T. Comparing the Impact of Different Supporting Ligands on Copper(I)-Ethylene Interactions. Polyhedron 2013, 52, 207-215; b) Jana, G.; Pan, S.; Chattaraj, P. K. Binding of Small Gas Molecules by Metal-Bipyridyl Monocationic Complexes (Metal = Cu, Ag, Au) and Possible Bond Activations Therein. J. Phys. Chem. A 2017, 121 (19), 3803-3817.
- 45. Nechaev, M. S.; Rayón, V. M.; Frenking, G. Energy Partitioning Analysis of the Bonding in Ethylene and Acetylene Complexes of Group 6, 8, and 11 Metals: (CO)_cTM-C₃H₄ and CI₂TM-C₃H₄ (TM = Cr, Mo, W), $(CO)_aTM-C_2H_u$ (TM = Fe, Ru, Os), and TM+-C₂H_u (TM = Cu, Ag, Au). J. Phys. Chem. A **2004**, 108, 3134-3142.
- 46. a) Tai, H.-C.; Krossing, I.; Seth, M.; Deubel, D. V. Organometallics versus P 4 Complexes of Group 11 Cations: Periodic Trends and Relativistic Effects in the Involvement of (n-1)d, n s, and n p Orbitals in Metal-Ligand Interactions. Organometallics 2004, 23 (10), 2343-2349; b) Pernpointner, M.; Hashmi, A. S. K. Fully Relativistic, Comparative Investigation of Gold and Platinum Alkyne Complexes of Relevance for the Catalysis of Nucleophilic Additions to Alkynes. J. Chem. Theory Comput. 2009, 5 (10), 2717-2725.
- 47. Lepetit, C.; Maraval, V.; Canac, Y.; Chauvin, R. On the Nature of the Dative Bond: Coordination to Metals and beyond. The Carbon Case. Coord. Chem. Rev. 2016, 308, 59–75.
- 48. Field, L. D.; Messerle, B. A.; Rehr, M.; Soler, L. P.; Hambley, T. W. Cationic Iridium(I) Complexes as Catalysts for the Alcoholysis of Silanes. Organometallics 2003, 22 (12), 2387–2395.
- 49. Li, C.; Li, W.; Henwood, A. F.; Hall, D.; Cordes, D. B.; Slawin, A. M. Z.; Lemaur, V.; Olivier, Y.; Samuel, I. D. W.; Zysman-Colman, E. Luminescent Dinuclear Copper(I) Complexes Bearing an Imidazolylpyrimidine Bridging Ligand. Inorg. Chem. 2020, 59 (20), 14772–14784.
- 50. Stefani, H. A.; Guadagnin, R. C.; Keppler, A. F.; Botteselle, G. V.; Comasseto, J. V.; Suganuma, C. A. Mechanistic Aspects of the Isomerization of Z-Vinylic Tellurides Double Bonds in the Synthesis of Potassium Z-Vinyltrifluoroborate Salts. Beilstein J. Org. Chem. 2008, 4, 5–9.
- 51. Krause, L.; Herbst-Irmer, R.; Sheldrick, G. M.; Stalke, D. Comparison of Silver and Molybdenum Microfocus X-Ray Sources for Single-Crystal Structure Determination. J. Appl. Crystallogr. 2015, 48 (1), 3-10.

- 52. Sheldrick, G. M. SHELXT Integrated Space-Group and Crystal-Structure Determination. *Acta Crystallogr. Sect. A Found. Crystallogr.* **2015**, *71* (1), 3–8.
- 53. Sheldrick, G. M. Crystal Structure Refinement with SHELXL. *Acta Crystallogr. Sect. C Struct. Chem.* **2015**, *71*, 3–8.
- Dolomanov, O. V.; Bourhis, L. J.; Gildea, R. J.; Howard, J. A. K.; Puschmann, H. OLEX2: A Complete Structure Solution, Refinement and Analysis Program. J. Appl. Crystallogr. 2009, 42 (2), 339–341.
- 55. Zins, E.-L.; Pepe, C.; Schröder, D. Energy-Dependent Dissociation of Benzylpyridinium lons in an lon-Trap Mass Spectrometer. *J. Mass Spectrom.* **2010**, *45* (11), 1253–1260.
- Carpenter, J. E.; McNary, C. P.; Furin, A.; Sweeney, A. F.; Armentrout, P. B. How Hot Are Your Ions Really? A Threshold Collision-Induced Dissociation Study of Substituted Benzylpyridinium "Thermometer" Ions. J. Am. Soc. Mass Spectrom. 2017, 28 (9), 1876–1888.
- 57. Rahrt, R.; Auth, T.; Demireva, M.; Armentrout, P. B.; Koszinowski, K. Benzhydrylpyridinium Ions: A New Class of Thermometer Ions for the Characterization of Electrospray-Ionization Mass Spectrometers. *Anal. Chem.* **2019**, *91* (18), 11703–11711.
- 58. Roithová, J.; Gray, A.; Andris, E.; Jašík, J.; Gerlich, D. Helium Tagging Infrared Photodissociation Spectroscopy of Reactive Ions. *Acc. Chem. Res.* **2016**, *49* (2), 223–230.
- 59. Jašík, J.; Navrátil, R.; Němec, I.; Roithová, J. Infrared and Visible Photodissociation Spectra of Rhodamine lons at 3 K in the Gas Phase. *J. Phys. Chem. A* **2015**, *119* (51), 12648–12655.
- Pritchard, B. P.; Altarawy, D.; Didier, B.; Gibson, T. D.; Windus, T. L. New Basis Set Exchange: An Open, Up-to-Date Resource for the Molecular Sciences Community. J. Chem. Inf. Model. 2019, 59 (11), 4814–4820.
- 61. Feller, D. The Role of Databases in Support of Computational Chemistry Calculations. *J. Comput. Chem.* **1996**, *17* (13), 1571–1586.
- 62. Schuchardt, K. L.; Didier, B. T.; Elsethagen, T.; Sun, L.; Gurumoorthi, V.; Chase, J.; Li, J.; Windus, T. L. Basis Set Exchange: A Community Database for Computational Sciences. *J. Chem. Inf. Model.* **2007**, *47* (3), 1045–1052.
- 63. Weigend, F.; Ahlrichs, R. Balanced Basis Sets of Split Valence, Triple Zeta Valence and Quadruple Zeta Valence Quality for H to Rn: Design and Assessment of Accuracy. *Phys. Chem. Chem. Phys.* **2005**, *7* (18), 3297.
- 64. Frisch, M. J.; Trucks, G. W.; Schlegel, H. B.; Scuseria, G. E.; Robb, M. a.; Cheeseman, J. R.; Scalmani, G.; Barone, V.; Petersson, G. a.; Nakatsuji, H.; Li, X.; Caricato, M.; Marenich, a. V.; Bloino, J.; Janesko, B. G.; Gomperts, R.; Mennucci, B.; Hratchian, H. P.; Ortiz, J. V.; Izmaylov, a. F.; Sonnenberg, J. L.; Williams; Ding, F.; Lipparini, F.; Egidi, F.; Goings, J.; Peng, B.; Petrone, A.; Henderson, T.; Ranasinghe, D.; Zakrzewski, V. G.; Gao, J.; Rega, N.; Zheng, G.; Liang, W.; Hada, M.; Ehara, M.; Toyota, K.; Fukuda, R.; Hasegawa, J.; Ishida, M.; Nakajima, T.; Honda, Y.; Kitao, O.; Nakai, H.; Vreven, T.; Throssell, K.; Montgomery Jr., J. a.; Peralta, J. E.; Ogliaro, F.; Bearpark, M. J.; Heyd, J. J.; Brothers, E. N.; Kudin, K. N.; Staroverov, V. N.; Keith, T. a.; Kobayashi, R.; Normand, J.; Raghavachari, K.; Rendell, a. P.; Burant, J. C.; Iyengar, S. S.; Tomasi, J.; Cossi, M.; Millam, J. M.; Klene, M.; Adamo, C.; Cammi, R.; Ochterski, J. W.; Martin, R. L.; Morokuma, K.; Farkas, O.; Foresman, J. B.; Fox, D. J. G16_C01. 2016, p Gaussian 16, Revision C.01, Gaussian, Inc., Wallin.
- Andrae, D.; Häußermann, U.; Dolg, M.; Stoll, H.; Preuß, H. Energy-Adjusted ab Initio Pseudopotentials for the Second and Third Row Transition Elements. *Theor. Chim. Acta* 1990, 77 (2), 123–141.
- Rappoport, D.; Furche, F. Property-Optimized Gaussian Basis Sets for Molecular Response Calculations. J. Chem. Phys. 2010, 133 (13), 134105.

Appendices

For detailed supplementary information: Mehara, J.; Watson, B. T.; Noonikara-Poyil, A.; Zacharias, A. O.; Roithová, J.; Rasika Dias, H. V. Binding Interactions in Copper, Silver and Gold Π-Complexes. Chem. – A Eur. J. 2022, 28 (13).

It can be accessed via https://doi.org/10.34973/pdan-6826 upon request of the promotor or the IMM data steward.

Experimental details of mass spectrometric studies:

The experiments were performed on either Thermo Scientific LTQ XL linear trap or Finnigan LCQ Deca XP mass spectrometer equipped with an electrospray ionization (ESI) source.²³ General conditions were as follows: sheath gas 5-30 arbitrary unit, auxiliary gas 0-5 arbitrary unit, capillary temperature 150-200 °C, spray voltage 2-5 kV, capillary voltage 0-20 V and tube lens 0-40 V.

The [LM]+ ions were generated from the 1 mM stock solution in DCM where L was either L₁, L₂ or L₃ while M was either Cu, Ag or Au. For 1mM metal DCM stock solutions, Cu(ACN), PF, or CuCl/AgPF, was the copper source, while AgPF, or AgSbF, served as the silver source, and AuCl/AgPF6 was used as the gold source. In the case of CuCl/AgPF6 and AuCl/AgPF6, the precipitated AgCl was filtered through a 0.22 µm filter (13mm Syringe Filter, Nylon 66) to prepare a stock solution. For the generation of $[LM(\pi-ligand)]^+$, to 1 ml of 1mM alkene or alkyne stock solution in DCM, 100 µM the Cu/Ag/Au stock solution was added, followed by the addition of 50 μ M of L₁/L₂/L₃ ligand stock solution. In some cases, especially for ligand L₃ cooling to -10 °C helped to generate the desired [LM(π -ligand)]⁺. In many cases where the $[LM(\pi-ligand)]^+$ complex in solution was not easily formed, we used the π -ligand as an auxiliary gas using nitrogen overpressure to generate the desired $[LM(\pi-ligand)]^+$ complex in the gas phase.

The energy-resolved collision-induced dissociation (CID) experiments were performed on LCQ Deca mass spectrometer with an ESI source. The collision energies in the LCQ ion trap was calibrated based on the measurements of dissociation energies of series of benzylpyridinium and benzhydrylpyridinium thermometer ions from the Armentrout group using Schroder's method.⁵⁵⁻⁵⁷ Each complex was measured for 2-4 times on different days to calculate the standard deviation. The Calibration and CID experiments were carried under the ion gauge pressure of 0.7 to 1.98 X 10e⁻⁵ Torr, activation Q of 0.25 and activation time of 30 ms.

Theoretical details

Geometrical structures were minimized at B3LYP-D3/def2TZVPP⁶⁰⁻⁶³ level using Gaussian 16 code.⁶⁴ Theoretically predicted IR spectra and the bond dissociation energies of the [LM(π -ligand)]⁺ complexes were calculated by B3LYP-D3/def2TZVPP level on all atoms except for metals i.e., def2TZVPPD⁶⁰⁻⁶³ was used for Cu^{63,66}, Ag^{63,65} and Au.^{63,65,66}

Results of mass spectrometric studies

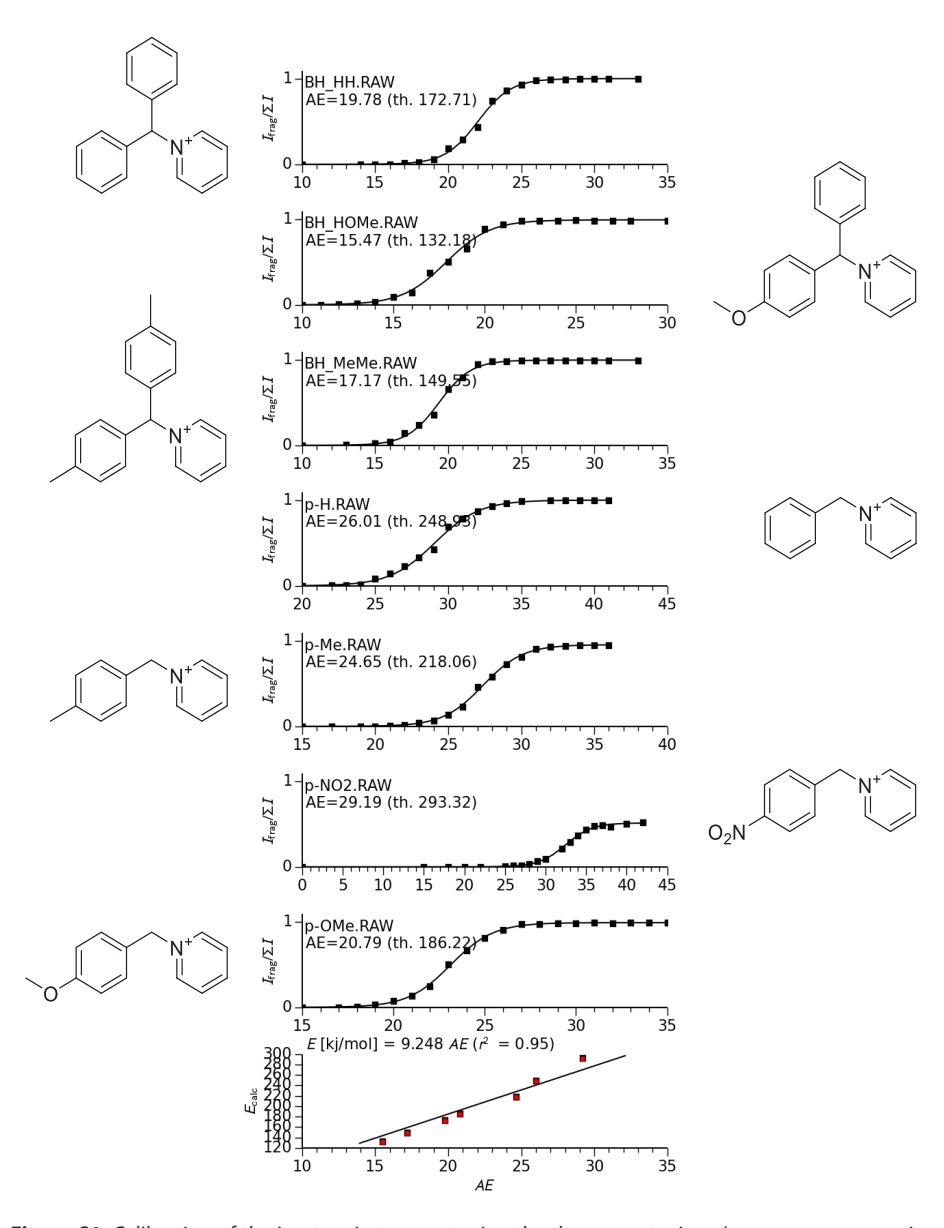


Figure S1. Calibration of the ion trap instrument using the thermometer ions (appearance energy i.e. AE for a set of thermometer ions is plotted against the known bond dissociation energy)

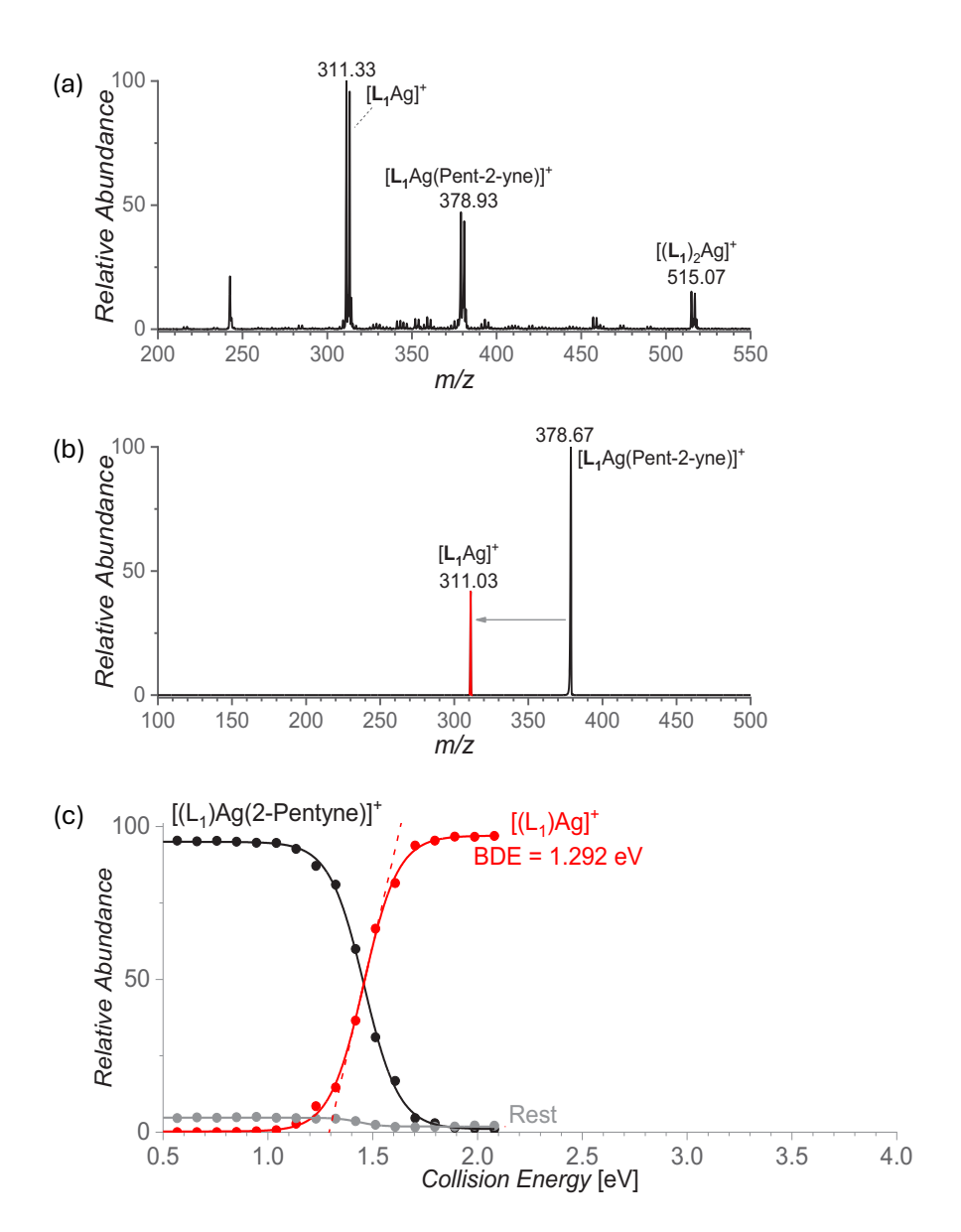


Figure S2. Determination of the experimental BDE of $[L_1Ag(2-pentyne)]^+$. (a) ESI-MS spectrum of dichloromethane solution of AgPF_{g'} L_1 and pent-2-yne, (b) CID spectrum of mass-selected ion m/z 379 $[L_1Ag(2-pentyne)]^+$ and (c) Energy resolved CID spectrum of m/z 379 $[L_1Ag(2-pentyne)]^+$ and the extrapolation of the fragmentation onset to determine the bond dissociation energy.

Similarly, for all the other complexes, the BDE was calculated.

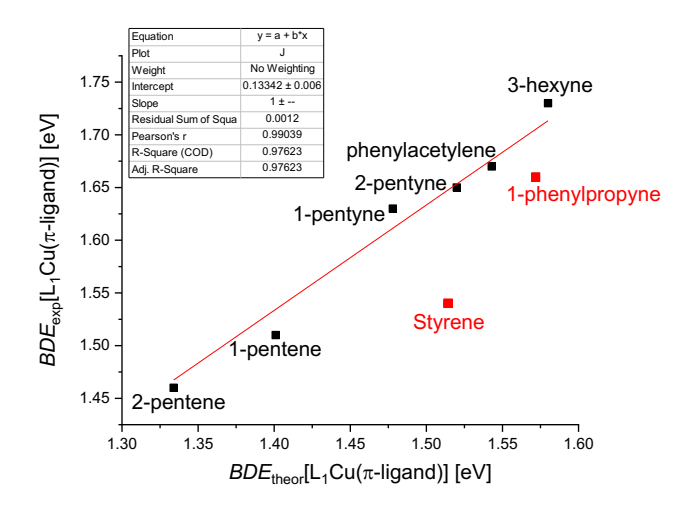


Figure S3. The correlation between the theoretically calculated and the experimental *BDE*s of [L,Cu(π ligand)]⁺ listed in Table 3. The red points were not taken into the linear fit.

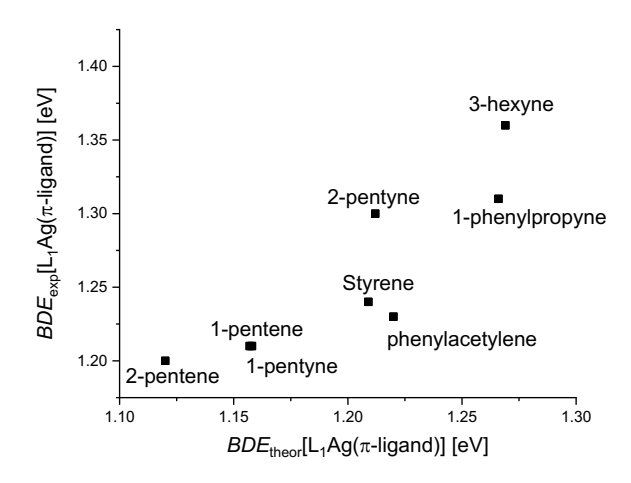


Figure S4. The correlation between the theoretically calculated and the experimental *BDE*s of [L,Ag(π ligand)] + listed in Table 3.

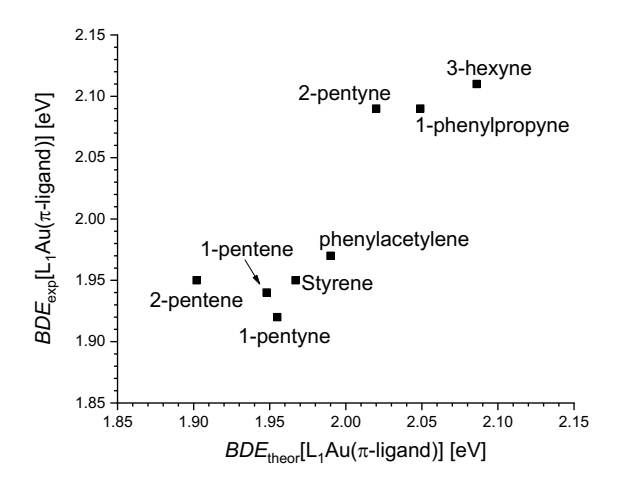


Figure S5. The correlation between the theoretically calculated and the experimental *BDEs* of $[L,Au(\pi-ligand)]^+$ listed in Table 3.

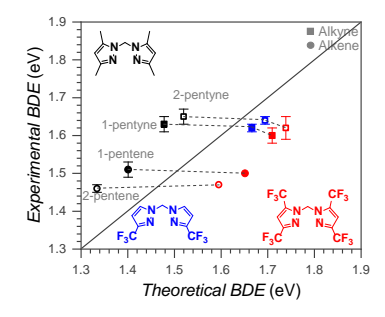


Figure S6. The correlation between the theoretically calculated and experimental *BDEs* of $[L_{(\kappa=1,2,8,3)}Cu(\pi-ligand)]^+$ listed in Tables 3-5.

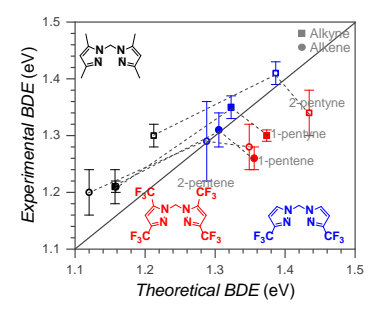


Figure S7. The correlation between the theoretically calculated and experimental *BDEs* of $[L_{(\kappa=1,2\&3)}Ag(\pi-ligand)]^+$ listed in Tables 3-5.

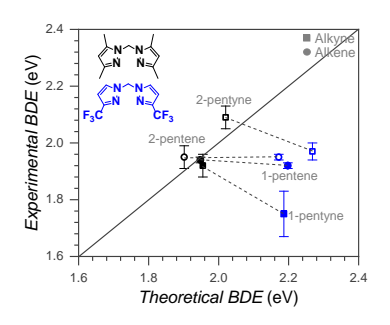


Figure S8. The correlation between the theoretically calculated and experimental BDEs of $[L_{(\kappa=1,\delta,2)}Au(\pi\text{-ligand})]^+$ listed in Tables 3 and 4.

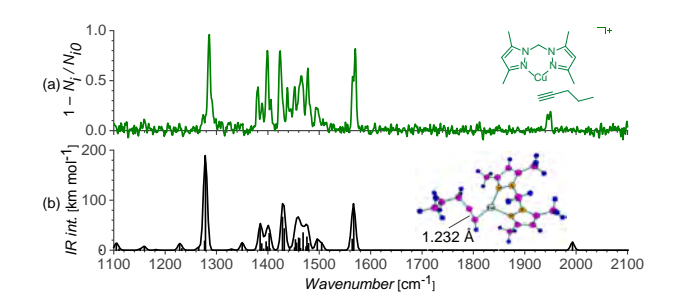


Figure S9. (a) The experimental IR spectra of [L,Cu(1-pentyne)]+ measured by helium tagging photodissociation spectroscopy and (b) Theoretically predicted IR spectra of [L,Cu(1-pentyne)]+ calculated by B3LYP-D3/def2TZVPP (def2TZVPPD on Cu), scaling factor: 0.98.

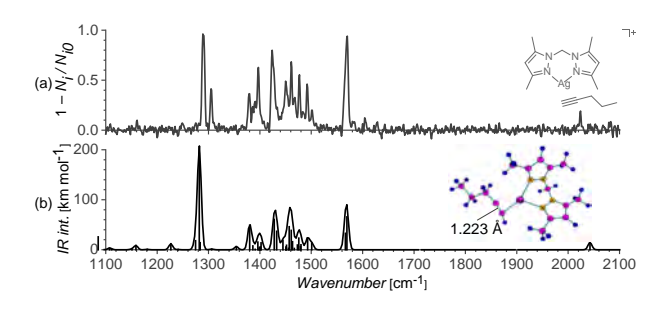


Figure S10. (a) The experimental IR spectra of [L,Ag(1-pentyne)]+ measured by helium tagging photodissociation spectroscopy and (b) Theoretically predicted IR spectra of [L,Ag(1-pentyne)]+ calculated by B3LYP-D3/def2TZVPP (def2TZVPPD on Ag), scaling factor: 0.98.

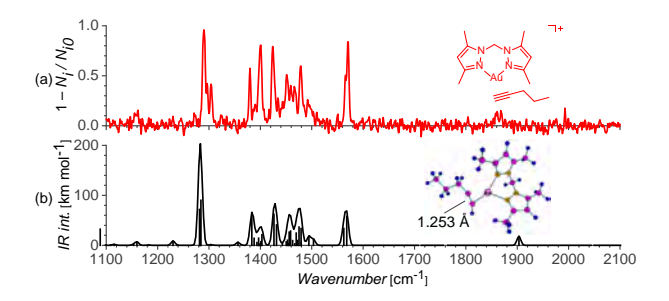


Figure S11. (a) The experimental IR spectra of $[L_1Au(1-pentyne)]^+$ measured by helium tagging photodissociation spectroscopy and (b) Theoretically predicted IR spectra of $[L_1Au(1-pentyne)]^+$ calculated by B3LYP-D3/def2TZVPP (def2TZVPPD on Au), scaling factor: 0.98.

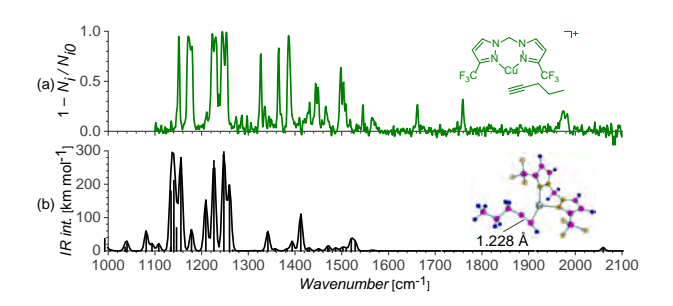


Figure S12. (a) The experimental IR spectra of $[L_2Cu(1-pentyne)]^+$ measured by helium tagging photodissociation spectroscopy and (b) Theoretically predicted IR spectra of $[L_2Cu(1-pentyne)]^+$ calculated by B3LYP-D3/def2TZVPP (def2TZVPPD on Cu), No scaling performed.

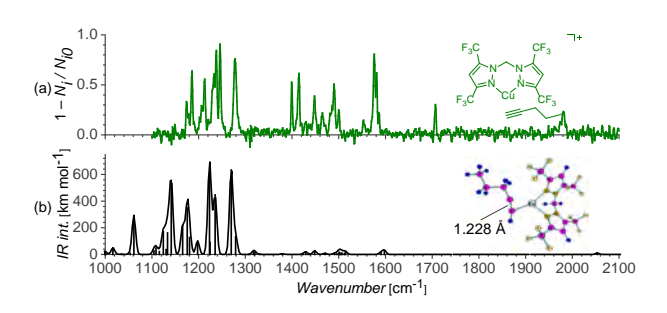


Figure S13. (a) The experimental IR spectra of $[L_3Cu(1-pentyne)]^+$ measured by helium tagging photodissociation spectroscopy and (b) Theoretically predicted IR spectra of $[L_3Cu(1-pentyne)]^+$ calculated by B3LYP-D3/def2TZVPP (def2TZVPPD on Cu), No scaling performed.

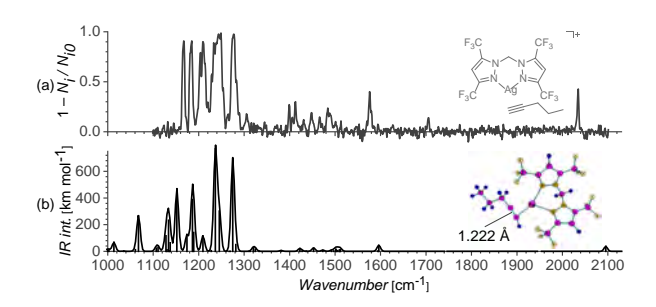


Figure S14. (a) The experimental IR spectra of [L,Ag(1-pentyne)]+ measured by helium tagging photodissociation spectroscopy and (b) Theoretically predicted IR spectra of [L,Ag(1-pentyne)]+ calculated by B3LYP-D3/def2TZVPP (def2TZVPPD on Ag), No scaling performed.



Chapter 7

Copper(II)-TEMPO interaction

The work in this chapter is published: Mehara, J.; Roithová, J. Copper(II)-TEMPO Interaction. *Isr. J. Chem.* **2023**, *63* (7–8).

Copper(II) complexes with N-oxyl reactants such as TEMPO can selectively oxidize alcohols to aldehydes or ketones. The proposed copper intermediates of the oxidation reaction were extensively theoretically studied, but they were never experimentally detected. Here, we present an analysis of "frozen" intermediates that contain alcohols without α-hydrogen atoms, thus preventing oxidation. The copper(II)-TEMPO complexes with a bipyridine-type ancillary ligand were isolated by electrospray ionization mass spectrometry and investigated spectroscopically by cryogenic photodissociation spectroscopy. The vibrational characteristics of the complexes suggest that TEMPO retains its unpaired electron even upon coordination with copper(II). In agreement, the electronic spectra of the TEMPOcopper(II) complexes show a characteristic band for gaseous copper(II) complexes. These results contradict some of the previous density functional theory (DFT) analyses of the possible reaction intermediates. The experimental data were confronted with theoretical results obtained by pure DFT (OPBE, TPSS) and hybrid DFT (TPSSH, B3LYP) calculations. The methods favor different ground states and capture various aspects of the experimental results, demonstrating a multiconfigurational character of the copper(II)-TEMPO complexes.

Introduction

Copper complexes are used in many catalytic oxidation reactions. 1-4 Typical oxidation reactions are 2-electron processes.⁵ Therefore, the mechanistic proposals either involve the Cu^{III}/Cu^I transition or the Cu^{II}₂/Cu^I₂ dimer transition.^{6,7} Alternatively, copper catalysts can act together with redox-active ligands, each accepting one electron.8 A prominent example of this reaction strategy is the method developed for alcohol oxidation by Stahl et al.9 The catalytic system relies on using copper(II) complex with N-based ligands in combination with TEMPO (TEMPO = (2.2,6.6-Tetramethylpiperidin-1-yl)oxyl, Scheme 1a).^{10,11} The proposed intermediate corresponds to the copper(II) complex bound to an alcoholate and TEMPO (X in Scheme 1a).12 The electron configuration of this elusive intermediate has been a subject of discussion. 13-18

Scheme 1. a) Proposed catalytic cycle for alcohol oxidation by copper(II)-TEMPO system. X: The proposed reactive intermediate, b) Possible electron configurations in the copper(II) – TEMPO binding.

The interaction between copper(II) and TEMPO has been investigated by X-ray absorption spectroscopy of [(TEMPO)₂Cu₂Cl₄] clusters.¹⁹ The experimental results and their matching with DFT calculations suggested that the interaction between copper(II) and TEMPO leads to the pairing of the unpaired electrons, and the resulting structure has a character of copper(I) interacting with temponium ions (structure **A** in Scheme 1b).

The intrinsically low concentrations of reactive complexes such as **X** in solution often preclude their investigation. Mass spectrometry can be used to isolate such complexes in the gas phase and study their structure and reactivity properties.^{20–23} The molecular and electronic structure of mass-selected ions can be studied in detail by photodissociation spectroscopy.^{24–29} Spectroscopy in the infrared range provides vibrational spectra. The bond stretching vibrations reflect the order of the bonds and, therefore, can be used to monitor the electron distribution in the ions.³⁰ In particular, we have shown that infrared photodissociation spectroscopy can monitor redox processes in copper complexes with redox-active ligands.^{31–33} We have shown previously that the electron transfer in the copper(II)-phenolate/copper(I)-phenoxy radical pair can be tracked by the C-O stretching frequency of the phenolato ligand.^{34,35} Here, we will use this experimental strategy to study the structure of the analogs of **X** (Scheme 1). The possible electronic configuration in the copper-TEMPO is shown in Scheme 1b.

Results and Discussion

Vibrational frequency scale for copper-TEMPO

The N-O stretching mode in the copper-TEMPO complexes should reflect the electron distribution between the binding partners. We have tested this assumption with a theoretical design of copper(I) complexes with different levels of electron localization at the copper center: [CuCl(TEMPO)]⁺, [Cu(pyridine)(TEMPO)]⁺, and [(bipy)Cu(TEMPO)]*. Calculations were performed at the B3LYP-D3/6-311+G(2d,p) level. Figure 1a shows the N-O stretching wavenumber and the spin localization at the N-O bond of TEMPO. The spin values show that one unpaired electron stays localized at the TEMPO ligand in all model copper(II) complexes. The [CuCl(TEMPO)]⁺ complex in the singlet state mimics the binding of copper(I) with the temponium cation with the N-O stretching frequency at 1469 cm⁻¹ (Figure 1). The free temponium ion has the N-O stretching frequency at ~1640 cm⁻¹ (the harmonic frequency scaled by 0.97). In the triplet state of [CuCl(TEMPO)]⁺, one unpaired electron is localized at the CuCl core and the second one in the π -bonding orbital of TEMPO, resulting in the N-O frequency of 1325 cm⁻¹. In comparison, free TEMPO has an N-O stretching frequency of 1375 cm⁻¹. The complexes [Cu(pyridine) (TEMPO)]+ and [(bipy)Cu(TEMPO)]+ are doublets and can thus mimic the possible equilibrium between copper(I)-TEMPO and copper(II)-temponium.²⁹ The electron distribution in the complexes suggests that the TEMPO ligand retains the unpaired electron in the π -bonding orbital of the N-O bond. The stretching frequencies of the N-O bonds are 1354 cm⁻¹ and 1340 cm⁻¹, respectively.

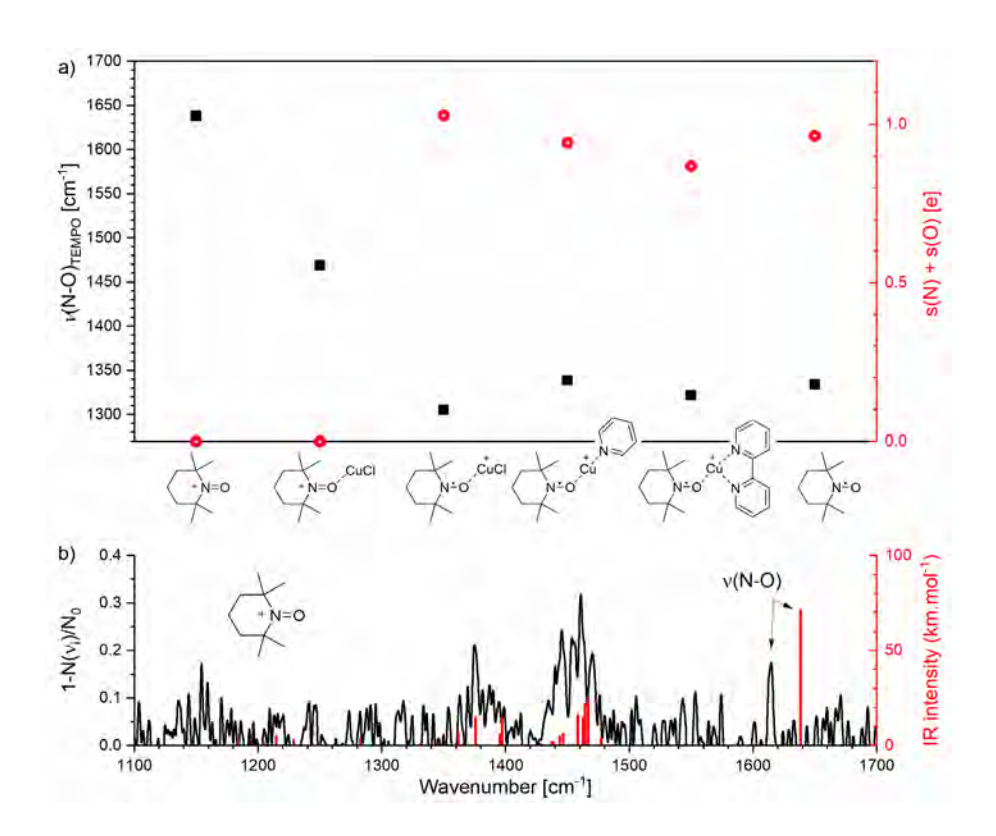
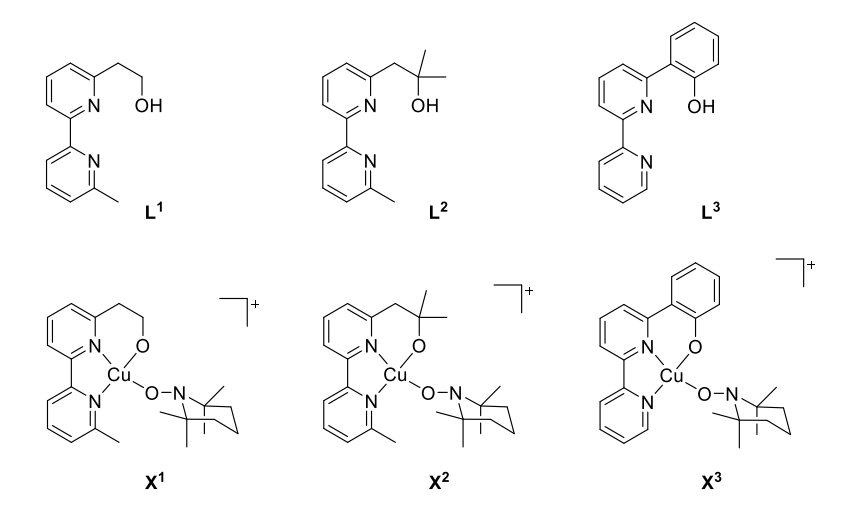


Figure 1. a) Theoretical N-O stretching wavenumber of various model compounds (black y-axis, black square) and the sum of the spin density at the N and O atoms of TEMPO determined by the Mulliken population analysis (red y-axis, red filled circle), using B3LYP-D3/6-311+G(2d,p). b) Experimental infrared helium tagging photodissociation spectrum of temponium ions (in black) and the theoretically predicted IR spectrum (red bars, B3LYP-D3/6-311+G(2d,p), scaling 0.97).

Having explored the model systems and the expected spectral characteristics of the different structures of the copper-TEMPO complexes, we have studied analogs of X. We have complexes having the 2,2'-bipyridine (bipy) type ligand bearing a primary or tertiary alcohol moiety as a side chain (L1 and L2 in Scheme 2). In addition, we also prepared a ligand with the phenol side chain (L3) to investigate the possible delocalization of unpaired electrons in the ligand system. To detect the reactive complexes $\mathbf{X}^1 - \mathbf{X}^3$, we mixed the corresponding ligand, CuCl₂ and TEMPO in acetonitrile (1:1:1 in 150-200 μ M final concentration). The experiments with L^1 led only to the detection of copper(I) complexes (Figures S8-S10). It suggests that the intermediates are short-lived and we can detect only increasing concentrations of copper(I) complexes produced by the oxidation of the alcohol moiety. The experiments with \mathbf{L}^2 and L^3 allowed us to detect X^2 and X^3 and study their structure (Figures S12, S16).



Scheme 2. Investigated copper complexes (X^1 , X^2 , and X^3) are models of reactive intermediates formed from the corresponding (L^1 , L^2 , and L^3) ligands containing side arms with an alcohol group. X^1 was not detected due to fast oxidation to the corresponding aldehyde.

Ion Spectroscopy

First, we investigated the structure of **X**² and **X**³ with helium-tagging IR photodissociation spectroscopy.^{24,36} The detected bands in the experimental IR spectra were assigned based on comparing all measured spectra and using the guide of theoretically calculated spectra (Figures S27- S36, either OPBE, TPSS, TPSSH, and B3LYP with 6-311+G(2d,p)). For comparison, we also measured the experimental He tagging IRPD spectra of complexes with closed-shell ligand pyridine *N*-oxide (PyO) instead of TEMPO. Using the **L**³ ligand, we were able to generate [(**L**³–H)Zn(TEMPO)]+ (zinc analog of **X**³), and [**L**³Cu(acetone)]+ complexes. Comparison of experimental spectra of **X**² with [(**L**²–H)Cu(PyO)]+ reveals that the N-O vibration of the TEMPO ligand in **X**² is located at 1363 cm⁻¹ (Figures 2a and 2b). The TEMPO ligand has other characteristic vibrations, one of them being an umbrella vibration of the methyl groups found in all investigated complexes at about 1380 cm⁻¹. The second characteristic vibration is a symmetric C-C vibration of the TEMPO ring, which is found between 1230 – 1245 cm⁻¹ (all bands assigned to TEMPO are highlighted in green in Figure 2).

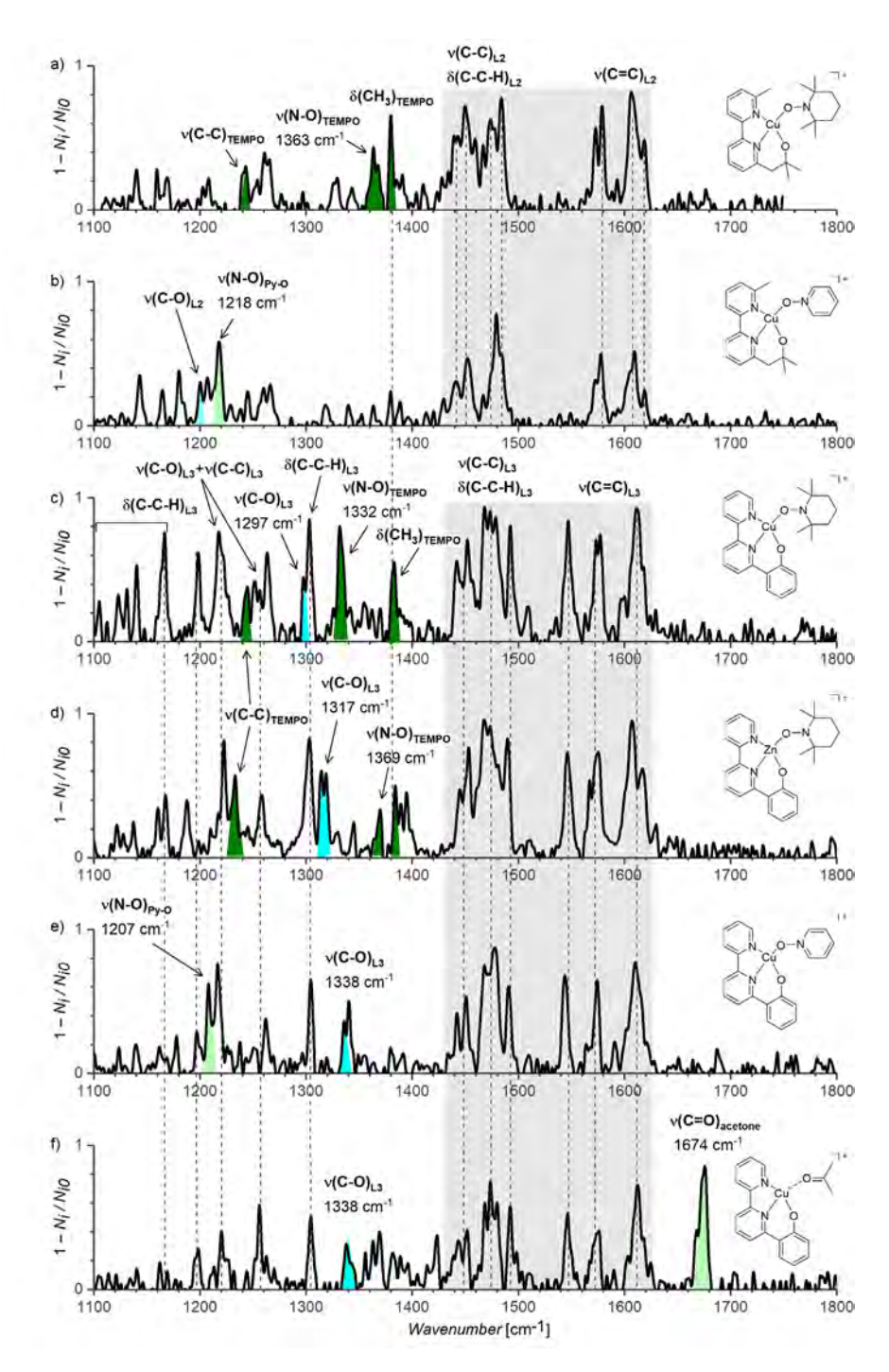


Figure 2. Experimental helium tagging IR photodissociation spectra. The tentative assignment is based on the comparison of the spectra and theoretical calculations.

The IR spectra of the complexes with the L³ ligand show only a minor effect of the labile ligand on the structure of the L³ ligand (the bands indicated by the vertical dashed lines in Figure 2c-f stay largely unaffected in all complexes). The C-O band of the phenoxy group is localized at 1338 cm⁻¹ for the [(L³-H)Cu(PyO)]+ and [L³Cu(acetone)]+ complexes. The C-O stretching mode is usually localized at about 1280 cm⁻¹ in other gaseous copper(II) phenolate complexes.³0,³¹ The blue shift observed here is likely associated with the delocalization of the negative charge over the aromatic backbone of L³. The TEMPO ligand in X³ and [(L³-H)Zn(TEMPO)]+ causes a planar distortion of L³. Accordingly, the C-O stretch of the phenoxy ligand red-shifts to 1297 cm⁻¹ and 1317 cm⁻¹, respectively. The N-O stretching vibration of TEMPO is localized at 1332 cm⁻¹ for X³ and 1369 cm⁻¹ for [(L³-H)Zn(TEMPO)]+.

The N-O stretching vibration of the TEMPO ligands in all investigated complexes does not suggest any indication of the possible temponium formation associated with the corresponding N-O vibration localized above 1400 cm⁻¹ (see the gray areas in Figure 2).

Next, we measured the visible spectra of complexes X^2 , X^3 , and $[(L^3-H)Cu(acetone)]^+$ (Figure 3). The spectra of all complexes contain a band at about 430 nm. Our laser source loses power below 420 nm (dotted lines in Figure 3); hence, the bands are likely broad towards the lower wavelength. Recently, we analyzed electronic excitations of the $[Cu(bipy)X]^+$ (X = CI and Br) complexes.³⁷ The spectra contained a band corresponding to the $\sigma(M-X) > \pi(M-X)^*$ transition (<450 nm for X=CI and 500 nm for X=Br). In analogy, the bands in the spectra presented here most likely correspond to the transition $\sigma(M-OR) > \pi(M-OR)^*$ (OR = the alcoholato or phenolato ligand). The additional bands in the vis spectrum of $[(L^3-H)Cu(acetone)]^+$ are probably due to the metal-to-ligand excitations involving acetone. We note that free TEMPO has a weak absorption band at 450 nm.³⁸

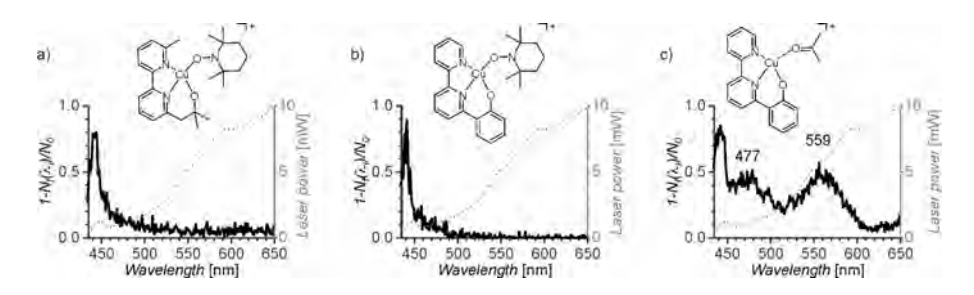


Figure 3. Visible photodissociation spectra of a) \mathbf{X}^2 , b) \mathbf{X}^3 , and c) $[(\mathbf{L}^3-H)Cu(acetone)]^+$ in black. The dotted line in grey show the laser power.

We have further analyzed the results using DFT calculations. We have used the B3LYP functional because it typically provides harmonic IR spectra that have a superior agreement with the experiment compared to other functionals.³⁹⁻⁴¹ At the B3LYP-D3 level with a triple zeta basis set, X2 and X3 have the triplet ground states. The closed-shell singlet states are about 20 kJ/mol higher in energy than the triplet states (Table 1). The attempts to converge the open-shell singlet states resulted in solutions converging to the geometry and wavefunction of the closedshell singlet structures.

Cheng et al. reported that the triplet state of [(bipy)Cu(PhCH₂O)(TEMPO)]⁺ lies higher in energy than the singlet state (~2 kcal/mol in the gas phase and ~4 kcal/mol in 2:1 acetonitrile/water solution). ¹² Based on the results of Cheng et al., the following DFT calculations on analogous systems did not consider the triplet states at all.

Hybrid DFT functionals such as B3LYP are known to stabilize the higher spin states.³⁷ To assess this effect, we have optimized the complexes with pure DFT functionals, OPBE and TPSS, and one more hybrid DFT functional, TPSSH. The pure DFT functionals energetically preferred the singlet states. The unrestricted optimization of the singlet state complexes led to the localization of the most stable geometry for the singlet states, and the solution corresponded in the end to the closed-shell singlet states. The hybrid TPSSH functional predicted singlet and triplet states close in energy, slightly favoring the triplet states.

The geometries of the \mathbf{X}^2 and \mathbf{X}^3 complexes optimized with different functionals were relatively similar (Table 1, Figure 4). The only exception was the triplet state of X² optimized with the OPBE functional, which predicted only a loose binding of TEMPO at a distance more than 3.5 Å (see Table 1); we thus do not discuss this outlier further. Generally, the geometry differences between the singlet and triplet states were small. The singlet states of the complexes have a shorter distance between the copper center and the oxygen atom of the TEMPO ligand (by ~ 0.07 -0.13 Å, d(Cu-O) in Table 1) and a slightly shorter N-O bond of the TEMPO ligand (by $\sim 0.02 - 0.03 \text{ Å, d(N-O)}$ in Table 1).

Table 1. Relative energies and selected geometry parameters of X² and X³ in the singlet and triplet states optimized with different DFT functionals.^a

	B3LYP-D3		B3LYP		TPSSH		TPSS		OPBE	
Complex	ΔΔΕ ^{οκ} kJ mol ⁻¹	d(Cu-O) ^b d(N-O) ^c φ(NNCuO) ^d	ΔΔΕ ^{οκ} kJ mol ⁻¹	d(Cu-O) d(N-O) ф(NNCuO)	ΔΔΕ ^{0K} kJ mol ⁻¹	d(Cu-O) d(N-O) ф(NNCuO)	ΔΔΕ ^{0K} KJ mol ⁻¹	d(Cu-O) d(N-O) ф(NNCuO)	ΔΔΕ ^{0K} kJ mol ⁻¹	d(Cu-O) d(N-O) ф(NNCuO)
X ² (S=0)	23.6	1.941 Å 1.264 Å 176°	34.9	1.962 Å 1.265 Å 177°	9.2	1.945 Å 1.277 Å 160°	-18.4	1.956 Å 1.289 Å 160°	-3.5	2.023 Å 1.264 Å 153°
X ² (S=1)	0.0	2.060 Å 1.289 Å 132°	0.0	2.119 Å 1.291 Å 132°	0.0	2.077 Å 1.297 Å 132°	0.0	2.076 Å 1.308 Å 131°	0.0	3.548 Å 1.266 Å 112°
X ³ (S=0)	18.4	1.948 Å 1.266 Å 174°	22.0	1.976 Å 1.266 Å 172°	0.2	1.945 Å 1.278 Å 173°	-28.9	1.956 Å 1.289 Å 173°	-28.8	2.018 Å 1.263 Å 172°
X ³ (S=1)	0.0	2.017 Å 1.286 Å 174°	0.0	2.043 Å 1.293 Å 175°	0.0	2.018 Å 1.299 Å 175°	0.0	2.024 Å 1.310 Å 175°	0.0	2.104 Å 1.285 Å 168°

^a The geometries were optimized with the listed DFT functionals with unrestricted wavefunctions using the 6-311+G(2d,p) basis set.

^b The distance between the copper atom and the oxygen atom of the TEMPO ligand.

^c The nitrogen-oxygen distance of the TEMPO ligand.

d The dihedral angle defined by the nitrogen atoms of the bipyridine core of the ligands, copper, and the oxygen atom of the TEMPO ligand.

Next, we compared the theoretical IR spectra of the triplet and singlet states of X² and X³ with the experimental IRPD spectra (Figure 4 and Figure S29). We discuss only the spectra of \mathbf{X}^2 here, the spectra of \mathbf{X}^3 show similar trends with even fewer differences between the individual spectra than found for \mathbf{X}^2 (Figure S29). The theoretical spectra contain several bands associated with the N-O vibration of the TEMPO ligand coupled with other vibrational modes. The most prominent bands are denoted in Figure 4 (and Figure S29). They correspond to the N-O vibration coupled with the C-C stretching of the bonds between C2-C3 and C5-C6 of TEMPO. The higher wavenumber band has more character of the N-O stretch, whereas the lower wavenumber band of the C-C stretch (we denote them as (N-O)_{TEMPO} and (C-C)_{TEMPO}, respectively). All the N-O coupled bands of the TEMPO ligand are predicted below 1400 cm⁻¹ regardless of the spin state of the DFT functional.

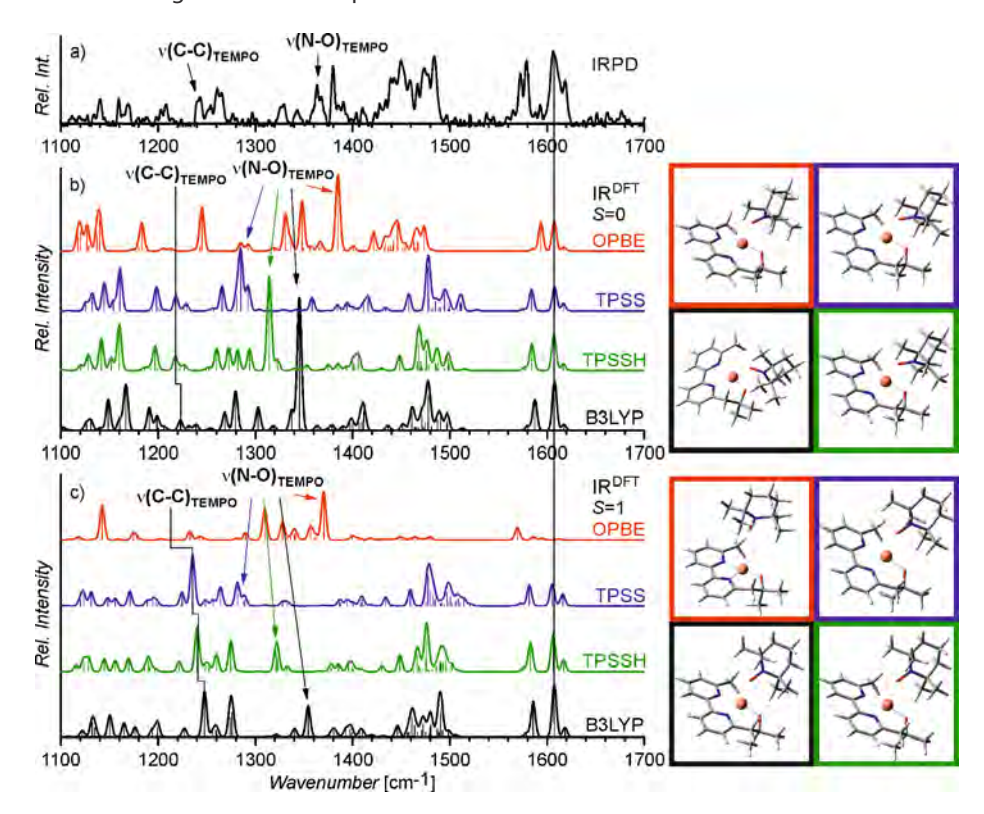


Figure 4. Comparison of the experimental helium tagging IRPD spectrum of \mathbf{X}^2 (a) with the theoretical harmonic IR spectra of X² optimized in the singlet (b) and triplet (c) states using different DFT functionals. The theoretical spectra were scaled so that the experimental C=C stretch at 1607 cm⁻¹ is reproduced (OPBE: 0.998; TPSS: 1.005; TPSSH: 0.987; B3LYP-D3:0.985), the scaling factor is the same for the singlet and triplet states. The structures show the optimized geometries with different DFT functionals (color-coded).

The significant difference between the theoretical IR spectra of the singlet and triplet state complexes is the prediction of the pronounced N-O stretching band in the singlet state that dominates the spectra of 1X2. In contrast, the other N-O coupled bands are much weaker. Such a pattern was not observed experimentally. On the other hand, the IR spectra of the triplet state complexes have two bands of similar intensity as observed experimentally. The second note is that the OPBE calculations predict the N-O stretching vibrations at higher wavenumbers (associated with a shorter N-O distance) than the rest of the functionals. All significant TEMPO vibrations in the OPBE calculated spectra are localized in the 1300 - 1400 cm⁻¹ range and similar for the singlet and triplet states. Note that TEMPO is only loosely bound in the triplet state and has a minimal vibrational coupling with the rest of the complex. This analysis suggests that the experimental spectrum is best reproduced by the spectra calculated at B3LYP and TPSSH levels for the triplet states of X^2 . However, the differences between all predicted spectra are slight, and most of the spectra could be considered an acceptable fit with the experimental spectrum (this is especially true for the X^3 complex).

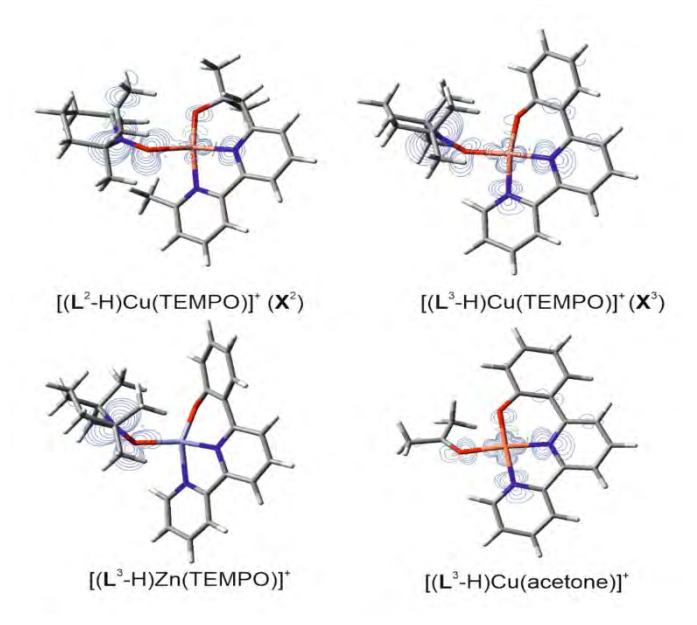


Figure 5. Optimized structures (B3LYP-D3/6-311+G(2d,p)) of complexes \mathbf{X}^2 and \mathbf{X}^3 in the triplet states and complexes $[(\mathbf{L}^3-H)Cu(acetone)]^+$ and $[(\mathbf{L}^3-H)Zn(TEMPO)]^+$ in the doublet states. The contours show spin density calculated as a single point at the B3LYP/6-311G(2d,p) level.

To further analyze the viable structure of the complex predicted at the B3LYP level, we studied the spin distribution in the complexes. We compared the localization of

the spin density in the investigated complexes \mathbf{X}^2 and \mathbf{X}^3 and the model complexes [(L³-H)Cu(acetone)]+ and [(L³-H)Zn(TEMPO)]+ calculated at the B3LYP level of theory (Figure 5). The spin density of the triplet states of **X**² and **X**³ reflect one unpaired electron localized at the TEMPO ligand (compare X² and X³ and [(L³-H)Zn(TEMPO)]⁺) and one unpaired electron localized at the copper center (compare X² and X³ and [(L³-H)Cu(acetone)]+). The calculations do not predict a significant impact of the copper ion on the electron distribution in TEMPO, as also evidenced in the IR spectra.

To assess the DFT calculated energies, we have experimentally determined bond dissociation energies (BDEs) of TEMPO in the studied complexes and compared them to the theoretical values calculated with different DFT functionals (Figure 6 and S37). The calculations tend to underestimate the binding energy of the labile ligands (TEMPO, Py-O, and acetone). The B3LYP-D3 method predicts the binding energies of Py-O and acetone within the experimental error, but the binding of TEMPO is underestimated by 27 – 40 kJ mol⁻¹ (Table 2). Without the D3 correction of dispersion interactions, all theoretical binding energies decrease by about 30 – 40 kJ mol⁻¹ (Table 2 and Figure 6). The TPSS and TPSSH functionals underestimate the binding energies by a similar amount as B3LYP. However, the TPSS functional predicts the binding energy of TEMPO in \mathbf{X}^2 and \mathbf{X}^3 with a similar offset as the other binding energies. The OPBE functional performs worst of all functionals with the most significant offset (~94 kJ mol⁻¹) from the experimental energies and a large spread of relative errors.

The calculations of the binding energies show that the hybrid DFT functionals describe the interaction between the copper(II) center and TEMPO in the triplet ground state as weaker than expected based on the other predicted values with these functionals (see Figures S37 and S38). The pure DFT functionals predict the binding energies of TEMPO in the singlet copper complexes with similar accuracy as other binding energies, with the TPSS functional providing the most consistent results.

Summarizing the theoretical results, it becomes evident that single-reference DFT methods can hardly describe the copper(II)-TEMPO complexes well. On the one hand, the IR spectra reflecting the structure of the complexes better correspond to the triplet state complexes predicted by pure DFT methods and thus suggest that the complexes correspond to structure B from Scheme 1. On the other hand, the binding energy between the copper center and TEMPO is more consistent for the singlet state complexes predicted by pure DFT methods, suggesting structure C from Scheme 1. Hence, the correct analysis of these complexes must be done with multiconfigurational methods that could consider the contribution of both configurations.

Table 2. Experimental^[a] and theoretical^[b,c] bond dissociation energies.

			•				
Complex	Fragment	BDE _{exp} [kJ mol ⁻¹]	$BDE_{\text{exp}}^{\text{[b]}}[ext{KJ mol-1}]$ $BDE_{ ext{B3LVP-D3}}^{\text{[b]}}[ext{KJ mol-1}]$	BDE _{B3LYP} [d	BDE _{TPSSH} [KJ mol ⁻¹]	BDE _{TPSS} [c] [KJ mol ⁻¹]	BDE _{OPBE} [d]
			B3LYP-D3	ВЗГУР	TPSSH	TPSS	OPBE
X ² (S=0)	TEMPO	000	[p](88)	(30)[d]	[P](09)	85	33
$X^{2}(S=1)$	TEMPO	0 H	112	65	69	[67) ^[d]	(30) ^[d]
[(L ²-H)Cu(PyO)]⁺	PyO	150±10	138	108	108	101	52
X ³ (S=0)	TEMPO		(124) ^[d]	(74) ^[d]	(102) ^[d]	126	78
X ³ (S=1)	TEMPO	01 H	143	96	102	[b](79)	(49) ^[d]
[(L³-H)Cu(acetone)] ⁺ acetone	acetone	120 ± 10	118	93	96	06	51
[(L ³-H)Cu(PyO)]⁺	PyO	189 ± 10	172	144	144	133	83
[(L³-H)Zn(TEMPO)]+	TEMPO	164 ± 10	160	111	116	114	79

(a) The experimental values were determined from energy-resolved CID experiments (see Figure S21-S26).

^[b] The theoretical values were calculated by using Gaussian 16, B3LYP (6-311+G(2d,p) basis set) using the empirical dispersion GD3.

^[c] The theoretical values were calculated by using Gaussian 16 for different DFT functionals (6-311+G(2d,p) basis set).

[[]d] Higher-energy lying spin state.

Conclusions

We have presented models of reactive intermediates in alcohol oxidation using a copper(II)-TEMPO catalytic system. In the model, copper intermediates X1, X2, and X³ contain a bipyridine-type ligand with alcohol as a side chain and the TEMPO ligand. We have successfully isolated only "frozen" intermediates that contained an alcohol moiety without α-hydrogen atoms (tertiary alcohol and phenol). Complexes with the ligand containing a primary alcohol moiety reacted with TEMPO; we could not detect intermediates and only detected copper(I) complexes as evidence of the redox reaction

Vibrational analysis of the isolated model intermediates X² and X³ demonstrated that the N-O vibrations of the TEMPO ligand (1363 cm⁻¹ and 1332 cm⁻¹, respectively) stay very similar to that of free TEMPO (1339 cm⁻¹). 42,43 We have also compared our model reactive complexes with a zinc analog, where no electron pairing or electron transfers are expected. The vibrational features of the zinc complex are very similar to that of the copper complex. These results strongly suggest that TEMPO coordinates as 2e-ligand and retains the unpaired electron at the $\pi^*(N-O)$ orbital. We have also measured the electronic spectra of the isolated complexes, which are consistent with the ranges of other copper(II) complexes, suggesting once more that TEMPO is not oxidized to a temponium-type ligand, as previously indicated in the literature.

Analysis of the investigated complexes with the density functional theory methods leads to a reasonable agreement with the experimental results. Hybrid DFT functionals predict that the complexes have a triplet ground state in which TEMPO retains one unpaired electron and the copper center the second one. However, the interaction between TEMPO and copper(II) is predicted to be somewhat weaker than expected based on the experiments. The bond dissociation energy of TEMPO in the complexes is theoretically underestimated by about 27 – 40 kJ mol⁻¹ at the B3LYP level. Accordingly, the theoretical N-O stretching vibrations are slightly red-shifted compared to the experiment. On the contrary, pure DFT functionals favor the singlet ground state of the complexes. They show a worse consistency with the IR spectroscopic features, but they predict the bond dissociation energies of the TEMPO ligand in consistence with the BDEs of other ligands. In summary, the theoretical results clearly show that copper(II)-TEMPO complexes have a multiconfigurational character. Accordingly, single-reference DFT calculations capture only a limited picture of the correct electronic and molecular structure of the complexes.

Experimental details

The L³ ligand was synthesized as previously reported.⁴⁴ The L¹ and L² ligand was synthesized using a modified procedure.⁴⁵ For L², LDA was added to the solution of the substrate at -76 °C, followed by addition of acetone. The mass spectrometric experiments were conducted using a linear trap instrument LTQ with an electrospray ionization (ESI) source. The electrospray voltage was 4 - 5 kV, and the capillary was heated to 200 - 220 °C. The sheath and auxiliary gas flow rates and capillary voltages were optimized to maximize the signal of the required ions. Energy-resolved collision-induced dissociation (CID) experiments for bond dissociation energies (BDEs) determination were measured with an LCQ Deca XP (Finnigan) ion trap mass spectrometer. The collision energies in the LCO instruments can be calibrated based on measurements of dissociation energies of thermometer ions^{46,47} using Schröder's method.⁴⁸ The experiments were performed in triplicates, and the appearance energy values are given with the experimental uncertainties of different measurements. The ions of interest were generated from the acetonitrile solution of the L ligand, copper chloride, and 2,2,6,6-tetramethylpiperidine 1-oxyl TEMPO free radical. For the L^1 and L^2 ligands, potassium tert-butoxide was used in addition to copper chloride and the TEMPO.

Infrared and visible spectra of the mass-selected ions were measured with the helium tagging photodissociation method using the ISORI (Ion Spectroscopy of Reactive Intermediates) instrument.³² Ions generated by electrospray ionization were mass-selected by the first quadrupole and transferred via a bender and an octopole to a linear quadrupole cold trap operated at 3 K. The ions were trapped and thermalized by the helium buffer gas. The thermalized ions attached a helium atom. These helium-tagged ions were then used for spectroscopic experiments. The ions were in alternative cycles irradiated. After irradiation, the ions were extracted, mass analyzed by a quadrupole, and detected by a conversion dynode and an electron multiplier. The spectra are constructed as $1-N(\cdot)/N_0$, where $N(\cdot)$ is the number of helium complexes after the irradiation and N_0 is the number of helium complexes in alternative cycles without the irradiation. The photon source was OPO/OPA LaserVision pumped by Nd: YAG laser Surelite EX from Continuum (tuning range 700-4700 cm⁻¹, FWHM ~ 1.5 cm⁻¹, 10ns pulse length) for the infrared spectra and SuperK Extreme for the electronic spectra. Due to the low absorption efficiency, the electronic spectra were measured with simple photodissociation, not helium tagging.

The DFT calculations were performed using functionals: OPBE, 49-52 TPSS, 53 TPSSH, 54,55 and B3LYP⁵⁶⁻⁵⁸ with the D3 dispersion correction⁵⁹ as implemented in Gaussian 16.⁶⁰ All calculations were done with the 6-311+G(2d,p) basis set.^{61,62} The geometries were fully optimized; the frequency calculation contained no imaginary frequency. The population analysis at the B3LYP level was performed for the optimized structures but using single-point calculations with the B3LYP/6-311G(2d,p) method to prevent false delocalization due to diffuse functions in the basis set.

References

- (1) Monnier, F.; Taillefer, M. Catalytic C-C, C-N, and C-O Ullmann-Type Coupling Reactions. *Angew. Chemie Int. Ed.* **2009**, *48* (38), 6954–6971.
- (2) Sambiagio, C.; Marsden, S. P.; Blacker, A. J.; McGowan, P. C. Copper Catalysed Ullmann Type Chemistry: From Mechanistic Aspects to Modern Development. *Chem. Soc. Rev.* 2014, 43 (10), 3525–3550.
- (3) Bhunia, S.; Pawar, G. G.; Kumar, S. V.; Jiang, Y.; Ma, D. Selected Copper-Based Reactions for C–N, C–O, C–S, and C–C Bond Formation. *Angew. Chemie Int. Ed.* **2017**, *56* (51), 16136–16179.
- (4) Semmelhack, M. F.; Schmid, C. R.; Cortes, D. A.; Chou, C. S. Oxidation of Alcohols to Aldehydes with Oxygen and Cupric Ion, Mediated by Nitrosonium Ion. J. Am. Chem. Soc. 1984, 106 (11), 3374–3376.
- (5) Allen, S. E.; Walvoord, R. R.; Padilla-Salinas, R.; Kozlowski, M. C. Aerobic Copper-Catalyzed Organic Reactions. Chem. Rev. 2013, 113 (8), 6234–6458.
- (6) Zhang, Q.; Tong, S.; Wang, M.-X. Unraveling the Chemistry of High Valent Arylcopper Compounds and Their Roles in Copper-Catalyzed Arene C–H Bond Transformations Using Synthetic Macrocycles. Acc. Chem. Res. 2022, 55 (19), 2796–2810.
- (7) McCann, S. D.; Stahl, S. S. Copper-Catalyzed Aerobic Oxidations of Organic Molecules: Pathways for Two-Electron Oxidation with a Four-Electron Oxidant and a One-Electron Redox-Active Catalyst. Acc. Chem. Res. 2015, 48 (6), 1756–1766.
- (8) Jazdzewski, B. A.; Tolman, W. B. Understanding the Copper-Phenoxyl Radical Array in Galactose Oxidase: Contributions from Synthetic Modeling Studies. Coord. Chem. Rev. 2000, 200–202, 633–685.
- (9) Badalyan, A.; Stahl, S. S. Cooperative Electrocatalytic Alcohol Oxidation with Electron-Proton-Transfer Mediators. *Nature* 2016, 535 (7612), 406–410.
- (10) Ryan, M. C.; Whitmire, L. D.; McCann, S. D.; Stahl, S. S. Copper/TEMPO Redox Redux: Analysis of PCET Oxidation of TEMPOH by Copper(II) and the Reaction of TEMPO with Copper(I). *Inorg. Chem.* **2019**, *58* (15), 10194–10200.
- (11) Hoover, J. M.; Stahl, S. S. Highly Practical Copper(I)/TEMPO Catalyst System for Chemoselective Aerobic Oxidation of Primary Alcohols. *J. Am. Chem. Soc.* **2011**, *133* (42), 16901–16910.
- (12) Ryland, B. L.; McCann, S. D.; Brunold, T. C.; Stahl, S. S. Mechanism of Alcohol Oxidation Mediated by Copper(II) and Nitroxyl Radicals. *J. Am. Chem. Soc.* **2014**, *136* (34), 12166–12173.
- (13) Cheng, L.; Wang, J.; Wang, M.; Wu, Z. Mechanistic Insight into the Alcohol Oxidation Mediated by an Efficient Green [CuBr 2 (2,2'-Bipy)]-TEMPO Catalyst by Density Functional Method. *Inorg. Chem.* **2010**, *49* (20), 9392–9399.
- (14) Belanzoni, P.; Michel, C.; Baerends, E. J. Cu(Bipy) 2+ /TEMPO-Catalyzed Oxidation of Alcohols: Radical or Nonradical Mechanism? *Inorg. Chem.* **2011**, *50* (23), 11896–11904.
- (15) McCann, S. D.; Stahl, S. S. Mechanism of Copper/Azodicarboxylate-Catalyzed Aerobic Alcohol Oxidation: Evidence for Uncooperative Catalysis. *J. Am. Chem. Soc.* **2016**, *138* (1), 199–206.
- (16) Iron, M. A.; Szpilman, A. M. Mechanism of the Copper/TEMPO-Catalyzed Aerobic Oxidation of Alcohols. Chem. - A Eur. J. 2017, 23 (6), 1368–1378.
- (17) Feng, C.; Cheng, L.; Ma, H.; Ma, L.; Wu, Q.; Yang, J. Unraveling the Mechanism of Aerobic Alcohol Oxidation by a Cu/Pytl-β-Cyclodextrin/TEMPO Catalytic System under Air in Neat Water. *Inorg. Chem.* 2021, 60 (18), 14132–14141.
- (18) Li, S.; Cheng, L.; Wu, Q.; Zhang, Q.; Yang, J.; Liu, J. Mechanism of Aerobic Alcohol Oxidation Mediated by Water-Soluble Cu II -TEMPO Catalyst in Water: A Density Functional Theory Study. ChemistrySelect 2018, 3 (4), 1268–1274.

- (19) Walroth, R. C.; Miles, K. C.; Lukens, J. T.; MacMillan, S. N.; Stahl, S. S.; Lancaster, K. M. Electronic Structural Analysis of Copper(II)-TEMPO/ABNO Complexes Provides Evidence for Copper(I)-Oxoammonium Character, J. Am. Chem. Soc. 2017, 139 (38), 13507–13517.
- (20) Serra, D.; Moret, M. E.; Chen, P. Transmetalation of Methyl Groups Supported by Ptll-Au I Bonds in the Gas Phase, in Silico, and in Solution. J. Am. Chem. Soc. 2011, 133 (23), 8914–8926.
- (21) Mehara, J.; Roithová, J. Identifying Reactive Intermediates by Mass Spectrometry. Chem. Sci. **2020**, 11 (44), 11960-11972.
- (22) Corinti, D.; Coletti, C.; Re, N.; Paciotti, R.; Maître, P.; Chiavarino, B.; Crestoni, M. E.; Fornarini, S. Short-Lived Intermediates (Encounter Complexes) in Cisplatin Ligand Exchange Elucidated by Infrared Ion Spectroscopy. Int. J. Mass Spectrom. 2019, 435, 7–17.
- (23) Schwarz, H. Ménage-à-Trois: Single-Atom Catalysis, Mass Spectrometry, and Computational Chemistry. Catal. Sci. Technol. 2017, 7 (19), 4302-4314.
- (24) Duncan, M. A. Infrared Spectroscopy to Probe Structure and Dynamics in Metal Ion-Molecule Complexes. Int. Rev. Phys. Chem. 2003, 22 (2), 407-435.
- (25) Oomens, J.; Sartakov, B. G.; Meijer, G.; von Helden, G. Gas-Phase Infrared Multiple Photon Dissociation Spectroscopy of Mass-Selected Molecular Ions. Int. J. Mass Spectrom. 2006, 254 (1-2), 1-19.
- (26) Roithova, J. Characterization of Reaction Intermediates by Ion Spectroscopy. Chem. Soc. Rev. **2012**, 41 (2), 547-559.
- (27) Boyarkin, O. V. Cold Ion Spectroscopy for Structural Identifications of Biomolecules. Int. Rev. Phys. Chem. 2018, 37 (3-4), 559-606.
- (28) Schwarz, H.; Asmis, K. R. Identification of Active Sites and Structural Characterization of Reactive Ionic Intermediates by Cryogenic Ion Trap Vibrational Spectroscopy. Chem. - A Eur. J. 2019, 25 (9), 2112-2126.
- (29) Niedner-Schatteburg, G.; Kappes, M. M. Advancing Inorganic Coordination Chemistry by Spectroscopy of Isolated Molecules: Methods and Applications. Chem. – A Eur. J. 2021, 27 (61), 15028-15043.
- (30) Straka, M.; Andris, E.; Vícha, J.; Růžička, A.; Roithová, J.; Rulíšek, L. Spectroscopic and Computational Evidence of Intramolecular Au I ···H + -N Hydrogen Bonding. Angew. Chemie Int. Ed. 2019, 58 (7), 2011-2016.
- (31) Roithová, J.; Milko, P. Naphthol Coupling Monitored by Infrared Spectroscopy in the Gas Phase. J. Am. Chem. Soc. 2010, 132 (1), 281-288.
- (32) Tsybizova, A.; Roithová, J. Copper-Catalyzed Reactions: Research in the Gas Phase. Mass Spectrom. Rev. 2016, 35 (1), 85-110.
- (33) Yassaghi, G.; Jašíková, L.; Roithová, J. Gas-Phase Study of Metal Complexes with Redox-Active Ligands. Int. J. Mass Spectrom. 2016, 407, 92-100.
- (34) Milko, P.; Roithová, J.; Tsierkezos, N.; Schröder, D. The C-O Stretch as an Unprecedently Large Spectral Marker for the Electron Transfer between Copper(II) and a Phenolate Anion. J. Am. Chem. Soc. 2008, 130 (23), 7186-7187.
- (35) Milko, P.; Roithová, J.; Schröder, D.; Lemaire, J.; Schwarz, H.; Holthausen, M. C. The Phenoxy/Phenol/ Copper Cation: A Minimalistic Model of Bonding Relations in Active Centers of Mononuclear Copper Enzymes. Chem. - A Eur. J. 2008, 14 (14), 4318–4327.
- (36) Roithová, J.; Gray, A.; Andris, E.; Jašík, J.; Gerlich, D. Helium Tagging Infrared Photodissociation Spectroscopy of Reactive Ions. Acc. Chem. Res. 2016, 49 (2), 223–230.

- (37) Mehara, J.; Koovakattil Surendran, A.; van Wieringen, T.; Setia, D.; Foroutan-Nejad, C.; Straka, M.; Rulíšek, L.; Roithová, J. Cationic Gold(II) Complexes: Experimental and Theoretical Study**. *Chem. A Eur. J.* **2022**, *28* (60), e202201794.
- (38) Koptyug V. A. Atlas of Spectra of Aromatic and Heterocyclic Compounds. 24. 1982, p 105.
- (39) Carbonniere, P.; Barone, V. Performances of Different Density Functionals in the Computation of Vibrational Spectra beyond the Harmonic Approximation. Chem. Phys. Lett. 2004, 399 (1–3), 226–229.
- (40) Martens, J.; van Outersterp, R. E.; Vreeken, R. J.; Cuyckens, F.; Coene, K. L. M.; Engelke, U. F.; Kluijtmans, L. A. J.; Wevers, R. A.; Buydens, L. M. C.; Redlich, B.; Berden, G.; Oomens, J. Infrared Ion Spectroscopy: New Opportunities for Small-Molecule Identification in Mass Spectrometry - A Tutorial Perspective. Anal. Chim. Acta 2020, 1093, 1–15.
- (41) Andris, E.; Jašík, J.; Gómez, L.; Costas, M.; Roithová, J. Spectroscopic Characterization and Reactivity of Triplet and Quintet Iron(IV) Oxo Complexes in the Gas Phase. *Angew. Chemie Int. Ed.* **2016**, *55* (11), 3637–3641.
- (42) Golubev, V. A.; Sen', V. D.; Rozantsev, É. G. Synthesis and Properties of Alkali Salts of 2,2,6,6-Tetramethyl-1-Hydroxypiperidine 1-Oxide. *Bull. Acad. Sci. USSR, Div. Chem. Sci.* **1979**, *28* (9), 1927–1931.
- (43) Rintoul, L.; Micallef, A. S.; Bottle, S. E. The Vibrational Group Frequency of the N-O{radical Dot} Stretching Band of Nitroxide Stable Free Radicals. *Spectrochim. Acta Part A Mol. Biomol. Spectrosc.* **2008**, *70* (4), 713–717.
- (44) Kagalwala, H. N.; Tong, L.; Zong, R.; Kohler, L.; Ahlquist, M. S. G. G.; Fan, T.; Gagnon, K. J.; Thummel, R. P. Evidence for Oxidative Decay of a Ru-Bound Ligand during Catalyzed Water Oxidation. ACS Catal. 2017, 7 (4), 2607–2615.
- (45) Maeyama, K.; Okumura, C.; Yonezawa, N. An Efficient Synthesis of ω-(2,2'-Bipyridyl)Alkyl Alcohols and Their Acrylates. Synth. Commun. 2002, 32 (20), 3159–3167.
- (46) Carpenter, J. E.; McNary, C. P.; Furin, A.; Sweeney, A. F.; Armentrout, P. B. How Hot Are Your lons Really? A Threshold Collision-Induced Dissociation Study of Substituted Benzylpyridinium "Thermometer" lons. J. Am. Soc. Mass Spectrom. **2017**, *28* (9), 1876–1888.
- (47) Rahrt, R.; Auth, T.; Demireva, M.; Armentrout, P. B.; Koszinowski, K. Benzhydrylpyridinium Ions: A New Class of Thermometer Ions for the Characterization of Electrospray-Ionization Mass Spectrometers. *Anal. Chem.* 2019, 91 (18), 11703–11711.
- (48) Zins, E.-L.; Pepe, C.; Schröder, D. Energy-Dependent Dissociation of Benzylpyridinium lons in an lon-Trap Mass Spectrometer. *J. Mass Spectrom.* **2010**, *45* (11), 1253–1260.
- (49) HANDY, N. C.; COHEN, A. J. Left-Right Correlation Energy. Mol. Phys. 2001, 99 (5), 403-412.
- (50) Hoe, W.-M.; Cohen, A. J.; Handy, N. C. Assessment of a New Local Exchange Functional OPTX. *Chem. Phys. Lett.* **2001**, *341* (3–4), 319–328.
- (51) Perdew, J. P.; Burke, K.; Ernzerhof, M. Generalized Gradient Approximation Made Simple. *Phys. Rev. Lett.* **1996**, *77* (18), 3865–3868.
- (52) Perdew, J. P.; Burke, K.; Ernzerhof, M. Generalized Gradient Approximation Made Simple [Phys. Rev. Lett. 77, 3865 (1996)]. Phys. Rev. Lett. 1997, 78 (7), 1396–1396.
- (53) Tao, J.; Perdew, J. P.; Staroverov, V. N.; Scuseria, G. E. Climbing the Density Functional Ladder: Nonempirical Meta–Generalized Gradient Approximation Designed for Molecules and Solids. *Phys. Rev. Lett.* 2003, 91 (14), 146401.
- (54) Staroverov, V. N.; Scuseria, G. E.; Tao, J.; Perdew, J. P. Comparative Assessment of a New Nonempirical Density Functional: Molecules and Hydrogen-Bonded Complexes. J. Chem. Phys. 2003, 119 (23), 12129–12137.

- (55) Staroverov, V. N.; Scuseria, G. E.; Tao, J.; Perdew, J. P. Erratum: "Comparative Assessment of a New Nonempirical Density Functional: Molecules and Hydrogen-Bonded Complexes" [J. Chem. Phys. 119, 12129 (2003)]. J. Chem. Phys. 2004, 121 (22), 11507.
- (56) Becke, A. D. A New Mixing of Hartree–Fock and Local Density-functional Theories. J. Chem. Phys. **1993**, *98* (2), 1372–1377.
- (57) Becke, A. D. Density-functional Thermochemistry. III. The Role of Exact Exchange. J. Chem. Phys. **1993**, 98 (7), 5648-5652.
- (58) Lee, C.; Yang, W.; Parr, R. G. Development of the Colle-Salvetti Correlation-Energy Formula into a Functional of the Electron Density. Phys. Rev. B 1988, 37 (2), 785-789.
- (59) Grimme, S.; Antony, J.; Ehrlich, S.; Krieg, H. A Consistent and Accurate Ab Initio Parametrization of Density Functional Dispersion Correction (DFT-D) for the 94 Elements H-Pu. J. Chem. Phys. 2010, 132 (15), 154104.
- (60) Frisch, M. J.; Trucks, G. W.; Schlegel, H. B.; Scuseria, G. E.; Robb, M. a.; Cheeseman, J. R.; Scalmani, G.; Barone, V.; Petersson, G. a.; Nakatsuji, H.; Li, X.; Caricato, M.; Marenich, a. V.; Bloino, J.; Janesko, B. G.; Gomperts, R.; Mennucci, B.; Hratchian, H. P.; Ortiz, J. V.; Izmaylov, a. F.; Sonnenberg, J. L.; Williams; Ding, F.; Lipparini, F.; Egidi, F.; Goings, J.; Peng, B.; Petrone, A.; Henderson, T.; Ranasinghe, D.; Zakrzewski, V. G.; Gao, J.; Rega, N.; Zheng, G.; Liang, W.; Hada, M.; Ehara, M.; Toyota, K.; Fukuda, R.; Hasegawa, J.; Ishida, M.; Nakajima, T.; Honda, Y.; Kitao, O.; Nakai, H.; Vreven, T.; Throssell, K.; Montgomery Jr., J. a.; Peralta, J. E.; Ogliaro, F.; Bearpark, M. J.; Heyd, J. J.; Brothers, E. N.; Kudin, K. N.; Staroverov, V. N.; Keith, T. a.; Kobayashi, R.; Normand, J.; Raghavachari, K.; Rendell, a. P.; Burant, J. C.; Iyengar, S. S.; Tomasi, J.; Cossi, M.; Millam, J. M.; Klene, M.; Adamo, C.; Cammi, R.; Ochterski, J. W.; Martin, R. L.; Morokuma, K.; Farkas, O.; Foresman, J. B.; Fox, D. J. G16 C01. 2016, p Gaussian 16, Revision C.01, Gaussian, Inc., Wallin. https://gaussian.com/citation/.
- (61) Krishnan, R.; Binkley, J. S.; Seeger, R.; Pople, J. A. Self-consistent Molecular Orbital Methods. XX. A Basis Set for Correlated Wave Functions. J. Chem. Phys. 1980, 72 (1), 650-654.
- (62) Clark, T.; Chandrasekhar, J.; Spitznagel, G. W.; Schleyer, P. V. R. Efficient Diffuse Function-Augmented Basis Sets for Anion Calculations. III. The 3-21+G Basis Set for First-Row Elements, Li-F. J. Comput. Chem. 1983, 4 (3), 294-301.
- (63) Ziessel, R.; Matt, D.; Toupet, L. Construction of a Phosphane-Based Metallo-Synthon Suitable for the Selective Formation of a Tetranuclear Ru 2 -Cu 2 Macrocycle. J. Chem. Soc., Chem. Commun. **1995**, *41* (19), 2033–2035.
- (64) Motloch, P.; Jašík, J.; Roithová, J. Gold(I) and Silver(I) π -Complexes with Unsaturated Hydrocarbons. Organometallics 2021, 40 (10), 1492-1502.

Appendices

Experimental details

Synthesis of L¹ and L² was carried out according to the procedure by Ziessel et al.⁶³

Synthesis of 2-(6'-methyl-[2,2'-bipyridin]-6-yl)ethan-1-ol L1

To a stirred solution of 6,6'-dimethyl-2,2'-bipyridine (250 mg, 1.36 mmol) in THF (4 mL) at -76 °C dropwise LDA (2 M, 0.82 mL,1.63 mmol) added. The color changes from light orange to dark green. After 1 hr., paraformaldehyde (48.9 mg, 1.63 mmol) suspension in THF (1 mL) was added dropwise, maintaining the temperature at -76 °C. The reaction mixture was then allowed to attain room temperature overnight. After 16 hrs., the reaction mixture was quenched with 25 mL water, followed by extraction with CHCl₃ (3 x 30 mL). Combined organic fractions were dried over the sodium sulfate and concentrated under reduced pressure. The crude obtained was purified to yield 93 mg (32 %). ESI-MS (LTQ XL): $[(\mathbf{L}^1)H]^+ \rightarrow 215$, $[(\mathbf{L}^1)Na]^+ \rightarrow 237$ and $[(\mathbf{L}^1)_2Na]^+ \rightarrow 451$ observed. ¹H NMR (400 MHz, CDCl₃) δ 8.30 (d, 1H), 8.07 (d, 1H), 7.77-7.67 (m, 2H), 7.18-7.15 (m, 2H), 4.64 (broad s,1H), 4.12-4.09 (t, 2H), 3.10-3.08 (t, 2H), 2.63 (s, 3H). ¹³C NMR (101 MHz, CDCl₃) δ 160.06, 158.01, 155.63, 155.15, 137.62, 137.14, 123.36, 123.24, 119.09, 117.90, 61.78, 38.56, 24.65.

Synthesis of 2-methyl-1-(6'-methyl-[2,2'-bipyridin]-6-yl)propan-2-ol L²

To a stirred solution of 6,6'-dimethyl-2,2'-bipyridine (250 mg, 1.36 mmol) in THF (4 mL) at -76 °C dropwise LDA (2 M, 1.22 mL, 2.44 mmol) added. The color changes from light orange to dark green. After 1 hr., acetone (~1 mL, 13.6 mmol) was added dropwise, maintaining the temperature at -76 °C. The reaction mixture was then allowed to attain room temperature overnight. After 16 hrs., the reaction mixture was quenched with 25 mL water, followed by extraction with CHCl₃ (3 x 30 mL). The combined organic fractions were dried over the sodium sulfate and concentrated under reduced pressure. The crude obtained was further purified by prep TLC in diethyl ether. ESI-MS (LTQ XL): $[(L^2)H]^+ \rightarrow 243$, $[(L^2)Na]^+ \rightarrow 265$ and $[(L^2)_2Na]^+ \rightarrow 507$ observed. ¹H NMR (400 MHz, CDCl₃) δ 8.33 (d, 1H), 8.06 (d, 1H), 7.76 (t, 1H), 7.67 (t, 1H), 7.19-7.10 (m, 2H), 2.99 (s, 2H), 2.62 (s, 3H), 1.26 (s, 6H). ¹³C NMR (101 MHz, CDCl₃) δ 159.23, 157.99, 155.34, 154.90, 137.84, 137.18, 124.26, 123.45, 119.11, 117.96, 70.82, 48.40, 29.52, 24.62.

Synthesis of 2-([2,2'-bipyridin]-6-yl)phenol L³

Firstly, the synthesis of 6-(2"-methoxyphenyl)-2,2'-bipyridine was followed from the procedure by Kagalwala et al.⁴⁴ 6-bromo-2,2'-bipyridine (293.75 mg, 1.25 mmol) and 2-methoxyphenyl boronic acid (189.95 mg, 1.25 mmol) were added to a 25 mL

pressure tube. The solids were dissolved in a mixture of toluene/EtOH (1:1 v/v, 10 mL) and purged with N₂ for 15 min. The K₂CO₃ dissolved in water (1 M, 2 mL) was added next, as well as the Pd(PPh₂), (72 mg, 5 mol%), which was added by dissolving in toluene (1 mL). The mixture was purged for another 15 min and subsequently closed and heated to 100 °C. The heating was applied for 48 hrs., after which no color change was observed. The reaction mixture was filtered, and water (5 mL) was added to the filtrate. This was subsequently extracted using (DCM 3 x 5 mL). The organic layers were combined, evaporating the solvent under reduced pressure. The final crude product was purified over an alumina column using heptane/ethyl acetate (9:1 v/v) as eluent. The final yield was 0.1136 g (0.43 mmol, 43 %). ESI-MS (LTQ XL): [MH]+ observed 263.

6-(2"-methoxyphenyl)-2,2'-bipyridine (0.1136 g, 0.43 mmol) was dissolved in a minimal amount of DCM and transferred to a 10 mL round-bottom flask. The DCM evaporated by air for 1 hr., and the final bit was boiled at 40 °C. Aqueous HBr solution (48% 4 mL) was added to the flask, and the mixture was refluxed at 120 °C for 24 hr. The reaction mixture turned from yellow to brown/orange during this period. The mixture was added to water (30 mL), upon which a white solid precipitated. The mixture was neutralized with KOH, which yielded a creamy white solid. The mixture was filtered, and the solids were purified using trituration. The final yield was a yellow solid (0.0665 g, 0.268 mmol, 62%). ESI-MS (LTQ XL): [(L³)Na]+ \rightarrow 271 and $[(\mathbf{L}^3)_3 \text{Na}]^+ \rightarrow 519 \text{ observed}.$

¹H NMR (400 MHz, CDCl₂) δ 14.59 (s, 1H), 8.75 (d, 1H), 8.34 (d, 1H), 8.21 (d, 1H), 8.05-7.95 (m, 2H), 7.92-7.84 (m, 2H), 7.42-7.32 (m, 2H), 7.08 (d, 1H), 6.98-6.94 (m, 1H). 13C NMR (101 MHz, CDCl₂) δ ¹³C NMR (101 MHz, CDCl₂) δ 159.78, 157.37, 154.62, 153.36, 149.65, 138.86, 137.37, 131.65, 126.49, 123.71, 120.81, 119.50, 119.29, 119.03, 118.98, 118.49.

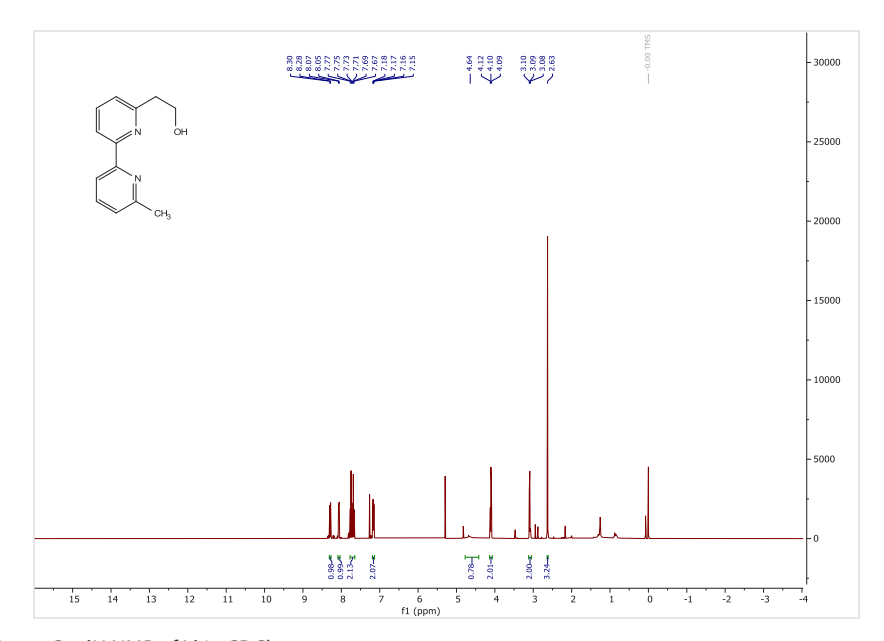


Figure S1: 1 H NMR of L 1 in CDCI $_{3}$ 1H NMR (400 MHz, CDCI3) δ 8.30 (d, 1H), 8.07 (d, 1H), 7.77-7.67 (m, 2H), 7.18-7.15 (m, 2H), 4.64 (broad s,1H), 4.12-4.09 (t, 2H), 3.10-3.08 (t, 2H), 2.63 (s, 3H).

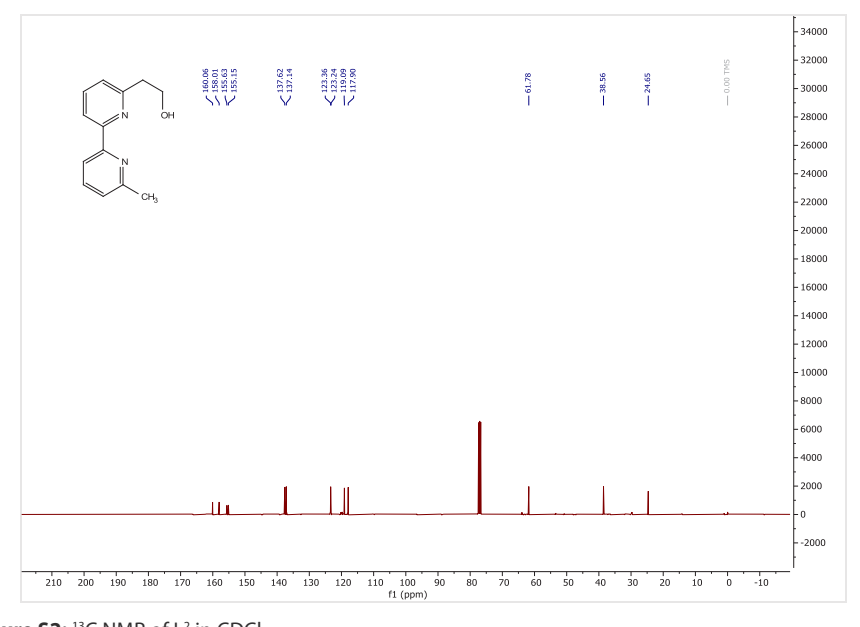


Figure S2: 13 C NMR of L 2 in CDCl $_{3}$ 13C NMR (101 MHz, CDCl $_{3}$) δ 160.06, 158.01, 155.63, 155.15, 137.62, 137.14, 123.36, 123.24, 119.09, 117.90, 61.78, 38.56, 24.65.

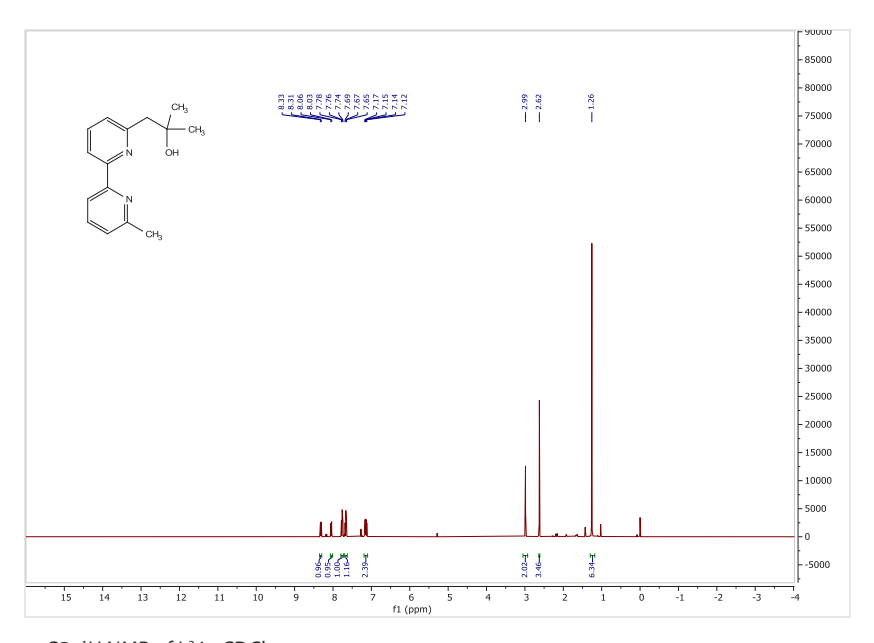


Figure S3: ¹H NMR of L² in CDCl₃ 1 H NMR (400 MHz, CDCl $_{3}$) δ 8.33 (d, 1H), 8.06 (d, 1H), 7.76 (t, 1H), 7.67 (t, 1H), 7.19-7.10 (m, 2H), 2.99 (s, 2H), 2.62 (s, 3H), 1.26 (s, 6H).

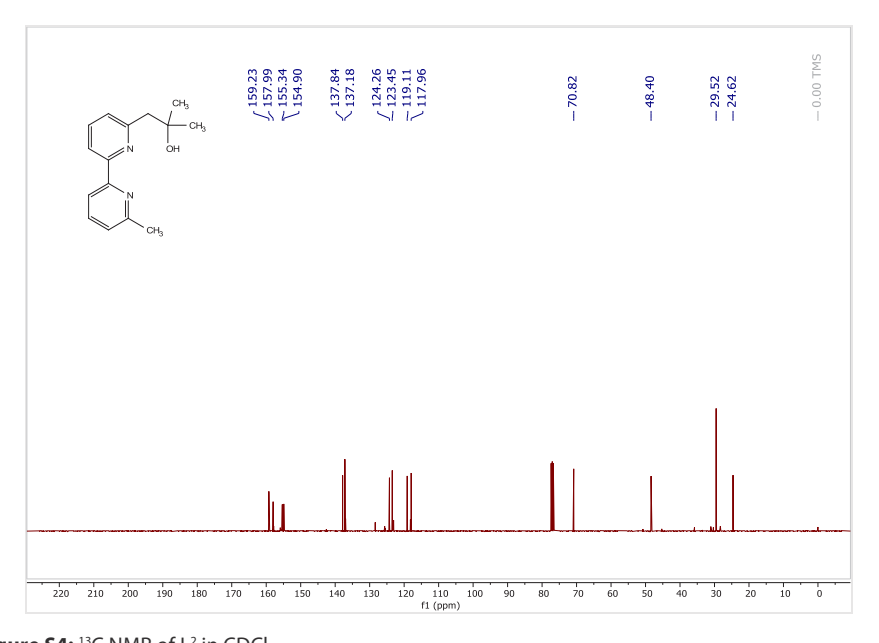


Figure S4: 13C NMR of L2 in CDCl, $^{13}\text{C NMR (101 MHz, CDCl}_{\text{\tiny 3}}) \ \delta \ 159.23, \ 157.99, \ 155.34, \ 154.90, \ 137.84, \ 137.18, \ 124.26, \ 123.45, \ 119.11, \ 124.26, \ 123.45, \ 119.11, \ 124.26, \ 123.45, \ 119.11, \ 124.26, \ 123.45, \ 119.11, \ 124.26, \ 123.45, \ 119.11, \ 124.26, \ 123.45, \ 119.11, \ 124.26, \ 123.45, \ 119.11, \ 124.26, \ 123.45, \ 119.11, \ 124.26, \ 123.45, \ 119.11, \ 124.26, \ 123.45, \ 119.11, \ 124.26, \ 123.45, \ 119.11, \ 124.26, \ 123.45, \ 119.11, \ 124.26, \ 123.45, \ 124.26, \ 123.45, \ 119.11, \ 124.26, \ 123.45, \ 119.11, \ 124.26, \ 123.45, \ 124.26, \ 123.45, \ 119.11, \ 124.26, \$ 117.96, 70.82, 48.40, 29.52, 24.62.

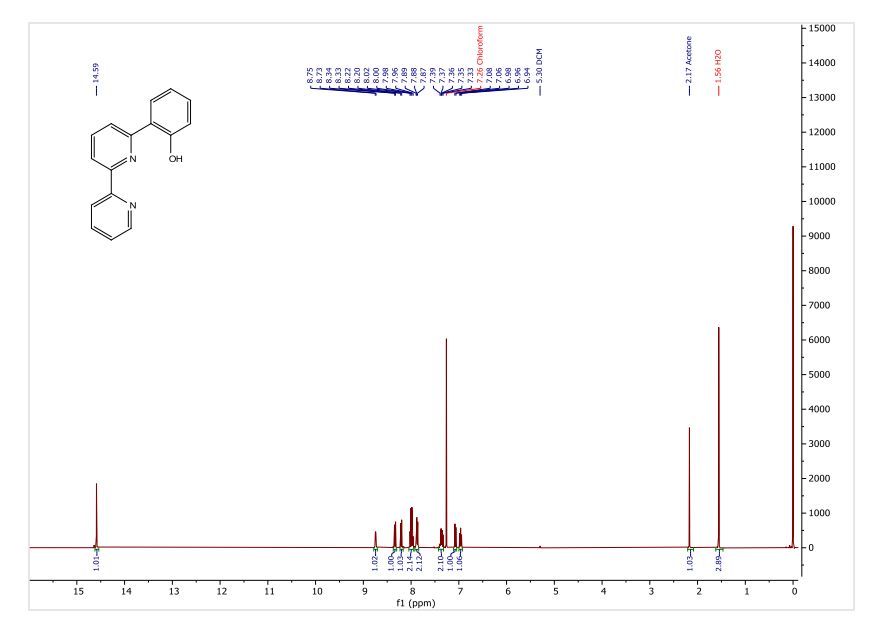
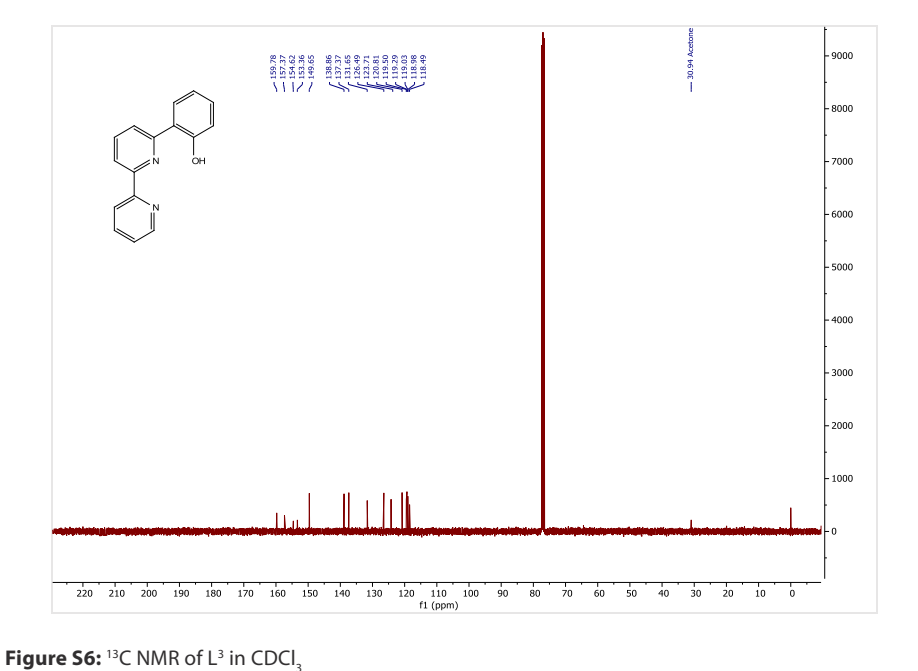


Figure S5: 1 H NMR of L³ in CDCl₃ 1H NMR (400 MHz, CDCl3) δ 14.59 (s, 1H), 8.75 (d, 1H), 8.34 (d, 1H), 8.21 (d, 1H), 8.05-7.95 (m, 2H), 7.92-7.84 (m, 2H), 7.42-7.32 (m, 2H), 7.08 (d, 1H), 6.98-6.94 (m, 1H).



¹³C NMR (101 MHz, CDCl₃) δ 159.78, 157.37, 154.62, 153.36, 149.65, 138.86, 137.37, 131.65, 126.49, 123.71, 120.81, 119.50, 119.29, 119.03, 118.98, 118.49.

Mass spectrometric studies

Mass spectrometric experiments were performed on Thermo Scientific LTQ XL or Finnigan LCQ Deca XP mass spectrometer equipped with an electrospray ionization (ESI) source.⁶⁴ General conditions were as follows: sheath gas 5-40 arbitrary unit, auxiliary gas 0-10 arbitrary unit, capillary temperature 150-220 °C, spray voltage 2-5 kV, capillary voltage 0-30 V, and tube lens 0-50 V. The energy resolved collision induced dissociation (CID) experiments were performed on an LCQ Deca mass spectrometer with an ESI source. The collision energies in the LCQ ion trap was calibrated based on the measurements of dissociation energies of a series of thermometer ion consisting of benzylpyridinium and benzhydrylpyridinium thermometer ions using Schroder's method. 46-48 The complexes were measured 2-4 times to calculate the standard deviation. The helium tagging photodissociation method measured the IR spectra of the mass-selected complexes on the ISORI instrument equipped with an ESI source.³⁶ The ISORI instrument features a wire quadrupole trap operated at 3-5 K; trapped ions are cooled down by the helium buffer gas. These cooled ions then attach a helium atom, the helium complexes on irradiation with the IR laser undergo helium detachment and the IR spectra is constructed as $(1 - N_i/N_{in})$, where N_i and N_{in} are numbers of helium complexes with and without laser irradiation. For irradiation, OPO/OPA system from LaserVision was used. SuperK was used to record the photofragmentation spectra.

ESI spectrums

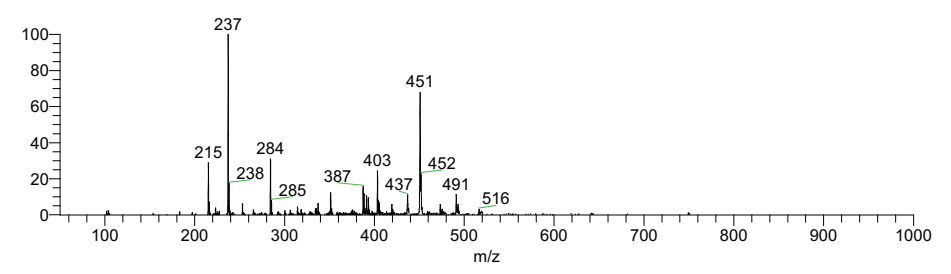


Figure \$7: L1 in acetonitrile

 $[(L^1)H]^+ \rightarrow 215, [(L^1)Na]^+ \rightarrow 237 \text{ and } [(L^1)_5Na]^+ \rightarrow 451$

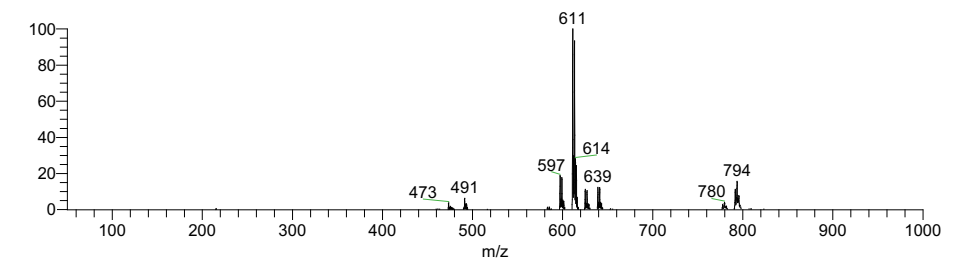


Figure S8: L^1 and $CuOAc_2$ in acetonitrile $[(L^1-H)_2Cu_2(OAc)]^+ \rightarrow 611$

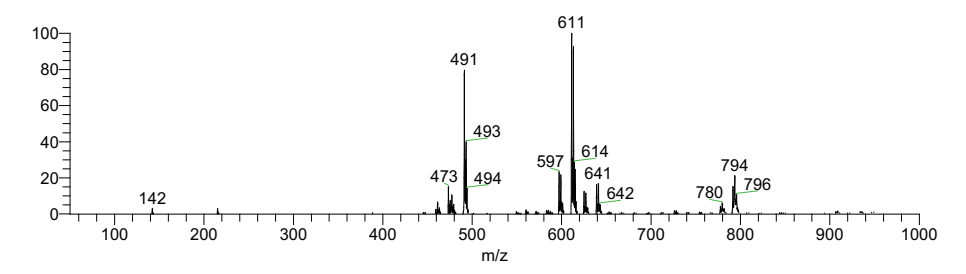


Figure S9: L¹ + CuOAc₂ + TEMPO in acetonitrile $[(L^1)_2Cu]^+ \rightarrow 491$ and $[(L^1-H)_2Cu_2(OAc)]^+ \rightarrow 611$

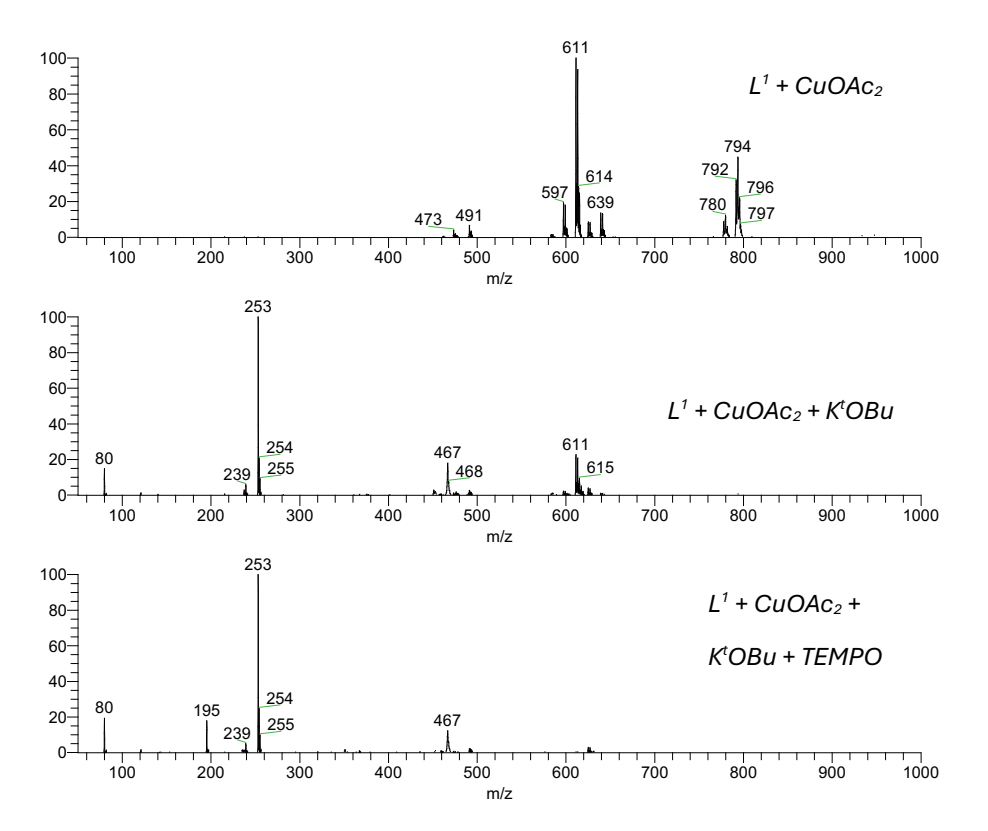


Figure S10: $L^1 + CuOAc_2 + K^tOBu + TEMPO$ in acetonitrile $(\mathbf{L}^1 - H)_2 Cu_2(OAc)]^+ \rightarrow 611; [(\mathbf{L}^1)K]^+ \rightarrow 253; [(\mathbf{L}^1)_2K]^+ \rightarrow 467$

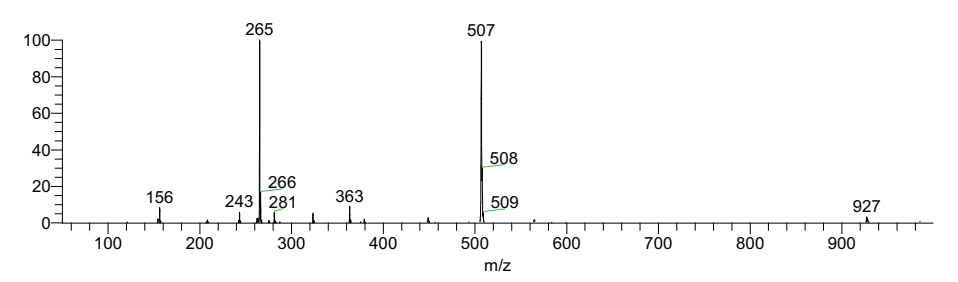


Figure S11: L² in acetonitrile $[(\mathbf{L}^2)H]^+ \rightarrow 243$, $[(\mathbf{L}^2)Na]^+ \rightarrow 265$ and $[(\mathbf{L}^2)_{_2}Na]^+ \rightarrow 507$

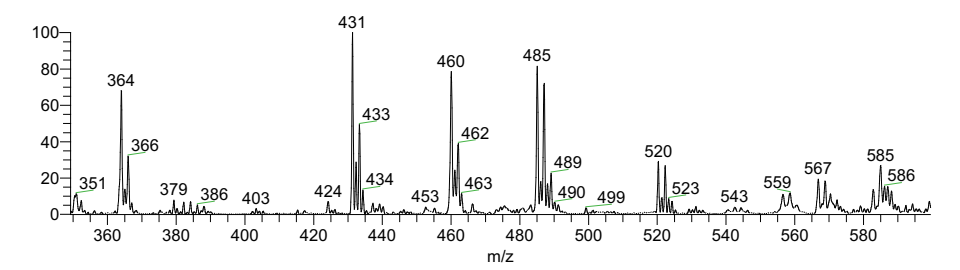


Figure S12: $L^2 + K^tOBu + Cu(OAc)_2 + TEMPO$ in Acetonitrile $[(L^2-H)Cu(TEMPO)]^+ \rightarrow 460$

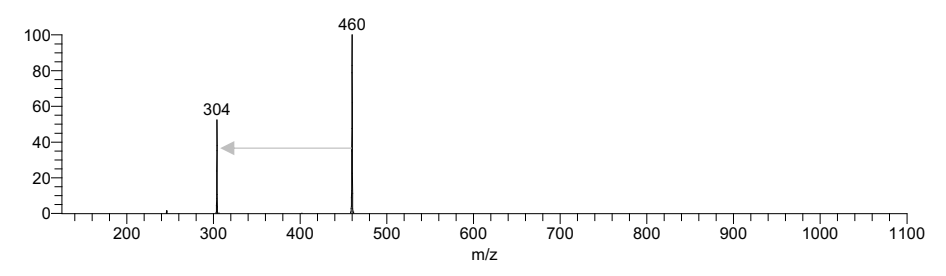


Figure S13: CID of m/z 460 **[(L**²-**H)Cu(TEMPO)]**⁺ at C.E = 16 %

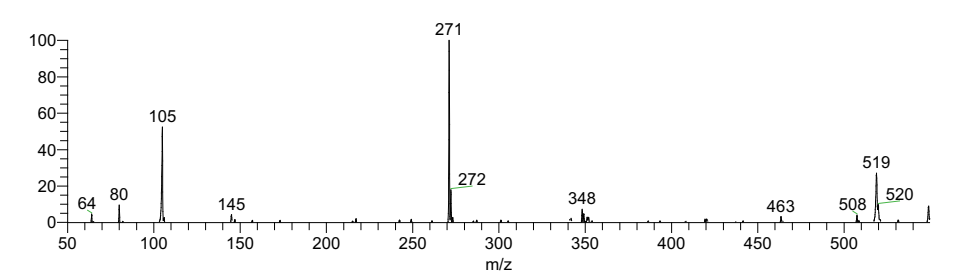


Figure \$14: L³ in acetonitrile $[(L^3)Na]^+ \rightarrow 271 \text{ and } [(L^3)_2Na]^+ \rightarrow 518$

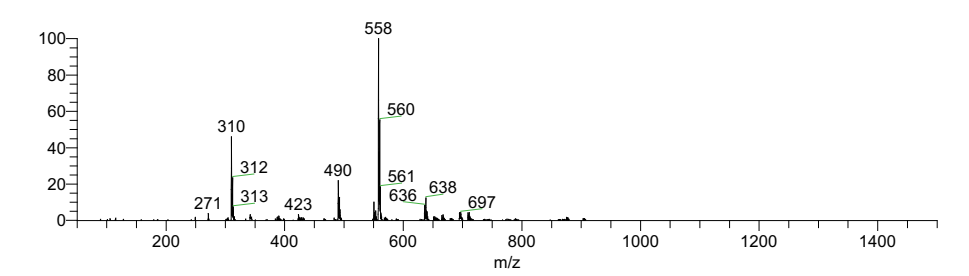


Figure S15: L^3 and $CuCl_2$ $[(L^3-H)Cu]^+ \rightarrow 310$ and $[(L^3)(L^3-H)Cu]^+ \rightarrow 558$

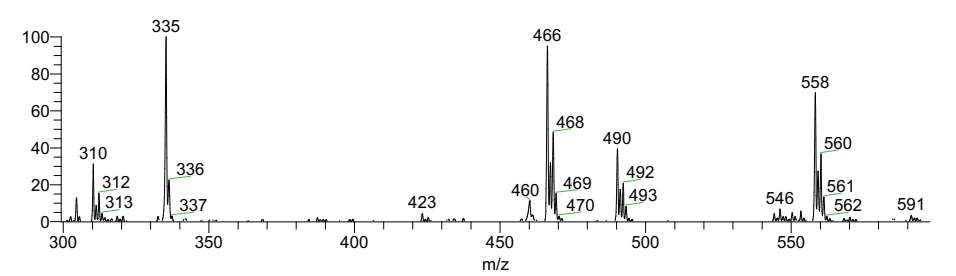


Figure \$16: L³ + CuCl₂ + TEMPO $[(\mathbf{L}^3\text{-H})\text{Cu}(\text{TEMPO})]^+ \rightarrow 466$

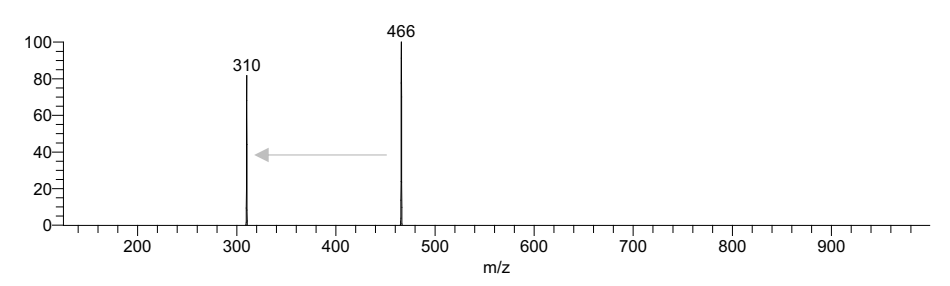


Figure S17: CID of m/z 466 [(L³-H)Cu(TEMPO)]⁺ at C.E = 21 %

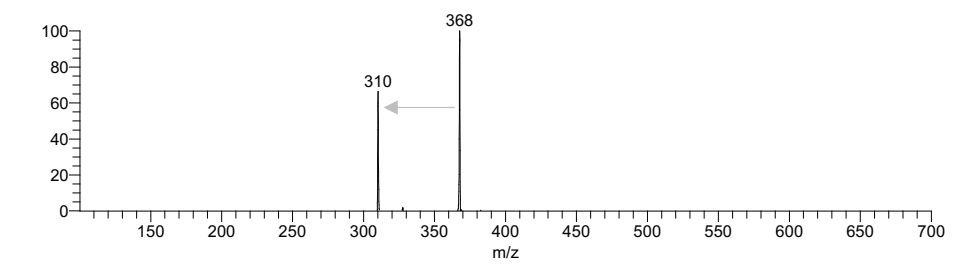


Figure S18: CID of m/z 368 **[(L**³**-H)Cu(acetone)]**⁺ at C.E = 14 %

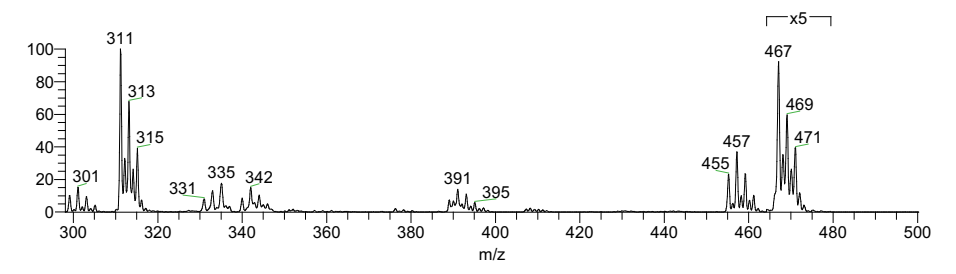


Figure \$19: L³ + ZnBr₂ + TEMPO $[(\mathbf{L}^3\text{-H})Zn]^+ \rightarrow 311 \text{ and } [(\mathbf{L}^3\text{-H})Zn(\text{TEMPO})]^+ \rightarrow 467$

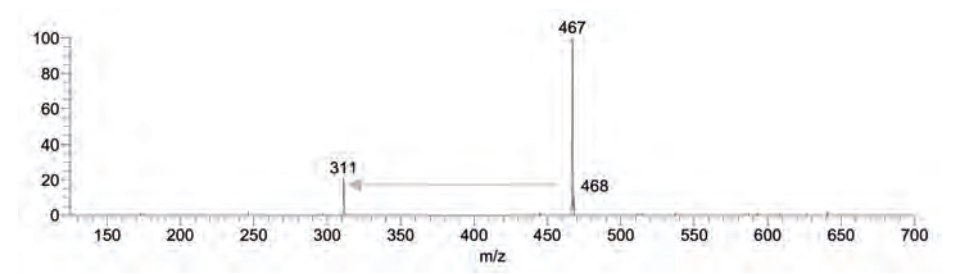


Figure S20: CID of m/z 368 [(L³-H)Cu(acetone)]⁺ at C.E = 17 %

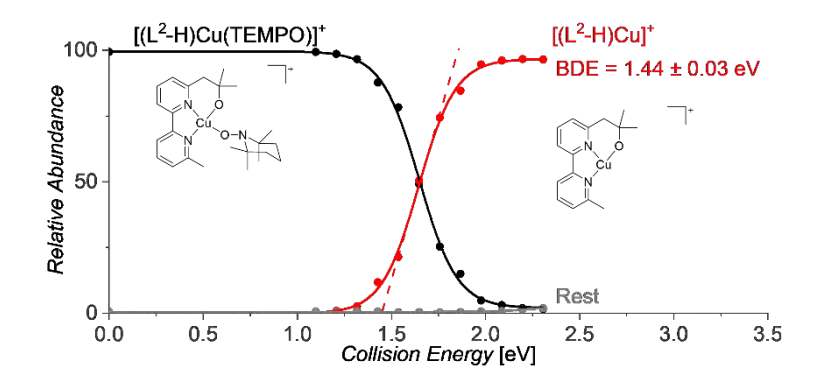


Figure S21: Energy resolved CID of m/z 460 [(L2-H)Cu(TEMPO)]+

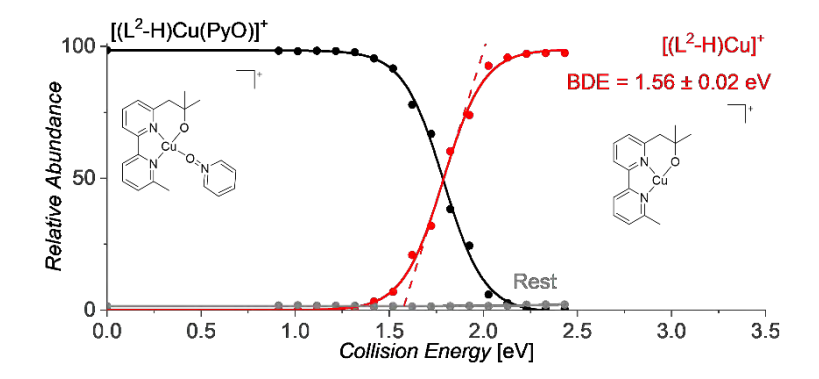


Figure S22: Energy resolved CID of m/z 399 [(L2-H)Cu(PyO)]+

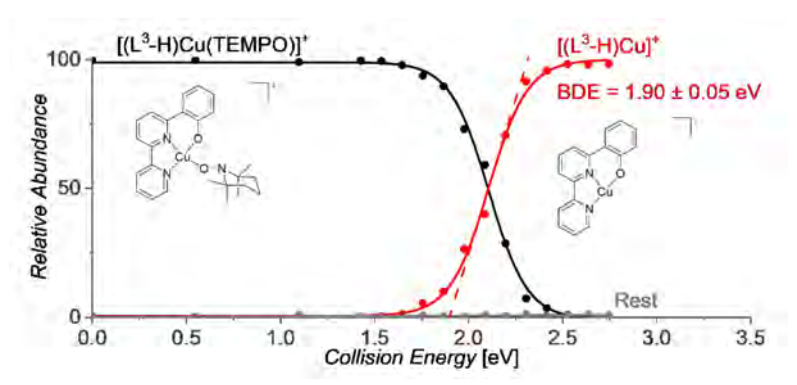


Figure S23: Energy resolved CID of m/z 466 [(L³-H)Cu(TEMPO)]+

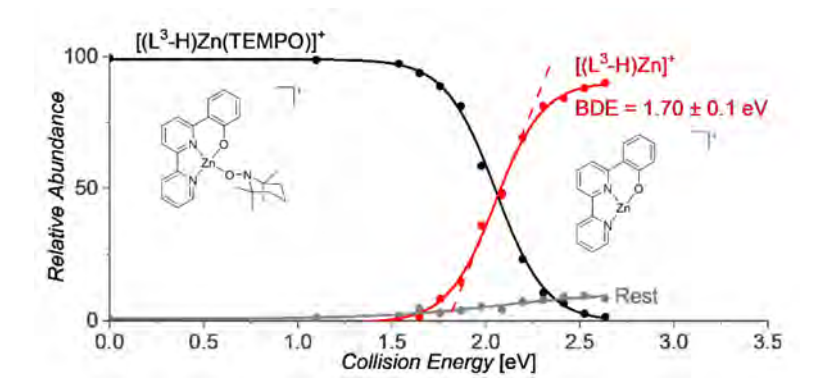


Figure S24: Energy resolved CID of m/z 467 [(L3-H)Zn(TEMPO)]+

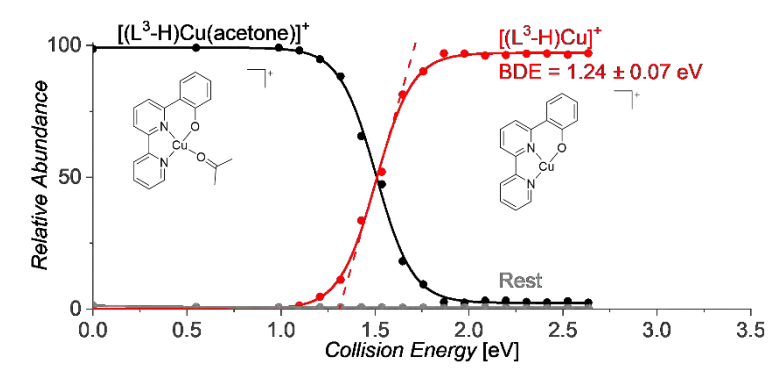


Figure S25: Energy resolved CID of m/z 368 [(L³-H)Cu(acetone)]⁺

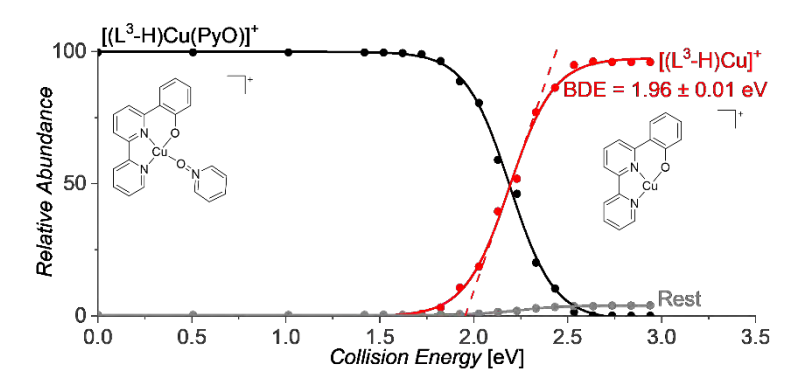


Figure S26: Energy resolved CID of m/z 405 [(L³-H)Cu(PyO)]+

Ion Spectroscopy

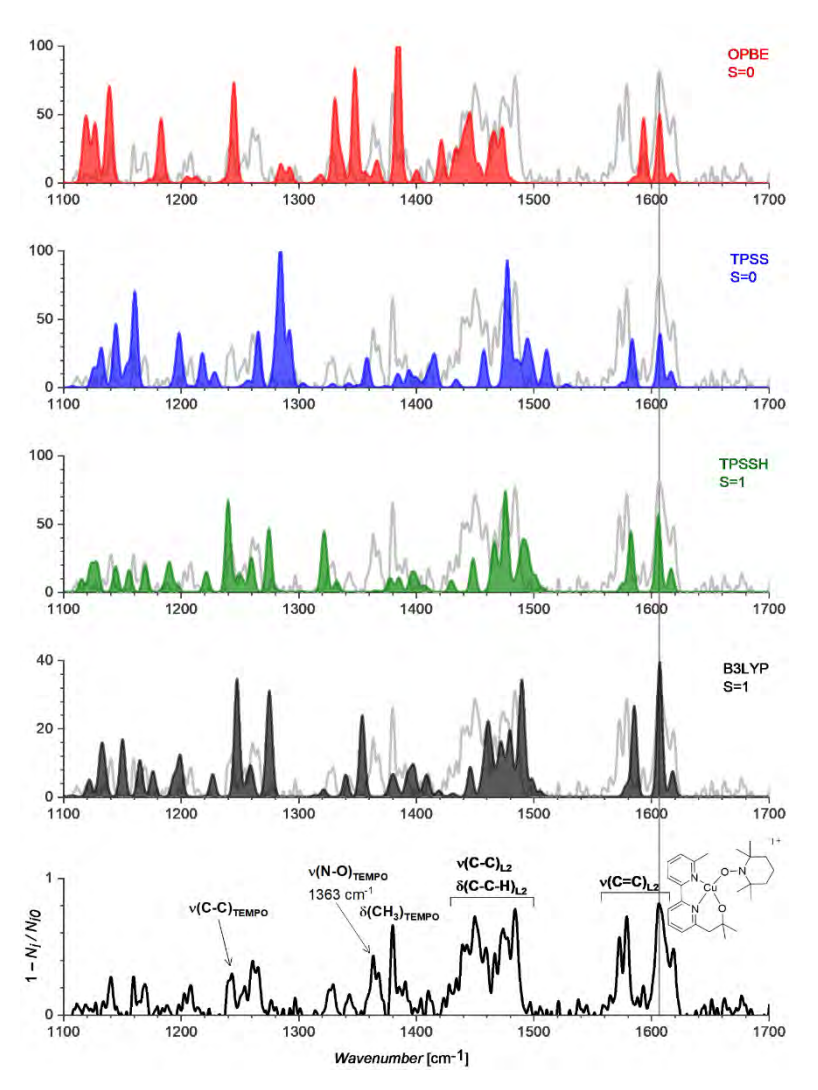


Figure S27: Comparison of the theoretical IR spectra of X² optimized in the singlet or triplet states using different DFT functionals (6-311+G(2d,p) basis set) with the experimental helium tagging IRPD spectrum. The theoretical spectra were scaled so that the experimental C=C stretch at 1607 cm⁻¹ is reproduced (OPBE: 0.998, red; TPPS: 1.005, blue; TPPSH: 0.987, green; B3LYP-D3:0.985, black).

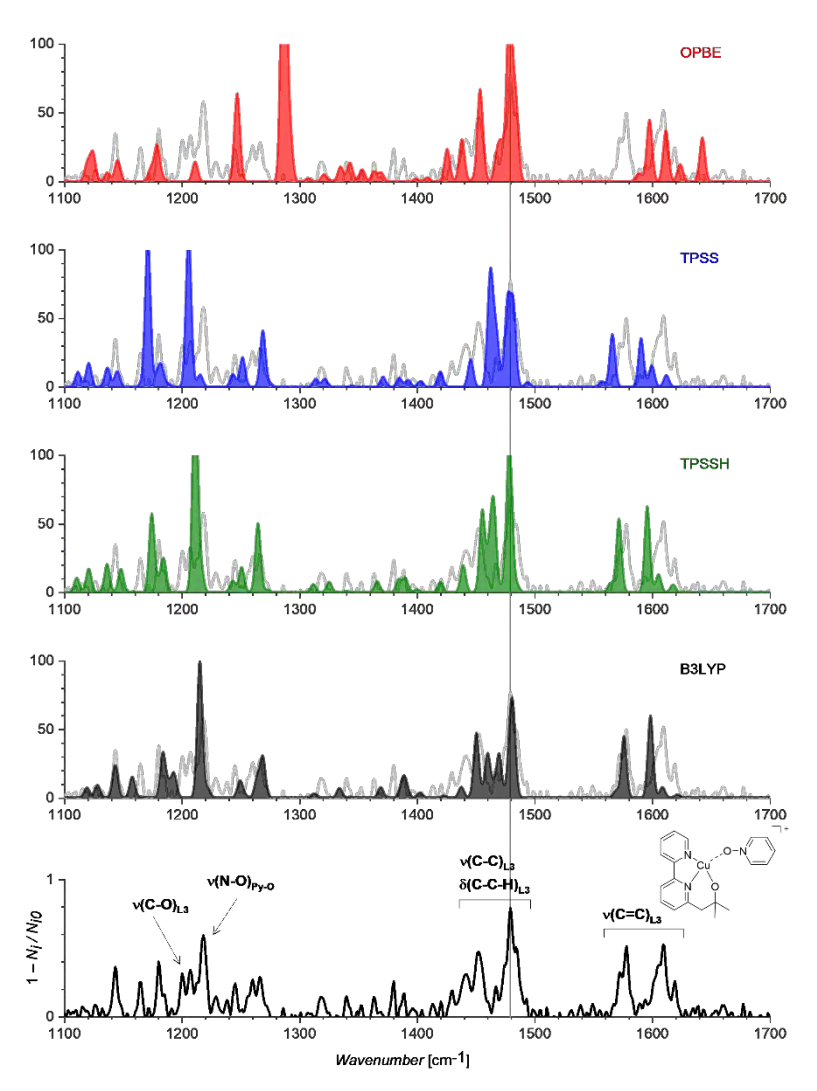


Figure S28: Comparison of the theoretical IR spectra of $[(L^2-H)Cu(PyO)]^+$ optimized using different DFT functionals (using 6-311+G(2d,p) basis set) with the experimental helium tagging IRPD spectrum. The theoretical spectra were scaled so that the experimental band at 1480 cm⁻¹ is reproduced (OPBE: 1.002, red; TPPS: 0.995, blue; TPPSH: 0.980, green; B3LYP-D3:0.979, black).

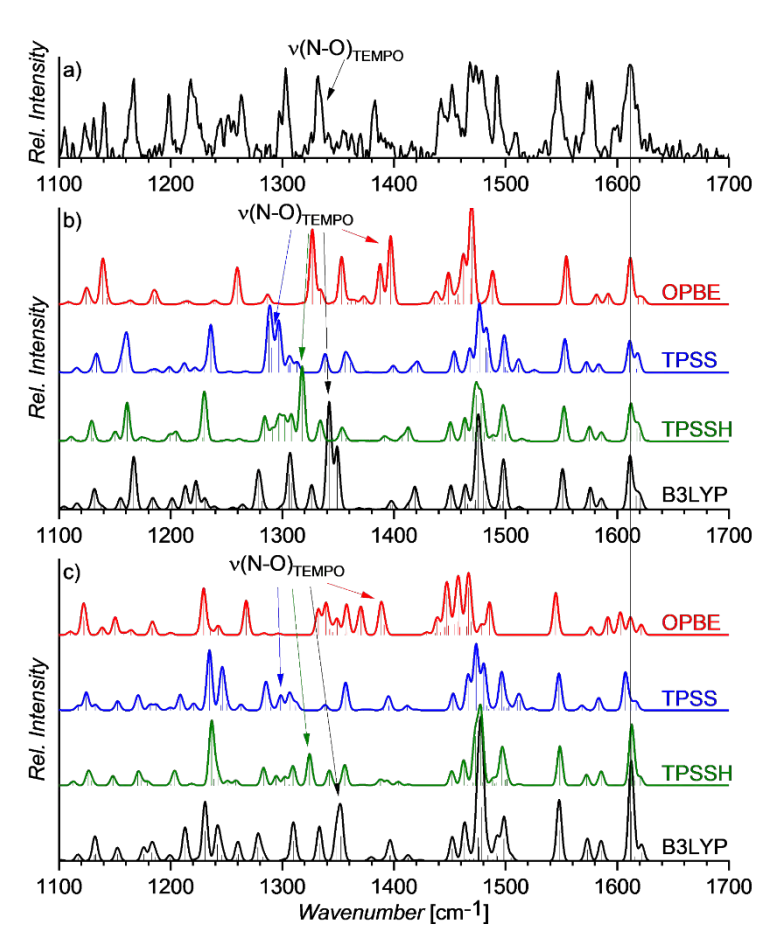


Figure S29: Comparison of the experimental helium tagging IRPD spectrum of \mathbf{X}^3 (a) with the theoretical harmonic IR spectra of X³ optimized in the singlet (b) and triplet (c) states using different DFT functionals. The theoretical spectra were scaled so that the experimental C=C stretch at 1612 cm⁻¹ is reproduced (OPBE: 1.0; TPPS: 1.006; TPPSH: 0.989; B3LYP-D3: 0.9865), the scaling factor is the same for the singlet and triplet states. The structures show the optimized geometries with different DFT functionals (color-coded).

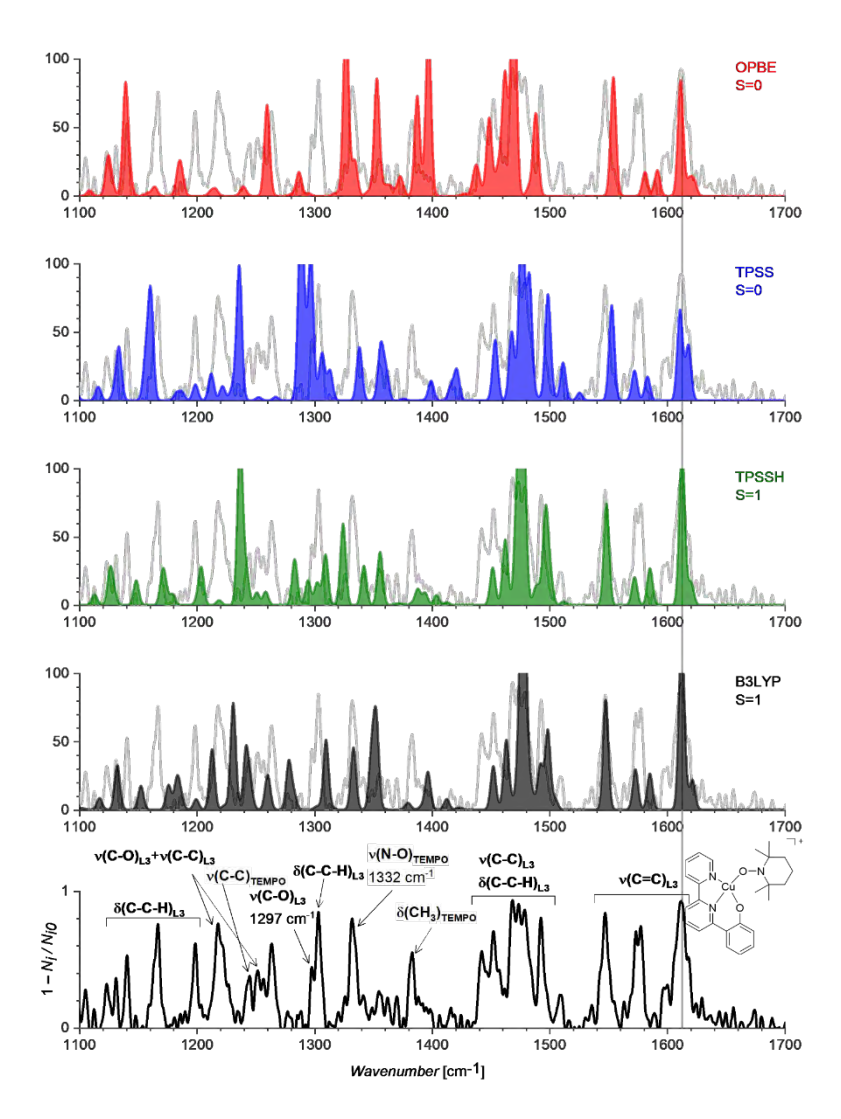


Figure S30: Comparison of the theoretical IR spectra of X³ optimized in the singlet or triplet states using different DFT functionals (using 6-311+G(2d,p) basis set) with the experimental helium tagging IRPD spectrum. The theoretical spectra were scaled so that the experimental C=C stretch at 1612 cm⁻¹ is reproduced (OPBE: 1.0, red; TPPS: 1.006, blue; TPPSH: 0.989, green; B3LYP-D3:0.9865, black).

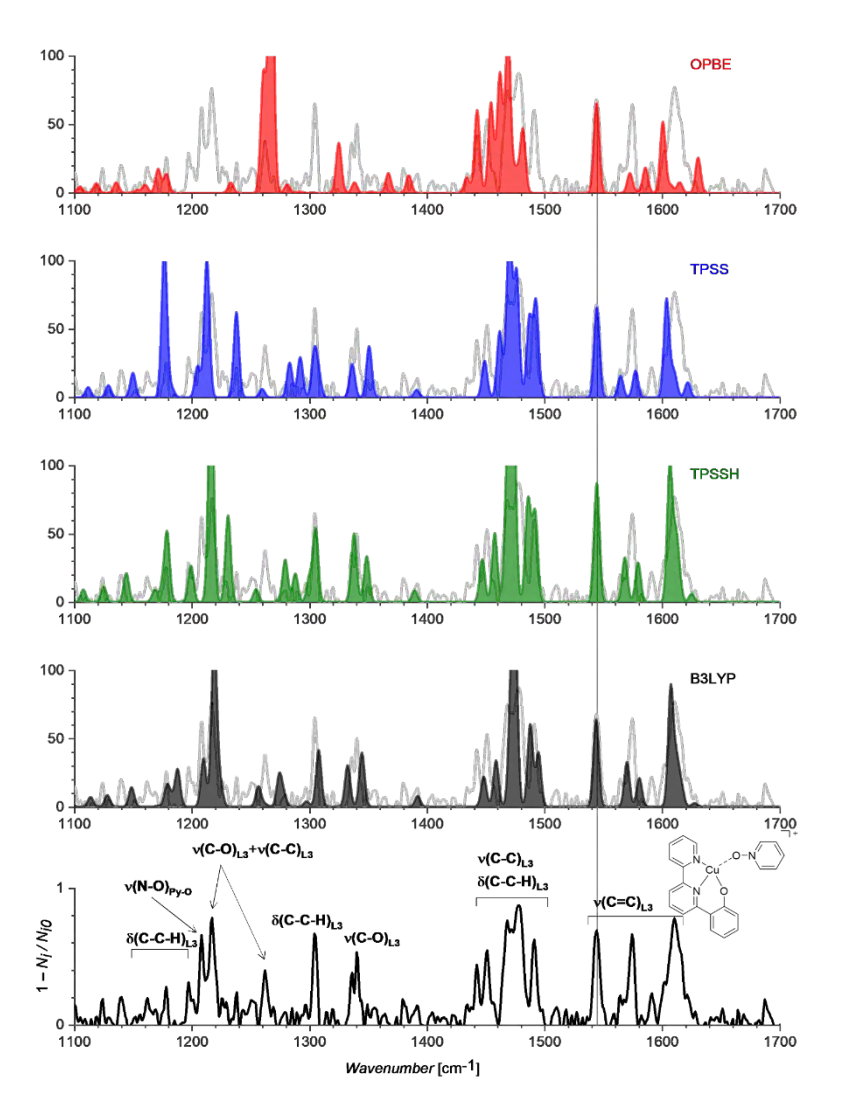


Figure S31: Comparison of the theoretical IR spectra of [(L³-H)Cu(PyO)]+ optimized using different DFT functionals with the experimental helium tagging IRPD spectrum. The theoretical spectra were scaled so that the experimental C=C stretch at 1545 cm⁻¹ is reproduced (OPBE: 0.996, red; TPPS: 1.002, blue; TPPSH: 0.985, green; B3LYP-D3:0.983, black).

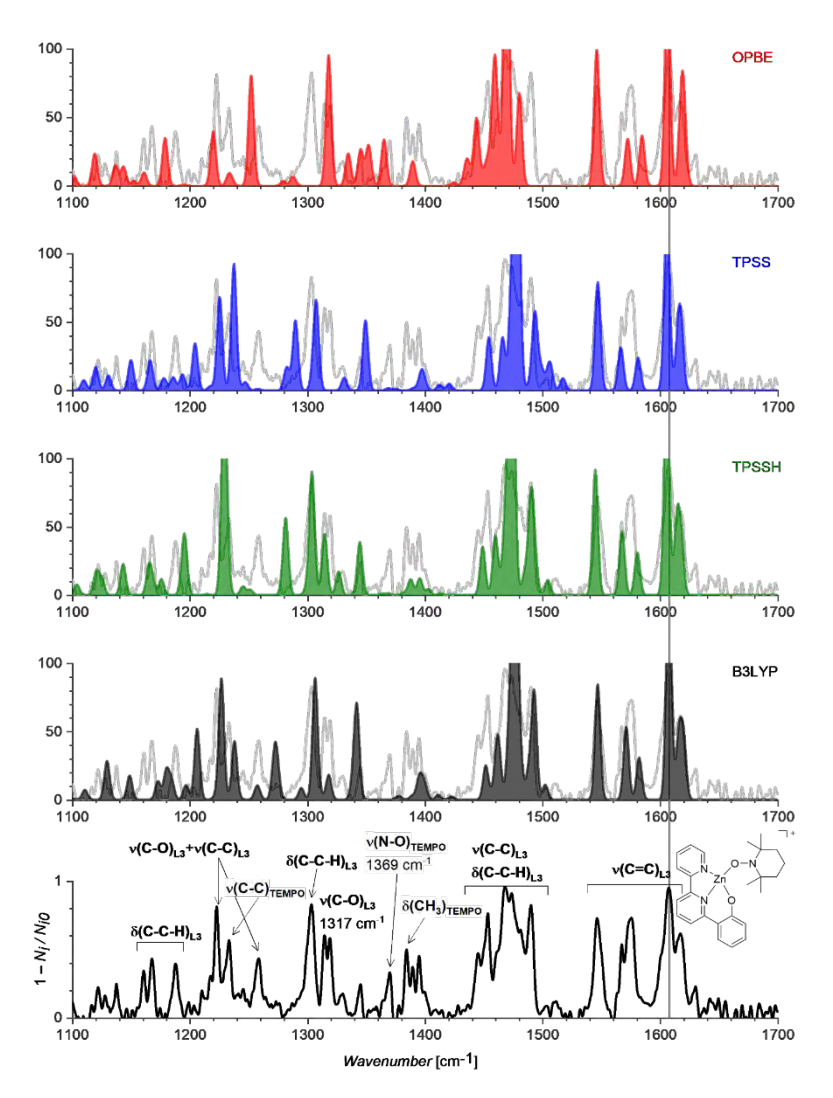


Figure S32: Comparison of the theoretical IR spectra of [(L³-H)Zn(TEMPO)]⁺ optimized using different DFT functionals with the experimental helium tagging IRPD spectrum. The theoretical spectra were scaled so that the experimental C=C stretch at 1607 cm⁻¹ is reproduced (OPBE: 0.996, red; TPPS: 1.004, blue; TPPSH: 0.986, green; B3LYP-D3:0.985, black).

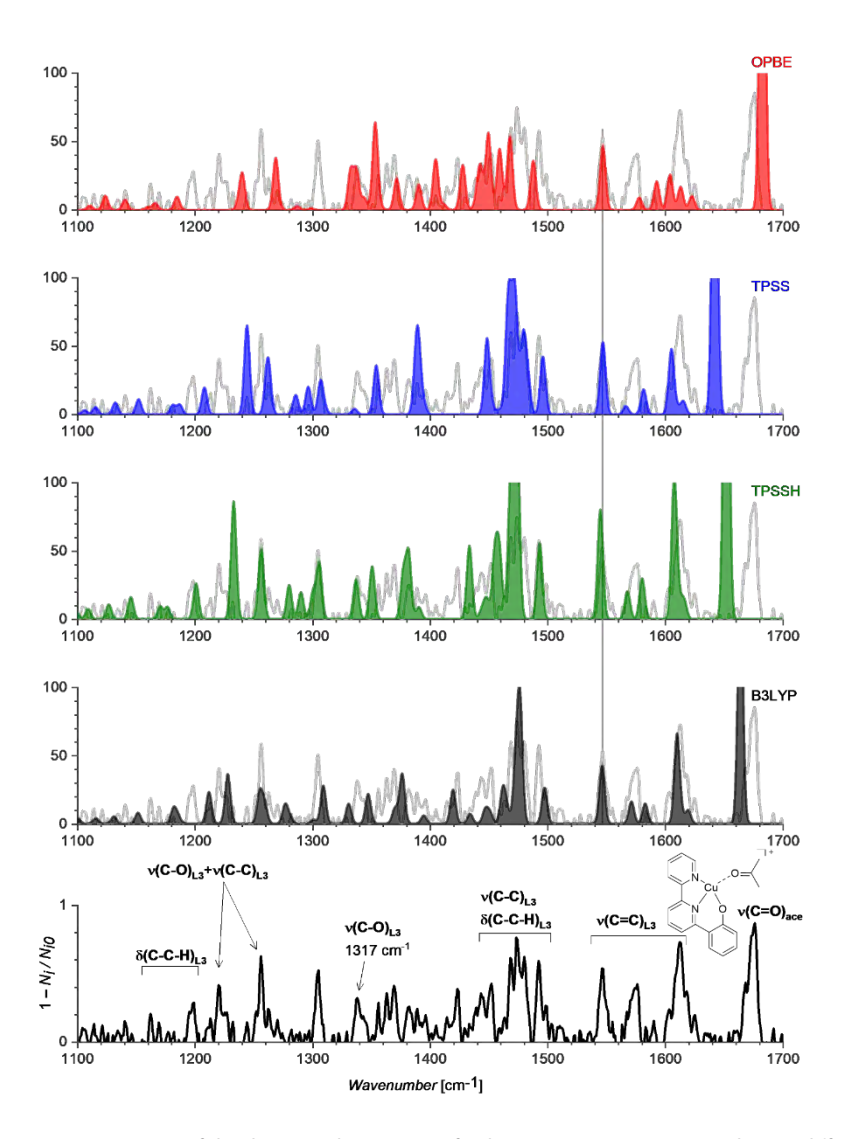


Figure S33: Comparison of the theoretical IR spectra of [(L³-H)Cu(acetone)]+ optimized using different DFT functionals with the experimental helium tagging IRPD spectrum. The theoretical spectra were scaled so that the experimental C=C stretch at 1545 cm⁻¹ is reproduced (OPBE: 1.001, red; TPPS: 1.005, blue; TPPSH: 0.986, green; B3LYP-D3:0.985, black).

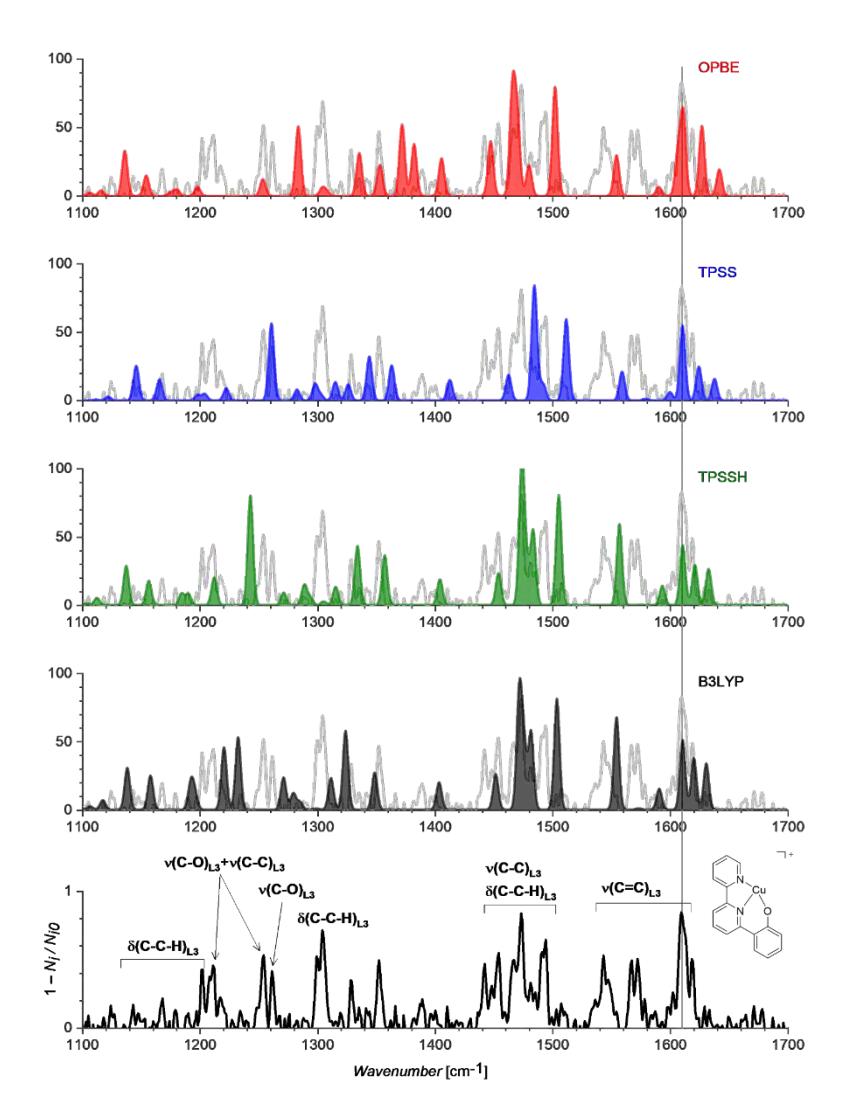


Figure S34: Comparison of the theoretical IR spectra of [(L³-H)Cu]+ optimized using different DFT functionals with the experimental helium tagging IRPD spectrum. The theoretical spectra were scaled so that the experimental C=C stretch at 1610 cm-1 is reproduced (OPBE: 1.012, red; TPPS: 1.018, blue; TPPSH: 0.996, green; B3LYP-D3:0.992, black).

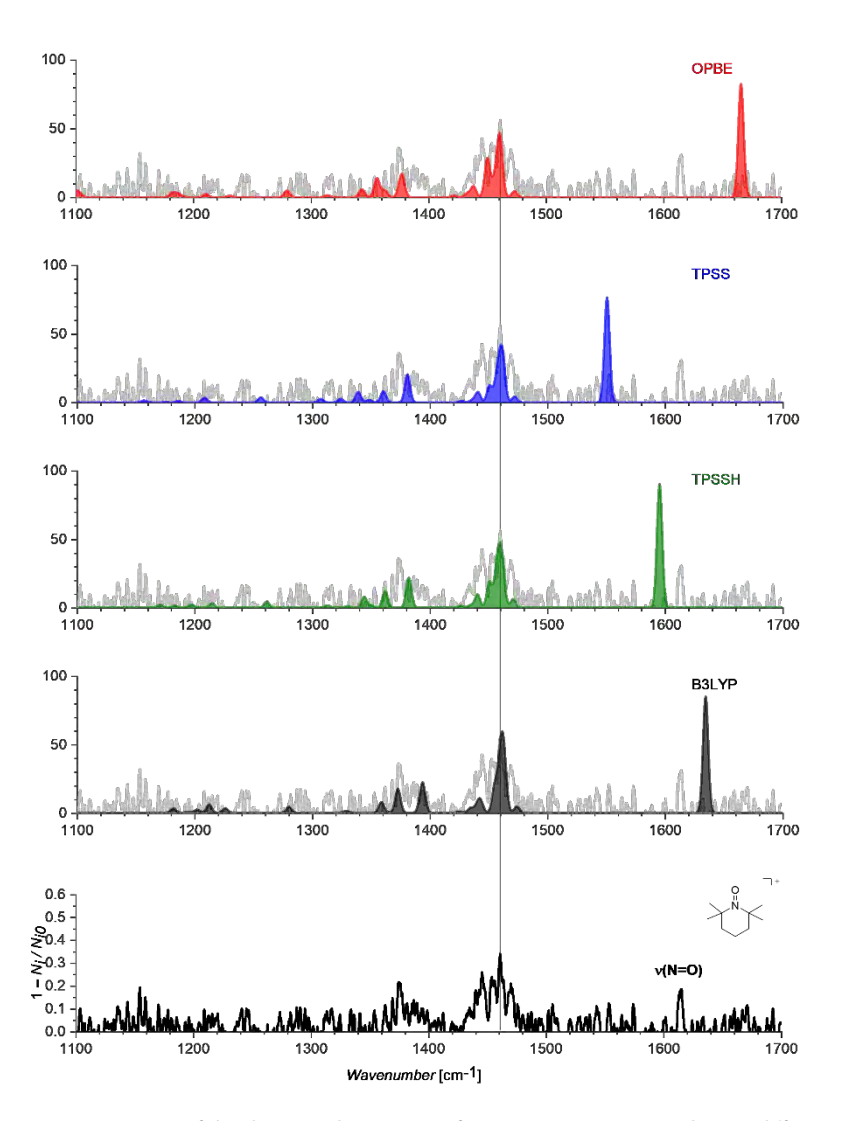


Figure S35: Comparison of the theoretical IR spectra of [Temponium]+ optimized using different DFT functionals with the experimental helium tagging IRPD spectrum. The theoretical spectra were scaled so that the experimental C=C stretch at 1461 cm⁻¹ is reproduced (OPBE: 1.012, red; TPPS: 1.018, blue; TPPSH: 0.996, green; B3LYP-D3:0.992, black).

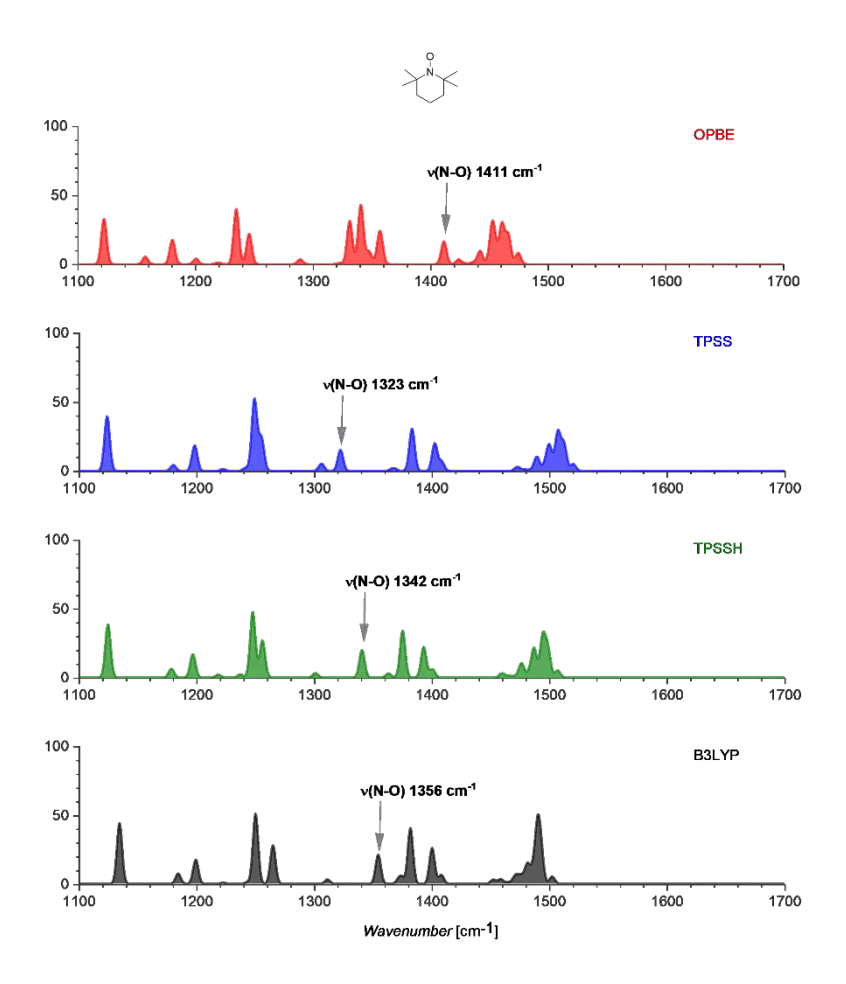


Figure S36: Overlay of the theoretical IR spectra of TEMPO optimized using different DFT functionals (OPBE: 0.998, red; TPPS: 1.005, blue; TPPSH: 0.987, green; B3LYP-D3:0.985, black).

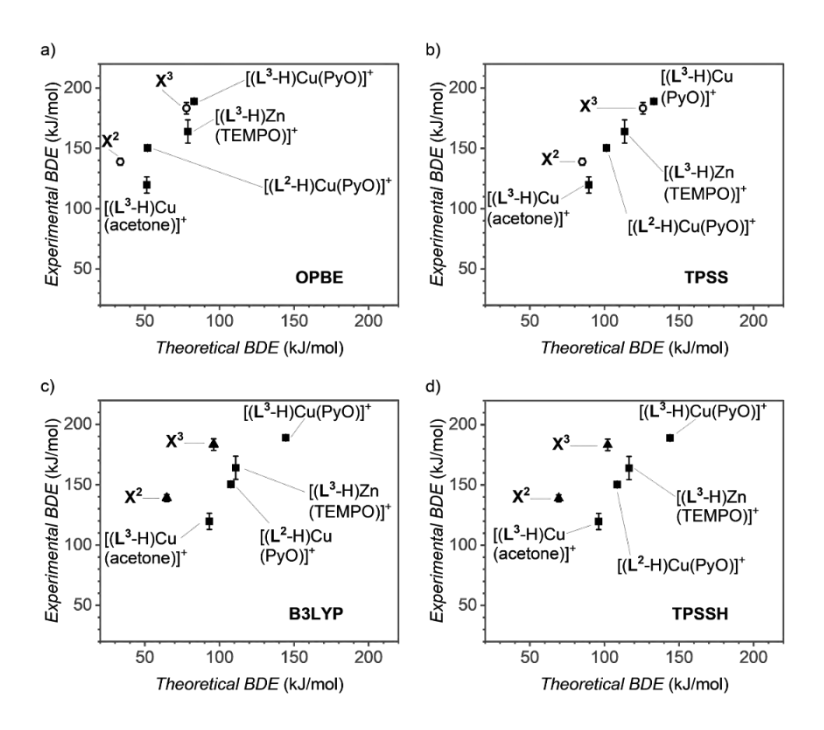


Figure S37: Correlation of the experimental and theoretical bond dissociation energies (BDEs) of TEMPO in complexes X2, X3 (triplet states), and [(L3-H)Zn(TEMPO)]+, BDE of acetone in [(L3-H) Cu(acetone)]⁺ and pyridine N-oxide (PyO) in [(L²-H)Cu(PyO)]⁺ and in [(L³-H)Cu(PyO)]⁺. The theoretical BDEs were calculated at the a) OPBE, b) TPSS, c) B3LYP, and d) TPSSH levels of theory using 6-311+G(2d,p) basis set; the depiction of the spin states: S=0 open circles, S=1/2 - solid rectangles, S=1 - solid triangles.

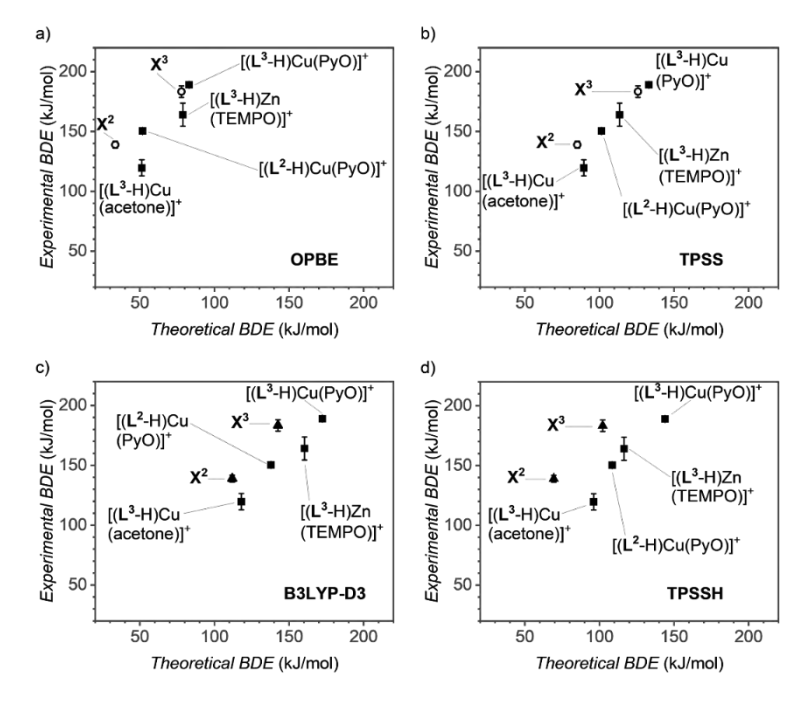


Figure 538: Correlation of the experimental and theoretical bond dissociation energies (*BDEs*) of TEMPO in complexes X^2 , X^3 (triplet states), and $[(L^3-H)Zn(TEMPO)]^+$, *BDE* of acetone in $[(L^3-H)Cu(acetone)]^+$ and pyridine *N*-oxide (PyO) in $[(L^2-H)Cu(PyO)]^+$ and in $[(L^3-H)Cu(PyO)]^+$. The theoretical *BDEs* were calculated at the a) OPBE, b) TPSS, c) B3LYP-D3, and d) TPSSH levels of theory using 6-311+G(2d,p) basis set; the depiction of the spin states: S=0 open circles, S=1/2 - solid rectangles, S=1 - solid triangles.



Appendices

Summary
Samenvatting
Concluding remarks
Research Data Management
List of publications
Curriculum Vitae
Acknowledgements
List of abbreviations

Summary

This thesis presents an investigation into reactive organometallic complexes by mass spectrometry, going beyond the detection of primary molecular ions. The complexity of organometallic reactions, low concentration, and the transient nature of their intermediates necessitate a sensitive analytical approach. Mass spectrometry, recognized for its high sensitivity to charged species, is employed in concert with conventional spectroscopic techniques. The study explores a range of mass spectrometric methodologies, including energy-resolved collision-induced dissociation, delayed reactant labeling, ion mobility spectrometry, and ion spectroscopy, to analyze reactive intermediates and metal complexes.

In **Chapter 1**, we highlight the various mass spectrometric approaches for the reaction mechanism studies. We reviewed advanced mass spectrometry techniques like energy-resolved collision-induced dissociation, delayed reactant labeling, ion mobility, and ion spectroscopy, using literature examples to showcase their use in identifying and elucidating the structures of elusive reactive intermediates.

Chapter 2 outlines the experimental methods employed in this thesis, including delayed reactant labeling, energy-resolved collision-induced dissociation, ion spectroscopy, and theoretical calculations.

In **Chapter 3**, we show how the reaction conditions and the choice of oxidant in the palladium-catalyzed methoxycarbonylation of styrene influenced the selectivity between two catalytic cycles, ultimately dictating the formation of saturated vs. unsaturated ester. The oxidant's role in steering the reaction mechanism offers insights into optimizing alkoxycarbonylation reactions. We detected the intermediates of the alkoxy cycle for the first time. Using delayed reactant labeling, we compared the relative kinetics of the intermediates in the hydride and alkoxy cycles.

Chapter 4 describes a study on Pd-catalyzed C-H olefination reactions of non-directed arenes, emphasizing the role of a novel S,O-ligand in enhancing the reactivity and selectivity of these reactions. Through mass spectrometric charge-tagging, we identified a key 'neutral' intermediate, supporting the proposed catalytic cycle. The findings illuminated the ligand's role in accelerating the reaction by promoting the formation of reactive Pd species, contributing to the understanding of ligand effects in catalysis.

Chapter 5 examines the catalytic potential of rare gold(II) complexes, investigating their formation, stability, and spectral properties. We revealed that certain bidentate and tridentate nitrogen donor ligands stabilize these complexes. Through a combination of mass spectrometric, electrochemical, and ion spectroscopic studies, we correlated the complexes' spectral properties with their electronic structures, offering parallels to stable copper(II) complexes.

Chapter 6 explores the interactions between copper(I), silver(I), and gold(I) metals with π -ligands, examining the role of σ -bonding and π -back-bonding. The findings, supported by X-ray crystallography, NMR, IR spectroscopy, and gas phase experiments, highlight the importance of π -back bonding and the influence of electron density on metal-ligand interactions.

In **Chapter 7**, we investigate the proposed copper intermediate for copper(II)-TEMPO complexes involved in alcohol oxidation, which were previously extensively theoretically studied, but never experimentally detected. Through electrospray ionization mass spectrometry and ion spectroscopy of 'frozen' intermediate, we presented experimental evidence of the complexes' vibrational and electronic characteristics. Our study revealed the multiconfigurational nature of these complexes, suggesting new avenues for understanding and optimizing coppercatalyzed oxidation reactions.

Samenvatting

Dit proefschrift presenteert een onderzoek naar reactieve organometaalcomplexen met behulp van massaspectrometrie, dat verder gaat dan de detectie van primaire molecuulionen. De complexiteit van organometaalreacties, de lage concentratie en de voorbijgaande aard van hun tussenproducten maken een gevoelige analytische benadering noodzakelijk. Massaspectrometrie, bekend om zijn hoge gevoeligheid voor geladen ionen, wordt gebruikt in combinatie met conventionele spectroscopische technieken. Het onderzoek verkent een reeks massaspectrometrische methodologieën, waaronder energy-resolved collisioninduced dissociation, delayed reactant labeling, ion mobility spectrometrie en ionenspectroscopie, om reactieve tussenproducten en metaalcomplexen te analyseren.

In **hoofdstuk** 1 belichten we de verschillende massaspectrometrische benaderingen voor het bestuderen van reactiemechanismen. We bespreken geavanceerde massaspectrometrische technieken zoals energy-resolved collision-induced dissociation, delayed reactant labeling, ion mobility en ion spectroscopie, waarbij we literatuurvoorbeelden gebruiken om hun gebruik bij het identificeren en ophelderen van de structuren van ongrijpbare reactieve tussenproducten te laten zien.

Hoofdstuk 2 beschrijft de experimentele methoden die in dit proefschrift zijn gebruikt, waaronder delayed reactant labeling, energy-resolved collision-induced dissociation, ionenspectroscopie en theoretische berekeningen.

In **hoofdstuk 3** laten we zien hoe de reactieomstandigheden en de keuze van het oxidatiemiddel in de palladium-gekatalyseerde methoxycarbonylering van styreen de selectiviteit tussen twee katalytische cycli beïnvloedden, waardoor uiteindelijk de vorming van verzadigde versus onverzadigde ester werd gedicteerd. De rol van de oxidant in het sturen van het reactiemechanisme biedt inzicht in het optimaliseren van alkoxycarbonyleringsreacties. We hebben voor het eerst de tussenproducten van de alkoxycyclus gedetecteerd. Met behulp van DRL vergeleken we de relatieve kinetiek van de tussenproducten in de hydride- en alkoxycyclus.

Hoofdstuk 4 beschrijft een studie naar Pd-gekatalyseerde C-H olefination -reacties van non-directed arenen, waarbij de rol van een nieuw S,O-ligand in het verbeteren van de reactiviteit en selectiviteit van deze reacties wordt benadrukt. Door middel van massaspectrometrische ladingstags identificeerden we een belangrijk 'neutraal' tussenproduct dat de voorgestelde katalytische cyclus ondersteunt. De

bevindingen belichtten de rol van het ligand in het versnellen van de reactie door de vorming van reactieve Pd-species te bevorderen, wat bijdraagt aan het begrip van ligandeffecten in katalyse.

Hoofdstuk 5 onderzoekt het katalytisch potentieel van zeldzame goud(II) complexen en onderzoekt hun vorming, stabiliteit en spectrale eigenschappen. We onthulden dat bepaalde bidentate en tridentate stikstof donorliganden deze complexen stabiliseren. Door een combinatie van massaspectrometrische, elektrochemische en ion spectroscopische studies, correleerden we de spectrale eigenschappen van de complexen met hun elektronische structuren, wat parallellen oplevert met stabiele koper(II) complexen.

Hoofdstuk 6 onderzoekt de interacties tussen koper(I), zilver(I) en goud(I) metalen met π -liganden, waarbij de rol van σ -binding en π -back-binding wordt onderzocht. De bevindingen, ondersteund door röntgenkristallografie, NMR, IR spectroscopie en gasfase experimenten, benadrukken het belang van π -binding en de invloed van elektronendichtheid op metaal-ligand interacties.

In **hoofdstuk 7** onderzoeken we de voorgestelde koperintermediairen voor koper(II)-TEMPO-complexen die betrokken zijn bij alcoholoxidatie, die eerder uitgebreid theoretisch werden bestudeerd, maar nooit experimenteel werden gedetecteerd. Door middel van electrospray ionization mass spectrometry- en ionenspectroscopie van het 'bevroren' tussenproduct hebben we experimenteel bewijs geleverd voor de vibrerende en elektronische eigenschappen van de complexen. Onze studie onthulde de multiconfigurationele aard van deze complexen, wat nieuwe manieren suggereert voor het begrijpen en optimaliseren van koper-gekatalyseerde oxidatiereacties.

Concluding Remarks

This thesis has investigated advanced mass spectrometric techniques to analyze reactive organometallic complexes, providing new insights into catalytic mechanisms and transient intermediates. By employing methods like energy-resolved collision-induced dissociation, delayed reactant labeling, charge tagging, MS/MS studies, ion mobility spectrometry, and ion spectroscopy, this research has successfully detected and characterized fleeting intermediates, enhancing our understanding of reaction pathways and ligand effects.

The findings underscore the versatility of mass spectrometry as a sensitive tool that complements traditional techniques. From studying palladium-catalyzed methoxycarbonylation to exploring gold and copper complexes, this work advances our understanding of complex reaction mechanisms and the role of ligands. By identifying previously undetected intermediates, this research demonstrates how mass spectrometry uncovers details that traditional methods alone cannot provide.

Throughout my PhD, I have aimed to develop expertise in monitoring and understanding chemical reactions through innovative analytical techniques, with mass spectrometry at the core. My goal is to apply these skills in an industrial setting, where combining mass spectrometry with other analytical methods offers a comprehensive approach to solving chemical challenges and promoting sustainable practices. This research has provided a strong foundation for that goal, equipping me with the skills to tackle challenges in chemical process development.

In conclusion, this work demonstrates the potential of mass spectrometry to deepen our understanding of organometallic chemistry and catalysis.

*

Research Data Management

This thesis research has been carried out under the institute research data management policy of the Institute for Molecules and Materials of Radboud University, The Netherlands.¹

- Data sets for chapters (1, 2, 4 7) are deposited in the Radboud Data Repository as a data sharing collection with a unique digital object identifier (DOI) 10.34973/pdan-6826. It can be accessed via https://doi.org/10.34973/ pdan-6826 upon request of the promotor or the IMM data steward.
- Data set for chapter 3 is deposited in the Radboud Data Repository as a data sharing collection with a unique digital object identifier (DOI) 10.34973/ cqxm-cv50. It can be accessed via https://doi.org/10.34973/cqxm-cv50 upon request of the promotor or the IMM data steward.

Data sets available are:

- Experimental IR and MS data as txt files.
- Output from DFT calculations as log files and xyz data of optimized geometry as txt file.
- ¹ https://www.ru.nl/rdm/vm/policy-documents/ (last accessed 5th April, 2024)



GRADUATE SCHOOL CERTIFICATE

This is to certify that

Jaya Mohansingh Mehara

has participated in the graduate training programme offered by the Graduate School

10 April 2024 Nijmegen, The Netherlands

Ralph Jaspers, Managing Director

List of Publications

- 1. <u>Mehara, J.</u>; Roithová, J. Identifying Reactive Intermediates by Mass Spectrometry. *Chem. Sci.* **2020**, *11* (44), 11960–11972.
- Andris, E.; Segers, K.; <u>Mehara, J.</u>; Rulíšek, L.; Roithová, J. Closed Shell Iron(IV)
 Oxo Complex with an Fe–O Triple Bond: Computational Design, Synthesis, and Reactivity. *Angew. Chemie Int. Ed.* 2020, 59 (51), 23137–23144.
- 3. Mehara, J.; Watson, B. T.; Noonikara-Poyil, A.; Zacharias, A. O.; Roithová, J.; Rasika Dias, H. V. Binding Interactions in Copper, Silver and Gold Π-Complexes. *Chem. A Eur. J.* **2022**, *28* (13).
- 4. <u>Mehara, J.</u>; Koovakattil Surendran, A.; van Wieringen, T.; Setia, D.; Foroutan-Nejad, C.; Straka, M.; Rulíšek, L.; Roithová, J. Cationic Gold(II) Complexes: Experimental and Theoretical Study**. *Chem. A Eur. J.* **2022**, *28* (60), e202201794.
- Naksomboon, K.; Gómez-Bengoa, E.; Mehara, J.; Roithová, J.; Otten, E.; Fernández-Ibáñez, M. Á. Mechanistic Studies of the Palladium-Catalyzed S,O-Ligand Promoted C–H Olefination of Aromatic Compounds. *Chem. Sci.* 2023, 14 (11), 2943–2953.
- 6. Mehara, J.; Roithová, J. Copper(II)-TEMPO Interaction. Isr. J. Chem. 2023, 63 (7–8).
- Mehara, J.; Anania, M.; Kočovský, P.; Roithová, J. Competing Mechanisms in Palladium-Catalyzed Alkoxycarbonylation of Styrene. ACS Catal. 2024, 14,5710–5719.

Curriculum Vitae

Education

· PhD in Chemistry

Radboud University, Netherlands

Thesis: "Understanding Reactive Organometallic Complexes through

Mass Spectrometry"

Supervisor: Prof. Dr. Jana Roithová

M.Sc. in Organic Chemistry

University of Mumbai, India (Jul 2015 – Apr 2017)

- B.Sc. in Chemistry
- University of Mumbai, India (Jul 2012 May 2015)

Research Experience

Chemist

BASF India, Innovation Campus Mumbai (Jan 2018 – Feb 2019)

- Synthesized target small molecules for Crop Protection R&D, specializing in insecticide development.
- · R&D Intern

BASF India, Innovation Campus Mumbai (Jun 2017 – Dec 2017)

- Focused on synthesis of heterocyclic compounds for crop protection research.

Teaching Experience

· Teaching Assistant

Radboud University, Netherlands (2019 – 2023)

- Taught "Synthesis Lab 1," an undergraduate organic chemistry lab course.
- · Student Supervision

Advised masters and bachelor students on research projects related to organometallic complexes and reaction mechanisms.

Awards and Fellowships

• INSPIRE Scholarship (2012 – 2017)

Awarded by the Department of Science & Technology, India, for academic excellence.

• IAS SRFP Fellowship (2016)

Selected for the competitive summer research fellowship by the Indian Academy of Sciences.

Acknowledgments

First and foremost, I would like to express my deepest gratitude to my supervisor, Prof. Roithová, for her invaluable guidance, continuous support, and profound expertise throughout this journey. Her encouragement and insight have been fundamental to this research, and I am deeply thankful for the opportunities she provided me. Jana, your open-door policy and willingness to teach us the mass spectrometers firsthand have been remarkable. I sincerely respect and admire you, not only for your mentorship but also for supporting me during challenging personal times—a support I will never forget.

I would also like to thank the members of my thesis committee, Prof. Harutyunyan, Prof. Chen, and Prof. Kentgens, for their constructive feedback and comments, which have enriched my work. Additionally, I am deeply grateful to the late Prof. Nolte and Dr. Elemans. Engaging with their group and benefiting from their insights greatly shaped aspects of my research, and I am thankful for it.

A special thank you goes to Mariarosa and Eric, whose guidance was instrumental during my early days in the lab. Mariarosa's patience in teaching mass spectrometry laid the foundation for much of my work, while Eric's brilliance helped me resolve key issue early in the project. I missed both of them deeply after they left, but their impact on my research remains profound.

To Guilherme and Noel, I am grateful that we began this journey within months of each other. Sharing courses brought a sense of camaraderie, and I still smile remembering the extra time you took writing during our quantum course exam, Guilherme, even after it had officially ended! Noel, your empathy and listening ear were invaluable—qualities I will truly miss. I wish both of you the utmost success.

Thank you, Jan, for your consistent support, guidance in the lab, and our engaging conversations on stock trading. Deeksha and Matthijs, I appreciate your companionship and for agreeing to be my paranymphs during such a busy period. Deeksha, your kindness and our conversations helped calm me down when I needed it most. Matthijs, I will always remember your fascinating, albeit complex, DRL data presentations in group meetings. Your work is exciting, and I look forward to reading that paper online! Max, thank you for your help with the 'labm8' setup. Adarsh, thank you for introducing me to electrochemistry and guiding me through CV studies. Adarsh, Abhinav, Deeksha, and Bowei, your presentations on electrochemistry have been immensely informative. Anamarija, Buze, and

Michalina, though we met briefly during my PhD, your energy in the group was wonderful. I wish all of you the best for the future.

I must also thank Theo Peters, Peter van Galen, and Paul White for their help with the general instruments, GCTOF, and NMR, respectively. Jesus, your hour-long debate with others on unicorns at the canteen still makes me smile. Quentin, thank you for teaching me timsTOF, and to Monica and Rob, I remember your excitement when the plasma setup for labeled hydrogen peroxide finally worked. Alex, thank you for assisting with ISORI measurements and for hosting, along with Anna, unforgettable barbecues, Halloween, and an Indian cooking day at your place. Anna, you are incredibly kind, and finding a friend who shares my love for books has been a gift. To all of you, I hope you are well and wish you every success.

To my students, Teun, I will always remember how the LTQ was both your best friend and nemesis at times! Niek, despite starting during the challenging pandemic period and only spending limited time in the lab, your synthesis work was excellent. Florian and Julia, you both joined towards the end of my PhD, and your dedication was impressive. I wish you all the best in your studies and future careers.

Thank you to Abbas and Tiemei for the enjoyable ping-pong sessions on the first floor. Jyoti, your guidance in the final steps of my PhD was invaluable.

My heartfelt thanks go to my collaborators, Marieke and Johanan, whose visits to Nijmegen brought energy, curiosity, and insightful questions that enriched the project. I would also like to acknowledge Aurelien, Fabien, and Luke, whom I visited in Lyon. Although our experiment's data proved complex, experiencing the homemade double ion mobility instrument in action was worthwhile, with all its charming "good and bad days." I also thank collaborators from the group of Prof. Rulíšek, Dr. Fernández-Ibáñez, and Prof. Dias.

My appreciation extends to the Faculty of Science at Radboud University and to Paula, Belinda, and Elisabeth for their constant assistance.

I would also like to express my gratitude to those who inspired me to pursue a PhD. In particular, Jagdish and Vinod, your mentorship and belief in my potential during my internship at BASF India were crucial in shaping my aspirations. I am also thankful to the team leaders who shared their PhD and postdoc experiences from various countries, giving me the courage to embark on this path.

Finally, I owe my deepest gratitude to my family. To my mother, your unwavering love, patience, and support have been my anchor. You have always believed in me, and for that, I am eternally grateful. To my late father, whose pride in me was a constant encouragement, I carry your love and support in my heart every day. I know you would have been proud of this accomplishment.

To my dear friends, thank you for the countless joyful moments and for keeping me grounded during the challenging times of this journey.

List of Abbreviations

ACN: acetonitrile

BDE: bond dissociation energy CCS: collision cross-section

CID: collision-induced dissociation

CV: cyclic voltammetry DCM: dichloromethane

DFT: density functional theory

DPPE: 1,2-Bis(diphenylphosphino)ethane
 DPPF: 1,1'-Bis(diphenylphosphino)ferrocene
 DPPM: 1,1-Bis(diphenylphosphino)methane
 DPPP: 1,3-Bis(diphenylphosphino)propane
 DPPB: 1,4-Bis(diphenylphosphino)butane

DRL: delayed reactant labeling

EPR: electron paramagnetic resonance

ESI-MS: electrospray ionization mass spectrometry

HRMS: high-resolution mass spectrometry

IMS-MS: ion mobility spectrometry-mass spectrometry

IR: infrared spectroscopy

IRPD: infrared photodissociation spectroscopy
ISORI: ion spectroscopy of reactive intermediates

KIE: kinetic isotope effect *m/z*: mass-to-charge ratio

NaOAc: sodium acetate

NMR: nuclear magnetic resonance

PSI-ESI-MS: pressurized sample infusion electrospray ionization mass spectrometry

RDS: rate-determining step

TEMPO: 2,2,6,6-Tetramethylpiperidine 1-oxyl TMEDA: N,N,N',N'-Tetramethylethylenediamine

UV-Vis: ultraviolet-visible spectroscopy

visPD: visible photodissociation spectroscopy

